

DEPARTMENT OF PHYSICS AND ASTRONOMY

HEIDELBERG UNIVERSITY

Master thesis in Physics

submitted by

PHILIPP IMMANUEL VOIGT

born in Friedrichshafen

2021



INVESTIGATION OF THE WATER-SIDED SHEAR  
LAYER AT A WIND-DRIVEN WAVY SURFACE  
BY ACTIVE THERMOGRAPHY

This Master thesis has been carried out by

PHILIPP IMMANUEL VOIGT

at the

INSTITUTE OF ENVIRONMENTAL PHYSICS

under the supervision of

PROF. DR. BERND JÄHNE



## ABSTRACT

A local, active thermographic measurement method was advanced and used for measuring the mean viscous shear stress in the water-sided boundary layer of a wind driven air-water interface in the presence of water waves, at low wind speeds up to  $u_{10} = (4.8 \pm 0.3)$  m/s. Higher wind speeds of up to  $u_{10} = (10.7 \pm 0.7)$  m/s were considered to explore the boundaries of the application of the method. The measurements were conducted at the annular wind-wave facility Aeolotron in Heidelberg, Germany. The measurement technique utilizes a thin line which is heated onto the surface perpendicular to the wind direction. The broadening of the line is enhanced by Taylor dispersion due to shear flow in the boundary layer. The temporal development of the line width is monitored by an infrared camera. The broadening is compared to numerically simulated line widths, enabling the determination of the viscous shear stress. This initial study with a rough surface showed promising results for both the evaluation of longer time intervals, and temporally resolved measurements on the order of few seconds. Stationary conditions with the air and water compartments in dynamical equilibrium, corresponding to a quasi-infinite fetch, and non-stationary conditions after turning the wind on were considered. The stationary results were compared to results for the viscous shear stress obtained by water-sided particle streak velocimetry, with results deviating by less than 15%. The non-stationary measurements indicated an overshoot in the viscous shear stress shortly after turning the wind on.

## ZUSAMMENFASSUNG

Eine lokale Messmethode für die mittlere viskose Schubspannung in der wasserseitigen Grenzschicht einer windgetriebenen und wellenbewegten Luft-Wasser Grenzfläche mittels aktiver Thermographie wurde weiterentwickelt und bei niedrigen Windgeschwindigkeiten bis  $u_{10} = (4.8 \pm 0.3)$  m/s angewandt. Höhere Windgeschwindigkeiten bis zu  $u_{10} = (10.7 \pm 0.7)$  m/s wurden betrachtet um die Grenzen der Anwendbarkeit der Methode zu untersuchen. Die Messungen wurden im ringförmigen Wind-Wellenkanal Aeolotron in Heidelberg, Deutschland, durchgeführt. Die Messmethode nutzt eine schmale Linie, die senkrecht zum Wind auf die Wasseroberfläche geheizt wird, deren Breite durch die von der Scherungströmung in der Grenzschicht verursachten Taylor Dispersion verstärkt zunimmt, und mittels einer Infrarotkamera gemessen wird. Die Verbreiterung wird mit numerisch simulierten Linienbreiten verglichen, was Rückschlüsse auf die viskose Schubspannung erlaubt. Diese Pilotstudie lieferte vielversprechende Ergebnisse für sowohl die Auswertung längerer Zeitintervalle, wie auch für höhere zeitliche Auflösungen in der Größenordnung von Sekunden. Stationäre Messbedingungen, mit Luft- und Wasserkörper im dynamischen Gleichgewicht, also quasi-unendlicher Windwirklänge, und instationäre Bedingungen nach dem Windeinschalten wurden berücksichtigt. Die stationären Ergebnisse wurden mit Referenzmessungen anhand Particle Streak Velocimetry verglichen, mit Abweichungen unter 15%. Die instationären Messungen deuten auf einen Überschuss der viskosen Schubspannung kurz nach dem Einschalten des Windes hin.



# CONTENTS

1	INTRODUCTION	1
2	THEORY	5
2.1	Fluid mechanics . . . . .	5
2.2	Wave theory . . . . .	9
2.3	Heat transport . . . . .	17
2.4	Refraction and reflection . . . . .	20
2.5	The viscous boundary layer and shear stress . . . . .	21
2.6	Measurement principle . . . . .	22
3	SURFACE COMPRESSION AND DILATION	25
3.1	Approach by the continuity equation . . . . .	25
3.2	An intuitive approach . . . . .	27
3.3	Linear case . . . . .	28
3.4	Finite amplitude case . . . . .	29
3.5	Implications for the thermographic measurement method . . . . .	32
3.6	Summary of chapter 3 . . . . .	39
4	SETUP AND MEASUREMENTS	41
4.1	The Aeolotron . . . . .	41
4.2	Setup January 2021 . . . . .	41
4.3	Setup by Arne Emmel [2017] . . . . .	44
4.4	Setup January 2019 - reference method (PSV) . . . . .	45
4.5	Measurements . . . . .	46
5	SIMULATION	49
5.1	Heating step . . . . .	49
5.2	Diffusion step . . . . .	50
5.3	Shifting step . . . . .	52
5.4	Boundary conditions . . . . .	52
5.5	Evaluation of the simulation . . . . .	52
5.6	Constants and parameters used in the simulation . . . . .	54
6	IMAGE PROCESSING AND DATA ANALYSIS	55
6.1	Calibration . . . . .	55
6.2	Preprocessing of the infrared images . . . . .	56
6.3	Tracking and evaluation of the heated lines . . . . .	58

6.4	Data analysis of the thermographic measurement . . . . .	62
6.5	Image processing and evaluation of the LHC images . . . . .	69
6.6	Particle streak velocimetry . . . . .	72
7	RESULTS AND DISCUSSION . . . . .	79
7.1	Evaluation of long time intervals . . . . .	79
7.2	Short time intervals and non-stationary conditions . . . . .	93
7.3	Surface compression and dilation . . . . .	98
7.4	Additional observations . . . . .	101
7.5	Reference measurement: PSV results . . . . .	106
8	SUMMARY AND OUTLOOK . . . . .	111
	BIBLIOGRAPHY . . . . .	115
A	APPENDIX . . . . .	121
A.1	Main results . . . . .	121
A.2	Long time interval evaluations . . . . .	125
A.3	Radial variations of the viscous shear stress . . . . .	129
A.4	Line width distributions (crest and trough) . . . . .	130
A.5	Non-stationary measurements . . . . .	132
A.6	Further PSV results . . . . .	135
B	MATHEMATICAL TOOLS . . . . .	138



# 1 | INTRODUCTION

The climate of the Earth is determined by the net energy flow to the planet and its surface (Stephens et al. [2012]), with the downward solar flux varying with both geographical location and season (Wild et al. [2013]). The spatially different inputs and outputs of energy cause circulation in both the air and water compartments of the climate system and drive the hydrological cycle. As implicated, the flow patterns of the atmosphere and the oceans are coupled. With the ocean covering about 71% of the Earth's surface (Roy-Barman and Jeandel [2016]), it has a large impact on the planet's climate. It is, for example, a large reservoir for heat and carbon, exchanging these quantities with the atmosphere. The current anthropogenic emissions of CO<sub>2</sub> perturb the energy balance of the Earth and hence the climate, with the ocean dampening these changes due to its uptake of both heat and about 1/3 of the CO<sub>2</sub> emissions (Gruber et al. [2019]). The global mean temperatures strongly depend on the ocean and its response to the present perpetuated forcing (Andrews et al. [2009]).

The coupling between the atmosphere and the ocean also leads to the interaction of the exchange processes. As the density and hence inertia of air is much lower than of water, the air flow velocities tend to be much higher. Thus, momentum is transferred from the air to the water compartment, leading to viscous shear stress and the build-up of water waves, with the stresses possibly also coupling to the state of the wave field (Reichl et al. [2014], Janssen [1997]). These processes are subject to complex and non-linear interaction mechanisms and flow fields, also altering the exchange of, for example, heat and gases, with many of the mechanisms not being completely understood (Liss and Johnson [2014]). Also surface active substances (surfactants) are able to modify the exchange processes (Jähne [2019]), thus biological processes which are a source of surfactants (Wurl et al. [2011]), play a role.

The exchanging quantities must cross the air-water interface. Whereas the fluid layers far from the interface tend to be well-mixed due to turbulent transport, the diminishing influence by eddies close to the surface limits the turbulent transport as the interface is approached. This gives rise to boundary layers, where diffusive transport mechanisms dominate. This simple picture is complicated by the formation and influence of wave breaking, surface renewal events, sea spray and the formation of bubbles, with these effects being important and their presence wind speed dependent (Krall et al. [2019], Wanninkhof et al. [2009]). The latter effects are less pronounced for low wind speeds. The thickness of the boundary layer, which is controlled by the viscous shear stress, is therefore of importance as the transfer velocities increase with a thinning of the layer (Jähne et al. [1987]). Moreover, the water-sided boundary layer also underlies a large influence by orbital motion associated with waves, these being of comparable magnitude as the velocities in the viscous boundary layer (Jähne [2019]).

The water-sided flow structures and exchange mechanisms have been investigated

by passive thermographic approaches (see e.g. Lu et al. [2021] and Lu et al. [2019]). Active thermographic methods have been developed and used to determine heat transfer velocities (Kunz and Jähne [2018]), and been combined with other techniques such as wave slope imaging and boundary layer imaging (Klein [2019]). The boundary layer imaging techniques based on laser induced fluorescence are used for visualizing the exchange processes (see Kräuter et al. [2014], Arnold [2015]). Also air-sided measurements of gas transfer velocities and boundary layer thicknesses relying on laser induced fluorescence have also been developed (Friman [2020]).

The momentum transfer may be measured in several ways. For air-sided measurements, it may be computed from the logarithmic wind profile, if present. For annular wind-wave facilities this approach is not possible due to secondary flows preventing a logarithmic wind profile (Bopp [2014]). Here, momentum balance may be used, which is an approach where the bulk velocities along with the friction from the channel walls are used to determine the momentum input (Ilmberger [1981], Schwenk [2019]). This has the disadvantage of the friction coefficients being difficult to measure.

Particle image or particle streak velocimetry (PIV and PSV), relying on tracking and/or illuminating particles for a known amount of time, enable the contactless measurement of flow velocities, are used to determine the momentum transfer. Both air-sided studies (e.g. Bopp [2018] and Buckley and Veron [2017]), as well as water-sided studies (e.g. Okuda [1982], Banner and Peirson [1995], Siddiqui and Loewen [2010]) have been conducted using PIV and PSV. Besides being rather laborious with respect to the setup, especially if more than one camera is used or field situations are considered, one of the drawbacks is limited temporal resolution as sufficient statistics must be obtained. On the other hand, there is a prospect of wave phase resolved measurements, enabling a closer insight into the flow associated with different wave amplitudes, steepnesses and shapes. Water-sided measurements require a water-sided camera, which is evidently easier to implement in a laboratory setting than in a field situation, particularly without disturbing the system.

Due to the influence of the viscous shear stress on the boundary layer thickness and the exchange processes, a measurement method that can be applied in the field is of interest. Moreover, due to changing measurement conditions in the field, and also the possibility of non-stationary measurements in a laboratory setting, high temporal resolution is desirable. This would open the pathway to study changes in the viscous shear stress for measurement conditions between the limited fetches, i.e. the length of water surface over which the wind can blow unrestrictedly, available in linear channels or with artificial fetch limitations in annular facilities, and the quasi-infinite fetch in circular wind-wave channels and stationary conditions. Hereby stationary measurement conditions refer to the wind and wave fields being in dynamical equilibrium.

As the viscous shear stress is proportional to the velocity gradient with respect to depth, the water-sided shear stress can be approached with a method relying on active thermography and Taylor dispersion, the latter describing an increased apparent diffusivity and diffusion coefficient due to the presence of shear flow. By active thermography, thin lines are heated perpendicular to the wind direction onto the water surface using a laser. The enhanced broadening of the lines with time is monitored, enabling the determination of the velocity gradient. The method was first proposed by Garbe et al. [2007], used in a similar fashion by Gutsche [2014], and further developed by Holtmann [2017], Emmel [2017] and Rembeck [2018], where issues regarding the relation between the observed line widths and the viscous shear stress were present. This was resolved

in Voigt [2019] by numerically simulating the line widths and comparing them with the measurements. This yielded a good agreement between the temporal development of the simulated widths and those experimentally found, with values for the viscous shear stress agreeing well with those found by particle tracking. Only conditions without the presence of waves were considered, achieved by the use of surfactants, since a large influence by waves on the line widths was observed. More specifically, the orbital motion distorts the spatial extents of the fluid parcels at the surface, thereby also distorting the line widths. Generally, as most measurement conditions include waves, it is crucial for the applicability of the method that also such conditions can be handled. Hence, the goal of this study is to further develop the measurement method, hereby exploring the influence of water waves on the line widths and the implications for the subsequent evaluation.

First the theoretical fundamentals will be given in chapter 2, with the main focus on fluid dynamics and wave theory. Also the measurement principle will be explained. In chapter 3 a theoretical model for the surface compression and dilation will be developed and used to discuss the impact on the active thermographic method in this thesis. Thereafter the experimental setup is presented in chapter 4, before a brief description of the numerical simulation is given in chapter 5. In chapter 6 the image- and data processing in will be explained. The experimental results are presented in chapter 7, with focus on both the determination of the viscous shear stress and the impact on the heated lines by the compression and stretching of the surface in light of the implications found in chapter 3. Also the results of a reference measurement by particle streak velocimetry will be presented. The findings are then summarized in chapter 8.



## 2 | THEORY

In this chapter, a brief overview of the most important fundamentals will be given. As the water-side of the air-water interface is of main interest in this thesis, most equations are stated for incompressible Newtonian fluids only.

### CONVENTIONS IN THIS THESIS

If not specified otherwise, the Cartesian coordinates  $(x, y, z)$  will be defined with  $z$  pointing upwards and  $z = 0$  corresponding to the equilibrium water elevation,  $x$  will point in wind direction, which leaves  $y$  as the second horizontal coordinate perpendicular to the wind direction. The velocity vector is defined as  $\vec{v} = (u, v, w)^\top$ .

Derivatives will be denoted analogous to  $\frac{\partial x_j}{\partial x_i} =: \partial_{x_i} x_j$ . The symbol  $d_x f$  will denote the total derivative of  $f$  with respect to  $x$ , whereas  $\partial_x f$  denotes the partial derivative.

Mostly, but not always, explicit denotation of functional and parameter dependencies will be left out for legibility, unless the explicit dependencies are deemed explanatory for the calculations. Generally, the dependencies of particle trajectories are given by  $\vec{x} = \vec{x}(t)$  and the velocity fields by  $\vec{v} = \vec{v}(\vec{x}, t)$ .

### LAGRANGIAN AND EULERIAN SPECIFICATIONS

Two distinctions are made with respect to the choice of viewpoint. The *Eulerian* frame of reference refers to describing the situation from a spatially fixed coordinate system, whereas the *Lagrangian* frame of reference follows an individual fluid parcel. With a quantity  $q = q(\vec{x}, t)$ , it follows by the chain rule,

$$d_t q = \partial_t q + (d_t \vec{x} \cdot \vec{\nabla}) q. \quad (2.1)$$

Hereby  $d_t q$  is the material or total time derivative, whereas  $\partial_t q$  is the local time derivative. Evidently,  $d_t q$  is path dependent as seen by the directional derivative  $d_t \vec{x} \cdot \vec{\nabla}$ , and corresponds to the total temporal change experienced by an individual fluid parcel with the given path, hence describing the Lagrangian view. The local derivative, on the other hand, gives the spatially fixed Eulerian view.

## 2.1

### FLUID MECHANICS

#### CONTINUITY EQUATION

Local conservation of a quantity  $q$  in a fluid requires that  $q$  within a (fixed) volume  $V$  may only change by flowing in or out of the volume, if no sources or sinks  $\gamma$  are

present. Denoting the density of  $q$  as  $\rho_q$  and the velocity field  $\vec{v}$ , the amount of  $q$  flowing through a surface element  $d\vec{S}$  of  $V$  with its normal vector pointing outwards is given by  $\rho_q \vec{v} \cdot d\vec{S} =: \vec{j} \cdot d\vec{S}$ , where the flux  $\vec{j}$  was defined. Hence, within the Eulerian frame of reference, the temporal change of  $q$  in  $V$ :

$$\partial_t q = \partial_t \int_V \rho_q dV = - \oint_{\partial V} \vec{j} \cdot d\vec{S} + \int_V \gamma dV = - \int_V \vec{\nabla} \cdot \vec{j} dV + \int_V \gamma dV, \quad (2.2)$$

where the divergence theorem was used in the last step. This is known as the continuity equation, often stated in differential form,

$$\partial_t \rho_q + \vec{\nabla} \cdot \vec{j} = \gamma, \quad (2.3)$$

and is an important conservation law. Importantly, with  $q$  being mass and  $\gamma = 0$ , one finds for an incompressible fluid, (i.e. derivatives of the density vanish) that

$$\vec{\nabla} \cdot \vec{v} = 0. \quad (2.4)$$

### 2.1.1

#### NAVIER-STOKES EQUATION

Another important conservation law is that of momentum. In the sense of continuum mechanics, Newton's laws of motion  $\vec{F} = d_t(m\vec{v})$ , with mass  $m$  and net force  $\vec{F}$ , can be normalized by volume, hence, for an incompressible, isotropic Newtonian fluid in an *inertial* frame of reference (Kundu [2008]) it is found that:

$$\rho d_t \vec{v} = \rho \partial_t \vec{v} + \rho(\vec{v} \cdot \vec{\nabla})\vec{v} = -\vec{\nabla} p + \rho \vec{g} + \mu \Delta \vec{v}, \quad (2.5)$$

with pressure  $p$ , fluid density  $\rho$ , gravitational acceleration  $\vec{g}$  and dynamic viscosity  $\mu$ . By Newtonian fluid a fluid whose viscosity only depends on the thermodynamic state is meant. This is referred to as the Navier-Stokes equation.

For a Newtonian fluid, the last term in equation (2.5) may be rewritten using Einstein's sum convention, which for the different velocity components  $v_j$  yields:

$$\mu \partial_{x_i}^2 v_j = \mu \left( \partial_{x_i}^2 v_j + \partial_{x_j} (\partial_{x_i} v_i) \right) = \partial_{x_i} \left( \mu (\partial_{x_i} v_j + \partial_{x_j} v_i) \right) =: \partial_{x_i} \tau_{\text{visc},ij}. \quad (2.6)$$

In the first step zero was added (equation (2.4)), in the second step the symmetry of the Hessian matrix was used, and lastly the viscous stress tensor  $\tau_{\text{visc},ij}$  was introduced. The  $\tau_{\text{visc},ij}$  component represents the transport of  $i$  momentum in negative  $j$  direction (Bopp [2018]).

### 2.1.2

#### REYNOLDS DECOMPOSITION AND MOMENTUM TRANSFER

If the inertia forces increase and become large in comparison to the viscous forces, described by the Reynolds number

$$\text{Re} = \frac{UL}{\nu}, \quad (2.7)$$

where  $U$  and  $L$  are a characteristic velocity and length scale, respectively, and  $\nu = \mu/\rho$  the kinematic viscosity, eddies form. These describe fluctuating, swirling flow patterns.

Beyond a critical (system dependent) value of  $Re$ , the flow transits to become turbulent, characterized by highly irregular flow patterns with a chaotic nature. The non-linear inertia term  $(\vec{v} \cdot \vec{\nabla}) \cdot \vec{v}$  in the Navier-Stokes equation enables the transfer of momentum across scales, hence couples these different scales, which is a typical feature of turbulent flow. The energy becomes dissipated at small scales, where viscosity again plays a role, often referred to as Kolmogorov micro scales. In order to cope with these chaotic flow properties, the quantities of interest can be split into a mean  $\bar{q}$  and a fluctuating part  $q'$ . In the presence of waves, when  $q$  is phase dependant, one may additionally average  $q$  keeping the phase  $\varphi$  fixed, in the sense that the average over all  $\varphi$  is  $\langle q \rangle = \bar{q}$  and for given  $\varphi$  is  $\langle q \rangle_\varphi = \bar{q} + \tilde{q}$ , and (Bopp [2018], Buckley and Veron [2016]).

$$q = \bar{q} + \tilde{q} + q', \quad (2.8)$$

known as a Reynolds triple decomposition. For example the velocity may be Reynolds decomposed. Absorbing  $g$  from the Navier-Stokes equation into the modified pressure  $p_g = p + \rho g z$  and averaging over time, yields the Reynolds averaged Navier-Stokes equation for a given phase  $\varphi$  (Bopp [2018]):

$$\partial_{x_i} (\rho(\overline{u_i u_j} + \overline{u_i \tilde{u}_j} + \overline{u_j \tilde{u}_i})) = \partial_{x_i} \left( \underbrace{-\rho \tilde{u}_i \tilde{u}_j}_{\tilde{\tau}_{\text{wave},ij}} - \underbrace{\rho \langle u'_i u'_j \rangle}_{\tilde{\tau}_{\text{turb},ij}} - \underbrace{p_g \delta_{ij}}_{\tilde{\tau}_{\text{pres},ij}} + \underbrace{\mu \partial_{x_i} (\overline{u_j} + \tilde{u}_j)}_{\tilde{\tau}_{\text{visc},ij}} \right), \quad (2.9)$$

with  $\delta_{ij}$  being the Kronecker delta and  $\tilde{\tau}$  denoting that the averaging is done for a given  $\varphi$  (in contrast to the average over phase  $\bar{\tau}$ ). The left hand side is an advection term similar to that found in the diffusion-advection equation (2.59) below. The right hand side shows, as indicated, different terms that can be interpreted as transfer of  $i$  momentum in  $j$  direction, the sum of which corresponds to a total momentum transfer  $\tilde{\tau}_{i,j}$ . The different terms represent the partitioning of  $\tilde{\tau}_{i,j}$ . Regarding the transfer of  $x$  momentum in  $z$  direction, due to the typical orbital motion in the upper water-sided layer (see section 2.2),  $\tilde{\tau}_{\text{wave},xz}$  is expected to be pronounced there.  $\tilde{\tau}_{\text{turb},xz}$  is vanishing in the viscous boundary layer as eddy sizes shrink and turbulent transport becomes neglectable in close proximity to the surface, whereas  $\tilde{\tau}_{\text{visc},xz}$  will have a large influence.

The terms in equation (2.9) may be averaged over  $\varphi$  as well, which removes all terms with  $\tilde{u}_j$  occurring only once, hence the correlation term  $\overline{u_i \tilde{u}_j}$  does not vanish. Assuming temporally and spatially invariant conditions in terms of the averaged quantities, one finds since the left side terms vanish in equation (2.9), for the phase averaged horizontal momentum transfer in vertical direction (Bopp [2018]):

$$\partial_z \left( \underbrace{-\rho \overline{u \tilde{u}}}_{\overline{\tau}_{\text{wave},xz}} - \underbrace{\rho \overline{u' w'}}_{\overline{\tau}_{\text{turb},xz}} + \underbrace{\mu \partial_z \overline{u}}_{\overline{\tau}_{\text{visc},xz}} \right) = \partial_z \overline{\tau}_{xz} = 0. \quad (2.10)$$

Hence the momentum transport may be partitioned into three terms, and is constant with depth. The mean contribution from each term, however, may vary with  $z$ . As these averaged quantities are of main interest in this thesis, the overline will mostly be skipped in the following, e.g.  $\overline{\tau}_{xz} =: \tau_{xz}$ . When this is not the case, it will be marked accordingly. The most important quantity in this thesis is the viscous contribution,  $\tau_{\text{visc},xz}$ . Further

on, the friction velocity  $u_*$  is often given instead of  $\tau_{xz}$ , given by

$$u_* = \sqrt{\tau_{xz}/\rho}. \quad (2.11)$$

Averaging as done above has its limitations with respect to  $z$ , since above the deepest point of the wave, both air and water is present when averaging over phase. In Bopp [2018] this is solved by doing the averaging in curvilinear, wave following coordinates, with the curvilinear coordinates. This gives rise to a pressure related term in the partitioning of the momentum transfer, also for the phase averaged equation. Else the contributions are the same, though the expressions change.

The term  $-\overline{\rho u' w'}$  may be expressed analogously to equation (2.6) by the macroscopic mean velocities and an effective turbulent diffusivity (Bopp [2018]):

$$\overline{u'_i u'_j} = -\nu_{\text{turb}} \left( \partial_{x_i} \overline{v_j} + \partial_{x_j} \overline{v_i} \right). \quad (2.12)$$

This introduces the concept of eddy diffusivity, as an approximation to resolve closure issues of the problems of mean quantities. Note that  $\nu_{\text{turb}}$  is a property of the flow, and not of the fluid itself. For more details, see for example Prandtl [2017].

### 2.1.3

#### BERNOULLI EQUATION

Considering an inviscid and incompressible fluid in steady state flow, the specific energy along a streamline is constant, and the following relation holds:

$$\frac{|\vec{v}|^2}{2} + \frac{p}{\rho} + gz = \text{constant}. \quad (2.13)$$

If the flow is additionally irrotational, then Bernoulli's equation may also be used to describe unsteady flows (Kundu [2008]). Let  $\phi$  be the velocity potential that in this special case can be found, such that  $\vec{v} = \vec{\nabla}\phi$ , then

$$\partial_t \phi + \frac{|\vec{v}|^2}{2} + \frac{p}{\rho} + gz = f(t), \quad (2.14)$$

where  $f(t)$  depends on time only. This allows for absorbing  $f(t)$  into the potential, namely by  $\Phi = \phi - \int^t f(t') dt'$ .

### 2.1.4

#### VORTICITY

Another important fluid dynamical quantity is the vorticity,

$$\vec{\omega} = \vec{\nabla} \times \vec{v}, \quad (2.15)$$

which is a measure for local “spinning” motion of the fluid parcels. In the well-known and illustrative case of rigid-body-like rotation of the fluid, the vorticity equals twice the angular velocity. Usually, shear flow has non-zero vorticity due to the velocity gradients, though this is not always true, e.g. for an ideal irrotational vortex. As non-zero vorticity implies that the fluid is rotational, the prerequisite of an irrotational flow field for potential theory does not hold for  $\vec{\omega} \neq 0$ .



## 2.2

### WAVE THEORY

As the measurements in this thesis are conducted in conditions with the presence of water waves, a brief introduction to wave theory is given below. Furthermore, the waves give rise to several phenomena that directly influence the outcome of the thermographic measurement method. This will be discussed in chapter 3.

#### THE IRROTATIONAL WAVE PROBLEM

In the following, the wave problem is approached using potential theory, meaning that the velocity is expressed as the gradient of a potential,

$$\vec{v} = \begin{pmatrix} u \\ w \end{pmatrix} = \vec{\nabla}\phi. \quad (2.16)$$

It directly follows that the curl of the velocity field is zero, and the solution hence will be irrotational. Furthermore, as indicated, the problem will be restricted to the  $x$ - and  $z$ -direction, with  $x$  being the direction of wave propagation and  $z$  the upwards directed coordinate as before.

Starting from the continuity equation (2.3) and inserting equation (2.16), one finds that in case of an incompressible fluid  $\phi = \phi(\vec{x}, t)$  must satisfy the Laplace equation

$$\Delta\phi = 0. \quad (2.17)$$

Considering the bottom,  $z = -h$ , to be impermeable, the flow in  $z$ -direction must vanish there, hence

$$w|_{z=-h} = \partial_z\phi = 0, \quad (2.18)$$

providing a boundary condition to equation (2.17). Note that  $z = 0$  describes the vertical coordinate of the free surface  $\eta = \eta(x, t)$  in equilibrium, i.e. in the absence of waves. Neglecting viscous forces, the Bernoulli equation (2.14) can be deployed, yielding a second boundary condition (dynamical) when evaluated at the free surface:

$$p/\rho = (p_a - \gamma\partial_x^2\eta)/\rho = -\partial_t\phi - \frac{1}{2}\left((\partial_x\phi)^2 + (\partial_z\phi)^2\right) - g\eta. \quad (2.19)$$

The pressure  $p(z = \eta)$  consists of the air pressure  $p_a$ , assumed temporally and spatially constant and may be taken as being zero, and a term related to the surface tension  $\gamma$ . The latter introduces a pressure jump across the air-water interface.

Lastly, within this framework, a fluid parcel at the surface remains there for all times, hence the following expression must be satisfied at  $z = \eta$ :

$$d_t\eta = \partial_t\eta + \partial_x\phi\partial_x\eta = \partial_z\phi, \quad (2.20)$$

yielding another boundary condition (kinematic).

As depicted, this problem has not been solved analytically. Several simplifications exist (Zhong and Liao [2018]), however, some of them outlined below.

## LINEARISED SOLUTION

The above problem may be linearised, known as Airy wave theory. Assuming the wave steepness

$$\epsilon = ka = \frac{2\pi a}{\lambda}, \quad (2.21)$$

with  $k$ ,  $a$  and  $\lambda$  being the angular wave number, amplitude and wavelength, respectively, to be  $\ll 1$ , equation (2.20) reduces to  $\partial_t \eta \approx \partial_z \phi|_{z=0}$ . Similarly, linearisation of (2.19) removes the quadratic velocity terms  $(\partial_{x_i} \phi)^2$ , and  $\phi$  is also evaluated at  $z = 0$  instead of  $z = \eta$ . Let

$$\varphi = k(x - ct) \quad (2.22)$$

be the phase of the wave, with  $c = c(k)$  being the phase velocity. Solving the linearised problem yields (Kundu [2008]):

$$\eta(x, z, t) = a \cos(\varphi), \quad (2.23)$$

$$\phi(x, z, t) = ac \frac{\cosh(k(z+h))}{\sinh(kh)} \sin(\varphi). \quad (2.24)$$

and, with angular frequency  $\omega$  also defining the dispersion relation,

$$c = \frac{\omega}{k} = \sqrt{\left(\frac{g}{k} + \frac{\gamma k}{\rho}\right) \tanh(kh)}. \quad (2.25)$$

## DISPERSION RELATION

Based on these equations, some regimes and characteristics may be defined, refer to figure 2.1 for a schematic. As the latter equation shows, surface tension apparently modifies the phase velocity, which increases with increasing  $\gamma$ , and may be absorbed by modifying  $g' = g + \gamma k^2/\rho$ . Accordingly, surface tension as a restoring force becomes increasingly important when  $k$  grows, that is, for small wavelengths, all the way until  $g$  is of negligible importance. This is then called the capillary regime. Likewise, for large wavelength the influence of surface tension may be neglected, leaving  $g$  as the main restoring force, giving rise to the gravity wave regime. Furthermore, as

$$\tanh(kh) = \begin{cases} kh, & kh \rightarrow 0 \\ 1, & kh \rightarrow \infty \end{cases}, \quad (2.26)$$

see upper plot of figure 2.1, another classification is that of water depth relative to wavelength. For gravity waves, the following classification related to the functional dependence of  $c$  is common (Toffoli and Bitner-Gregersen [2017]):

- shallow water:  $\lambda > 20h$ ,  $c^2 \approx gh$ ,
- deep water:  $\lambda < 2h$ ,  $c^2 \approx g/k$ ,
- intermediate water depth:  $20h < \lambda < h/2$ ,  $c = c(k, h)$ .

It follows that the phase speed is limited by water depth for shallow water waves, whereas for deep water waves  $c$  is largely independent of the water depth. In this thesis the deep water regime is the relevant regime. As capillary waves are subject to shorter wavelengths

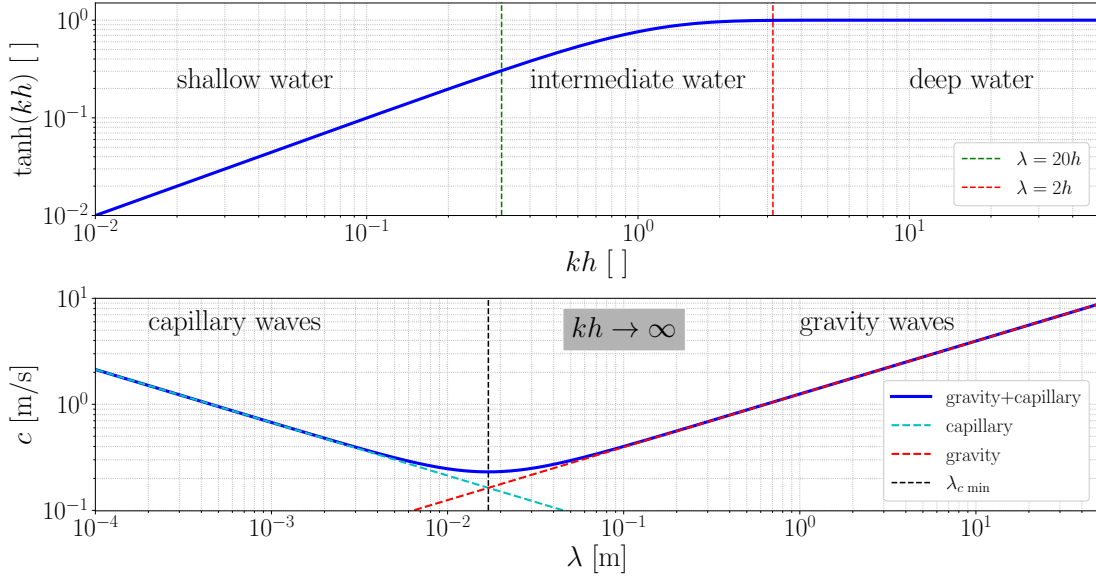


FIG 2.1.: The upper plot shows  $\tanh(kh)$  and the resulting classification of water depth  $h$  relative to  $k$ . The lower plot shows the deep water dispersion relation, i.e.  $\tanh(kh) = 1$ , and the resulting regimes. The coloured dashed lines show the separate contributions by surface tension and gravity as restoring force, respectively, see equation (2.25), whereas the black dashed line shows the wavelength associated with equation (2.27).

than gravity waves, the  $\tanh(ka)$  term in equation (2.25) may be omitted in the deep water regime also when including surface tension effects. As equation (2.25) also shows, there will be a  $k_{c \min}$  for which  $c$  is minimal;

$$k_{c \min} = \sqrt{\frac{g\rho}{\gamma}}. \quad (2.27)$$

For water at standard state this equals to about  $k_{c \min} = 369/\text{m}$  or equivalently a wavelength of about 1.7 cm, yielding  $c_{\min} = 23 \text{ cm/s}$ . Based on the description above,  $k_{c \min}$  divides the capillary from the gravity wave regime, with smaller  $k$  corresponding to gravity waves. Note that there is a range around  $k_{c \min}$  for which both effects should be considered, depending on the required accuracy. As gravity waves are of main importance in this thesis, surface tension effects will mostly be left out in the following.

## STOKES DRIFT

Continuing the consideration of gravity deep water waves in the linear framework, a second order property can be derived, namely the Stokes drift. It describes a mean drift of the fluid parcels due to the presence of waves, and is derived here since it will be important in chapter 3.

The velocity potential (2.24) for deep water waves simplifies to:

$$\phi(x, z, t) = ace^{kz} \sin(\varphi), \quad (2.28)$$

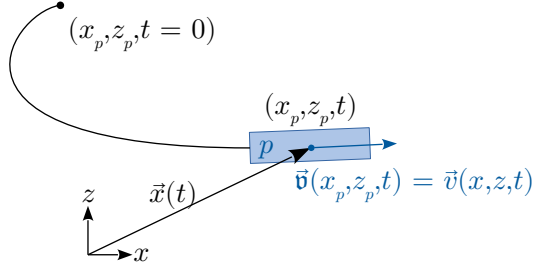


FIG 2.2.: A sketch of the described situation for the derivation of the Stokes drift.

yielding

$$\vec{v} = akce^{kz} \cdot \begin{pmatrix} \cos(\varphi) \\ \sin(\varphi) \end{pmatrix}. \quad (2.29)$$

This means that the Eulerian horizontal velocities are maximal at the wave crest ( $\varphi = 0$ ) and minimal in the trough ( $\varphi = \pi$ ). The vertical velocities reach their extremal values at  $\varphi = \pm\pi/2$ . Consequently, the fluid parcels move oscillatory. For vanishing wave steepness, that is, a diverging wavelength as compared to amplitude, both velocity components oscillate symmetrically around zero as the change in  $z$  due to the particle excursions in the exponent in equation (2.29) vanishes. Hence fluid parcel trajectories become closed circles. This changes, however, if a small but non-vanishing steepness is allowed for. Let  $\vec{x}(t)$  be the position of a fluid parcel  $p$ , with  $\vec{x}(0) = (x_p, z_p)$ , moving with the Lagrangian specified velocity  $\vec{v} = (u, w)^T$ , then

$$\vec{x}(t) = \begin{pmatrix} x_p + \int_0^t u(x_p, z_p, \tau) d\tau \\ z_p + \int_0^t w(x_p, z_p, \tau) d\tau \end{pmatrix}. \quad (2.30)$$

Refer to figure 2.2 for a sketch of the situation. Hereby note that the coordinates of the fluid parcel, seen from the (Lagrangian) perspective of the parcel itself, do not change. At given time  $t$  the Lagrangian velocity of a fluid parcel must equal the Eulerian velocities, equation (2.29), at position  $\vec{x}(t)$ , specifically  $\vec{v}(x_p, z_p, t) = \vec{v}(x, z, t)$ . In the limiting case of closed orbits the temporal average of both components of both flow field specifications are zero, e.g.  $\bar{u} = \bar{w} = 0$ . For small, but finite  $\epsilon$ , this does not hold for the  $x$  components any more. Taylor expanding to first order of the Eulerian  $u$  yields:

$$u(x_p, z_p, t) = u(x_p, z_p, t) + (x - x_p)\partial_x u|_{(x_p, z_p, t)} + (z - z_p)\partial_z u|_{(x_p, z_p, t)}. \quad (2.31)$$

Taking the temporal average yields zero for the first term on the right hand side. As  $\epsilon \ll 1$  the fluid parcel excursions are small relative to wavelength, and the terms  $x - x_p$  and  $z - z_p$  may be approximated in the framework of linear theory as  $x - x_p = -a \exp(kz_p) \sin(\varphi(x_p))$  and  $z - z_p = a \exp(kz_p) \cos(\varphi(x_p))$ . Plugging these expression into 2.31 and time averaging yields:

$$\overline{u(x_p, z_p, t)} - \overline{u(x_p, z_p, t)} \approx ca^2 k^2 e^{2kz_p} =: u_S. \quad (2.32)$$

$u_S$  is known as Stokes drift, and yields a net transport by the waves in the direction of propagation. A glance at figure 3.4 may clarify the situation. It results from the orbits having higher horizontal velocities at the crests than in the troughs. The vertical

component does not possess such an asymmetry, which would also lead to unphysical behaviour. As a consequence, particle orbits are no longer closed circles, as will also be seen in chapter 3. It should be noted that the Stokes drift is a second order property, as seen by the quadratic amplitude, here calculated in the framework of Airy wave theory, but still present for higher order approximations. As it is strongly decaying with decreasing  $z$ , its importance is mainly restricted to the layers in proximity of the surface. In these layers it introduces a velocity gradient for the fluid parcels, and may additionally disperse e.g. near surface contaminants with a non-negligible vertical distribution.

For typical parameters relevant for this thesis, with dominating wavelengths on the order of ten up to some tenth of centimetres, and for  $\epsilon \sim 0.2$ , the Stokes drift at the surface will be of order of some centimetres per second. This corresponds to about a quarter of the mean drift velocity at the surface when subtracting the bulk drift. Of more important influence for the thermographic measurement method is the vertical velocity gradient introduced by the Stokes drift,

$$\partial_z u_S = 2ca^2 k^3 e^{2kz}, \quad (2.33)$$

contributing up to some millipascal to the mean shear stress at the surface. For typical measurement conditions of  $u_{10} \sim 5$  m/s this would be of order  $< 10\%$ , refer to section 7.1. The quadratic dependence on wave steepness or  $\partial_z u_S \propto k^{3/2}$  when inserting the dispersion relation (2.25) suggest it to be of largest importance for short and steep waves. Furthermore, as  $e^x \approx 1 + x$  for small  $x$ , the vertical velocity gradient associated with the open orbits of the fluid parcels would contribute linearly to the mean total gradient. Note that this requires boundary thickness  $\delta \ll \lambda$ . Furthermore, it must be emphasized that this results from the velocity fields in the framework of potential theory, which is not applicable if there is vorticity present in the flow. For the boundary layer, where the velocity gradient is measured in this thesis, vorticity is large due to the momentum transfer and resulting shear flow (Okuda [1984]), so the interpretation of the above results should be taken with care.

## STOKES WAVE

For real world applications, the assumption of an infinitesimal wave steepness often does not hold. Hence the need for finite amplitude waves arises. Several approaches exist. In the following, a brief look at Stokes waves as an approximation to more realistic gravity waves will be given, staying with deep water waves and irrotational wave theory.

Stokes [1847] approached the problem given in at the beginning of section 2.2 by a perturbation series approach for  $\phi$  and  $\eta$ . Furthermore,  $u$ ,  $w$  and pressure  $p$  are assumed functions of  $x - ct$  and  $z$  only. Using the wave steepness as expansion parameter,

$$\eta = \epsilon\eta_1 + \epsilon^2\eta_2 + \epsilon^3\eta_3 \dots, \quad (2.34)$$

$$\phi = \epsilon\phi_1 + \epsilon^2\phi_2 + \epsilon^3\phi_3 \dots, \quad (2.35)$$

can then be inserted into the governing equations. Terms with equal powers of  $\epsilon$  may then be sorted and solved separately. The series is then truncated at some power in  $\epsilon$ , yielding the Stokes wave at that respective order. Furthermore, also  $c$  must be corrected for a dependence on  $\epsilon$ , in order to avoid secular terms (Tsuchiya and Yasuda [1981]). This was already done by Stokes [1847] by perturbing the angular frequency analogously

to equation (2.34).

Being describing periodic waves, Stokes [1847] gave the general expressions for  $\eta$  and  $\phi$  as Fourier series, based on his analysis leaving out the odd and even harmonic terms, respectively:

$$\eta = a \cos(\varphi) + \sum_{r=2}^{\infty} a^r A_r \cos(r\varphi) \quad (2.36)$$

and

$$\phi = Bt + Cx + \sum_{r=1}^{\infty} a^r D_r \cosh(rk(h+z)) \sin(r\varphi). \quad (2.37)$$

Here  $A_r$  and  $D_r$  are coefficients to be determined, noting that  $a^r$  might be absorbed in them and that  $\cosh(rk(h+z)) = e^{rk(h+z)}$  in the deep water case, and  $B$  and  $C$  are constants. The term  $Bt$  acts by merely introducing a constant in the dynamical boundary condition, equation (2.19), whereas  $C$  give rise to an offset in  $u$ , hence describes a uniform underlying drift.

### 2.2.1

#### DOPPLER SHIFT DUE TO DRIFT

$C$  in equation (2.37) introduces a Doppler shift. Observing the waves from a coordinate system  $(\tilde{x}, \tilde{z})$  fixed at the bottom, they will propagate by  $\tilde{c} = c_{\text{ref}} + C$ , where  $c_{\text{ref}}$  is the phase speed in a co-moving reference frame with the uniform drift. This may be seen by plugging  $x_{\text{ref}} = \tilde{x} - Ct$  into equation (2.22), collecting the time dependent terms and using that  $\varphi$  does not depend on the reference system. In the bypassing it should be noted that  $k$  is unaffected by the transform, and hence the Doppler shift  $\Delta\omega = \tilde{\omega} - \omega_{\text{ref}} = k \cdot (\tilde{c} - c_{\text{ref}})$ .

Likewise, due to the Stokes drift, a co-moving reference frame located at height  $z_c$  close to the surface will experience an additional drift, hence observing  $c' = c_{\text{ref}} - u_S(z_c)$ .

In the expressions for  $c$  given, e.g. equation (2.40) below,  $C$  is zero and hence correspond to  $c_{\text{ref}}$ . This corresponds to Stokes' first definition of wave celerity, where each point in space has a zero mean Eulerian velocity,  $\bar{u}(x, z) = 0$  (Song et al. [2012]).

#### THIRD ORDER STOKES WAVE

As an approximation to somewhat more realistic water waves, still keeping the algebraic expressions reasonable simple, third order Stokes waves are often deployed. Stokes [1847] gives the expressions, substituted the  $\epsilon = ka$ :

$$\eta = a \cos(\varphi) + \frac{1}{2}ka^2 \cos(2\varphi) + \frac{3}{8}k^2a^3 \cos(3\varphi), \quad (2.38)$$

$$\phi = ac(1 - \frac{5}{8}k^2a^2)e^{kz} \sin(\varphi) \quad (2.39)$$

and

$$c = (1 + \frac{1}{2}k^2a^2) \sqrt{\frac{g}{k}}. \quad (2.40)$$

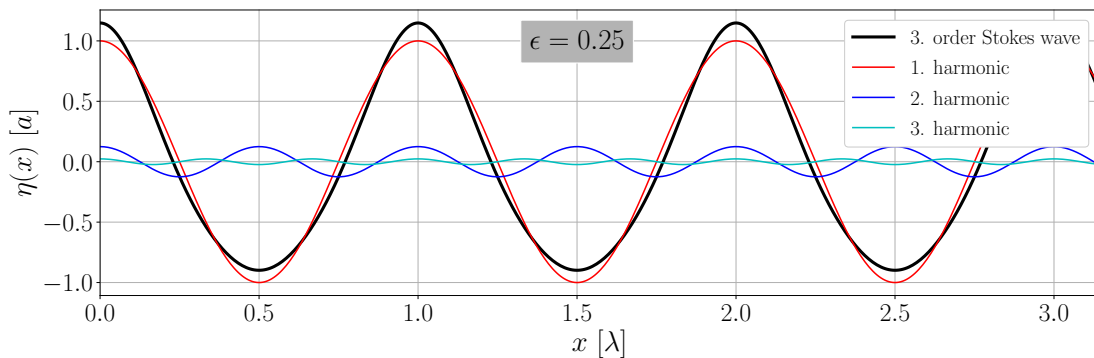


FIG 2.3.: The figure shows a third order Stokes wave for  $\epsilon = 0.25$ , along with its different order contributions, see equation (2.38). The asymmetry about  $z = 0$ , sharper crests and flatter troughs are clearly visible when compared to the symmetric lowest order component, which corresponds to the linear wave (2.23).

Several interesting aspects might be noted.  $c$  is no longer independent of amplitude, as higher waves travels faster. This leads to an amplitude dispersion as well as the dispersion related to wavelength known from linear waves. Moving on, the expression for  $\phi$  still exhibits the simple form of the linear solution, with second and third order terms vanishing, though a modification related to  $\epsilon^2$  enters. The velocity field hence consists of circular motion at each point in space. Lastly, the expression for  $\eta$  is not symmetrical about  $z = 0$ , see figure 2.3, and the shape is not sinusoidal. The crests are steeper whereas the troughs are flatter. Also the wave height  $H$ , defined as the distance between  $\eta_{\max}$  and  $\eta_{\min}$ , is not twice the linear amplitude:

$$H = 2a \left( 1 + \frac{3}{8} k^2 a^2 \right) \quad (2.41)$$

As a consequence of these asymmetries, the vertical midpoint between  $\eta_{\max}$  and  $\eta_{\min}$  lies at  $z = \frac{1}{2}ka^2$ . Recall that  $z = 0$  corresponds to the water level in equilibrium. This means that when considering a fluid parcel located at the water surface in the presence of waves, it oscillates about a vertical mean position that lies above the water surface at rest. The integral over one period of  $\eta$  is still zero, however, being a necessity of mass conservation and the assumption of incompressibility.

#### MAXIMUM WAVE STEEPNESS AND WAVE BREAKING

Another important aspect of finite amplitude waves is the maximum wave steepness. Stokes [1847] calculated the maximum angle of a Stokes wave crest, which is then sharp, to  $120^\circ$ , measured through the water. Michell [1893] estimated the corresponding maximum ratio  $H/\lambda = 0.142$ , and also Schwartz [1974] reaches the similar highest ratio of  $H/\lambda = 0.1412$ . This corresponds to  $\epsilon_{\max} \approx 0.44$ . Experiments have found comparable results (Bopp [2018]).

Wave height and steepness is limited by increasing energy density, which in the end leads to wave breaking. Hereby the processes become highly non-linear. Peregrine et al. [1980] lists some typical features for a breaking wave, these being velocities greater than  $c_{\max}(k)$  at the crest, regions on the leeward side of the crest featuring fluid parcels with

accelerations up to several times  $g$  (Schwartz and Fenton [1982]), and regions on the windward side with low particle accelerations. This then causes some fluid parcels to overtake others, rendering the wave unstable, which then breaks.

#### ENERGY AND POWER DENSITY SPECTRA FOR WAVE FIELDS

The wavy surface observed in reality is mostly much more complicated than the two dimensional approximations given above, with superposing modes. Hence the need for statistical characterizations of the wave field arises.

Waves cause motion and displacement of fluid parcels relative to their equilibrium state, with the free undisturbed surface located at  $z = 0$ , and are hence associated with both kinetic and potential energy. Starting with the latter and ignoring surface tension effects, a fluid layer located at depth  $z$  with horizontal extent  $\delta x$  will contribute by  $dU = \rho z \delta x dz$  to the total potential energy. Referencing the energy to the undisturbed state and integrating over the water column and averaging over one wavelength yields:

$$\bar{U} = \int_0^{2\pi} \frac{d\varphi}{2\pi} \int_{-h}^{\eta} dU - \int_{-h}^0 dU = \frac{1}{2} \rho g \overline{\eta^2}. \quad (2.42)$$

This then expresses the potential energy per unit horizontal area.

Similarly for the kinetic energy  $dT = \rho \delta x dz |\vec{\nabla} \phi|^2 / 2$ , being given by the motion of fluid parcels. For a third order Stokes wave with the velocities given by equation (2.39) in deep water one finds:

$$\bar{T} = \overline{\int_{-h}^{\eta} \delta T} = \frac{\rho g a^2}{4} \left( 1 + \frac{3}{4} \epsilon^2 + \mathcal{O}(\epsilon^4) \right), \quad (2.43)$$

where the orthogonality of the sinusoidal functions was used. Furthermore, with equation (2.38),

$$\bar{U} = \frac{\rho g a^2}{4} \cdot \left( 1 + \frac{\epsilon^2}{4} + \mathcal{O}(\epsilon^4) \right), \quad (2.44)$$

and consequently for the total energy  $E$  per unit horizontal area

$$\bar{E} = \bar{U} + \bar{T} = \frac{\rho g a^2}{2} \left( 1 + \frac{1}{2} \epsilon^2 + \mathcal{O}(\epsilon^4) \right). \quad (2.45)$$

Hence both the potential and kinetic energy increases with increasing amplitude. For the lowest (quadratic) order in amplitude, the potential and kinetic energy is equal. These terms correspond to the first order approximation of linear waves, and the equipartition of energy is as expected for a harmonic oscillator. For higher order terms, however, this equipartition is not longer the case, with  $\bar{T} \geq \bar{U}$ . The sign and magnitude of these higher order terms are here given for the third order Stokes wave, and can be different for other order Stokes waves (Longuet-Higgins [1975]), due to cross terms, with  $\bar{T} \geq \bar{U}$  still holding.

In the case of a stationary wave field,  $\eta(t)$  at a given location can be expressed in terms of its Fourier transform

$$\eta(\vec{x}, t) = \mathcal{F}^{-1} \{ \mathcal{F} \{ \eta(\vec{x}, t) \}_{\vec{k}, \omega} \}_{\vec{x}, t} = \mathcal{F}^{-1} \{ \hat{\eta}(\vec{k}, \omega) \}_{\vec{x}, t}. \quad (2.46)$$



Taking the spatial and temporal average over (infinitely extended) domain  $\Omega$  of  $\eta^2(\vec{x}, t)$  yields:

$$\overline{\eta^2} = \frac{\int_{\Omega} |\eta(\vec{x}, t)|^2 d\Omega}{\int_{\Omega} d\Omega} = \frac{\int_{\Pi} |\hat{\eta}(\vec{k}, \omega)|^2 d\Pi}{\int_{\Omega} d\Omega} \quad (2.47)$$

where the Parseval - Plancherel identity was used, and  $\Pi$  describes the domain of Fourier (spectral) modes. It is therefore possible to express the mean total energy density by the Fourier modes of  $\eta(\vec{x}, t)$ , to quadratic order in amplitude, by

$$\overline{E} \approx \rho g \overline{\eta^2} \propto \int_{\Pi} |\hat{\eta}(\vec{k}, \omega)|^2 d\Pi. \quad (2.48)$$

Integrating out some of the variables, for example the spatial modes, yields the reduced spectra, in this case to the frequency power density spectrum

$$S_{xx}(f) = \lim_{T \rightarrow \infty} \frac{1}{T} |\hat{\eta}(\omega/(2\pi))|^2. \quad (2.49)$$

In the real world applications, the wave field is not temporally stationary for an infinite domain as described above. Therefore  $S_{xx}$  will be calculated and approximated for limited spacial domains and time windows. Especially in the case of non-stationary wave fields this becomes critical. With the spatial extent of measurement being small, also time intervals must be kept small in order to only allow for minor changes in the spectra during evaluation. This of course comes with poor statistics.

The main application of the frequency power spectra will be to compute the dominating wave, with the corresponding dominating properties. This is adapted from Bopp [2018]. In this work it will be defined as the reconstructed surface profile  $\eta(x, t)_{\text{dom}}$  for frequencies  $f$  in the range

$$\frac{f_m}{2} \leq f \leq \frac{3}{2} f_m, \quad (2.50)$$

where  $f_m$  is the frequency corresponding to the maximum value of  $S_{xx}(f)$ . This range corresponds to that used in Bopp [2018].

## 2.3

### HEAT TRANSPORT

Another important aspect for this work is heat transport. Three general mechanisms can be identified, namely molecular diffusion, advection and radiative transfer. Often also convection is mentioned when describing heat transport, in this thesis convection is defined as the combined transport by advection and diffusion.

#### 2.3.1

##### RADIATIVE TRANSFER

Starting with radiative transfer, this transport is a result of every object with a temperature above absolute zero emitting radiation. The spectral radiance  $L(\lambda, T)$  in case of a

black body is described by Planck's law,

$$L(\lambda, T) = \frac{2hc^2}{\lambda^5} (e^{\frac{hc}{\lambda k_B T}} - 1)^{-1}, \quad (2.51)$$

describing the power emitted per unit area, unit solid angle and unit wavelength. Moreover,  $T$  is the temperature,  $h$  is the Planck constant,  $c$  is the speed of light in the medium, and  $k_B$  the Boltzmann constant. The absorbed fraction of incident radiation onto an object is described by the spectral absorptivity  $\alpha(\lambda) \leq 1$ . For an ideal black body  $\alpha(\lambda) = 1$ , per definition, for real objects  $\alpha(\lambda) < 1$ . Similarly, the fraction of emitted radiation at a given wavelength, as compared to a black body, is called the spectral emissivity  $\epsilon(\lambda) \leq 1$ . By Kirchhoff's law of thermal radiation, for a specific wavelength and for a body in thermal equilibrium, the emissivity and absorptivity must be equal,

$$\alpha(\lambda) = \epsilon(\lambda). \quad (2.52)$$

If there is no dependence on the wavelength in the emissivity, the body is referred to as a grey body. The two cameras used for thermal imaging in this thesis both fall in the wavelength range between  $3 - 5 \mu\text{m}$ , where water has an emissivity  $\epsilon \approx 0.97$  (Haußecker [1996]).

If the incident radiation on a body is not absorbed, it can be either transmitted or reflected. The wavelength dependent fractions of the incident radiation that are transmitted and reflected,  $\tau(\lambda)$  and  $\rho(\lambda)$ , respectively, must due to energy conservation add up to the remaining fraction that is not absorbed, i.e.

$$\alpha(\lambda) + \tau(\lambda) + \rho(\lambda) = 1. \quad (2.53)$$

The radiation will penetrate into a body, described by a wavelength dependent penetration depth  $\zeta(\lambda)$ . The fraction of incident radiation remaining after passing through  $\delta z$  of a homogeneous material, the transmittance  $\mathcal{T}$ , can be described with Lambert-Beer's law,

$$\mathcal{T}(\delta z, \lambda) = \frac{\Phi(\delta z, \lambda)}{\Phi_0(\lambda)} = \exp\left(-\frac{\delta z}{\zeta(\lambda)}\right), \quad (2.54)$$

where  $\Phi_0(\lambda)$  is the incoming spectral radiant flux, and  $\Phi(\delta z, \lambda)$  the flux remaining after passing through  $\delta z$ .

### 2.3.2

#### ADVECTION

When bulk motion of a fluid carries along a substance or quantity, it is referred to as advection. For example thermal energy or a dissolved gas in water can be transported, giving rise to an advection term in transport equation, with an associated flux as described in section 2.1.

### 2.3.3

#### DIFFUSION

Heat transported by thermal motion, vibration and collision on a molecular scale is referred to as diffusion or heat conduction. It can in an isotropic medium be described

by Fick's second law,

$$\frac{\partial}{\partial t} T = \alpha \Delta T, \quad (2.55)$$

respectively, with temperature  $T = T(\vec{x}, t)$ ,  $c$  the specific heat capacity, and  $\alpha = \kappa/(\rho c)$  the thermal diffusivity.  $\kappa$  is the thermal conductivity. By taking the Fourier transform of equation (2.55) with respect to spatial dimensions one finds:

$$\frac{\partial}{\partial t} \hat{T}(\vec{k}, t) = -\alpha \vec{k}^2 \hat{T}(\vec{k}, t), \quad (2.56)$$

where the transfer function of the Laplacian operator  $\Delta f \rightsquigarrow -\vec{k}^2 \hat{f}$  was used for the differentiable (for all  $\vec{x}$ ) function  $f$  (Jähne [2012]), with solution

$$\hat{T}(\vec{k}, t) = \hat{T}_0(\vec{k}) \cdot \exp(-\alpha \vec{k}^2 t). \quad (2.57)$$

This shows that diffusion in Fourier space multiplies the initial temperature distribution  $\hat{T}_0(\vec{k})$  by a Gaussian. From an intuitive point of view, this means that for small  $|\vec{k}|$ , corresponding to large spatial structures of the temperature profile, little alteration by diffusion happens for short times, whereas small spatial structures, associated with large  $|\vec{k}|$ , are more quickly dampened away.

By the convolution theorem (B.7), it thereby follows by inverse transformation that (Voigt [2019])

$$T(\vec{x}, t) = \frac{1}{\sqrt{2\pi}^3} \cdot \frac{1}{\sqrt{2\alpha t}^3} \exp\left(\frac{-\vec{x}^2}{4\alpha t}\right) * T_0(\vec{x}), \quad (2.58)$$

where the asterisk  $*$  denotes the convolution operator. Therefore, in real space, diffusion acts by convolving the initial temperature profile by a Gaussian of width  $\sigma = \sqrt{2\alpha t}$  in each spatial dimension.

### 2.3.4

#### DIFFUSION-ADVECTION EQUATION FOR HEAT AND TAYLOR DISPERSION

Inserting the advection and diffusion related fluxes for heat into the continuity equation 2.3 yields, after division by  $\rho c$ :

$$\partial_t T = \vec{\nabla} \cdot (T \vec{v} - \alpha \vec{\nabla} T) \stackrel{\vec{\nabla} \cdot \vec{v} = 0}{=} \vec{v} \cdot \vec{\nabla} T - \alpha \Delta T. \quad (2.59)$$

In the last step incompressibility was,  $\rho c \cdot \vec{j}_T$  being the heat flux, whereby assumed. Equation (2.59) is known as the diffusion-advection equation, where the first term on the right hand side describes the advection related transport, and the second describes a smoothing of the temperature profile caused by diffusion.

In the case of a uniform flow field, the contribution from the advection term is of no influence for the Lagrangian view of a fluid parcel. If there is shear present in the flow field, however, this is no longer the case. Imagining a temperature profile encompassed in the fluid parcel exposed to shear flow, the profile will be deformed along with the parcel. This changes the derivatives of the temperature profile in equation (2.59), as adjacent fluid parcels are pulled apart. The actual temporal temperature development is dependent on both the flow and initial profile, at some point the profile is dispersed faster

than it would due to diffusion only. This apparent enhancement of the diffusivity by shear flow is referred to as Taylor dispersion. The thermographic measurement method in this work exploits this enhanced smearing of the temperature profile, more details are given below in section 2.6.

## 2.4

### REFRACTION AND REFLECTION

In the following processes close to the interface between two different media, air and water, are approached with imaging and active thermographic techniques. Naturally, both refraction and reflection enter the considerations. For the latter the most important relation is that the angle of incidence equals that of reflection, when both angles are referenced to the surface normal of the interface, as depicted in figure 2.4.

Refraction occurs when the two media with the interface have different refractive indices  $n_{\text{med}}$ , because the speed of light changes with the medium according to  $c_{\text{med}} = c/n_{\text{med}}$ , where  $c$  is the speed of light in vacuum. As the frequency is unchanged across the interface, the wave vector has to change. Only the normal component of the wave vector is conserved across the interface, resulting in Snell's law:

$$n_1 \sin \theta_1 = n_2 \sin \theta_2, \quad (2.60)$$

where the angles are measured relative to the normal of the interface, refer to figure 2.4.

When a ray from the medium with the higher refractive index, here still  $n_2$ , hits the surface at an angle  $\theta > \theta_c$ , instead of being refracted, it is reflected back into the medium. This is called total internal reflection, depicted by the red ray in figure 2.4, with

$$\theta_c = \arcsin \left( \frac{n_1}{n_2} \right). \quad (2.61)$$

This can be understood from the fact that the refraction angle is always larger than the incident angle when coming from the medium with higher refractive index. Then, when increasing the incident angle, at some points the refraction angle reach it maximum at  $90^\circ$ , which corresponds to the critical angle. For the water-air interface  $\theta_c \approx 49^\circ$ .

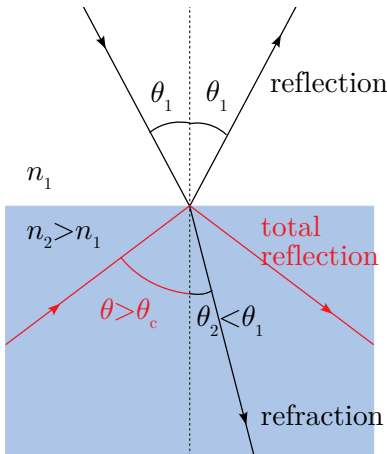


FIG 2.4.: A sketch of the reflection and refraction at the interface between two media, where the refractive index  $n_1$  in the white medium is smaller than that of in the blue medium,  $n_2$ .  $\theta_1$  is the angle of incidence, equal to the angle of reflection, whereas angle of refraction  $\theta_2 < \theta_1$ . The dotted line is normal to the surface. The red ray represents total reflection at an angle larger than the critical angle  $\theta_c$ .

## 2.5

### THE VISCOUS BOUNDARY LAYER AND SHEAR STRESS

As found in 2.1.2, horizontal momentum is transferred downwards in vertical direction, and stems from different contributions. The input comes from wind blowing over the surface. Assuming a non-slip condition at the surface, the momentum transfer must be continuous across the interface. The thin layers close to the interfaces are referred to as boundary layers, where transport by molecular diffusion dominates over turbulent transport, in the sense that  $D > K$ . Hereby  $D$  is the diffusion constant and  $K$  the turbulent (eddy) diffusivity defined in analogy to equation (2.12) for the  $xz$  component. The reason for the diminishing turbulence is that eddies cannot reach trough the surface, and vanish towards the interface. Depending on the diffusion constants, the boundary layer thickness  $\delta$  varies. For the momentum considerations the corresponding layer is referred to as the viscous boundary layer, and is on the water side on the order of 0.25-3 mm. For comparison, the water sided heat boundary layer and mass boundary layers are of the order of 0.1-1.5 mm and 10-350  $\mu\text{m}$ , respectively, whereas the air-sided boundary layers are of similar thickness and  $\sim 0.1$ -1.5 mm (Kunz and Jähne [2018]).

Due to the higher wind velocities and the non-slip condition at the interface, the topmost water layers will possess a higher velocity than the lower layers, giving rise to a shear flow in the surface layer. Considering the stationary case, the most simple model for the velocity profile in the viscous boundary layer corresponds to the topmost layer moving with  $u_s$  and the layer at depth  $\delta$  with the bulk velocity, see figure 2.5, corresponding to the stagnant film model. The situation is identical to that of a Couette flow, and the Navier-Stokes equation can be solved analytically. This yields a linear velocity profile, with the viscous shear stress

$$\tau_{\text{visc},xz} = \mu \frac{\partial u}{\partial z} = \text{constant}. \quad (2.62)$$

Exchange processes at the interface are to a large extent determined by boundary layer thickness, especially at lower wind speeds when highly non-linear processes such as sea spray formation or wave breaking of the gravity waves are less important. As boundary layer thickness is highly influenced by  $\tau_{\text{visc},xz}$ , a measurement of the latter is of interest for parametrizing the exchange processes. In the following, for simplicity and legibility,  $\tau_{\text{visc},xz}(z = \eta) =: \tau_{\text{visc}}$ , where  $\eta(\vec{x}, t)$  describes the surface elevation.

Clearly, the situation depicted above is an approximation only, as the eddies to some degree also influence the viscous boundary layer, especially the lowermost parts and other events such as for example micro scale wave breaking (see Klein [2019]) and surface renewal is not accounted for. Furthermore, in the presence of waves, the water sided flow fields are also heavily influenced by the orbital movement of the fluid parcels, see section 2.2 for more details. Additionally, the viscous shear stress is also expected to be wave phase dependent (Bopp [2018]), which then to some extent would introduce curvatures in the velocity profiles. However, due to the large complexity of the problem and the need for a simple representation of the system, in this thesis, the simple picture with a linear gradient in the topmost surface layer is used.

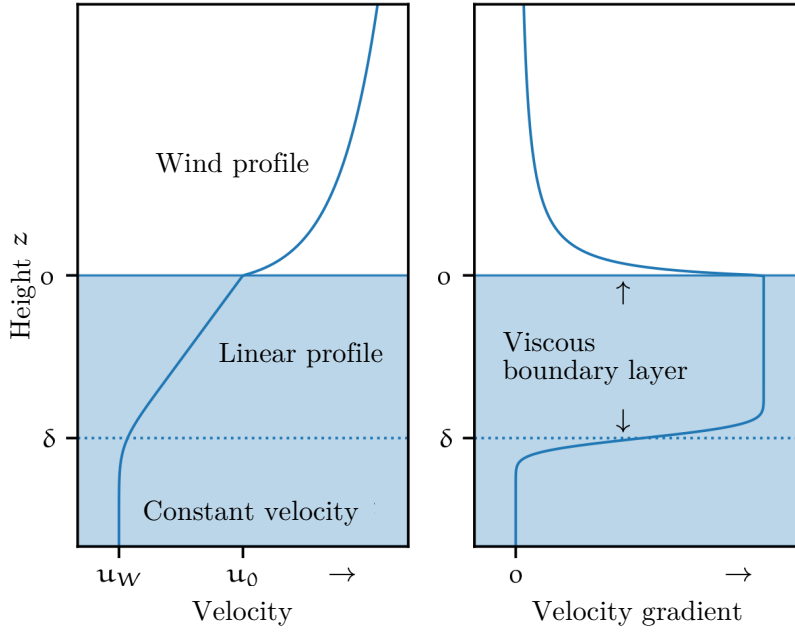


FIG 2.5.: Simplified representation of the viscous boundary layer. The constant velocity gradient in the boundary layer in the right figure is proportional to  $\tau_{\text{visc},xz}$ . The figure is taken from Voigt [2019], originally adapted and edited from Emmel [2017].

## 2.6

### MEASUREMENT PRINCIPLE

In order to determine  $\tau_{\text{visc}}$ , active thermography is deployed. Hereby a line is heated with e.g. an near-infrared (NIR) laser perpendicular to the wind. The amplitude of the resulting temperature profile is low, initially  $\sim 0.4^\circ\text{C}$ , in order not to disturb the flow in the boundary layer by inducing convection or giving rise to a stable stratification. The broadening of the line width  $\sigma(t)$  with time is measured. Generally, this is described by equation (2.59). Now, due to the shear flow in the boundary layer, the heated line is subject to Taylor dispersion, see section 2.3.3, which leads to an increased broadening of the line depending on the velocity gradient. Hence, by measuring the line broadening, a determination of  $\tau_{\text{visc}}$  is possible (Voigt [2019]). This is done by numerically simulating the system, and then comparing the observed line widths to the simulated ones. See figure 2.6 and 2.7 for a simulated vertical cross-section showing the heated line directly after heating and after 0.7 s.

Firstly looking at the case of  $\vec{v} = 0$ , and assuming the laser beam to be Gaussian, the width of the (Gaussian) temperature profile will broaden in accordance with 1D diffusion, i.e.

$$\sigma^2(t) - \sigma_0^2 = 2\alpha t, \quad (2.63)$$

with  $\sigma_0$  being the initial width (Voigt [2019]). The profile does not move, and is only smoothed out by diffusion, hence gets wider and the maximum temperature decreases. Now, in the presence of shear flow as seen in figure 2.7, the profile tilts with time.

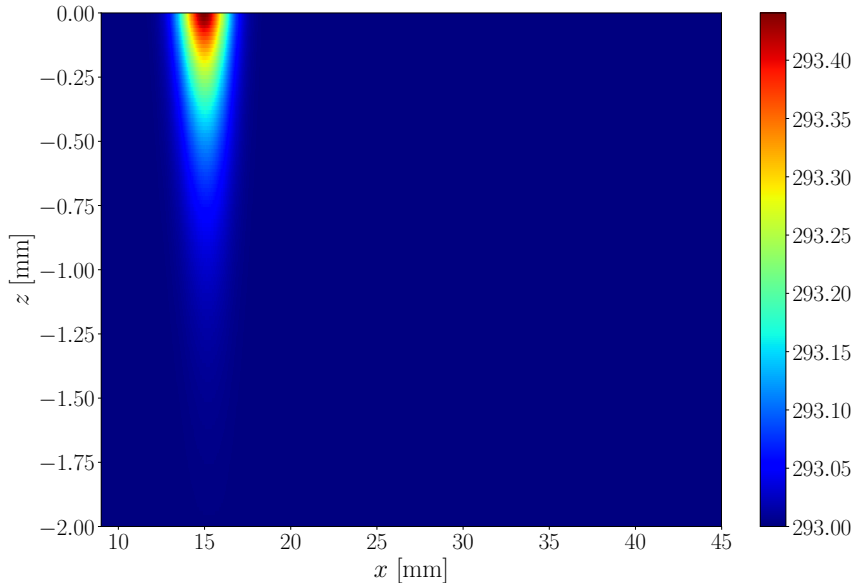


FIG 2.6.: The figure shows a heated line directly after heating, with penetration depth of the laser =  $355\ \mu\text{m}$ . The colours indicate the temperature in Kelvin. The depicted cross-section is then followed, corresponding to a Lagrangian description. Other parameters were:  $\partial_z u = 30/\text{s}$ ,  $\partial_y u = 0/\text{s}$  and  $\sigma_0 = 1\ \text{mm}$ .  $z$  describes the depth, and the wind direction is in *negative*  $x$ -direction. The figure is taken from Voigt [2019].

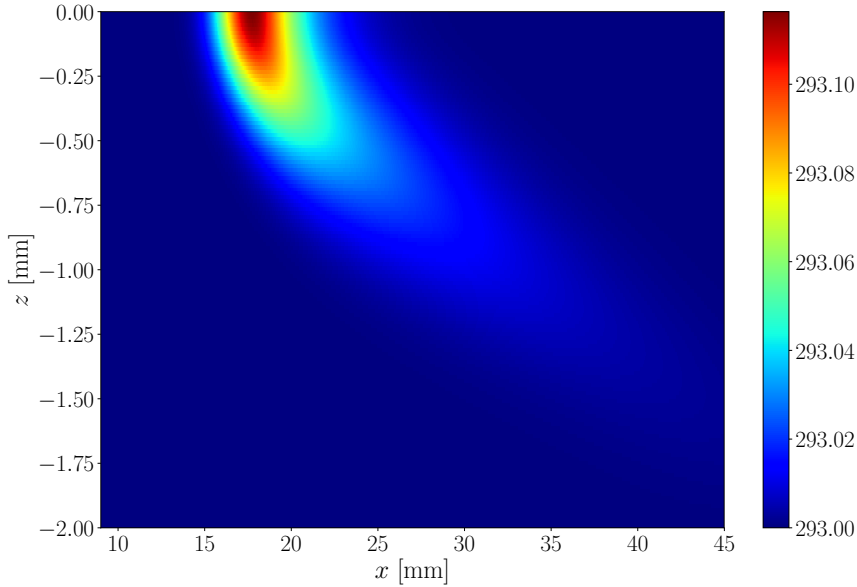


FIG 2.7.: The heated line from figure 2.6 after 0.7 s. The shear flow is tilting the temperature profile, and the line is broader than what would be expected from diffusion only (2.63). The bend towards the surface is caused by the profile “locking” water inbetween itself and the surface, which is then heated by the profile. Downwind (negative  $x$ -direction) there is more cold water available, which is therefore heated less. Note the somewhat skewed surface temperature profile, and the displacement of the temperature maximum relative to  $t = 0$  caused by the bending; the surface layer does not move. The figure is taken from Voigt [2019].

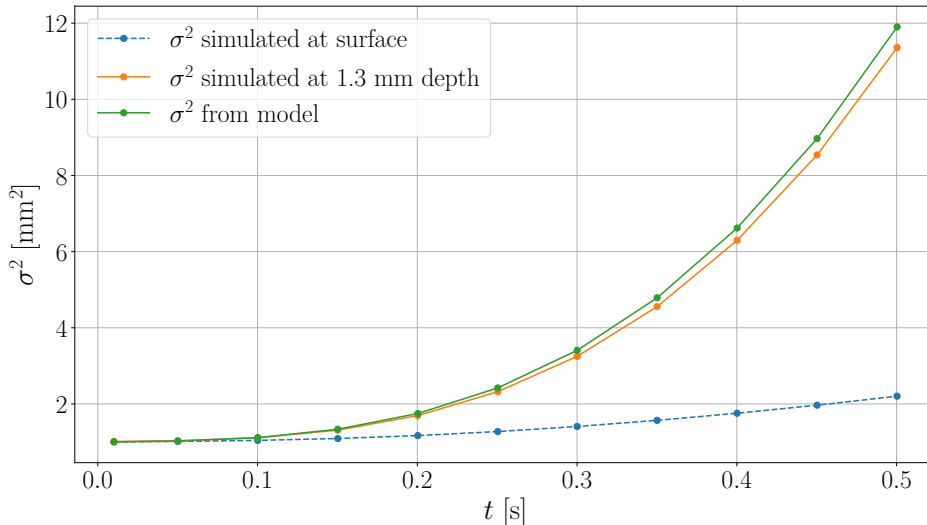


FIG 2.8.: The figure shows the simulated quadratic line widths  $\sigma^2$  at the surface and at 1.3 mm depth, compared to the widths computed by the analytical model (2.64). For the surface  $\sigma(t)^2 \propto t^2$  for high  $t$ , in contrast to the model  $\sigma(t)^2 \propto t^3$ . This is caused by the in section 2.6 explained effect by the surface on temperature profile. Parameters were  $\partial_z u = 30/s$ ,  $\partial_y u = 0/s$  and  $\sigma_0 = 1$  mm. The figure is taken from Voigt [2019]

Loosely speaking, this increases the surface of the profile, whilst keeping its volume constant, resulting in the excess broadening associated with Taylor dispersion. Emmel [2017] solved (2.59) analytically far away from any interface, finding

$$\sigma(t)^2 = \sigma_0^2 + 2\alpha t \left( \frac{1}{3} (\partial_z u)^2 t^2 + 1 \right). \quad (2.64)$$

Note that for high  $t$  the temporal dependence is  $\sigma(t)^2 \propto t^3$ . Whilst the simulated profiles reproduce this description away from the surface, it is found that at the interface, the width of the profiles  $\sigma(t)^2 \propto t^2$  for high  $t$ , see figure 2.8. This is caused by the bend in the temperature profile seen in figure 2.7, caused by the smaller amount of water locked in between the surface and profile in upwind direction (positive  $x$ -direction in the figure) as compared to downwind, which then is heated more by the profile and causes the observed bend. The bend also causes skewed temperature profiles observed at the surface. That the bend causes a strong decrease in the broadening with time, even with a lower exponent, can be understood by the subsequent up-straightening or “untilting” of the profile, which decreases the surface of the profile and counteracts the Taylor dispersion.

Lastly, the line may also be sheared in the direction along the line, if a horizontal velocity gradient in  $y$ -direction is non-zero. This causes a tilting of the profile in analogy to the presence of shear flow with depth, except that the analogy to the surface is missing in  $y$ -direction. This means that the broadening of the line subject to  $\partial_y u \neq 0$  is described by equation (2.64) when substituting the respective velocity gradient, as verified in Voigt [2019]. As may be deduced from figure 2.8 and expected from the  $t^3$  behaviour, even small  $\partial_y u$  can have a large influence on  $\sigma(t)$ . It is therefore crucial to evaluate only parts of the heated lines that are not subject to a velocity gradient in  $y$ -direction.



### 3 | SURFACE COMPRESSION AND DILATION

Having introduced the most important equations describing gravity waves, it is now possible to calculate a critical aspect for the thermographic measurement method, caused by the flow field of the wave associated motion. Though water in the context of this work is an incompressible fluid, the fluid parcels are stretched and compressed by tangential (to the surface) gradients in the velocity field varying with the wave phase, referred to as surface dilation and compression, see figure 3.1 for a sketch of the situation. Imagining the heated lines whose width is used to determine the viscous shear stress, located within a fluid parcel undergoing such a distortion, clarifies the issue. First, the stretching and compression will be considered in the framework of a single set of wave parameters, i.e. amplitude and wave length in the case of deep water waves (and dispersion), before the situation of a wave field is approached by letting the parameters be distributed.

#### 3.1 APPROACH BY THE CONTINUITY EQUATION

The problem can be approached by starting with the continuity equation, in principle adapting the approach by Osborne [1965], who considered the limiting case of linear waves and small amplitudes. This approach will in this section be extended for finite amplitudes. By the continuity equation and restricting the analysis to the  $xz$ -plane, one finds:

$$\partial_t \rho + \vec{\nabla}(\rho \vec{v}) = d_t \rho + \rho \vec{\nabla} \vec{v} = 0, \quad (3.1)$$

hence

$$-\frac{d_t \rho}{\rho} = -d_t \ln(\rho) = \partial_{x_{\parallel}} u_{\parallel} + \partial_{z_{\perp}} u_{\perp}, \quad (3.2)$$

where the rotated coordinate system  $(x_{\parallel}, z_{\perp})$  was introduced. Equation (3.2) hence describes the normal strain on the fluid parcel in the rotated coordinate system. The vanishing divergence of an incompressible velocity field is unchanged by a rotation, which is also intuitively clear as the fluid parcel cannot be compressed, no matter its orientation. Let the rotation be by angle  $\theta = \theta(x, t) = \arctan(\partial_x \eta(x, t))$ , i.e. such that  $x_{\parallel}$  is tangential to  $\eta(x, t)$  and

$$x_{\parallel} = x \cos(\theta) + z \sin(\theta) \quad (3.3)$$

$$z_{\perp} = -x \sin(\theta) + z \cos(\theta). \quad (3.4)$$

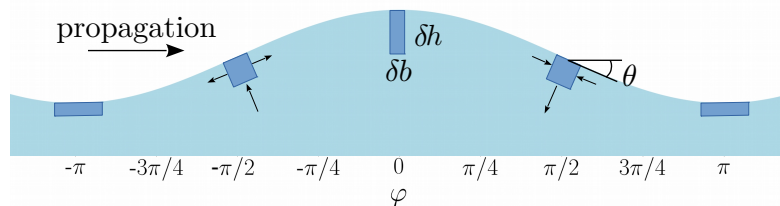


FIG 3.1.: A sketch of a fluid parcel (dark blue) at different wave phases. The arrows depict the (momentary) alteration of the fluid parcel height  $\delta h$  and width  $\delta b$  in the system rotating according to the surface inclination. The surface angle  $\theta$  is indicated for the wave phase  $\varphi = \pi/2$ . The  $\delta b$  is maximal in the wave trough ( $\varphi = \pi$ ) and minimal at the crest ( $\varphi = 0$ ). The wave propagates to the right.

The velocities transform correspondingly. Considering an infinitesimally small fluid parcel arbitrarily close to the surface with perpendicular and tangential extent with respect to the surface  $\delta h$  and  $\delta b$ , respectively, and unit extent in  $y$ -direction, its volume  $\delta V = \delta b \delta h \delta y =: \delta A \delta y = \delta A$  must be conserved due to incompressibility, and the same applies to its mass  $\delta m$ . Therefore, with  $\rho = \delta m / \delta A$ :

$$-d_t \ln(\rho) = d_t [\ln(\delta A) - \ln(\delta m)] = d_t [\ln(\delta b) + \ln(\delta h)]. \quad (3.5)$$

Associating the tangential velocity gradient with the logarithmic rate of change of the fluid parcel's width, one can find the absolute change of width by integration over time. The following differential equation and solution arises,

$$d_t \ln(\delta b) = \partial_{x_{\parallel}} u_{p,\parallel} \text{ and } \delta b(\vec{x}, t) = \delta b_0 \exp\left(\int_{t_0}^t \partial_{x_{\parallel}} u_{p,\parallel} dt'\right), \quad (3.6)$$

where the label  $p$  was added to emphasize the dependence of the velocity on the parcel's trajectory. Expressing the tangential directional derivative of the tangential velocity component at the location of the parcel  $\vec{x}$  at time  $t$  in the unrotated reference system yields:

$$\partial_{x_{\parallel}} u_{\parallel}|_{\vec{x},t} = \partial_x u \cos^2(\theta) + (\partial_z u + \partial_x w) \cos(\theta) \sin(\theta) + \partial_z w \sin^2(\theta). \quad (3.7)$$

In the framework of potential theory (section 2.2), the velocity field is conservative, and the expressions may be simplified by using the Cauchy-Riemann relations,  $\partial_z u = \partial_x w$  and  $\partial_x u = -\partial_z w$ . Furthermore, the velocity components are functions of  $x - ct$ , see equation (2.37), hence  $c \partial_x u = -\partial_t u$  and likewise for  $w$ , and one finds after trigonometric reformulation:

$$\partial_{x_{\parallel}} u_{\parallel} = -\frac{1}{c} \partial_t u \cos(2\theta) - \frac{1}{c} \partial_t w \sin(2\theta). \quad (3.8)$$

This can be inserted back into equation (3.6b), and may then be integrated numerically if expressions for  $\phi$  and  $\eta$  are known. It should be noted that this generally also requires the calculation of the fluid parcel trajectories  $\vec{x} = \vec{x}(t)$ , as for non-infinitesimal wave steepness, and both the partial derivatives of the velocity components and surface inclination angle (i.e.  $\theta$ ) are dependent on  $(\vec{x}(t), t)$ . A plot of these equation in the framework of third order Stokes theory can be found below, see figure 3.4.

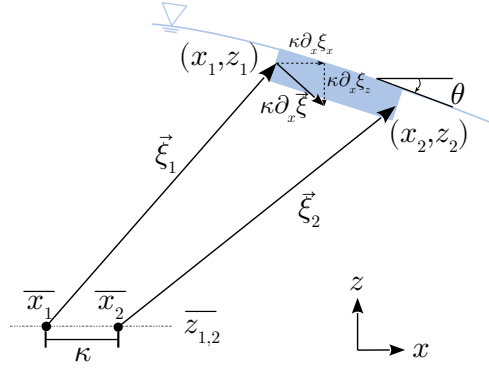


FIG 3.2.: A (momentary) sketch of the fluid parcel at the surface for calculating the compression and dilation in section 3.2.

## 3.2

### AN INTUITIVE APPROACH

Equation (3.8) has some disadvantages for the practical application of describing the stretching and compression of the heated lines. Regarding  $\partial_t u$  for example, it could be determined from the measured horizontal position  $x(t)$  of the heated line, encompassed in the fluid parcel, differentiating it twice, while  $\partial_t w$  and  $\theta$  could be computed by measuring  $\eta(x, y, t)$  and assuming that a fluid parcel at the surface must stay there and hence follow its motion. However, twice differentiating the respective estimated positions, in practice not measured by the same apparatus in combination with a complex wave field, and then approximating the integral by a sum, could be a difficult and error prone task. The applicability of potential theory is another critical aspect.

Having gained some insights into wave associated motion, one can approach the problem from a more intuitive perspective, staying in the framework of a single set of wave parameters. A fluid parcel at the surface will oscillate by  $\vec{\xi}(\varphi)$  about a mean position  $\vec{x}(t)$ , the latter moving with a mean surface drift  $U_d$ . In the unrotated coordinate system, let the down- and upwind edges of this infinitesimal fluid parcel be  $x_1$  and  $x_2$ , see figure 3.2, the width of which is then given by  $\delta b = (x_2 - x_1) / \cos(\theta)$ .  $\theta$  is the surface inclination angle relative to the  $x$ -axis as before. Both these edges are associated with their respective mean positions  $\bar{x}_1$  and  $\bar{x}_2$  (mean  $z = \bar{z}_{1,2}$  is equal for both). Let  $U_d$  be spatially constant on the relevant scale for the fluid parcel, such that  $\kappa := \bar{x}_2 - \bar{x}_1$  is constant with time. A temporal change in parcel width is hence caused by a slight phase difference between the two points, corresponding to a slight change in  $\vec{\xi}(\varphi)$ . Keeping in mind that  $\varphi = k(x - ct)$  yields, by Taylor expansion:

$$\begin{aligned}
 x_2 - x_1 &= \bar{x}_2 + \xi_x(\varphi_2) - \bar{x}_1 - \xi_x(\varphi_1) \approx \kappa + \xi_x(\varphi_1) + \kappa \partial_x \xi_x|_{\varphi_1} - \xi_x(\varphi_1) \\
 &= \kappa \left(1 - \frac{1}{c} \partial_t \xi_x|_{\varphi_1}\right) = \kappa \left(1 - \frac{u}{c}\right).
 \end{aligned} \tag{3.9}$$

Referencing to a horizontal length  $a_0$  related to a reference state, see below, yields

$$\delta b(\vec{x}, t) = \frac{a_0}{\cos(\theta(\vec{x}, t))} \cdot \left(1 - \frac{u(\vec{x}, t)}{c}\right). \quad (3.10)$$

This is an expression better suited for the practical application than equation (3.6b), as  $u$  may be obtained by once differentiating the heated line position  $x(t)$  and also  $\theta$  is readily obtained in an experimental setting, with  $c$  and  $a_0$  still to be determined. Also the critical integration of measured quantities occurring in equation (3.6b) is not needed. As a side note, while it may be tempting to identify  $1 - u/c$  as the Taylor expansion of  $\exp(-u/c)$ , similarly to equation (3.6), the derivation of the latter does not apply in this situation, and numerically speaking it also yields clearly deviating results for larger values of  $\epsilon$ .

It would be advantageous being able to reference  $\delta b$  to some selected state. By defining  $a_0$  as

$$a_0 := \delta b_{\text{ref}} \cdot \cos(\theta_{\text{ref}}) \left(1 - \frac{u_{\text{ref}}}{c}\right)^{-1}, \quad (3.11)$$

one finds, when the parcel is in its reference state,  $u = u_{\text{ref}}$  and  $\theta = \theta_{\text{ref}}$ ,  $\delta b/\delta b_{\text{ref}} = 1$ . The effort of relating to a given reference state becomes useful later.

As  $\delta b(t)$  refers to the width of a fluid parcel, it must be the same whether the reference system moves by a constant velocity or not. The same holds true for  $\theta$ , as it depends only on position and time. The situation is different for  $u$ , and as briefly noted in section 2.2, also for  $c$ . However, by rewriting (3.10) and collecting the invariant terms on the left hand side one finds:

$$\frac{\delta b}{\delta b_{\text{ref}}} \frac{\cos(\theta)}{\cos(\theta_{\text{ref}})} = \frac{c - u}{c - u_{\text{ref}}} = \frac{c - U + U - u}{c - U + U - u_{\text{ref}}} = \frac{c' - u'}{c' - u'_{\text{ref}}}, \quad (3.12)$$

where  $c' = c - U$ ,  $u'_{\text{ref}} = u_{\text{ref}} - U$  and  $u' = u - U$ . This is nothing but transforming the velocities into a reference system moving by horizontal velocity  $U$ . Thereby it is clear that the right hand side is indeed invariant with respect to this kind of transformation.

### 3.3

#### LINEAR CASE

Given the two different expressions for the surface dilation and compression, namely equations (3.6) and (3.10), it is illustrative looking at the limiting case of small wave steepness  $\epsilon$ , i.e.  $a \ll 1/k$ , and linear waves to simplify the problem. In this case  $\theta \approx 0$  for all  $(\vec{x}, t)$ . Moreover, the influence by the Stokes drift decreases along with  $\epsilon$  and the amplitude of the oscillation of  $\vec{x}(t)$  around the mean position, hence the local and material derivatives are approximately equal,  $\partial_t \ln(\delta b) \approx d_t \ln(\delta b)$ . Now, with  $u = c\epsilon \cos(\varphi)$  (see equation (2.29)) and the first order Taylor expansion of the exponent in equation (3.6), one finds:

$$\delta b(t) = \delta b_0 (1 - \epsilon \cos(\varphi)) = \delta b_0 \left(1 - \frac{u}{c}\right), \quad (3.13)$$

with  $\delta b_0$  describing the average width of the fluid parcel. Osborne [1965] reaches a corresponding (phase shifted) result for the vertical boundary layer thickness  $\delta h(t)$  under

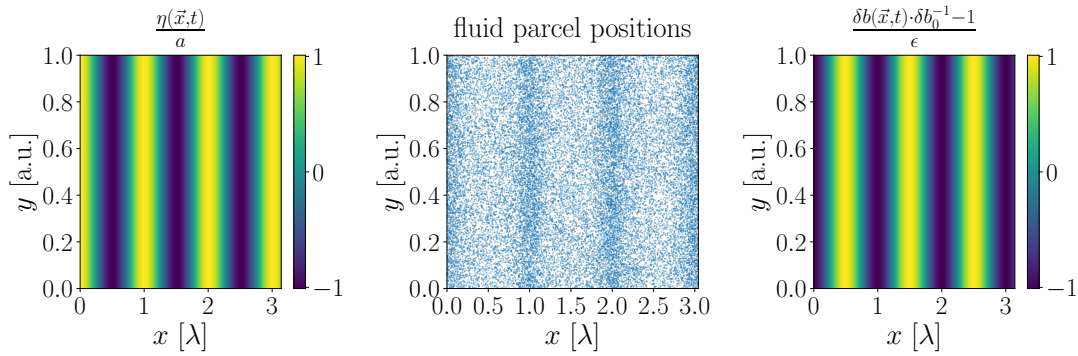


FIG 3.3.: The figure shows the normalized by amplitude elevation  $\eta(\vec{x}, t)$  of a linear wave with a single set of parameters (left), the position of some randomly picked fluid parcels (middle) and the fluctuation of the fluid parcel width normalized by wave steepness calculated by equation (3.13) (right). As can be seen, at the wave crests (bright colours, left plot) the fluid parcel density is at its highest, corresponding to small widths  $\delta b$  and elongation in  $z$ -direction. The situation is the opposite in the wave trough. A (unrealistically) high value of  $\epsilon = 0.45$  was chosen for visibility of the density fluctuations, with everything calculated in the linear wave framework.

the influence of linear waves. Expression 3.13 is also identical to equation (3.10) in the limiting case, when setting  $u_{\text{ref}} = \bar{u} = 0$  and  $\delta b_{\text{ref}} = \delta b_0$ .

As can be seen by equation (3.13), again viewing the water surface as an one dimensional compressible fluid, the compression is maximal for  $\varphi = 0$ , corresponding to the wave crest, and the dilation at the trough for  $\varphi = \pi$ , see figure 3.3. The fluid parcel encompassing the heated line will undergo periodic changes of  $\delta b$ , with the wave steepness giving the amplitude of the oscillation of the relative width  $\delta b(t)/\delta b_0$ . The important implication is that the width of the heated line will be altered accordingly. This will be discussed in further detail below.

### 3.4

#### FINITE AMPLITUDE CASE

Bringing it all together for the finite amplitude case, turning to the third order Stokes wave, equations (3.6) and (3.10) may be compared to directly numerically calculated quantities. Choosing two barely separated starting points at the water surface  $(x_1, \eta(x_1, t_0))$  and  $(x_2, \eta(x_2, t_0))$ , with  $\eta$  described by equation (2.38), their trajectories can be calculated by numerically integrating the velocities at their subsequent positions  $(\vec{x}_i, t)$ , see figure 3.4. Hereby  $c$  and  $\phi$  are given by equation (2.40) and (2.39), respectively, and the explicit Runge-Kutta 45 algorithm is used for integration with error control. The starting points represent the up- and downwind edges of a fluid parcel, their distance may therefore be used to verify the expressions for  $\delta b(t)$ . Furthermore, the situation is also easily viewed from a co-moving (constant drift) reference system, by letting all  $x$ -values drift by  $-u_S$ , with the Stokes drift calculated at mean vertical position of the fluid parcels  $ka^2/2$ , refer to section 2.2.1.

Starting with the clearly visible open orbit seen in figure 3.4(a), it is associated with Stokes drift (section 2.2), resulting in a moving mean parcel position  $\bar{x}(t)$ . As expected,

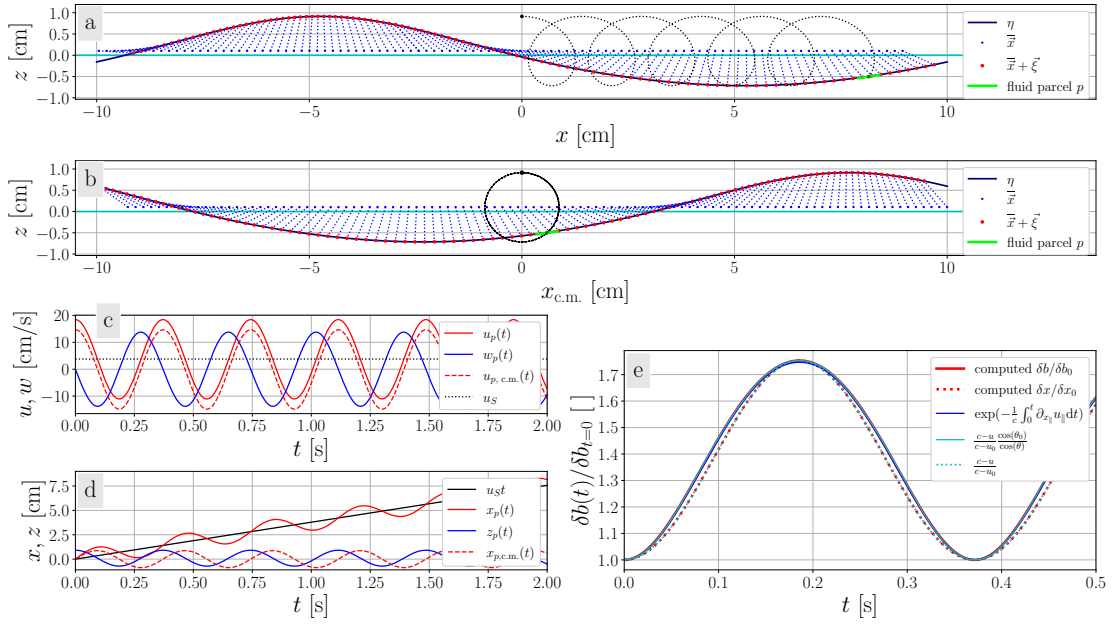


FIG 3.4.: The figure shows the surface layer of a 3. order Stokes wave with  $\epsilon = 0.25$  with no underlying current, from a reference system locked at the bottom (a) and one co-moving (c.m.) with the Stokes drift  $u_S$  (b), both at same time  $t = 2$  s. The horizontal and vertical scales are equal (i.e. equal aspect ratio), hence the shape is undistorted. The wave propagates in positive  $x$ -direction. The fluid parcel (lime) is followed from a starting point at  $\varphi = 0$  (black dot) and is the same in both plots, with the black dotted line marking its trajectory. The size of the depicted fluid parcel is exaggerated as compared to the one used for the analysis. Other evenly spaced (relative to their mean position  $\bar{x}(t)$ , blue dots) fluid parcels are also shown. The red dots mark their current position  $\vec{x}(t) = \bar{x}(t) + \xi(t)$ , with the parcel deflection  $\xi(t)$ , while the blue dotted lines guide to their corresponding  $\bar{x}(t)$ . For clarity,  $\bar{x}(t)$  are moving with speed  $u_S$  in the upper plot, and correspondingly non-moving in the moving reference system. Note that the mean vertical position  $\bar{z}_p = ka^2/2$  of the fluid parcels lie above  $z = 0$  (cyan line). This is also evident in (d) for  $z_p(t)$ .

Subplot (c) and (d) show the velocity components and positions, respectively, as function of time of the lime fluid parcel, with red corresponding to the  $x$ -components and blue to  $z$ . Dashed lines indicate the  $x$ -components in the moving reference frame, which are the only ones that change between the frames. The black dotted line in (c) marks the magnitude of the Stokes drift, also evident by the offset in  $u_p$  relative to  $u_{p,c.m.}$ . Likewise, in (d), the mean of  $x_p(t)$  increases corresponding to  $u_{St}$ .

Subplot (e) shows the temporal development of the fluid parcel width  $\delta b(t)$  relative to its reference width at  $t = 0$  s (red curve, barely visible), along with the curves following from equation (3.6) in combination with the equations (3.8) (blue) and (3.10) (cyan). The dotted lines show the computed  $x$ -component  $\delta x$  of the width relative to its initial value  $\delta x_0$ . Note that  $\delta x_0/\delta b_0 = \cos(\theta_0)$ . The development is shown for somewhat more than one period in the co-moving system,  $T'$ . As can be seen, both equation (3.6) and (3.10) describe the development well, with equation (3.6) deviating most.

when moving the reference frame with the very same velocity,  $\bar{x}$  become stationary in that frame, whereas the orbit of the fluid parcel relative to  $\bar{x}$  becomes nearly circular (i.e. circular for  $\epsilon \rightarrow 0$ ), closed orbits. The difference between the reference systems are also seen in plot (c), since the horizontal velocities are offset by  $u_S$  relative to the horizontal velocity in the co-moving system. Likewise in plot (d),  $x_p$  oscillates around a mean position drifting by  $u_S \cdot t$ .

Noting that the wavelength is unchanged between the systems, the Doppler shift mentioned in section 2.2 becomes evident. One wave period in the moving system equals to  $T' = 2\pi/(c'k) = 2\pi/((c - u_S)k)$ , with  $c$  given by equation (2.40) in the non-moving reference frame, hence the periods are longer in the moving frame than in the fixed frame. As the fluid parcels drifts by  $u_S$ , the curves in (c)-(e) all possess a periodicity of  $T'$ .

In the two topmost plots in figure 3.4, the compression at the crest and dilation in the trough can be clearly seen by the distance between the red points and the corresponding angles between the blue dotted lines and deflections  $\vec{\xi}(t)$  from their mean position. For the analysed fluid parcel, starting at  $\varphi = 0$ , its change of relative width is shown in (e), red curve, for roughly one orbit. The width was thereby referenced to its width at  $t = 0$ . Firstly, it should be noted that the width is always larger or equal to the initial width, which is a consequence of referencing to the width at  $\varphi = 0$ , where the fluid parcels reach their minimal widths. Furthermore, regarding only the  $x$ -contribution to  $\delta b$  and its relative change (red dotted line), it can be described by equation (3.9) when referencing to an initial state analogous to equation (3.11). The deviation from  $\delta b/\delta b_{t=0}$  are small ( $\sim 5\%$ ), which is adequately explained by  $\theta$  being small and the deviations caused by ignoring  $\cos(\theta)^{-1}$  in (3.10). The deviations are largest where  $|\theta|$  is largest, as expected.

More importantly, both equation (3.6), with the temporal derivative of the tangential velocity expressed by equation (3.8) (blue curve in figure 3.4e) and equation (3.10) (cyan curve) describe  $\delta b/\delta b_{t=0}$  well, with equation (3.10) being slightly better (relative deviations of  $\sim 5\%$  compared to  $\sim 1\%$ ). This is most likely caused by the numerical integration in (3.6b) in combination with the third order Stokes wave approximation being, at  $\epsilon = 0.25$ , quite far from the small wave steepness assumption by Stokes [1847]. These deviations also tend to approach the numerical error tolerances as  $\epsilon$  becomes smaller, for  $\epsilon = 10^{-6}$  the deviations are of order  $10^{-12}$ .

Furthermore, the description of the derivative of the tangential velocity in (3.8) was based on potential theory, as the Cauchy-Riemann relations were used. This is questionable within the boundary layer in the presence of shear forces, as this introduces vorticity and hence breaks the assumption of irrotationality. Equation (3.10) was based on using that a wave of spatially non-varying shape may be described by  $x - ct$ , which is not altered by vorticity present in the boundary layer. However, verifying (3.10) for a rotational wave remains, which could be approached numerically (Francius and Kharif [2017], also see Murashige and Choi [2020]), the same holds true for higher order Stokes waves or other solutions to the wave problem in section 2.2.

Based on this, equation (3.10) is used for describing the surface compression and dilation in the rest of this thesis, thereby yielding an expression reasonable for practical application. It must be emphasized, however, that the relation is derived for a single set of parameters  $a, k$  yielding a value for  $c$ . In reality, there will be much more complicated wave fields. As will be explained in chapter 6, this will be handled by using estimated parameters for the dominating wave.

## 3.5

### IMPLICATIONS FOR THE THERMOGRAPHIC MEASUREMENT METHOD

As already mentioned, the above findings have some direct impact on the measurement technique for the viscous shear stress, as the surface compression and dilation alters the widths of the heated lines, and hence their distributions. As the method relies on analysing a *characteristic* line width, the question remains how it is best described. In the case of waveless conditions, the distributions were approximately of Gaussian shape (Voigt [2019]), easing the characterization due to the symmetry of the normal distribution, as both maximum count, mean and median equal the same value. As will be argued in this section, this is no longer the case in the presence of waves, making the characteristic line width more ambiguous.

#### 3.5.1

##### SINGLE SET OF WAVE PARAMETERS

Firstly, the initial widths of the heated lines  $\sigma_0$  are influenced by the surface velocity, as the laser always points at the same point in space during the heating of the lines and is turned on for a finite amount of time  $t_{\text{laser on}}$ , during which the surface moves. Subsequently, as the velocity depends on wave phase, this is also true for the initial line width. For simplicity, in the following assume that the laser with a Gaussian beam of width  $\sigma_{\text{laser}}$  is directed purely vertically, the horizontal surface velocity component is of sinusoidal shape superposed with a mean drift,  $u = \tilde{u}_0 \cos(\varphi) + U_d$  and the influence by surface inclination on the line width is negligible. Also neglecting shear flow in the boundary layer and diffusion, which has only a minor influence on the profile for such small times, the temperature profile yielding the initial width will be given by:

$$T(x) \propto \int_0^{t_{\text{laser on}}} \exp\left(-\frac{(x-ut)^2}{2\sigma_{\text{laser}}^2}\right) dt \quad (3.14)$$

If the wave phase is sampled uniformly, the velocity probability density function can be described by an arcsine density distribution (Crooks [2019]):

$$P(u) = \frac{1}{2\pi} \frac{d\varphi}{du} = \frac{1}{\pi} \frac{1}{\sqrt{(u + \tilde{u}_0 - U_d)(\tilde{u}_0 + U_d - u)}}, \quad (3.15)$$

see figure 3.5.

Hence, the most likely velocity to influence the initial width is  $u = U_d \pm \tilde{u}_0$ . Since the wave period is long compared to the heating time of the lines, the velocity is approximately constant during the heating process, and therefore also the distribution of  $\sigma_0$  is expected to show two peaks, corresponding to those extremal values, if  $t_{\text{laser on}}$  and  $u_0$  are high enough, refer to the right plot of figure 3.5, and  $U_d \neq 0$ . The latter must be true in order to not get symmetric velocities for both extrema, which yield the same  $\sigma_0$ . It also requires  $\sigma_0$  to be sharply distributed and the presence of only a single wave mode to avoid smearing of the distributions, which in practice is not given. However, as it is illustrative, this framework will be carried on. Also diffusion will be neglected, as the focus lies solely on alteration of the distributions caused by the wave motion as discussed in this chapter.

Moving on to surface dilation and compression, the line width will oscillate in accordance with the fluid parcel that encompasses it, and is thereby described by



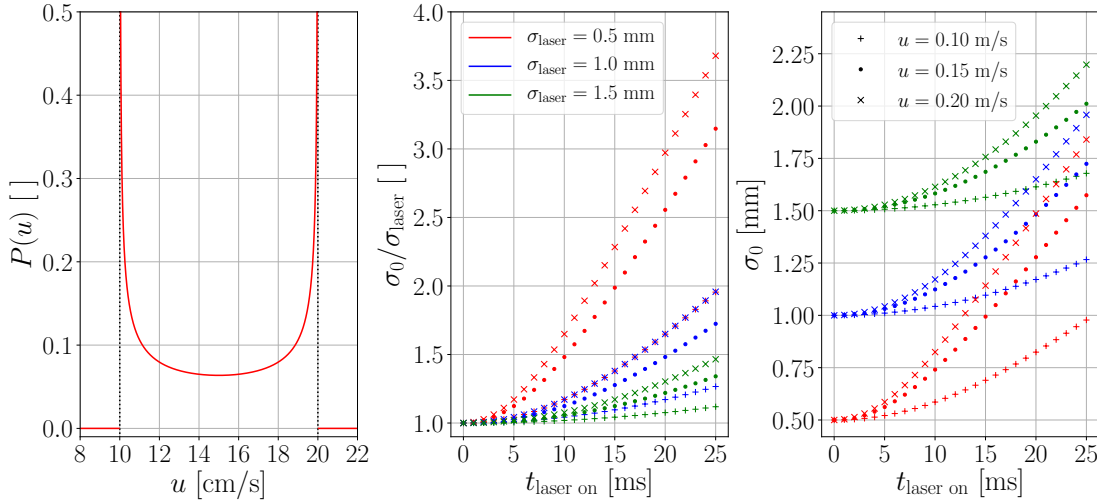


FIG 3.5.: The left plot shows the arcsine distribution (3.15) for  $\tilde{u}_0 = 5$  cm/s and  $U_d = 15$  cm/s, which diverges for  $u = U_d \pm \tilde{u}_0$ , in the sense that the integral still equals 1. The middle and right subplot shows the initial line width  $\sigma_0$  for different heating times  $t_{\text{laser on}}$  under the influence of horizontal surface flow velocities  $u$ , relative to the width of the laser beam  $\sigma_{\text{laser}}$  (middle) and absolute (right). Markers and colours are equal in both (right and middle) plots. As can be seen, the relative and absolute alteration is largest for high velocities and small  $\sigma_{\text{laser}}$ . For high  $t_{\text{laser on}}$ ,  $\sigma_0$  is expected to increase  $\propto u \cdot t_{\text{laser on}}$ , when the shape of the temperature profile, equation (3.14), changes from Gaussian to exhibiting a plateau of constant temperature. Correspondingly, for small  $t_{\text{laser on}}$  the profile remains of Gaussian shape due to the width of the beam, hence only minor changes in  $\sigma_0$  occur. The smaller  $\sigma_{\text{laser}}$ , the faster the transition, hence both  $\sigma_0 - \sigma_{\text{laser}}$  and  $\sigma_0/\sigma_{\text{laser}}$  are largest for small  $\sigma_{\text{laser}}$  for given  $t_{\text{laser on}}$ . Diffusion was neglected.

equation (3.10). The reference width for that line, however, will always be given by  $\sigma_0$ . For example, if a line is heated in the trough of the wave, the surface dilation there is maximal, and the line will be compressed for all other wave phases until again reaching its original width in the next trough. As the (Eulerian) velocity and hence  $\sigma_0$  in the trough is minimal, see e.g. figure 3.4, one would expect the over all lowest possible line widths for each phase. Correspondingly,  $\sigma_0$  is expected to be maximal at the crest and stretched for all other wave phases, yielding the maximum line width for each phase. Moreover, these two extrema also correspond to the most likely events, as expected from the arcsine distribution. Since the measurement technique is based on finding a *representative* line width, this tendency towards the extrema is a rather unfortunate phenomenon.

More quantitative, one finds by equation (3.10):

$$\frac{\sigma(t)}{\sigma_0 \cdot g(t)} = \frac{\delta b(t)}{\delta b_0} = \frac{\cos(\theta_0)}{\cos(\theta)} \cdot \frac{c - u}{c - u_0} =: f(t), \quad (3.16)$$

when referencing to the parameters at  $t = 0$ , i.e. the initial wave phase  $\varphi_0$  when heating the line. See figure 3.6 for a plot of  $f$  for different  $\varphi_0$ . The function  $g(t)$  was added to account for diffusion related broadening of the line, such that in the absence of waves

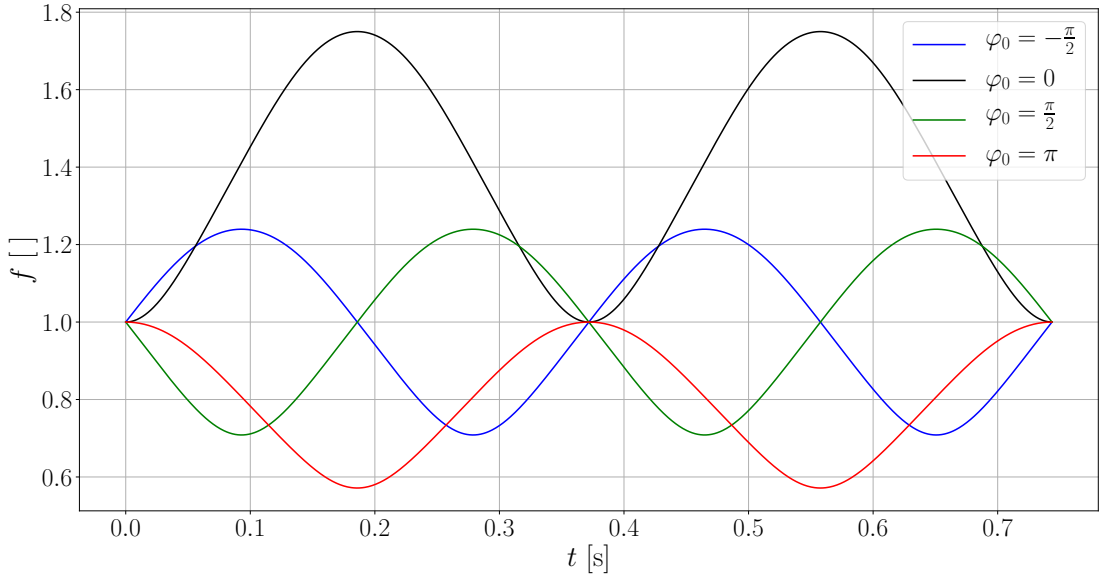


FIG 3.6.: A plot of  $f(\varphi_0)$ , equation (3.16), for a third order Stokes wave with  $\epsilon = 0.25$  and  $\lambda = 0.2\text{m}$ , equal to that in figure 3.4. Note that  $f$  is independent on the underlying bulk drift, as seen in section 3.2, whereas  $\sigma_0$  is not. Seen is the asymmetry in stretching and compression of the line widths, arising from  $\sigma_0$  fixing the reference width. For the lines heated at the crest, expected to be wider than those starting in the trough for a non-vanishing mean surface velocity,  $f(\varphi_0 = 0) \geq 1$  for all  $t$ , whereas  $f(\varphi_0 = \pi) \leq 1$  for those in the trough. Note that  $\max\{f(\varphi_0 = 0)\} = (\min\{f(\varphi_0 = \pi)\})^{-1}$ , and  $\max\{f_{\varphi_0}(t)\}/\min\{f_{\varphi_0}(t)\}$  is equal for all  $\varphi_0$ .

$f(t) = 1$  for all  $t$ . Neglecting diffusion in the following, one can set  $g(t) = 1$ . By equation (3.16) one finds  $f(t = 0) = f(t = T') = 1$ , with  $T'$  being one wave period seen from the co-moving perspective of the line. Furthermore, the magnitude of  $f$  is dependent on  $\varphi_0$ , as for example  $(c - u_{\min})^{-1} \leq (c - u_{\max})^{-1}$  in the case of the discussed extrema. This introduces an asymmetry in the distributions of the line widths for  $t \neq T'$  (and integer multiples), with the range of high values of  $\sigma(t)$  (i.e. for  $f > 1$ ) being larger than the range of the small  $\sigma(t)$  (i.e.  $f < 1$ ). To clarify, the lines heated at the crest undergo a larger absolute change in width when stretched, compared to the lines in the trough when compressed, even if their initial widths were equal. The discussed dependence of  $\sigma_0$  on  $\varphi_0$  comes on top of this, and further exaggerates the tendency towards large  $\sigma(t)$ . Also noting that the ratio of  $\max\{\sigma_{\varphi_0}(t)\}/\min\{\sigma_{\varphi_0}(t)\} = (c - u_{\min})/(c - u_{\max})$  is independent of  $\varphi_0$  when assuming  $\theta = 0$  when  $u$  is extremal, in contrast to the line widths themselves, further supports the impression of the asymmetric distributions. That the ratio must be constant is clear from the fact that the width of the fluid parcel encompassing the line will always oscillate in the same manner, irrespective of the initial state of the line.

With several aspects coming together, it is helpful to look at a numerical example with a large number of randomly picked initial phases, still in the idealized framework of a fixed  $\sigma_{\text{laser}}$  and a single set of wave parameters. The result is shown in figure 3.7. As can be seen in the topmost plot for  $\sigma_0$ , the two expected peaks from the arcsine distribution are seen. The peak for the lower value of  $\sigma_0$ , corresponding to  $u = -\tilde{u}_0 + U_d \approx 0$ , is more pronounced, however. This can be explained by the low value of  $u$ , causing only a

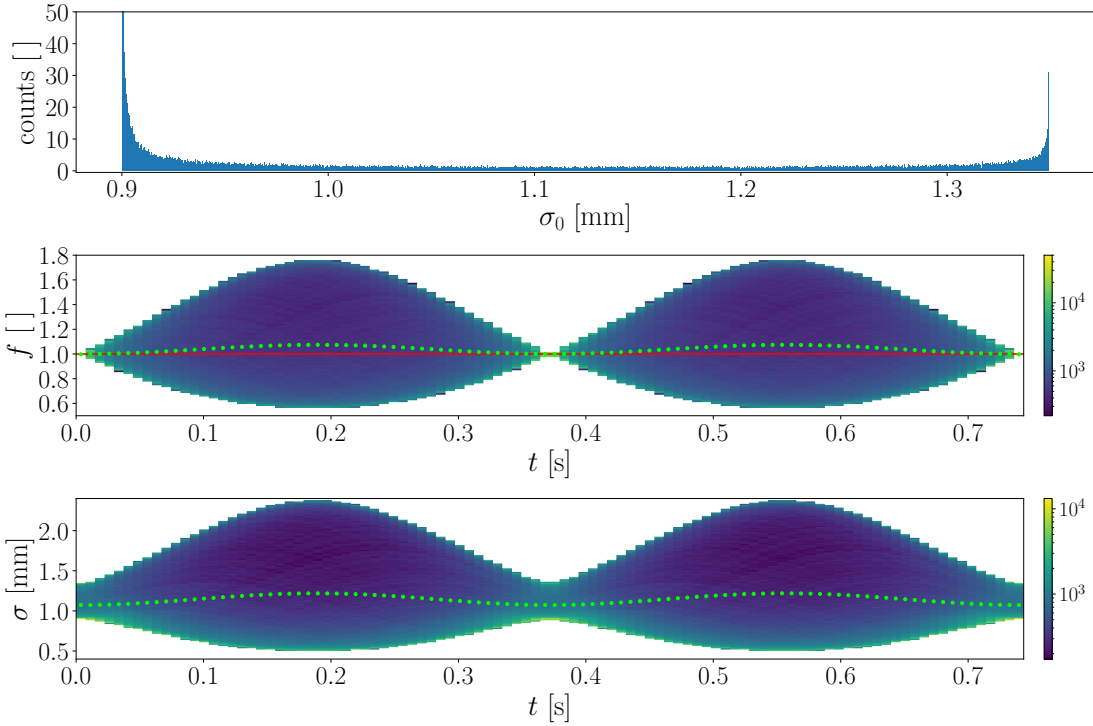


FIG 3.7.: The figure shows the result of  $5 \cdot 10^4$  randomly initiated (with respect to phase), heated lines on a third order Stokes wave, under the assumption of constant velocity during heating the line. Diffusion was omitted in order to enclose only the aspects discussed above. The topmost plot shows the distribution of the initial line width  $\sigma_0$ , the middle plot a (2D) histogram of  $f(t)$ , see equation (3.16) and the lower plot the histogram of the temporal evolution of the line width  $\sigma$ . The red line in the middle plot marks  $f = 1$ . Lime dots mark the average values of the respective distributions, note the slight tendency toward high values at  $t \sim T'/2$  compared to  $t = 0$ . A logarithmic color scale in the lower two plots was used. Parameters were:  $\epsilon = 0.25$ ,  $t_{\text{laser on}} = 10 \text{ ms}$ ,  $\sigma_{\text{laser}} = 0.9 \text{ mm}$ ,  $\lambda = 0.2 \text{ m}$  and  $U_d = 0.15 \text{ m/s}$ .

minor change in  $\sigma_{\text{laser}}$  (figure 3.5), such that a larger range of velocities  $u$  get sampled per bin than for the upper peak of  $\sigma_0$ .

The two lower plots of 3.7 show the explained asymmetry, and the higher counts at the extremal values of both  $f$  and  $\sigma(t)$ , with more counts at the minimum, reflecting the distribution of  $\sigma_0$ . The return to the initial state at  $t = T'$  is also clearly visible. Furthermore, the averaged values of the distributions are not constant, both the mean  $f$  and  $\sigma$  tend towards slightly higher values at  $t \sim T'/2$  than at  $t = 0$ .

### 3.5.2

#### DISTRIBUTED PARAMETERS

Having gained some insights on what to expect for an idealized situation, one might approach the problem of the characteristic line width using a slightly more complex, although still highly simplified, scenario. Besides, noting that the characteristic line width must correspond to  $f = 1$  in order to represent and correspond to  $\sigma_0$ , it is time to progress beyond looking at only one set of wave parameters. Longuet-Higgins [1952]

derived that the wave height distribution of ocean waves approximately follow a Rayleigh distribution,

$$R(x; s) = \frac{x}{s^2} e^{-x^2/(2s^2)}, \quad (3.17)$$

with  $s$  being the scale parameter, corresponding to the maximum of the distribution. In order to derive this result, Longuet-Higgins [1952] assumed a narrow frequency band and a large number of modes interfering from different directions. Since  $\omega = ck \approx \sqrt{k}$  for deep water gravity waves, this implies that also  $k$  must be narrowly distributed. In the following, it will still be assumed that each individual heated line is only affected by one (randomly drawn) wave with a single set of parameters, for simplicity.

Since  $a$  is then Rayleigh distributed and  $k$  of little variation, also the wave steepness  $\epsilon$  follows approximately a Rayleigh distribution. As found in section 3.3, the compression and dilation is determined by  $\epsilon$ . With the wave associated velocity  $\tilde{u}_0 \approx ack$  (see equation (2.29)), the magnitude of  $f$  is strongly dependent on  $a$ , with  $f(t) = 1$  for  $a = 0$ . Therefore, in the depicted situation, one expects the pronounced extrema of  $f$  as seen in the middle plot of figure 3.7 to be more evenly but skewly distributed towards higher values in accordance with the underlying distribution of  $a$ . Furthermore, irrespective of  $\varphi_0$  and  $a$ , as long as each individual line is affected by one set of wave parameters, it will revisit  $f = 1$  for  $t > 0$  at least once per  $T'$ . One therefore might assume that the distributions of  $f$  peak at  $f \approx 1$  for all times after heating the line, with varying degrees of skewness and distribution width. Hence, as long as  $\sigma_0$  is approximately independent on  $\phi_0$ , corresponding to low values of  $t_{\text{laser on}}$  and some spatial variation of  $\sigma_{\text{laser}}$ , there will be a single peak in the distribution of  $\sigma(t)$ , which indeed corresponds to  $f = 1$ . How sharp this peak is, however, will depend on the circumstances.

Due to  $|u_{\text{min}}|$  being closer to zero than  $|u_{\text{max}}|$ , a skewed distribution of  $\sigma_0$  is expected, with the long tail towards higher values corresponding to high values of  $u_0$ . In analogy to the reasoning for  $f$ , the peak would correspond to  $u = U_d$ , as this value is visited for all  $a$ , whereas the width would also depend on the circumstances.

Again considering a numerical example, see figure 3.8, one sees that the above reasoning to a large extent holds true in this simplified framework. Of course, care must be taken, as this highly simplified situation is far from the real world application. Still, some valuable information about the phenomenology may be found. The distributions of the parameters used may be compared to measured distributions in figure 6.8, note that  $k$  is broader distributed in reality, however.

In addition to the Rayleigh distribution of the amplitudes, both  $k$  and  $\sigma_{\text{laser}}$  were described as normally distributed, i.e.:

$$\mathcal{N}(x; \mu, \sigma) = \frac{1}{\sqrt{2\pi}\sigma} \exp\left(-\frac{(x - \mu)^2}{2\sigma^2}\right) \quad (3.18)$$

each with a width of 5% of the respective mean values. What can be seen, is that for  $f(t)$  (second lower plot) the maximal value of the distributions (red dots) lies at about  $f = 1$ , with a minor tendency of deviating about 5% towards lower values when the distributions reach their maximal width at  $t = T'/2$ . There are also some fluctuations of the maximum values, as expected due to the randomness of the initial parameters and the resulting distributions. Also the mean values (lime dots) of  $f(t)$  at each  $t$  is stable at  $f \approx 1$ , with a tendency towards larger values (deviations  $\sim 1\%$ ).

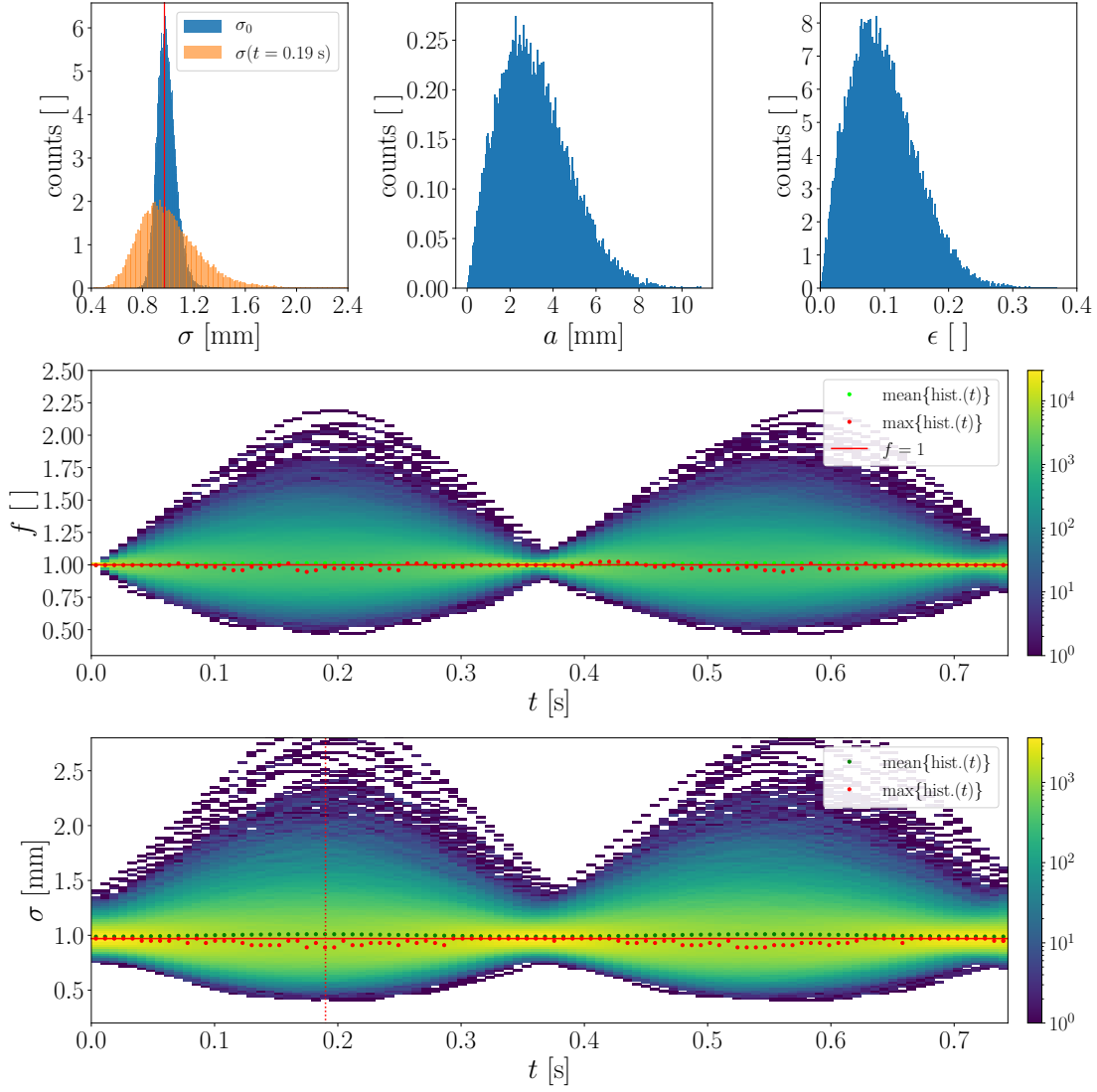


FIG 3.8.: The figure is similar to figure 3.7, but with distributed parameters. It shows the result of  $3 \cdot 10^4$  randomly initiated heated lines on a third order Stokes wave. Diffusion was omitted. The 3 topmost plots show the distribution of the line widths  $\sigma(t)$  initially ( $\sigma_0$ ) and at  $t = 0.19 \text{ s} \approx T'/2$  (left), the Rayleigh distributed amplitude  $a$  (top, middle) and wave steepness  $\epsilon$  (right). The two latter may be compared to measured distributions, see figure 6.8 for the  $u_{10} \approx 4.8 \text{ m/s}$  measurement. The second lowest plot shows a histogram of  $f(t)$ , with the maxima (red dots) and mean values (lime dots) given for each  $t$ . The thin red line shows  $f = 1$ . The lowest plot shows the histogram of  $\sigma(t)$ , with red dots representing the maxima of the distributions and green dots the mean values. The initial line width is represented by the red line, also shown in the upper left plot for reference. Note the logarithmic colour scale in the two lower plots. Parameters were:  $a = H/2$ ,  $H \sim R$  ( $s = 5 \text{ mm}$ ),  $t_{\text{laser on}} = 10 \text{ ms}$ ,  $\sigma_{\text{laser}} \sim \mathcal{N}(\mu = 0.9 \text{ mm}, \sigma = 0.045 \text{ mm})$ ,  $k \sim \mathcal{N}(\mu = 2\pi/0.2, \sigma = 2\pi/4)$  and  $U_d = 0.12 \text{ m/s}$  (latter realistic for  $u_{10} \approx 4.8 \text{ m/s}$ , else compare to figure 6.8).

Moving on to the distributions of  $\sigma(t)$  (bottom plot), the expected skewed distributions towards high values are clearly evident, especially for  $t \sim T'/2 \approx 0.19$  s. The maximum of the distributions (red dots) are rather stable, for all times. The values at  $t \sim T'/2$  again tend to somewhat lower values than at  $t = 0$ , deviating on average by  $\sim 5\%$ . This is mainly caused by the high number of lines corresponding to the low extrema of  $f$ , as seen also for a single wave in figure 3.7. The mean of the distributions are depicted by the green dots, and yield stable values with respect to  $t$ , lying a bit above the values of the distribution maxima. The initial line width is depicted as the red line. For reference, this line is also shown in the upper left plot, along with the distribution of line widths at  $t = 0$  and  $t = 0.19$  s. Note the different peak positions, deviating by  $\sim 5\%$  as mentioned above, and that both distributions are skew as expected, especially that for  $t = 0.2$  s. In the case of a sufficiently narrow distribution of  $\sigma_0$ , the peaks of  $\sigma(t)$  correspond to those of  $f(t)$ .

Based on the reasoning above and numerical example in figure 3.8, the peaks of the distribution of  $\sigma(t)$  will approximately correspond to  $f = 1$ , and may therefore be used as the characteristic line width since they then correspond to the unaltered (by surface compression and dilation) line widths. The deviations are smaller for  $t \approx nT'$  than at  $t \approx nT'/2$ , for integer  $n > 0$ . The main reason for preferring the peak positions as the estimator for the characteristic line widths over the mean, is that experimentally speaking, the mean is prone to a bias caused by outliers. As line widths are strictly non-negative, low value outliers will be restricted to the range between zero and the actual  $\sigma(t)$ , whereas high value outliers are unrestricted, simply leading to the elongation of the tails of the (skew) distributions. Due to the rather heavy tails, defining a cut-off for outlier detection is questionable, as this may influence the resulting mean value. Hence, evaluating the peak of the distribution is a more stable estimator.

As the real wave fields consist of superposing waves and a wider frequency band than allowed for in the numerical example above, it is to be expected that the narrowing of the distributions seen in figure 3.8 at  $T'$  vanishes as the periodicity is no longer as sharply determined, and that the distributions are overall broader than in this simplified example. Furthermore, diffusion, under the influence of shear flows in several directions, will add another contribution towards even broader distributions, in addition to a general increase in  $\sigma(t)$ . The observed distributions of  $\sigma(t)$  are indeed both skewed and peaked, mostly without the narrowing at  $T'$ .

### 3.5.3

#### INFLUENCE ON THE DIFFUSION RELATED BROADENING

As a final aspect, the stretching and compression of the lines may also alter the broadening of the heated lines. By viewing the diffusion process acting on a temperature profile as a convolution with a Gaussian kernel, see section 2.3.3, one can argue that altering the spatial dimensions of a fluid parcel will have impact on the smoothing of temperature profiles associated with diffusion. This can be thought of as the Gaussian kernel being unaltered, whilst the spatial temperature structures of the fluid parcel (such as temperature gradients or widths of distributions) will be changed. In the case of horizontal stretching, for example, with a localized temperature gradient purely in  $x$ -direction, this gradient would become smaller. The horizontal distance a particle would need to surpass by random walk in order to escape the gradient would also be longer.

For simplicity, regarding  $\delta b(t)$  described in the linear case of section 3.3, the extremal values of the width of the fluid parcel will be  $\delta b_{\text{extr.}} = \delta b_0(1 \pm \epsilon)$ , with mean width  $\delta b_0$ .

In the most relevant measurement conditions, that is for low wind speeds,  $\epsilon$  of the dominating wave is mostly a rather small number with subsequent low changes of the extent of the fluid parcels encompassing the heated lines. With the wave period being smaller or similar to the life time of the heated lines, the individual line will undergo both stretching and compression and the subsequent alterations of the temperature profiles, and only spend short times at the extrema, i.e. maximal stretching and compression.

Furthermore, assuming laminar alteration of the fluid parcel during the dilation and compression, the shape of the temperature profile will return to its original except diffusion related smoothing. For the line this would mean that it stays a line during and after completing a wave cycle. This brings along another point; in contrast to shear flow, which deforms the shape of the profiles, the surface compression and dilation acts by normal strain, hence predominantly alters the spatial extents of the fluid parcel without shearing it. To clarify, this is reflected by their respective dependencies;  $\partial_{z_{\perp}} u_{\parallel}$  for the shear flow and  $\partial_{x_{\parallel}} u_{\parallel}$  for the normal strain, with  $x_{\parallel}$  and  $u_{\parallel}$  tangential and  $z_{\perp}$  normal to the surface, respectively. For conditions similar to those depicted in figure 3.8 above (i.e.  $u_{10} \approx 4.8$  m/s),  $\partial_{x_{\parallel}} u_{\parallel}$  is roughly 10 times smaller than  $\partial_{z_{\perp}} u_{\parallel}$ .

Based on this, the effect of Taylor dispersion corresponding to the enhancement of line broadening due to the presence of shear flow, is assumed to dominate the broadening of the lines. Hence the effect of surface compression and dilation on the broadening due to diffusion is neglected in the following. Note that this must not be confused with the compression and stretching of the fluid parcels, causing the discussed alterations in the line widths; solely the effect on the diffusive broadening is neglected.

## 3.6

### SUMMARY OF CHAPTER 3

The most important implications found above regarding the influence by waves for the thermographic method:

- The heated lines undergo an alteration of their width  $\sigma(t)$  associated with wave induced surface compression and dilation. This is in the following described by equation (3.16), and is wave phase dependent.
- The peaks of the expectedly skew distributions of  $\sigma(t)$  are used as an estimator for the characteristic line widths, with the smallest deviations for times corresponding to an integer multiple of the wave period in the reference system following the mean surface velocity. It is advantageous to sample (i.e. heating the lines) such that both different wave phases and the -field is reflected.
- It is preferential to keep the heating time of the line at a minimum in order to minimize the width and wave phase related skewness of the distribution of  $\sigma_0$ .
- The influence by the compression and dilation on the diffusion related line broadening is neglected.





# 4 | SETUP AND MEASUREMENTS

In this chapter the setup, measurements and the wind-wave facility will be presented. All image acquisition was done and controlled by scripts written in Heurisko.

## 4.1

### THE AEOLOTRON

All measurements were conducted at the Aeolotron annular wind-wave facility, see figure 4.1, located at the Institute of Environmental Physics in Heidelberg, Germany. The outer diameter is about 10 m and channel width approximately 61 cm. Filled to approximately 100 cm this corresponds to a water volume of roughly  $18 \text{ m}^3$ . The height of the air compartment is then about 140 cm, with the wind being driven by four evenly spaced axial ventilators. The annular shape gives rise to secondary flows, which prevent a logarithmic wind profile as found in for example linear facilities and additionally makes the wind field inhomogeneous (Bopp [2014]). As a consequence, it is more difficult to reference the wind speed in the Aeolotron to the usual reference to the wind speed at a height of 10 meters,  $u_{10}$ . Estimations exist (refer to Bopp [2014] for details), however, and are given in 4.1 for the measurements included in this thesis. These are given for the frequency used to control the axial ventilators (possible range between 0 and 50 Hz). In the this work, since the wind generator frequencies are given and the estimates of  $u_{10}$  might change, the former will be referred to in this thesis, for future reference.

## 4.2

### SETUP JANUARY 2021

The setup consisted of the a combined configuration for the active thermography and a system for measuring the surface elevation along a line parallel to the wind direction, see figure 4.3. The active thermography setup consisted of the infrared sensitive camera FLIR X8501sc with a FLIR 50 mm (i.e. focal length) lens, gratefully lent from FLIR systems, and a near-infrared (NIR) laser. The camera is sensitive in the spectral range of  $3.0 - 5.0 \mu\text{m}$ , and has a resolution of  $1280 \times 1024$  pixels along with a thermal sensitivity of  $\leq 30 \text{ mK}$  (FLIR Systems [2020]). The detector material is indium antimonide (InSb) with a detector pitch of  $12 \mu\text{m}$ , cooled by a Sterling cooler. This yields along with the used lens and roughly 1.5 m object distance a observed pixel size of  $12 \mu\text{m}/\text{px} \cdot \frac{1500 \text{ mm}}{50 \text{ mm}} \sim 460 \mu\text{m}/\text{px}$ . This is comparable to the calibrated  $\sim 420 \mu\text{m}/\text{px}$ . The camera was mounted at an angle of about  $20^\circ$  relative to the vertical direction and facing upwind, see figure 4.3. This was done in order to not see the reflection of the cooled camera detector (Kunz [2017]).

In the measurements, only half-frame images ( $640 \times 512$  pixels) were acquired. This

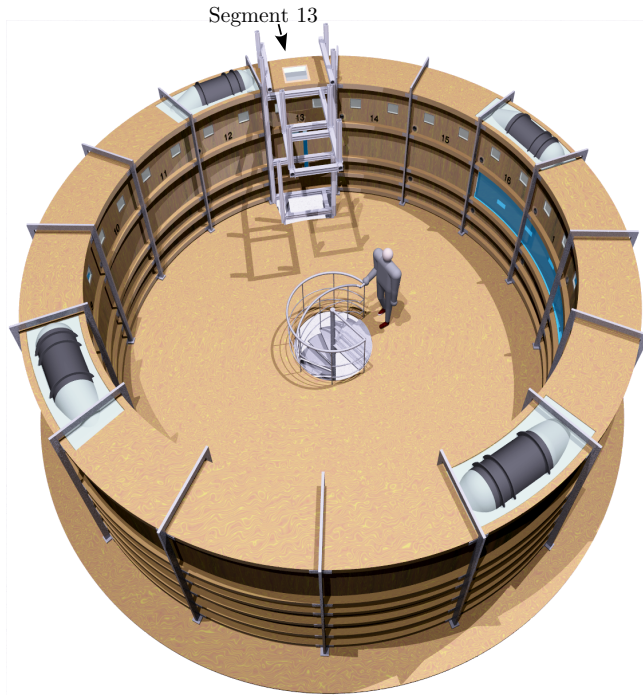


FIG 4.1.: Schematic of the Aeolotron. The experiment was conducted at segment 13, where the optical access is located. Modified from Krall [2013].

was done in order to reduce the amount of data, without compromising the measurement. Frame rates were 200 fps and exposure time of 4.8 ms for wind reference frequency  $< 15$  Hz and 250 fps and an exposure time of 3.8 ms at wind reference frequency higher than 15 Hz.

The laser used consists of 9 SemiNex T09-181-161 Laser diodes, divided into two separately controllable blocks, emitting in the NIR at  $\lambda = 1450 \pm 20$  nm, see figure 4.2 for the characteristic curves. The diodes already have a line-like shape, with an emitter width of  $95 \mu\text{m}$  and height of  $1 \mu\text{m}$ . Together with aspherical lenses with a focal length of 4.6 mm and object distance of 1450 mm, the heated lines were expected to be  $\sim 28 \times 0.3$  mm. This was not the case, however, with only 3 sharp lines, all in one block, with a width of  $\sigma_{\text{laser}} = 0.9 \pm 0.1$  mm dimension was off by a few millimetres, but is less critical. Hence only this block was used, containing four diodes, which were oriented perpendicular to the wind direction and at an angle relative to the vertical direction of about  $8^\circ$  in radial direction towards the channel center (refer figure 4.3). One of the four diodes in the block gave rise to a highly unsharp signal, hence the three lines were a result of merely 3 diodes. They were supplied by 8 A, enabled by a 40 F capacitor pack, referring to the characteristic curves in figure 4.2 this yields a power per centimeter line of about 0.8 W/cm. A supply voltage of 10 V was used. The penetration depth in water at  $27^\circ$  is  $\zeta_{\text{laser}} = (318 \pm 4) \mu\text{m}$  (Palmer and Williams [1974]), which is assumed correct also at  $\sim 20^\circ\text{C}$  at the measurement.

The laser was pulsed at frequencies between 1 and 5 Hz, with heating time of the line  $t_{\text{laser on}} = 15$  ms, using custom electronics and a Teensy microcontroller. When temporally feasible, the laser frequency was adjusted during the measurements, to heat a high number of non-overlapping lines. The maximum frequency depends on the water

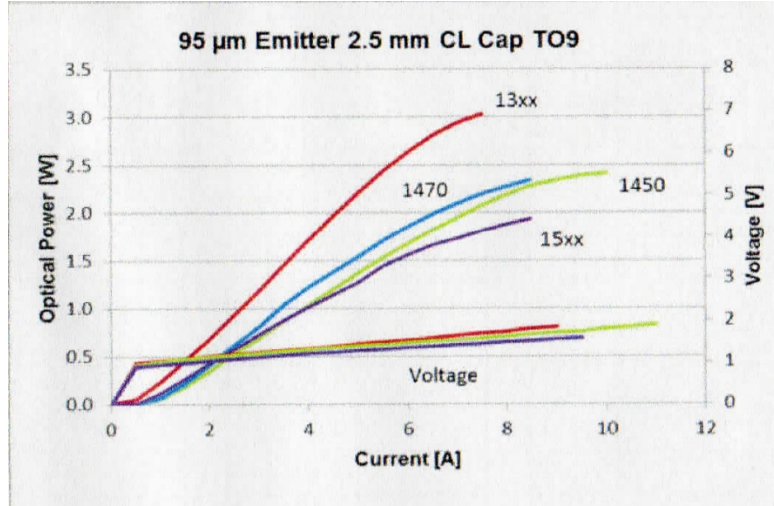


FIG 4.2.: Characteristic curves for the NIR-diodes SemiNex T09-181-161. They were used at 8 A supply current.

surface velocity. For that reason, an IR image was displayed every 5 seconds, giving an handle for how high the frequency could be and adjust it accordingly.

The water elevation was measured simultaneously, using a second camera (laser height camera, LHC) sensitive in the visible wavelength range in combination with a laser sheet that was non-pulsed and a fluorescent dye. The laser height camera was triggered by the IR-camera, hence acquiring images at the same rate and timing.

The camera was Basler acA1920-155um (1500x667 pixel section was used, compared to detector resolution of 1920x1200 pixel) with a 17 mm Tokina wide angle lens, mounted with a Scheimpflug adapter (see Scheimpflug [1906]) and a green band pass filter (525 nm). This enabled mounting the camera well above the water surface at an angle of about  $30^\circ$  relative to the horizontal direction, see figure 4.3, while still seeing the vertical plane in focus. Hence problems with wetting of the measurement window and subsequent unsharp images were avoided. The wide angle lens furthermore enabled a broad enough field of view for all measurement conditions. At the water surface, the resolution was  $\sim 200 \mu\text{m}/\text{px}$ , which is enough for the dominant wave field parameters that were needed for evaluation. An exposure time of 3 ms was used.

The laser used for the LHC measurement consisted of three blocks of Nichia NUBM08 Diode Bank, emitting at  $(455 \pm 5) \text{ nm}$ . These formed a laser sheet, oriented parallel to the wind. About 13.5 cm were seen by the camera at the surface, which was the maximum limited by the measurement window installed in the facility. The three block were supplied with  $46.5 V_{DC}$ , which along with the current yields a total power of about 90 W. The mounting angle relative to the vertical direction was about  $4^\circ$  downwind.

The water was dyed with  $(10 \pm 0.1) \text{ g}$  Pyranine (Trisodium 8-hydroxypyrene-1,3,6-trisulfonate), corresponding to  $\sim 10^{-6} \text{ mol/L}$ , in combination with  $5 \cdot 10^{-5} \text{ mol/L}$  sodium hydroxide (NaOH). Pyranine's fluorescent properties are pH dependent (Schwarz [2016]), and has the advantage of possessing a rather large Stokes shift at the wavelength of the deployed laser. This means that it is excited at 455 nm (corresponds to blue), but emits at about 511 nm (green, Kräuter [2015]). Hence, by using the mentioned green band pass filter, most reflexes from the laser can be filtered out, easing the water level detection.

Due to the large amounts of data continuously (cyclically) acquired simultaneously

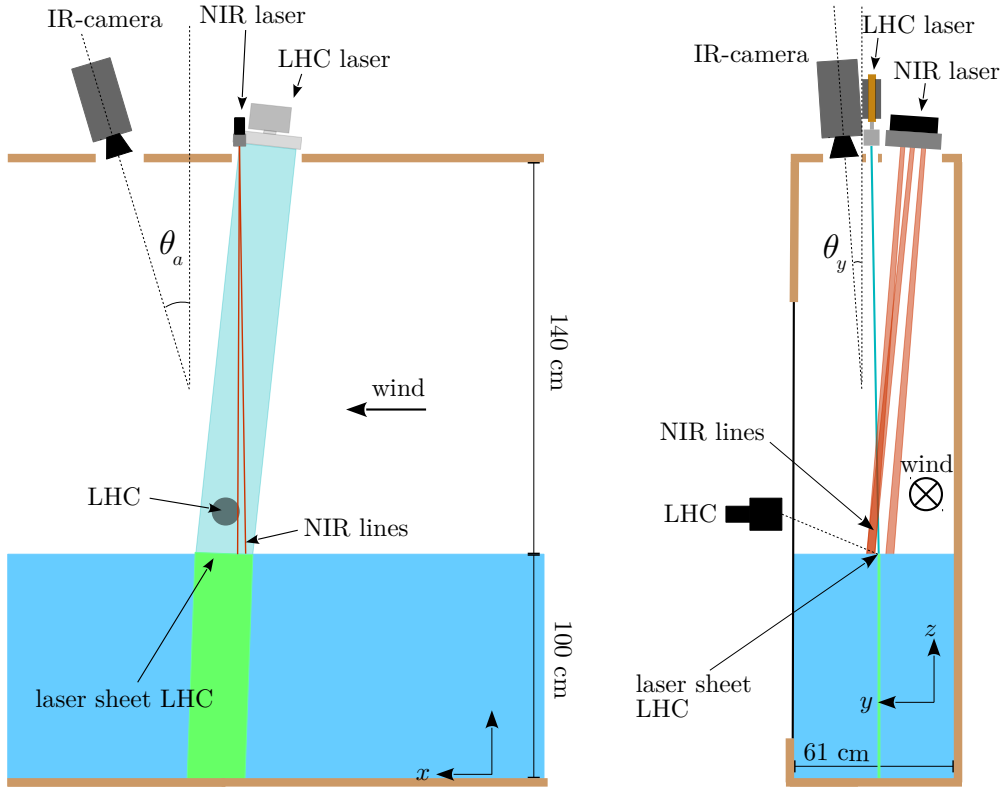


FIG 4.3.: Schematic of the setup, tangentially (left) and radially (right) to the wind-wave facility. Active thermography: The NIR-laser is pointing vertically ( $xz$ -plane) and at an angle of  $8^\circ$  in the  $yz$ -plane at the surface. The heated line direction is perpendicular to the wind.  $\theta_a$  is about  $20^\circ$ , whereas  $\theta_y \approx 0$ . The length of the 3 heated lines are  $(30 \pm 5)$  mm, and width  $(0.9 \pm 0.1)$  mm. The LHC (laser height camera)-laser is vertical in the  $xy$ -plane and angled downwind by  $4^\circ$  in the  $xz$ -plane. Note the angle depicted for the LHC, this is achieved by the Scheimpflug principle, and the camera sees a sharp plane in the vertical direction. The water was dyed with the fluorescent dye Pyranine. Emmel [2017] deployed a setup that in principle is similar, without the LHC associated setup. Furthermore the water was dyed yellow by Tartrazine, in order to absorb a blue laser used for heating the lines, instead of the NIR laser. The line was about 28 cm long and  $(0.6 \pm 0.1)$  mm thick.

by the two cameras, rarely and for unknown reasons, image packets were not saved in time, meaning that new images had overwritten older ones in the ring buffer before the old were saved. Therefore both buffer position and the count of acquired images were saved in the filenames. By comparing these number to buffer size, it was possible to detect the affected images and discard the corresponding data.

### 4.3

#### SETUP BY ARNE EMMEL [2017]

Some of the measurements conducted by Arne Emmel were reanalysed. Emmel used a setup similar to that described above, refer to Emmel [2017] for further details.

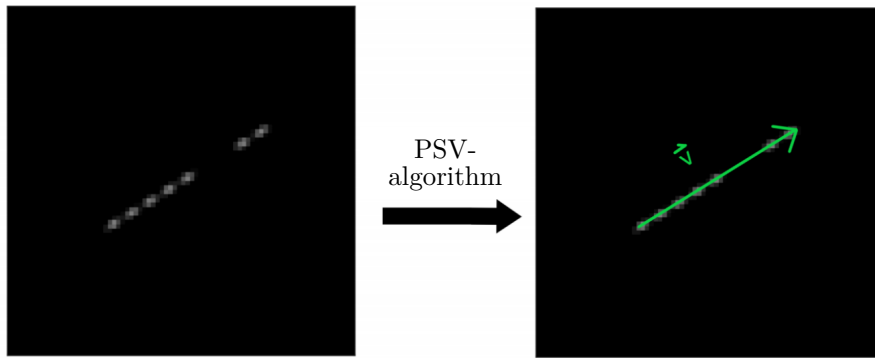


FIG 4.4.: A particle from the PSV method, illuminated by one series of pulses. Based on the pattern and streak length, both velocity and direction can be determined. The figure is modified and adapted from Schwenk [2019].

The IR-camera deployed was IRCAM Velox 327k with a 50 mm lens, yielding about  $700 \mu\text{m}/\text{px}$ , and acquisition with 100 fps. The camera is sensitive in the range  $3.5 - 5.0 \mu\text{m}$ . Furthermore, instead of the NIR-laser, the water was dyed yellow using Tartrazine, absorbing in the blue spectrum. Hence a blue laser was used for creating the line, with power per centimeter heated line  $\sim 1.3 \text{ W}/\text{cm}$  and a penetration depth of  $\zeta_{\text{laser}} \approx 725 \mu\text{m}$ . The length of the line was 28 cm, and found here to have a beam width of  $\sigma_{\text{laser}} = (0.6 \pm 0.1) \text{ mm}$ .

#### 4.4

#### SETUP JANUARY 2019 - REFERENCE METHOD (PSV)

In the framework of Voigt [2019] also water-sided particle streak velocimetry (PSV) data in conditions with waves were acquired. Since the viscous shear stress also can be determined by the PSV method, the data is analysed in this thesis as a reference measurements. Two cameras of type Basler acA1920-155um were used, one above the water for surface elevation measurement with a Canon 50 mm lens ( $\sim 61 \mu\text{m}/\text{px}$  (observed resolution),  $1900 \times 600$  pixels, 200 Hz), and the other water-sided for the particle images with a Zeiss 100 mm macro lens ( $\sim 21 \mu\text{m}/\text{px}$ ,  $1900 \times 1200$  pixels, 50 Hz). Similar to the setup in January 2021, Pyranine was used to dye the water, and a blue laser used to create a laser sheet parallel to the wind direction, and a green band pass filter (525 nm) for the LHC. The laser sheet was pulsed, with a frequency of 1200 Hz for creating a streak pattern, see figure 4.4, with a series of 5 pulses, a pause of 2 and then further 2 pulses. This makes the direction unambiguous. The particles had a size of about  $30 \mu\text{m}$ . Correspondingly, the exposure time of the PSV camera was 8 ms for seeing the whole streak in one image. The LHC was triggered at pulse number 2 and 6, when not counting the pause. Further two LHC images were acquired per cycle. The exposure time of the LHC was 0.5 ms. The setup of the experiment was conducted by Maximilian Bopp.

Both lenses of the cameras were mounted with Scheimpflug adapters, looking up and down at the water surface, respectively, seeing the vertical plane in focus, see figure 4.5 for reference. The reason for using two cameras in the first place, is that the water sided camera cannot detect the water surface with certainty due to total reflection, see section 2.4.

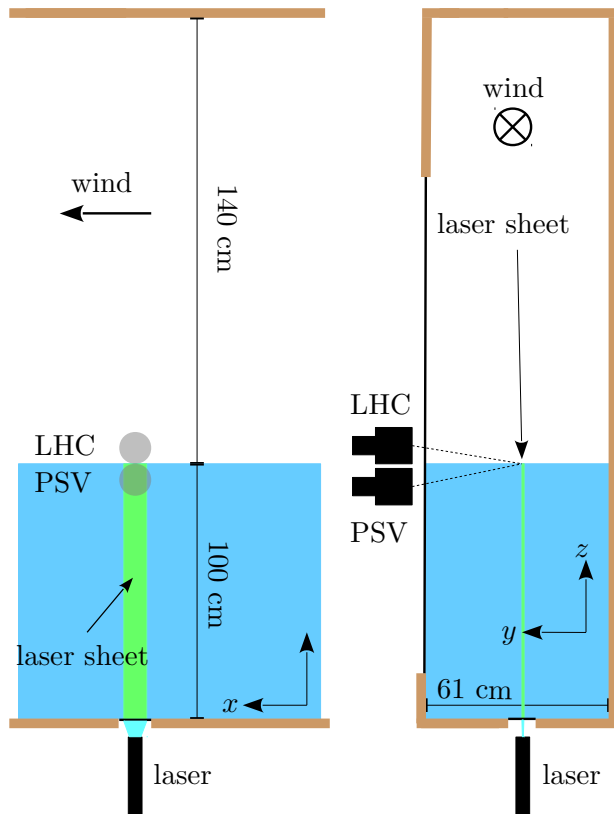


FIG 4.5.: Particle streak velocimetry (PSV) setup: The cameras are observing the laser sheet at an angle from above and below the surface, using the Scheimpflug principle. The laser sheet is vertically oriented, and parallel to the wind direction.

## 4.5 MEASUREMENTS

The evaluated measurement are listed below. Two kinds of measurement conditions were examined: non-stationary (type St) and stationary (type NSt). The latter describes the situation when wind- and wave field are in a dynamical equilibrium, achieved by turning on the wind and then waiting until the water bulk velocity does not change any more. Depending on the wind velocity, this waiting time should at least be 90 minutes for the lower wind settings, and longer for higher wind speeds.

The non-stationary kind of measurement evaluated in this thesis, is to turn on the wind after starting the measurement, thereby seeing the temporal development during the build-up of the wave field. Depending on wind speed, the changes in the wave field are minor beyond about 10-20 minutes for the relevant conditions in this thesis. This does not mean, however, that the bulk velocities have reached their asymptotic values. This might influence the momentum transfer. The non-stationary measurements were continued for a few minutes after turning off the wind. Starting next the measurement with a slight water velocity remaining from the last measurement, avoids heating the lines on top of each other before the wind is turned on.

In the non-stationary measurement by Emmel [2017] the wind generator frequency was first set to 15 Hz for 5 s before turning down to 10 Hz, in order to build of the wind field faster.

$f_{\text{wind}}$ [Hz]	$u_{10}$ [m/s]	Duration [min]	Type	$t_{\text{laser on}}$ [ms]	Date	Reference
2.5	$0.9 \pm 0.2$	20	NSt	15	30.01.2021	12
5.0	$2.4 \pm 0.2$	25	NSt	15	30.01.2021	11
6.3*	$3.1 \pm 0.2$	25	NSt	15	30.01.2021	14
7.5	$3.7 \pm 0.2$	20	NSt	15	30.01.2021	13
8.8*	$4.3 \pm 0.3$	30	NSt	15	30.01.2021	15
10.0	$4.8 \pm 0.3$	50	NSt	15	30.01.2021	06
12.5	$6.1 \pm 0.4$	30	NSt	15	30.01.2021	07
15.0	$7.3 \pm 0.4$	35	NSt	15	30.01.2021	08
17.5	$8.9 \pm 0.5$	35	NSt	15	30.01.2021	09
20.0	$10.7 \pm 0.7$	35	NSt	15	30.01.2021	10
5.0	$2.4 \pm 0.2$	5.5	St	10	30.08.2017	Emmel [2017]
6.3*	$3.1 \pm 0.2$	5.5	St	10	30.08.2017	Emmel [2017]
7.9*	$3.9 \pm 0.2$	5.5	St	10	29.08.2017	Emmel [2017]
10.0	$4.8 \pm 0.3$	5.5	St	5	31.08.2017	Emmel [2017]
10.0	$4.8 \pm 0.3$	5.5	St	10	31.08.2017	Emmel [2017]
10.0	$4.8 \pm 0.3$	5.5	NSt	10	01.09.2017	Emmel [2017]
5.0	$2.4 \pm 0.2$	10	St	n.a.	11.01.2019	46-PSV
5.0	$2.4 \pm 0.2$	10	St	n.a.	11.01.2019	47-PSV
7.5	$3.7 \pm 0.2$	12	St	n.a.	10.01.2019	43-PSV
10.0	$4.8 \pm 0.3$	10	St	n.a.	10.01.2019	44-PSV
10.0	$4.8 \pm 0.3$	10	St	n.a.	14.01.2019	48-PSV

TABLE 4.1.: An overview over the measurements included in this thesis. For the upper 10 measurements, the duration describes the approximate duration the wind was on during the measurement. For the lower 11, the duration described the duration of the actual measurement. The approximate relations between the wind generator frequency and reference wind speed at 10 m height  $u_{10}$  are also given, values provided by Maximilian Bopp. Wind speeds for conditions denoted by an asterisk (\*) are interpolated. Interpolation error was small compared to the uncertainties of the interpolated values. The reference denotes the measurement labels, provided for future reference. “n.a.”: not applicable.





# 5 | SIMULATION

In this chapter a short summary of the simulation deployed for solving the problem described in section 2.6 will be given for sake of completeness. The approach was developed in Voigt [2019], and is mostly applied as described there, therefore more detailed derivations are left out in the following. Minor changes to the original approach will be indicated. An example of a simulated temperature profile of heated line is provided in figure 2.7.

The problem is described in an Lagrangian frame of reference, with the topmost fluid layer not moving. Only the part of the boundary layer encompassing the heated line is considered, the size of which is adapted to the prescribed velocity gradient in order to ensure that calculated heated temperature profile is not influenced by the size of the simulated volume. In this thesis only the shear stress in  $z$ -direction,  $\partial_z u$ , is of interest, hence the problem is restricted to two dimensions with unit extent in  $y$ -direction in order to save computational effort. This can be done since the heated line is homogeneous in  $y$ -direction, hence no heat will flow in that direction.

The volume to be simulated is divided into voxels with variable side lengths  $\Delta x_i$ , however constant for each dimension. As the vertical scale is smaller and preferentially higher resolved,  $\Delta z \leq \Delta x$  in practice. The procedure followed for each time step is (Voigt [2019]):

- a heating step as long as the laser is on and the line heated,
- a diffusion step,
- a shift of the volume in  $x$ -direction corresponding to the shear flow, with cubic interpolation accounting for shifts not equal to a multiple of  $\Delta x$ .

## 5.1

### HEATING STEP

Assuming a laser profile that is Gaussian in  $x$ -direction centred at  $x_0$  with width  $\sigma_{\text{laser}}$  and box shape of unit length in  $y$ -direction, the irradiance flux  $E$  hitting the surface can be described by:

$$E(x, t) = \frac{P_l}{\sqrt{2\pi}\sigma_{\text{laser}}} \exp\left(-\frac{(x + U_d t - x_0)^2}{2\sigma_0^2}\right), \quad (5.1)$$

where  $P_l$  is the laser power per unit line length and  $U_d$  is the drift velocity of the surface. This corresponds to moving the laser with  $U_d$  while keeping the surface fixed. The approach of accounting for the surface drift velocity, instead of adjusting  $\sigma_{\text{laser}}$  in order to cover a range of initial line widths, is changed from the original work. Though

representing a more realistic approach, it yields a minor correction only for relevant values of the parameters, however, and is found to alter the result the estimated  $\tau_{\text{visc}}$  by  $\sim 1\%$  and may hence be neglected. Also some smaller values of  $\sigma_{\text{laser}}$  were simulated in order to account for events where the measured and estimated initial line width was slightly smaller than  $\sigma_{\text{laser}}$ .

The change in temperature  $\Delta T$  per time step  $\Delta t$  due to  $E(x, t)$  is given by:

$$\Delta T(x, z, t; \lambda) = \frac{E(x, t) \cdot \Delta t}{\xi(\lambda) \rho c_V} \exp\left(-\frac{z}{\zeta(\lambda)}\right), \quad (5.2)$$

with penetration depth  $\zeta(\lambda)$ ,  $\rho$  is the density of the water and  $c_V$  its specific heat, and Lambert-Beer's law, equation (2.54), was used.

In practice  $\Delta T$  corresponds to a matrix of same dimensions as the simulation volume. As the heating time  $t_{\text{laser on}}$  is longer than the time step size  $\Delta t$ , heating for several time steps is needed. This is done most cost efficient by precalculating  $\Delta t$  and shifting it according to  $U_d$  and  $\partial_z u$  before being added to the simulation volume.

## 5.2

### DIFFUSION STEP

This idea was originally adapted from Haußecker [1996], who used a similar approach.

As seen in section 2.3.3, diffusion acts on a temperature profile by convolving it with a Gaussian of width  $\sqrt{2\alpha t}$  per dimension. With the advantages of the fast Fourier transform (FFT), however, doing the corresponding multiplication in Fourier space becomes an option. Somewhat dependent on array sizes, this is advantageous, as a multiplication is less expensive for large arrays than a convolution.

The Gaussian still must be discretized. The mask or operator found in Voigt [2019] is in two dimensions:

$$\mathbf{M}_{xz} = \begin{bmatrix} \beta_x \beta_z & \beta_z(1 - 2\beta_x) & \beta_x \beta_z \\ \beta_x(1 - 2\beta_z) & (1 - 2\beta_x)(1 - 2\beta_z) & \beta_x(1 - 2\beta_z) \\ \beta_x \beta_z & \beta_z(1 - 2\beta_x) & \beta_x \beta_z \end{bmatrix}, \quad (5.3)$$

with

$$\beta_{x_i} = \frac{\alpha \Delta t}{\Delta x_i^2}. \quad (5.4)$$

The latter equation links the time step to the spatial discretization. Note that  $\mathbf{M}_{xz}(\kappa_x, \kappa_z)$  may be separated,  $\mathbf{M}_{xz} = \mathbf{M}_x * \mathbf{M}_z$ , such that due to the associative property of convolution, it is possible to multiply the simulation volume in Fourier space by one dimensional masks at a time, additionally saving computational effort. For the transfer function of  $\hat{\mathbf{M}}_{xz}(\kappa_x, \kappa_z)$ , see equation (B.4), one finds

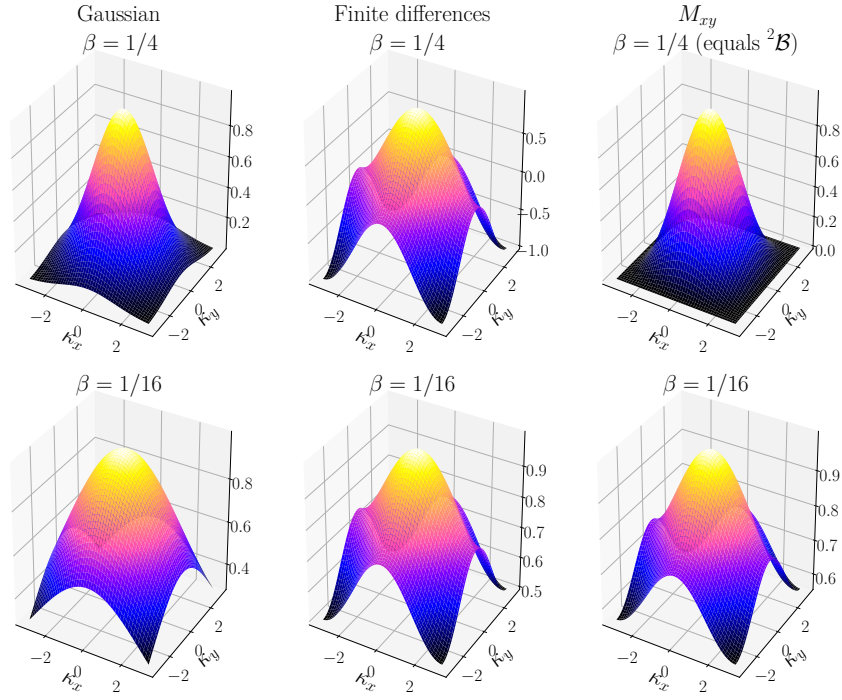


FIG 5.1.: The transfer functions of the ideal (Gaussian) operator, see equation (2.58)  $\exp(-\beta k^2)$  (left), compared to the method of finite differences (middle, refer to Voigt [2019]) and the chosen mask  $\mathbf{M}_{xy}$  (right). The functions are depicted  $\beta_x = \beta_y = \beta = 1/4$  (above) and  $\beta = 1/16$  (below). For  $\beta = 1/4$ ,  $\mathbf{M}_{xy}$  yields the binomial mask  ${}^2\mathcal{B}$ , with a particular isotropic transfer function. For small  $\kappa$ , as equation (5.5) shows,  $\mathbf{M}_{xy}$  is isotropic for all values of  $\beta$ . Note that the  $xy$  plane is shown, and that the expressions stay the same. The figure is taken from Voigt [2019].

$$\hat{\mathbf{M}}_{xz}(\kappa_x, \kappa_z) =$$

$$(1 - 2\beta_x)(1 - 2\beta_z) + 2\beta_x(1 - 2\beta_z) \cos(\kappa_x) + 2\beta_z(1 - 2\beta_x) \cos(\kappa_z) + 4\beta_x\beta_z \cos(\kappa_x) \cos(\kappa_z)$$

$$= 1 - \beta_x\kappa_x^2 - \beta_z\kappa_z^2 + \mathcal{O}(\kappa^4). \quad (5.5)$$

The full expression is stated here since it yields a correction to the corresponding expression in Voigt [2019], though the result is the same. Note that  $\hat{\mathbf{M}}_{xz}(\kappa_x, \kappa_z)$  is isotropic for  $\beta_x = \beta_z$ , as expected for an operator representing a diffusion process. If  $\Delta x \neq \Delta z$ , however, then  $\beta_x \neq \beta_z$  and  $\hat{\mathbf{M}}_{xz}(\kappa_x, \kappa_z)$  is anisotropic. This is a necessity for keeping the diffusion homogeneous. Furthermore, one must require  $\beta \leq 1/2$  both for avoiding more heat to flow out of each cell than contained in it and numerical stability (Crank [1975]).  $\beta = 1/4$  yields the second order binomial mask  ${}^2\mathcal{B}$  (see equation (B.9)), with a particular isotropic transfer function, see figure 5.1.  $\beta_z$  is always set to  $1/4$ , since  $\Delta z$  as mentioned above is the smallest grid cell size, thereby fixing the time step. This leaves the  $\Delta x \geq \Delta z$  free to be chosen.

To summarize, for each time step the diffusion is simulated by

$$T(t + \Delta t) = \mathbf{M}_{xz} * T(t). \quad (5.6)$$

### 5.3

#### SHIFTING STEP

This step implements the deformation by the shear flow that leads to the Taylor dispersion. The simulation volume geometry is kept unchanged, however, implying that only the temperature distribution is shifted. This is achieved by cubic spline interpolation of the temperature profile at each (discrete)  $z$ , and the whole row is then shifted by the same amount,

$$\delta i(k) = \frac{\partial u}{\partial z} \cdot k \Delta z \cdot \frac{\Delta t}{\Delta x}, n \quad (5.7)$$

where  $\delta i$  is the shift in  $x$ -direction in units of  $\Delta x$  and  $k$  is the (integer) row index, hence  $z = -k \Delta z$ . Missing values at the boundary due to the shift are replaced by the surrounding water temperature, i.e. the temperature the volume had before heating the profile. Values shifted “out” of the volume are discarded.

### 5.4

#### BOUNDARY CONDITIONS

Boundary conditions are crucial for representing the desired system. In this case these must be found with respect to the convolution of the temperature profile. The heat loss through the air-water interface is neglected, corresponding to a no-flow (Neumann) boundary condition. This is justified by the low heat capacity of air compared to water, and the “sky” corresponding to the channel walls, having a similar temperature as the water. On the open ocean this would change. The no-flow boundary can simply be implemented by applying a mirror symmetric boundary for the convolution. The other edges are all, in the real world picture, in contact with the surrounding water, hence heat flow may occur. This can be achieved by keeping the outermost cells along these edges of the volume constant at the surrounding water temperature. This has the advantage that no special boundary handling must be implemented in the convolution, hence the whole volume can be convolved with the same mirror symmetric boundary handling. Naturally, this requires the convolution to be done first, before resetting the temperature in the respective cells. Moreover, it requires the volume to be large enough to avoid artefacts associated with steep temperature gradients if the heated profile is too close to the boundary. This also is one of the reasons for keeping the surface layer fixed, being the most important part of the profile, and shifting the deeper layers.

### 5.5

#### EVALUATION OF THE SIMULATION

First, the profile seen by the camera must be calculated. The radiation reaching the detector originates not solely from the surface layer as somewhat deeper layers also contribute, a consequence of the (small) penetration depth in the spectral range where the camera is sensitive. In Voigt [2019] three different approaches are implemented,

(i) using the surface layer only, (ii) assuming the camera angle  $\theta_a$  sufficiently small to neglect the watersided angle after refraction and assuming a mean penetration depth  $\zeta_{\text{mean}} = 44 \mu\text{m}$  (Downing and Williams [1975]) and (iii) considering both the refraction angle  $\theta_w$  (see equation (2.60)) and integrating over the spectral range as well. For an air-sided camera with mounted angle  $\sim 20^\circ$  and a sensitivity for  $3.5 \mu\text{m} \leq \lambda \leq 5 \mu\text{m}$ , the difference between (ii) and (iii) was negligible, whereas (i) deviated by  $\sim 5\%$  from the others. In this work, approach (iii) is used.

The final expression for the intensity observed by a detector element in the sensitive range  $\frac{dI(x, z=0)}{dS_D}$  for approach (iii) is (Voigt [2019]):

$$\frac{dI(x, z=0)}{dS_D} \propto \int_{\lambda_1}^{\lambda_2} \int_0^{z_{\text{max}}} \frac{L(T(x + z \sin(\theta_w), z), \lambda)}{\zeta(\lambda)} \exp\left(-\frac{z}{\cos(\theta_w)\zeta(\lambda)}\right) dz d\lambda, \quad (5.8)$$

where  $L$  is the spectral radiance, equation (2.51), and  $\zeta(\lambda)$  is the penetration depth of the laser Lambert-Beer's law, equation (2.54), was applied. Since the shape of the temperature profile is of interest, only the proportionality is stated in equation (5.8). Furthermore, it was found that  $dI_{z=0}(T_c)/dS_D$  is well approximated by a linear function  $f(T_c) = aT_c + b$ , such that the shape could be evaluated without first converting to a temperature. The expression above must also be discretized. For further details refer to (Voigt [2019]).

Having calculated the shape temperature distribution seen by the camera, this is then evaluated by fitting a Gaussian, analogously to how the line widths in the real world data are evaluated. As discussed in section 2.6, the temperature distribution close to the surface is skewed. Fitting a Gaussian still approximates the width well (Voigt [2019]).

## 5.6

### CONSTANTS AND PARAMETERS USED IN THE SIMULATION

Constant or parameter	Symbol	Value
Grid cell length in $z$ -direction	$\Delta z$	10-15 $\mu\text{m}$
Grid cell length in $x$ -direction	$\Delta x$	10-30 $\mu\text{m}$
Domain length in $z$ -direction	$l_z$	2 mm
Domain length in $x$ -direction	$l_x$	30 - 120 mm
Time step	$\Delta t$	0.4 ms
Heating time	$t_{\text{laser on}}$	15 ms (a) and 10 ms (b)
Time step between evaluating the temperature profile		25 ms
Simulated total time of the signal	$t_{\text{max}}$	0.3 - 1.1 s
Velocity gradient in $z$ -direction	$\partial u/\partial z$	0 - 100 $\text{s}^{-1}$
Step size of $\partial u/\partial z$		1 $\text{s}^{-1}$ (a) and 0.5 $\text{s}^{-1}$ (b)
Velocity gradient in $y$ -direction	$\partial u/\partial y$	0 $\text{s}^{-1}$
Dynamic viscosity	$\mu$	1001.6 $\mu\text{Pa}\cdot\text{s}$
Width of laser beam	$\sigma_{\text{laser}}$	0.7-0.9 mm (a) and 0.3-0.6 mm(b)
Drift velocity	$U_d$	0-36 cm/s
Thermal diffusivity	$\alpha$	1.4 $\cdot 10^{-7}$ $\text{m}^2/\text{s}$
Penetration depth laser	$\zeta_{\lambda_1}$	318 $\mu\text{m}$ (a) and 725 $\mu\text{m}$ (b)
IR camera sensitive range		3.0 - 5.0 $\mu\text{m}$ (a) and 3.4 - 5.0 $\mu\text{m}$ (b)
Initial temperature	$T_0$	293 K
Power of laser per unit line length	$P_l$	0.8 (a) W/cm and 1.3 W/cm (b)
Density of water at 20°C	$\rho$	998.2 $\text{kg}/\text{m}^3$
Specific heat capacity of water	$c_V$	4182 J/(K $\cdot$ kg)
Angle of observation, air	$\theta_a$	20°
Angle of observation, water	$\theta_w$	14.7°
Refractive index water	$n_w$	1.33

TABLE 5.1.: The constants and parameters used in the simulation and for the analysis. The labels (a) and (b) refer to parameters differing for the evaluated measurements, corresponding to the measurements of January 2021 and Emmel [2017], respectively, see chapter 4

# 6 | IMAGE PROCESSING AND DATA ANALYSIS

In this chapter the process from the raw images to the measurement results is described. Being the most important for this work, the active thermographic method is described in greater detail than the processing of the particle streak velocimetry (PSV) data, the latter being described in detail in Bopp [2018]. Changes and adaptation to water sided measurements made to the PSV-processing are described separately below, see section 6.6. The calibration of the images is identical, however, refer to section 6.1.

The processing of the data from Emmel [2017] is in principle analogous to that of the measurements conducted in the framework of this thesis, with the exception of a few simplifications. Therefore the process will be described and showed on the basis of the 2021 measurement.

## 6.1 CALIBRATION

The cameras were first calibrated, with images of checker boards or square patterns of known dimensions, enabling mapping from pixel coordinates  $(x_{\text{px}}, y_{\text{px}})$  to the real world coordinates  $(x_{\text{r}}, y_{\text{r}})$ . A mapping function described by

$$\begin{aligned}
 x_{\text{r}} &= \frac{ax_{\text{px}}^2 + by_{\text{px}}^2 + cx_{\text{px}}y_{\text{px}} + dx_{\text{px}} + ey_{\text{px}} + f}{gx_{\text{px}}^2 + hy_{\text{px}}^2 + ix_{\text{px}}y_{\text{px}} + jx_{\text{px}} + ky_{\text{px}} + 1} \\
 y_{\text{r}} &= \frac{lx_{\text{px}}^2 + my_{\text{px}}^2 + nx_{\text{px}}y_{\text{px}} + ox_{\text{px}} + py_{\text{px}} + q}{gx_{\text{px}}^2 + hy_{\text{px}}^2 + iy_{\text{px}}x_{\text{px}} + jx_{\text{px}} + ky_{\text{px}} + 1}
 \end{aligned} \tag{6.1}$$

was fitted. This accounts for both perspective distortions and possible distortions due to the lenses (Bopp [2018]). For the infrared images of both measurements (January 2021 and Emmel [2017]), the maximal projection error were on the order of few pixels, caused primarily by poor detection in the calibration points. Note that the most important quantity in these images are the line widths, hence relative positions in the images, and not the exact real world coordinates. For the LHC measurement of January 2021, LHC for the PSV measurement and the PSV measurement itself, mean projection error relative to the resolution were  $\sim 25\%$ ,  $\sim 30\%$  and  $\sim 80\%$ , respectively.

## 6.2

### PREPROCESSING OF THE INFRARED IMAGES

In this section the processing of the heated lines is described. The image processing is done using the uncalibrated raw images, only the resulting data is transformed to real work coordinates. The goal is to determine the line width as function of time,  $\sigma(t)$ , and their horizontal positions  $(x, y)$ . The latter is especially important since the angles of the lines relative to the wind direction must be calculated, and only the parts of the lines that stay perpendicular to the wind are evaluated (Voigt [2019]). One of the main challenges is that, as explained in section 4.2, the measurements of January 2021 were conducted with a line heating frequency that was adapted to the present conditions, i.e. the water surface velocity. Subsequently, the script must also automatically detect and adapt to the number of lines present per time. Furthermore, overlaps between lines, arising when the heating frequency was chosen too high or orbital movements displaced the old line upwind, must be detected, as those falsify the line width.

As the temporal broadening of the lines is of key interest, the individual lines must also be applied with a time stamp and a line label, tracked and kept separated over the course of up to several hundred images. Clearly, if that fails, the line width and position is assigned to the wrong line and later evaluated for the incorrect signal time (i.e. time since heating the line). Simply using the relative position to other lines for time labelling is insufficient for higher signal times, due to the complexity of the flow, as some lines may disappear faster than others and their  $y$ -coordinates, i.e. the direction perpendicular to that of the wind, may change in the course of time. Two of the heated lines are also parallelly shifted at the same  $y$ -position, see figure 6.2, further complicating the approach of position based labelling. Lastly, as a setup for measuring the surface elevation is applied simultaneously, based on using a powerful laser which gets hot, the reflexes of the warm laser casing are also regularly seen as the waves cause the necessary surface inclination for the reflexes to be seen by the infrared camera (refer to figure 4.3 for a sketch of the setup). These reflexes are bright, and must not be mistaken for a heated line by the script for not falsifying the measurements and cause issues with tracking the lines.

#### 6.2.1

##### PREPROCESSING

First a flat field correction is done by subtracting the background of the images. Only the part of the images containing the heated lines and a small surrounding area was considered. This background is calculated for each image sequence of 1024 images, by median filtering of an temporally averaged image with a mask size in pixels of (10, 30), corresponding to the directions parallel to the lines and the wind, respectively. The asymmetrical size was chosen for a smaller vertical range, since the mean image was influenced by the presence of the heated lines in the respective areas. In order to not subtract this footprint of the signal, the part of the mean image where the heated lines were located was interpolated linearly from the surrounding edges. This posed no problem, as the signals were only contained in a relatively narrow middle part (160x400 pixels) of the full image (1024x1280 pixels), where the image quality was good.

Having subtracted the background, erroneous pixels were corrected. Two kinds of errors were differentiated, namely dead and hot pixels and pixels with a high standard deviation. The former were detected in the mean (background corrected) image, by using



it's mean and standard deviation, and a detection threshold of 3 standard deviations. For the images of January 2021, this yielded very few pixels, likely due to a precorrection done by the camera itself. The slight influence by the heated lines on the mean image did not lead to wrong detections. The pixels with high standard deviations were detected similarly; a temporal pixel-wise standard deviation was calculated, and compared to the average standard deviation of the part of the image containing the signal shortly after heating the lines. Pixels deviating by more than 3 standard deviations from the mean were classified as erroneous. Note that the part of the image containing the signal shortly after heating the lines were used as reference, since these are prone to large fluctuations and represent the worst case scenario. This was found to be sufficient for the given image quality and low amplitude of the signals, with no need for further efforts. For more challenging image qualities than with the FLIR camera, or in the presence of a high number of heated lines, it can be suggested to use images without any signal for detecting the error pixels.

The mean of the temporally averaged image without the detected error pixels was then calculated. The deviating pixels were in the first step replaced by the mean in an temporary image sequence, which was then slightly smoothed by convolving with a degree two dimensional binomial mask  ${}^2\mathcal{B}$  (see equation (B.9) and Jähne [2012]). The error pixels in the images were then replaced by the corresponding values from the smoothed image sequence. As the convolution is cost (computational) efficiently done in Fourier space, it was found that this approach was faster than iterating through the images and replacing the error pixel values with those from neighbouring pixels.

For the images of the measurement by Emmel [2017], there was a substantial amount of both dead, hot and fluctuating pixels. The flat field correction was also more important due to the large spatial extent of the line and thereby larger inhomogeneities. However, as laser frequencies were low, specifically 0.5 for the lowest two wind speeds and 1 Hz for the two highest settings, the mean images were barely influenced by the presence of the lines and could be used directly for median filtering and error pixel detection. Due to the low resolution compared to the line widths, error pixels were replaced by the mean value of their surrounding pixels in  $y$ -direction, i.e. parallel to the line. This avoided as much alteration of the line width as possible.

### 6.2.2

#### DETECTION OF NEW LINES

Since all lines are heated at the same place on the water surface, the detection of new signals is fairly easy. First, the average pixel values in the respective section of the image of interest can be calculated for each image. Then the median for each image sequence of 1024 of these values can be calculated and subtracted. This correction by the median is done for shifting the pixel averaged values to comparable values in case that the mean surface temperature changes somewhat during the measurement, which can be the case especially shortly after turning the wind on. For example when the channel air happens to be dry, causing cooling by evaporation of the surface layer, turning on the wind can enhance mixing with warmer bulk water and also the heat exchange by thinning of the boundary layer, causing the surface temperature to drift somewhat.

The temporal gradient of the pixel average values is also calculated, being positive and high when a new line is heated. Fitting the gradient distribution by a Gaussian (equation (6.3)) yields it's width, which is used to define a threshold for the detection of new lines. The maximum of the gradient comes just before the maximum of the average

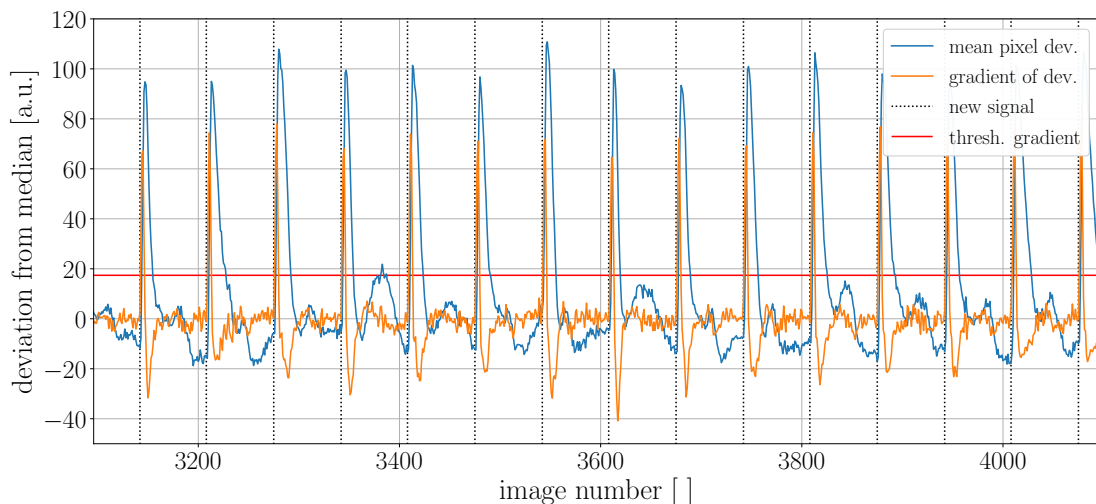


FIG 6.1.: The figure shows an example of the detection of new lines, marked by the black dotted lines. The blue line depicts the pixel averaged deviation from the median (latter calculated for the image sequence) of the section of the images where the new lines are expected. The orange curve depicts it's gradient. Note that the algorithm starts the search 3 images before the maximum of the gradient. The frame rate was 200 fps. Note the small peaks in the pixel average values between the new signals, these are caused by line 2 (refer to figure 6.2) passing through the initial position of line 3.

pixel values. So, finding both the local maxima of the gradient and of the pixel averaged values, requiring the maxima of the gradient to come slightly first, combined with the threshold for the gradient, turned out to be a stable way of detecting the new lines. Lines that return back into the initial position due to orbital movement were found to not be detected, as the gradient were lower. Also, since line 2 and 3 have about the same  $y$ -position (refer to figure 6.2), a small peak arises when line 2 passes through the initial position of line 3. The gradient does not strongly peak simultaneously, however, and the advantage of stable triggering on all 3 lines overweights the disadvantage of those minor peaks. Furthermore, the algorithm starts looking for the new line 3 frames before the maximum of the gradient, making sure also the start of the heating process is captured, assuring a precise start of the time stamp. For comparison, with 15 ms heating time and 200 fps, the heating is captured with at least 3 images. An example of detected new lines is shown in figure 6.1.

In the following, a set of three lines heated at the same time, is referred to as a *signal unit*. These are labelled with numbers  $\{1, 2, 3\}$  according to their starting position relative to each other, this being fixed by the position of the laser.

### 6.3

#### TRACKING AND EVALUATION OF THE HEATED LINES

After detection, the new lines are evaluated, this will be explained in further detail below. The line labels must be kept associated with the same line and the signal units (set of three lines) separated for all following images, until the maximum evaluation time for the signal unit is reached. This is achieved through several steps for each image:

- tracking the signal unit to the new image,
- evaluating it,
- adjusting the signal unit extent, expected to become larger with time,
- passing this new extent to the next image for tracking, and so on.

Figure 6.2 shows an example for the measurement with the 10 Hz wind generator frequency setting.

### 6.3.1

#### TRACKING

The lines are tracked by using a small subsection of the last image containing the signal unit, and minimizing the squared difference to the next image. Both the small section of the last image and the next image is smoothed by convolving with a two dimensional 2. degree binomial mask  ${}^2\mathcal{B}$  in order to lessen the possibility of tracking the signatures of possible uncorrected error pixels. For large images, this is done (computationally) most efficiently in Fourier space by the use of the convolution theorem, equation (B.7), for small image sections as in this thesis, however, it was found to be faster to just convolve without the transformation.

The least square difference  $D$  is given by

$$D = \sum_{i,j} (I_{k,ij} - I_{k-1,ij})^2, \quad (6.2)$$

with  $I_k$  being the new image and  $I_{k-1}$  the last, and  $i, j$  the pixel coordinates in the small image section used for tracking. This is rather expensive, but the cost can be considerably reduced by realising that only a minor range must be searched for the minimal  $D$ . With the resolution of about 0.4 mm/px and 200 fps, even a velocity of 40 cm/s, which is a lot for most measurement conditions, corresponds to a shift of 5 pixel per image. Furthermore, the shift in  $x$ -direction is larger than in  $y$ -direction. Note that it should also be accounted for that the last detection can be off by a few pixels, the shape of the lines to change somewhat and that the movement could be against the wind direction due to orbital motion. In the end a range of  $\pm 4$  pixels perpendicular to the wind direction, and  $\pm 5$  pixels in wind direction was used.

Furthermore, tracking using a cross correlation was tested, with the advantage of being much more faster. As the signals were relatively weak, it turned out that this approach was not stable enough. Especially the reflections of the casing of the surface elevation laser, which were bright, caused the cross correlation to “jump” onto these reflections and drift off. The problem became larger for higher signal times, as the lines themselves became weaker. The least squares was more stable also in the case of the reflections. See figure 6.2 for an example of both the tracking and a few, small laser casing reflections.

With the shift in the position known, a section of the new image of the same size as the tracked window can be passed on for evaluation.

### 6.3.2

#### EVALUATION OF THE LINE WIDTHS

Since the initial line positions are known and additionally the signals strong, with exception of the very first image of the lines appearing, the lines are easily evaluated

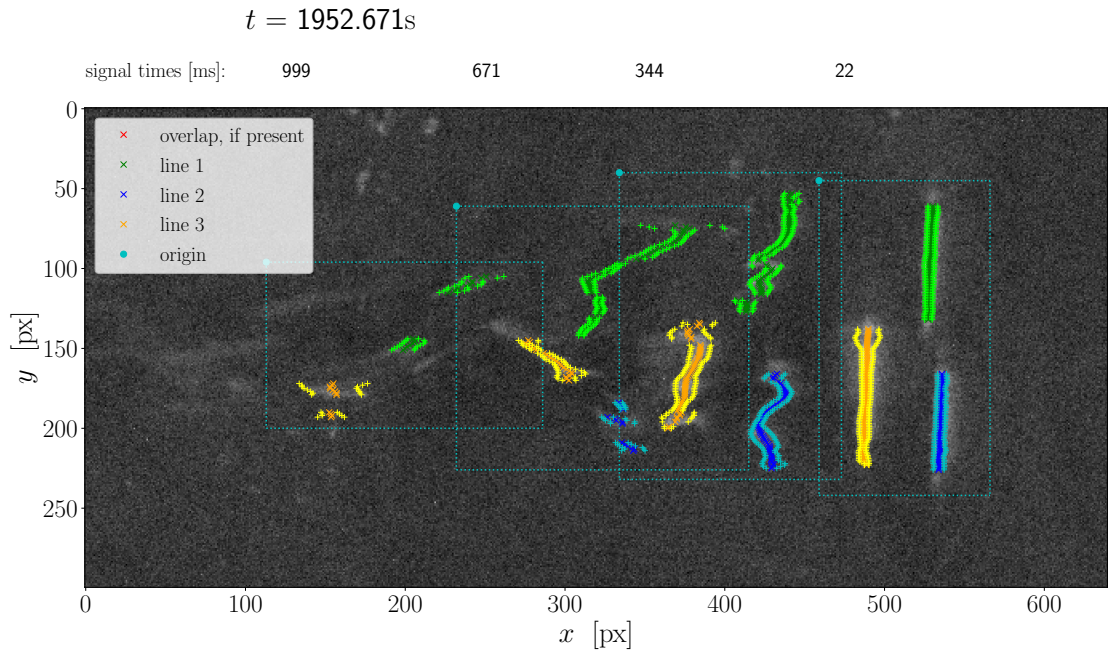


FIG 6.2.: The tracking and evaluation of four signal units of the 10 Hz measurement at  $t \approx 1953\text{s}$  after starting the measurement. The oldest line has been tracked for close to 200 images, and the newest line was heated 22 ms ago. The wind direction is in negative  $x$ -direction. The markers 'x' indicate the line positions, and the '+' mark the line widths. The cyan dashed lines show the smaller evaluation- and tracking windows containing a signal unit each. The overlap between these windows is expected, and not *all* lines within them belong to the same signal unit (set of lines  $\{1,2,3\}$ ). Notice the outliers of large line width for small  $y$  in line 1 in the window with signal time 671 ms, and the spots in the upper left corner next to the legend. The spots originate from the warm laser casing of the laser used for the surface elevation measurement, and may be both brighter and more frequent.

and labelled by the mentioned line number  $\{1, 2, 3\}$  in the first few images. Later, with the advantage of the tracking the lines, only a small windows or sections of the image containing the lines must be evaluated.

The small image section is first copied and smoothed by convolving it with a 4. degree 2 dimensional binomial mask  ${}^4\mathcal{B}$  (see equation (B.9)). For each row in this image section, local peaks are detected, fulfilling requirements to width and prominence, the latter determined based on the standard deviation of the smoothed section in order to not evaluate random fluctuations. For clarity, these peaks correspond to local maxima in the temperature distribution, i.e. optimally the heated lines, and their peaks coincide since  ${}^4\mathcal{B}$  is symmetric and hence the peak is not shifted.

The found peaks are then checked for agreement with the expected positions, calculated based on the result of the last image and the shift resulting from the tracking. All peaks deviating by more than 2 pixels in  $y$ -direction and 4 in  $x$ -direction are discarded. Peaks fulfilling the positional requirement are evaluated, and labelled according to the corresponding point in the last image, and with the associated updated signal time.

The evaluation is prepared by taking the original, unsmoothed image section, and

smoothing it with a one dimensional  ${}^2\mathcal{B}$  (see equation (B.9)) *only* in  $y$ -direction, in order to not artificially broaden the line. Then, for row  $i$  containing the validated peak, also the data points of row  $i - 1$  and  $i + 1$  are collected in order to increase the number of data points. These are then fitted by a Gaussian profile,

$$G(x) = A \cdot \exp\left(\frac{-(x - \mu)^2}{2\sigma^2}\right) + b, \quad (6.3)$$

with  $\sigma$  being the sought line width and  $\mu$  the line's  $x$ -position.  $\mu$  must be strictly restricted to the found peak in order for the fit to converge to the correct peak, and not for example a stronger, neighbouring signal. The  $y$ -position is given by  $i$ . Naturally, both these are related to edges of the small image section, which again are given relative to the section of the original images used for further processing (depicted in figure 6.2). Moreover, as only half frame images were acquired, another offset must be added in order to calibrate the data using a full frame calibration image.

Lastly, it may seem unnecessarily complex to track the lines in addition to evaluating them, considering that the spatial steps from image to image are small. The tracking allowed for being much more rigorous with respect to the updated line positions when evaluating the new image, however, as more information regarding what to expect was available. Taking into account that the positions might shift somewhat in the  $y$ -direction with time, and the lines may even travel upwind due to the orbital movement, clarifies the situation. A drift in  $y$ -direction without tracking the lines may also cause problems keeping the lines within a signal unit separated. Furthermore, the reflexes could mostly be excluded by the strict position criteria. The exception was if the reflex coincidences with the line. As the reflexes travelled much faster than the line, however, and the tracking was stable in this regard, the reflexes are "lost" again due to the maximum allowed tracking step size, such that the influence is kept at a neglectable level.

### 6.3.3

#### DYNAMICALLY ADJUSTING THE EVALUATION

As mentioned initially, the script must handle a varying number of signal units. This is solved by using lists of data blocks, each containing the information of one unit. Each of them carries all the necessary information needed, including the section of the last image needed for tracking. These lists are equally effortlessly passed on to the next image sequence, such that a seamless transition and evaluation is possible. In case that one signal unit has become too faint to be evaluated before reaching the maximum evaluation time, the whole data block can be saved and deleted from the lists. Lastly, these lists are also saved, such that in the case of an interruption, the script and evaluation may be continued.

### 6.3.4

#### DETECTION OF OVERLAP AND JUMPS

The last aspect is the detection of possible overlap between lines of different signal units. This may either be detected simultaneously with the above described evaluation or separately, the principle is the same. Due to the similar  $y$ -position of line 2 and 3, these were the main overlapping lines. The overlaps were detected by comparing the positions of the individual lines, and must only be done once when a new signal unit is heated. Line 1 is only overlapping with itself if the surface velocity is either low or

negative due to orbital motion, which is rarely the case. For each new signal unit, the position of the pre-existing lines *before* the heating of the new signal started must be compared to the initial position of the new lines. This is important, as the new lines might be close enough to the old signal to disturb the temperature distribution of the latter to the extent that only the new peak is detected. Then, due to the strict position criteria, the old lines apparently vanish, and the overlap is not detected. In these cases the temperature distributions of the new lines are excessively broad, so it is important to detect these overlap events. Once an overlap is detected, all data points of the new line and all data points of the old line since the heating of the new unit are labelled accordingly.

Lastly, sometimes when inhomogeneities in the flow field bring the ends of two lines closer, the algorithm may incorrectly assign the line labels at the end parts of the lines. This may happen if for example a reflex by the laser casing “bridges over” the gap in one time step. Due to the implementation regarding only one signal unit at a time, such jumps just occur within the unit itself, which is of small importance since all lines have the same properties, and may be counted as one if they are connected closely enough. Jumps between signal units can just occur if two lines are sufficiently close and the gap is bridged, and can be detected as an overlap suddenly occurring. This is possible as the part of the corresponding line is (mistakenly) evaluated twice for both signal units. In this case only the jumping line can be discarded, since this is an artefact of evaluation and not a physical overlap. Such jumps are rather rarely found in the older, weaker signals.

## 6.4

### DATA ANALYSIS OF THE THERMOGRAPHIC MEASUREMENT

The line widths can be corrected for surface inclination, if such data is available (see section 6.5 for details), by

$$\frac{\sigma_{\text{corr}}}{\sigma_{\text{meas}}} = \frac{\cos(\theta_a)}{\cos(\theta_a - \theta)}, \quad (6.4)$$

with  $\sigma_{\text{corr}}$  the corrected line width,  $\sigma_{\text{meas}}$  the observed line width,  $\theta_a$  the mounting angle of the camera relative to the vertical direction (refer to figure 4.3) and the surface inclination  $\theta(x, t) = \arctan(\partial_x \eta(x, t))$ .

Note that for  $\theta = \theta_a$  a correction  $\leq 1$  occurs. This is due to the camera being calibrated on a horizontal surface, hence seeing only a projection of the target. This leads to an overestimation of the line width if the camera view is parallel to the surface normal. With  $\theta_a \approx 20^\circ$  in the used setup and a (close to breaking) Stokes wave at maximal angle, see section 2.2.1, the maximal (upwind) correction would be close to 50%. Especially at lower wind speeds, surface inclination is mostly small and the correction may be neglected. For most measurement conditions used in this thesis, it was experimentally found (refer to section 7.1.2) to not make a marked difference in the determined values for the viscous shear stress in this work. For the measurements of Emmel [2017], the surface elevation data is not available and subsequently the corrections are left out. Moreover, for localized surface inclination measurements, such as in this thesis, where only a vertical sheet in wind direction was considered, the correction is questionable since  $\theta$  may vary considerably with position along the line. This would particularly be the case if the line is long. This can be seen by measurements considering a larger part

of the surface, see for example Rennebaum [2017].

The simulated line widths are in the framework of this thesis only subject to non-zero velocity gradients with respect depth, i.e.  $\partial_z u \neq 0$  and  $\partial_y u = 0$ , hence also the measured line widths used in the evaluation must reflect this in order to not falsify the determined values of the viscous shear stress (Voigt [2019]), see section 2.6 for further details. Even small values of  $\partial_y u$  are capable of considerable influence on the broadening of the lines by Taylor dispersion. Since varying flow velocities along the line, corresponding to  $\partial_y u \neq 0$ , lead to displacements of different parts of the line,  $\partial_y u \neq 0$  is associated with a change of the angle  $\theta_s$  of the line relative to the initial angle  $\theta_{0s}$ . Hereby  $\theta_s$  describes the angle in the horizontal plane between the line and the direction perpendicular to the wind, hence  $\theta_{0s}$  is close to zero.  $\theta_s$  is given by (Voigt [2019]):

$$\theta_s = \arctan(d_y x(y)), \quad (6.5)$$

with temporal development

$$\theta_s(t) = \arctan(\partial_y u \cdot (t - t_0) + \tan(\theta_{0s})). \quad (6.6)$$

The angle along the lines is calculated by cubic spline interpolation of the line position  $x(y)$  combined with equation (6.5). This is another reason why precise tracking of the lines is important; if the algorithm jumps between two parallel lines, this would correspond to large and incorrect values of  $\theta_s$ . For reference, Voigt [2019] estimated the influence on the determined viscous shear stress by including by including  $|\partial_y u| \leq 0.2 \text{ s}^{-1}$  to be  $\sim 1\%$ , this limit is mostly adapted in the following.

The sorted data set for the time interval of the measurement of interest can then be processed further. A look at figure 6.5 is illustrative. For this, a two dimensional histogram of the line widths as function of time  $t$  since heating is calculated. As argued in section 3.5, the peaks of the resulting distributions for each  $t$  will be used as representative line widths. As the distributions are of noisy nature, the maximum is estimated by a fit. Empirically, this is done by fitting skew Gaussians to the distribution, given by

$$h(x) = A \exp\left(-\frac{(x-l)^2}{2s^2}\right) \left[ \int_{-\infty}^{\alpha \frac{x-l}{s}} \exp\left(-\alpha \frac{t^2}{2}\right) dt \right] + b \quad (6.7)$$

where  $\alpha$  relates to the skewness of the distribution,  $l$  to it's location, and  $s$  to the width. Although this function generally describes the peaks of the distribution well, these being the important parameter, the tails of the line width distributions are not always well described. Especially for high signal times and wind velocities they tend to be heavier, possibly due to more outliers. Inspired by equation (6.7), a similar approach is therefore chosen with a student's  $t$ -distribution, known for it's heavier tails, with probability density function  $\tau(x)$

$$\tau(\mathbf{t}) = \frac{\Gamma(\frac{\nu+1}{2})}{\sqrt{\nu\pi}\Gamma(\frac{\nu}{2})} \left(1 + \frac{\mathbf{t}^2}{\nu}\right)^{-\frac{\nu+1}{2}} \quad \text{with } \mathbf{t} := \frac{x-l}{s}. \quad (6.8)$$

Here  $\nu > 0$  is the (integer) number of degrees of freedom, and  $\Gamma(n) = (n-1)!$ . As only it's shape is of interest, the prefactor and  $\nu > 0$  may be treated as fit parameter. Hence

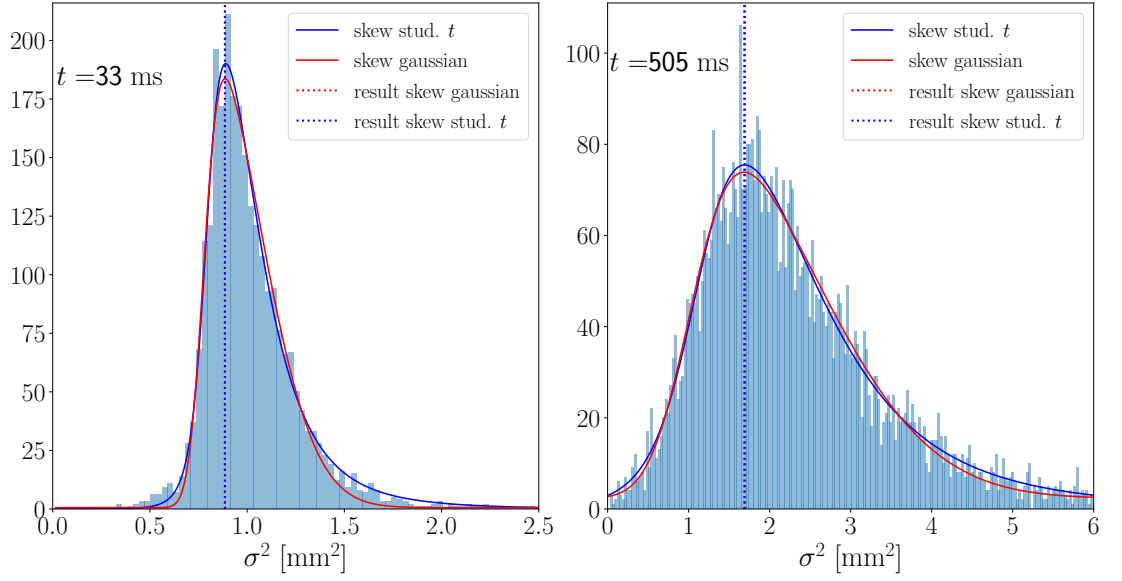


FIG 6.3.: The figure shows the fitted distributions of squared line widths  $\sigma^2$  for the 7.5 Hz measurement shortly after heating the lines (heating time 15 ms) (left) and after about half a second (right). The expressions (6.7) (red curve) and (6.9) (blue) were fitted. As can be seen, the distributions are skew, and both fits describe the shape and peak position well. The dotted lines depict the estimated maximum points for the distributions, and are here hardly distinguishable. Both fits are performed as the convergence of the fits is slightly different, enabling a more robust evaluation. Note that the times since heating the lines are given for the centre of the deployed binning interval.

the following fit function is deployed for the distributions as well:

$$g(x) = A \cdot \tau(t; \nu) \left[ \int_{-\infty}^{\alpha \frac{x-l}{s}} \tau(t; \nu) dt \right] + b. \quad (6.9)$$

It must be emphasized that this is a purely empirical approach, not based on a theoretical foundation. There are mainly two reasons for using equation (6.9); firstly, due to the heavier tails and better agreeance in shape, the fits converge more reliably than for equation (6.7), and secondly the two different estimates can be compared as a handle for uncertainty and convergence of the fits. Mostly, the difference between the resulting peak positions from the two fits is neglectable. Note that while both equations might seem complicated, they are readily implemented with build-in-functions for both cumulative- and probability density functions for the respective underlying distributions.

The question remains whether the squared or non-squared line widths are used for calculating the distributions that are fitted. Not squaring first translates to a quadratic increase in bin sizes with increasing line widths when compared to the squared case. Ideally, if the distributions are sufficiently sharply peaked, this to be of little importance. This was the case in the wave-less conditions in Voigt [2019]. For the line widths in the presence of waves, however, it indeed makes a marked difference, especially in the measurements with higher wind speeds, as the distributions get broader and the peaks flatter.



The system is seemingly better described by the squared line widths. For one dimensional diffusion without any velocity gradient, one expects equation (2.63) to hold, as explained in section 2.6. Taylor dispersion acts by introducing an apparent, enhanced diffusion constant, in this case time dependant, hence it is plausible that the system is well described by  $\sigma^2(t)$ . Note that the expression (2.64), suitable away from the surface, also shows this dependence. Turning to the simulation, this also suggests that  $\sigma^2(t)$  represents the system well, see figure 6.4, with  $\sigma^2(t) - \sigma_0^2$  being similar for a given value of  $\partial_z u$ . Note, however, that there also is a modest dependence of  $\sigma^2(t) - \sigma_0^2$  on  $\sigma_0$ . Such a clear relation is not found for  $\sigma(t)$ . In the practical application a large number of heated lines with a distribution of  $\sigma_0$  is collectively evaluated, hence the best possible representation is important, especially if the distribution of  $\sigma_0$  is not narrow. As a side note, division by  $\sigma_0$  or  $\sigma_0^2$  yields no pattern as seen in the right plot in figure 6.4. Therefore the distributions of the *squared* line widths are used for calculating the representative widths.

If the distribution of  $\sigma_0$  is broad due to wave phase selective influence on the initial line widths, as explained in section 3.5, and the resulting distribution is dominated by a particular range of phases, this might lead to an evaluation of the line widths that does not represent the whole system. This is further exaggerated by the viscous shear stress also being wave phase dependant. The relation found in figure 6.4 can be used to diminish this systematic error by shifting the measured squared line widths relative to a representative value of the squared initial widths, i.e.

$$\sigma_{\text{shifted}}^2(t) = \sigma_{\text{meas}}^2(t) - \sigma_{\text{meas},0}^2 + \sigma_{\text{rep},0}^2, \quad (6.10)$$

with  $\sigma_{\text{meas}}^2(t)$  and  $\sigma_{\text{meas},0}^2(t)$  being the measured line widths of an individual line,  $\sigma_{\text{rep},0}^2$  the representative, squared line width and  $\sigma_{\text{shifted}}^2(t)$  the shifted, squared line widths used for evaluation the viscous shear stress. Note that this approach neglects the dependence of  $\sigma^2(t) - \sigma_0^2$  on  $\sigma_0$ , but as long as  $\sigma_{\text{rep},0}^2$  is similar to the observed line widths, the error is small. Due to the long heating time of the lines  $t_{\text{laser on}} = 15 \text{ m/s}$  used in the measurements of January 2021, the shifting (6.10) is done for all the evaluations considering a large number of lines at once. This yields the best estimate for the viscous shear stress. The results corresponding to the unshifted data sets are also given, however, for comparison and reference.

The characteristic line widths are fitted in an evaluation time window by a cubic polynomial for outlier reduction, see figure 6.5. This time window has to be chosen with care; it is advantageous to evaluate the lines as late as possible, since the effect by Taylor dispersion needs some time to develop, and this increases the discrepancy between the different  $\partial_z u$ . At some point, these points introduces a bias, as the lines undergoing a strong broadening will yield weaker signals and in the end not be evaluable. Hence only the thinner lines remain, and causing the mentioned bias in the characteristic line widths.

The stretching and compression of the line widths by the wave associated motion, refer to section 3.5, may, depending on the setup, introduce another bias towards too low characteristic line widths for  $t \sim T'/2$ . Here  $T'$  describes the wave period in the reference system drifting with the mean surface velocity, hence the period experienced by the lines. This bias and it's manifestation will be discussed in detail in section 7.1, but it can be mentioned here that in order to avoid the bias, the evaluation of the line widths should be conducted at  $t \gtrsim T'$ . Naturally, this is especially important if there is a pronounced influence on the characteristic line widths.

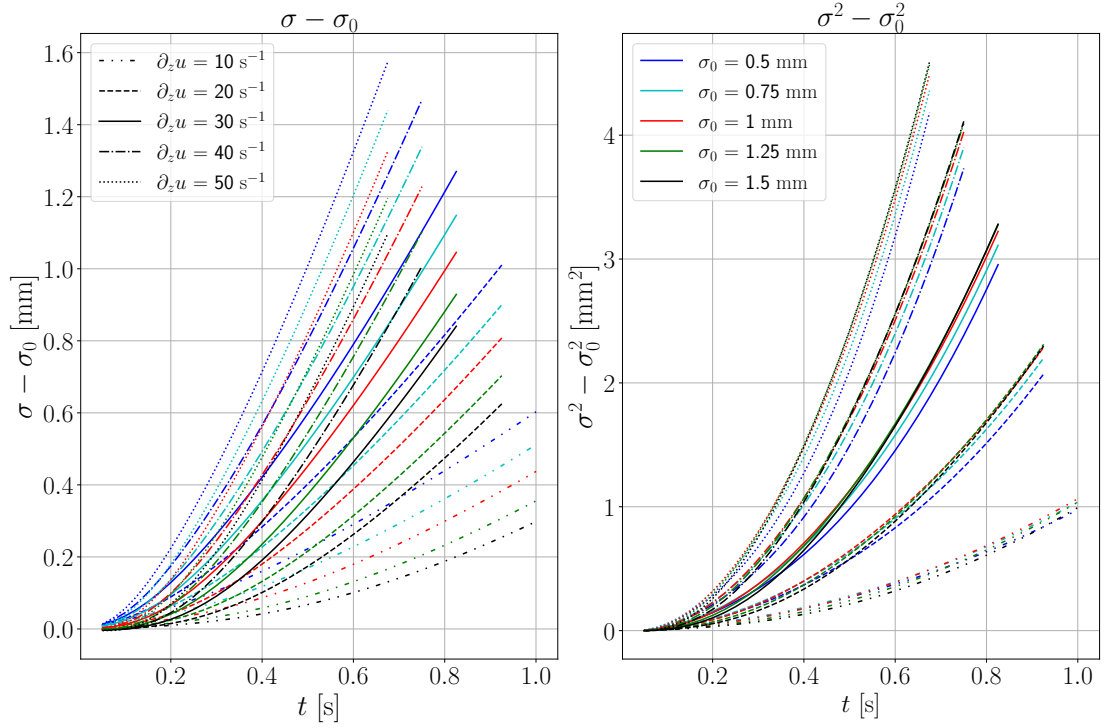


FIG 6.4.: The figure shows simulated line widths for several  $\sigma_0$  and  $\partial_z u$ , specifically it shows  $\sigma - \sigma_0$  (left) and  $\sigma^2 - \sigma_0^2$  (right) as functions of time since heating the line. The subtraction by the initial quantities is done for improved comparability. As seen, the squared line widths describe the system better with respect to different  $\sigma_0$ , with a much smaller spread for the same  $\partial_z u$ . In the real world application, lines of distributed initial width are collectively evaluated, hence the best representation is important. Hereby  $\sigma_0^2$  approximately represents an offset in  $\sigma^2(t)$ , with the exception of a modest dependence of  $\sigma^2 - \sigma_0^2$  on  $\sigma_0$ . Hence, this favours a narrow distribution of  $\sigma_0^2$ . Colours and markers are the same in both plots, hence both legends apply to the whole figure.

For short times after heating the line,  $t > t_{\text{laser on}}$ , but after the heating process is finished, the characteristic line widths are used to determine  $\sigma_0$ . This is preferable done by extrapolating these points to  $t = 0$  using the expression for one dimensional diffusion (2.63), which holds since the influence by the shear stress is still neglectable. If there is a higher degree of scattering, the mean in the interval  $t_{\text{laser on}} \leq t \leq 8 \text{ ms}$  is used instead.

The fit for representing  $\sigma(t)$  in the evaluation window and  $\sigma_0$  is then compared to the simulation. Depending on the scattering of the characteristic line widths, which is strongly dependent on how many lines are evaluated at once, the simulated data is either used as a look-up table or interpolated and then evaluated. Importantly, the simulation gives the relationship  $\sigma = h(t, \sigma_0, \partial_z u)$  for discrete sets of input parameters. In the case of scattered data, the first approach is used, since it is much faster and the resolution of the simulated data set is high enough for not introducing further uncertainties. Specifically, first the closest  $\sigma_0$  in the data set is found, then for  $t$  in the time evaluation window the closest  $\sigma^2(t)$  is found, yielding the corresponding  $\partial_z u$ . The approach changes if  $\sigma(t)$  is less scattered, such that using only the look-up table could introduce noticeable uncertainties, then  $\partial_z u$  is interpolated as a function of  $t, \sigma_0$  and  $\sigma(t)^2$ . Inserting the experimentally

determined quantities and  $\sigma^2(t)$  from the cubic fit within the evaluation interval, into the interpolated function, then returns the result as  $\tau_{\text{visc},xz} \propto \partial_z u$ . These returned values are then averaged. The procedure is repeated within an larger uncertainty evaluation window, reflecting that the sensitivity to the choice of evaluation time window. The standard deviation of the values returned for this larger window is used as an uncertainty estimate.

With the evaluation of longer time intervals ( $\gtrsim 300$  s) of the measurement, more lines are considered and statistics improve. In these cases, the statistics are good enough to subdivide the time intervals into  $\sim 100$  s without introducing large uncertainties due to the statistics and evaluation method. The deviations in the results of  $\tau_{\text{visc}}$  evaluated for these intervals is then stated as an additional uncertainty estimate in table A.2. Also the uncertainty related to  $\sigma_0$  may be of comparable magnitude in these cases. The sensitivity of the result of  $\tau_{\text{visc},xz}$  with respect to this uncertainty can be evaluated by repeating the evaluation of the data for  $\sigma_0 \pm \Delta\sigma_0$ , where  $\Delta\sigma_0$  describes the uncertainty.

For the measurements of January 2021, also the characteristic life time of the heated lines was computed. This was done by determining the time at which the number of data points has dropped to half of the maximum number of points, using the *unsorted* dataset. The unsorted set was chosen in order to avoid any selection caused by sorting the lines, and also to represent the whole flow field, not only without horizontal shear flow.

Finally, for the measurements of January 2021, also surface dilation and compression was experimentally approached, by the description given by equation (3.16). For this, the phase speed was determined from the surface elevation data and by a correlation of the orbital horizontal motion between line 2 and 3, see section 6.5.1. It was estimated twice, since both methods were prone to scattering, and the value fitting best to the observation of the line widths chosen. Furthermore, the phase speed was assumed constant for the duration of the individual line. The observed (for  $\partial_y u \approx 0$ ), non-squared line widths were slightly sorted using the 20th and 80th percentile as a cut-off, then averaged, and these values fitted by equation (3.16), describing the part of the observed widths relating to the stretching and compression of a fluid parcel, multiplied by the square root of a second order polynomial to account for diffusive broadening, to the observed  $\sigma(t)$  for each individual line. The input parameters for equation (3.16) were allowed to vary by 20% in the fit, and a small time shift accounting for a phase shift in the horizontal velocity of the line due to the mounting angle of the camera was allowed for. The second order polynomial was found in Voigt [2019] to describe the temporal development of the *squared* line widths caused by Taylor dispersion well, and the derivative was forced to be positive in the fit. The horizontal velocity of the line was calculated by spline interpolation of its position  $x(t)$  and subsequently taking the temporal derivative.

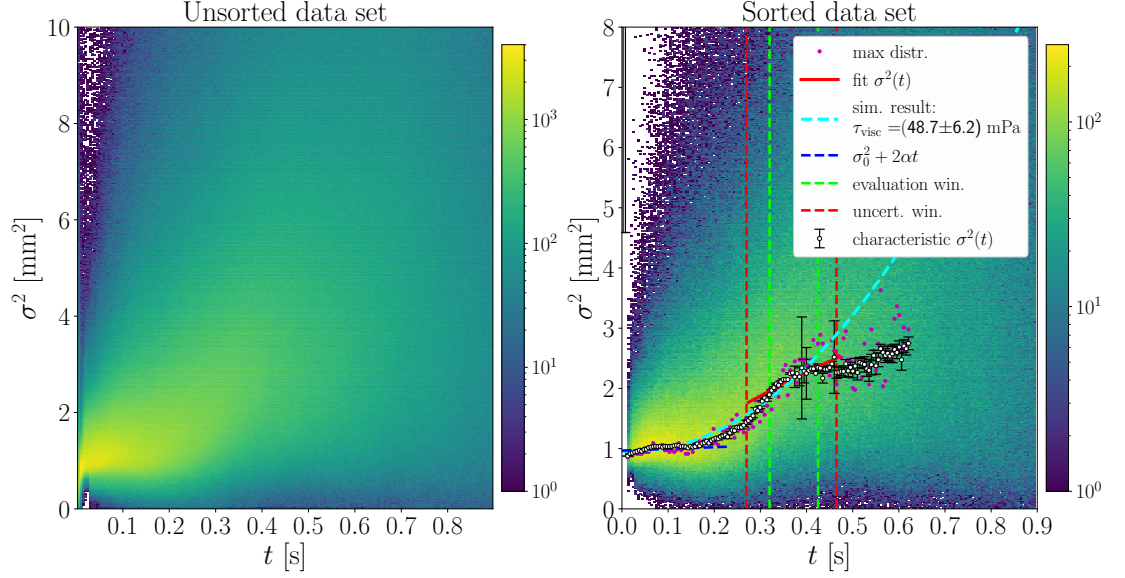


FIG 6.5.: An unsorted (left) and the evaluation of a sorted (right) data set containing the squared line widths  $\sigma^2$  for time  $t$  since heating the lines, in a time interval of [600 s, 1000 s] after turning the wind on, of the 10 Hz measurement. The set was sorted according to equation (6.6) for  $\partial_y u = (0 \pm 0.2)/\text{s}$ . As can be seen, the unsorted set contains broader distributions. The scattering of the data points at  $t \approx 0$  is caused by the new lines being weak in brightness whilst heating, thus more prone for being mixed up with reflexes or similar bright spots. The sorted data set is fitted with the expressions (6.9) and (6.7) for each  $t$ , yielding approximations for the peaks position of the distributions, which are then averaged (characteristic  $\sigma^2$ , white dots). The maxima of the (slightly smoothed) distributions are shown by magenta points, and scatter more than the fits. The characteristic  $\sigma^2$  for small times are extrapolated to  $t = 0$  using equation (2.63) yielding the initial squared line width  $\sigma_0^2$  (blue dashed line), whereas they are fitted by a third degree polynomial in the evaluation window (lime dashed line) and uncertainty estimation window (red dashed line), respectively. These are then compared to the simulation, returning the best estimate for  $\tau_{\text{visc}}$  for the evaluation window and the uncertainty in  $\tau_{\text{visc}}$  within the uncertainty window. The corresponding simulated curve is also shown (cyan dashed curve).

## 6.5

### IMAGE PROCESSING AND EVALUATION OF THE LHC IMAGES

In this section the analysis of the laser height camera (LHC) images for surface elevation measurements will be summarized. More detailed descriptions about the principle can be found for example in Schwarz [2016], also the used workflow is mostly similar. The process is described for the data of the experiment conducted in January 2021, but is similar for the PSV-measurement.

The images were first smoothed for noise reduction by convolution with  ${}^4\mathcal{B}$  as described above. There were two marked steps in the brightness of the images, the upper corresponding to the transition between channel wall and (background) water surface, and then between this background water surface and the surface illuminated by the laser sheet. The surface was first roughly detected using a threshold given by the brightness of the second step and finding the first significantly brighter pixel per column. From these values standard deviation and mean were calculated, in order to sort out the strongest deviating values, which arose due to inhomogeneities in the laser sheet. Based on this, a section of the image containing the water surface was used for further processing. Firstly, it was median filtered in horizontal direction for noise reduction, and for each row the brightness values above and below (image coordinates) the surface were found. The average then defined a threshold, and the water surface was detected by the weighed mean of the pixels position closes to 90%, 100% (weighted twice) and 110% of the threshold value, similar to Schwarz [2016].

Another approach was also implemented, namely by estimating the position of the water surface by the maximal gradient of the small section of the image containing the surface. The gradient was calculated by convolving the image with a (5 tap) kernel for horizontal interpolation and a (5 tap) kernel for differentiation, see Farid and Simoncelli [1997] for further details, and see equation (B.10) for the kernels. It was found that for most measurement conditions, the gradient approach was the most stable method, though differences were small. See figure 6.6 for an example. The resulting surface detections are then labelled with the time corresponding to the image and calibrated. By median filtering in the  $t$ - $x$ -plane, outliers could be detected, which were then interpolated by cubic splines. An analogous interpolation on the *uncalibrated* is also shown in figure 6.6.

With the surface elevation  $\eta(x, t)$  known, properties of the wave field could be calculated. The surface inclination  $\partial_x \eta$  was found through the derivative of the spline interpolation. Moreover, the frequency power spectrum was calculated for 5 second intervals due to the non-stationary wave field, see equation (2.49), using Welch's method (refer to Welch [1967]) for a trade-off between frequency resolution and noise reduction. The peak frequency was then found, defining a cut-off frequency range  $\frac{1}{2}f_m \leq f \leq \frac{3}{2}f_m$  for the dominating wave (Bopp [2018]).

By reconstructing the dominating wave using fast Fourier transforms, a Hilbert transform, refer to B in the appendix and equation (B.12) of the dominating signal could be computed. This retrieves phase  $\varphi$  information as well as the signals envelope. More information can be found in Oppenheim and Schaffer [2010]. At the endpoints of the signal, both the envelope and phase was unreliable, hence an overlap to the neighbouring interval was included in the calculation. From the phase information, also the local dominating wave number  $k$  and frequency  $\omega$  were estimated, namely as

$$k_{\text{dom}} = d_x \varphi \text{ and } \omega_{\text{dom}} = d_t \varphi. \quad (6.11)$$

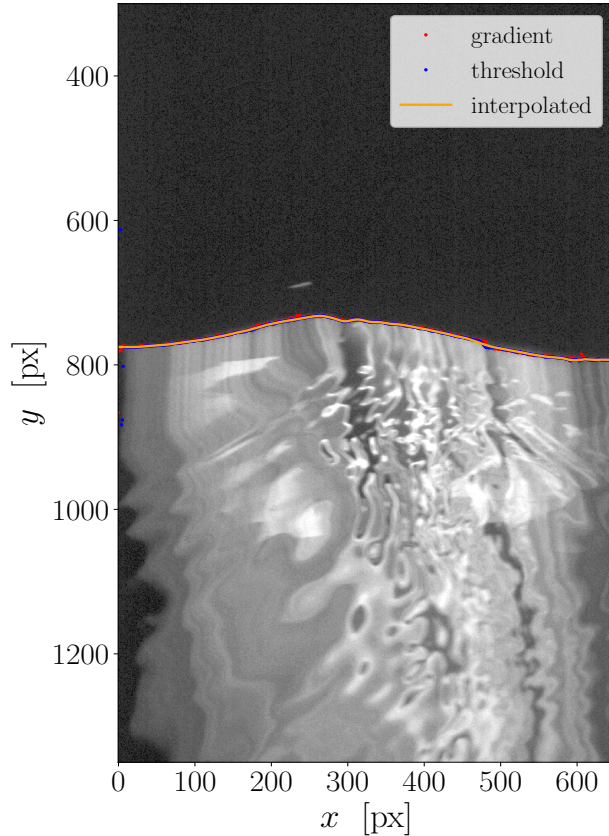


FIG 6.6.: The surface detection of an image from the 12.5 Hz measurement. The red dots depict the surface computed by the maxima of the vertical gradients, whereas the blue dots are determined by the threshold approach described in section 6.5. The orange line shows the interpolated result. The gradient approach was found to be slightly more stable for various measurement conditions. Note the small step in the surface position at  $x \approx 500$  px, caused by an inhomogeneity in the laser sheet.

The phase was unwrapped and interpolated before the derivatives were calculated. For the parts of the signals with a small amplitude, the phase information from the Hilbert transform became inaccurate, such that the phase information could not be relied on. Hence, the water surface treated as flat in these low-amplitude cases, this being of particular relevance for the PSV evaluation. This was also done in Bopp [2018].

For an example of the determined quantities from the surface elevation measurements, see figure 6.7 showing a 10 s interval of the 10 Hz measurement of January 2021.

### 6.5.1

#### PHASE SPEED

In order to explore the surface compression and dilation and the validity of equation (3.16), the phase speed  $c$  is needed. This was estimated in two ways for the *co-moving* reference system with the mean surface drift velocity  $U_d$ ; by  $c_{\text{dom}} = \omega_{\text{dom}}/k_{\text{dom}} - U_d$  and by using the equation for a third order Stokes wave (2.40). The latter must then be corrected by subtracting the Stokes drift, equation (2.32), and needs an estimate of the wave steepness. This was approximated by  $k_{\text{dom}} \cdot H/2$ , where  $H$  is the wave height found by interpolating the surface elevation at the crests and troughs, see figure 6.7. The dominating amplitude was deemed too fluctuating due to the asymmetry of the wave elevation about the mean water level.

As a side note, due to the spatial and temporal information of the surface elevation, the phase speed could also be determined by a cross-correlation of the temporal development at two different positions. This, however, revealed wave phase dependent time shifts between the signals. Further explanation would likely require elevation measurements

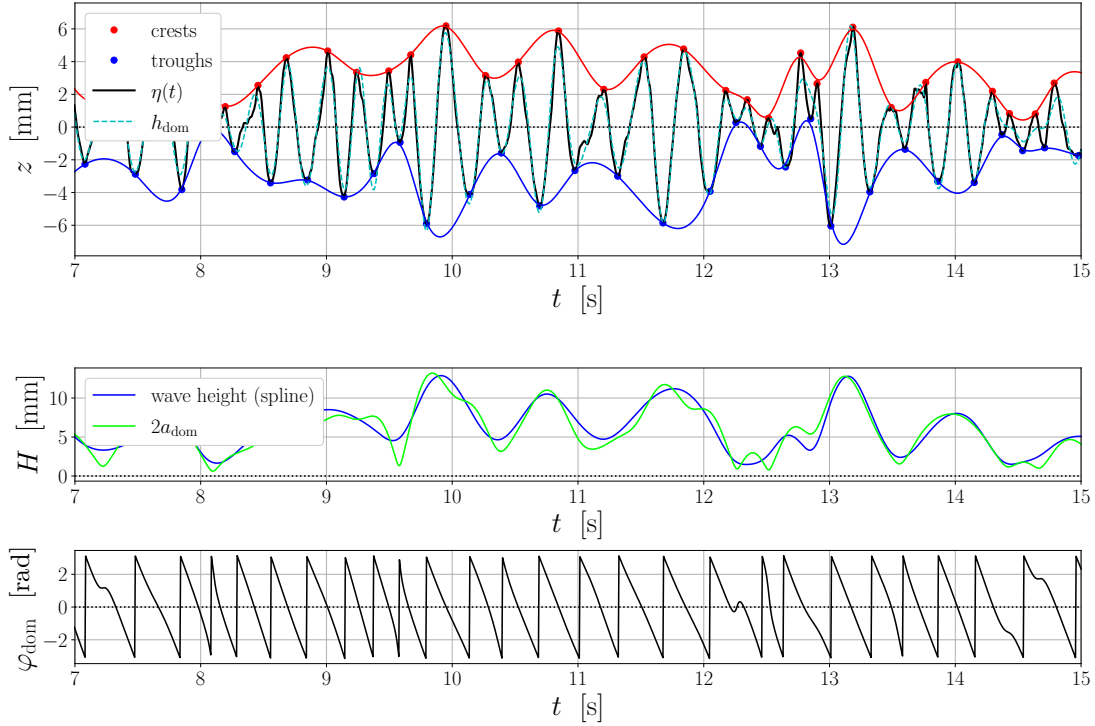


FIG 6.7.: The topmost plot shows the water elevation (black line) along with the dominating wave (cyan dashed line), and the splines used for wave height estimation, in dependence of time at a fixed position in the middle of the laser sheet. When the change in the (extremal) surface elevation was large, the splines for the wave height estimation sometimes overshoot. The resulting waveheight for the dominating wave is shown in the middle plot (blue), along with the more fluctuation envelope of the Hilbert transform (lime). The fluctuations are caused by the waves being asymmetric around the water level. The lower plot shows the wave phase calculated by the Hilbert transform. Note the unreliability when the wave heights are low.

of a larger part of the surface, which is out of scope in this thesis, but this led to a determined phase speed dependent on the (random) extent of the signal considered. Being an artefact of the evaluation, this approach was discarded.

Lastly, due to two lines (line number 2 and 3, see figure 6.2) of the measurements of January 2021 located at similar  $y$ -positions (i.e. perpendicular to the wind), the phase speed in the co-moving system could also be calculated by the temporal shift between the horizontal orbital velocities, i.e. from the thermographic data. Hereby the positions of the individual lines after heating  $x(t)$  were considered. The mean drift velocity and mean relative position of the was determined by a linear fit of  $x(t)$ , with the slope corresponding to the mean surface velocity  $u_s$  and the offset to the relative position. The instantaneous velocity of the line were found by spline interpolation and differentiation of  $x(t)$ . The mean velocities  $u_s$  were subtracted, and a cross correlation performed. The distance between in their relative positions divided by the temporal shift then yielded the phase speed. If only single lines are used, this method for determining  $c$  is still applicable if the heating frequency of the lines is higher than the Nyquist frequency requirement. Hence at least to lines must be present per (dominating) wavelength.

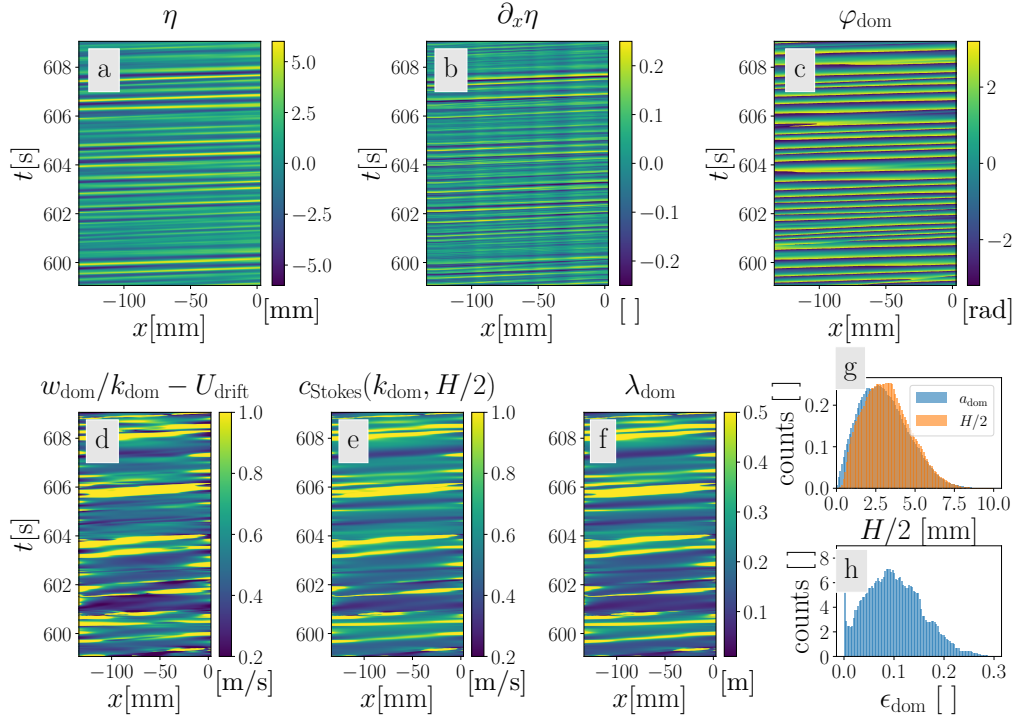


FIG 6.8.: An example of the LHC result, for a 10 interval of the 10 Hz measurement. Wind direction is in positive  $x$ -direction. Upper row: (a) surface elevation  $\eta$ , (b) surface slope  $\partial_x \eta$ , (c) dominating wave phase  $\varphi_{\text{dom}}$ , with negative phases corresponding to upwind direction. Lower row: (d) calculated phase speed by  $c_{\text{dom}} = \frac{\omega_{\text{dom}}}{k_{\text{dom}}}$  in the (co-moving) reference system drifting with mean surface velocity, (e) the phase speed calculated by equation (2.40) in the co-moving system (middle), and (f) dominating wavelength  $\lambda_{\text{dom}}$ . The colours indicate the magnitude of the quantities, with the unit given below the colour bar. Note the fluctuations in the quantities with time, and the predominant agreement between the two calculations of the phase speed. The last two plots show (g) comparison of the distributions of half the wave height  $H/2$  (orange) estimated by cubic splines and from the Hilbert transform  $a_{\text{dom}}$  (blue), and (h) estimated wave steepness  $\epsilon = k_{\text{dom}} \cdot H/2$ .

## 6.6

### PARTICLE STREAK VELOCIMETRY

The reference measurement with particle streak velocimetry will briefly be explained in the following. The method was developed by Bopp [2018] for air-sided measurements. Only minor adjustments, mainly preprocessing and streak detection, had to be performed for the water-sided evaluation, hence refer to Bopp [2018] for further details.

The raw images were subject to large brightness differences, both from image to image and within an image. Differences within the images resulted from an inhomogeneous laser sheet. In the original algorithm for air-sided measurements, threshold limits for the streak detection were found by a fit of two Gaussian distribution to the image pixel value distribution, one corresponding to the (bright) water surface, and the other to the dark air-side background. Due to the large brightness variation and the



total reflection at the surface, this was found to not yield sensible threshold values on the water-side. Furthermore, background calculation purely by median filtering as in Bopp [2018], was found to be suboptimal. Even for relatively large masks, bright particles or similar spots - especially frequently located at the interface - had a notable influence on the calculated median. Spatial changes in brightness on small scales also tended to favor smaller masks, which further exaggerates the problem of the influence by the bright particles. Subsequently, brighter backgrounds resulted in the area nearby bright streaks, then reducing the brightness of the streak when the background is subtracted. Darker neighbouring streaks then often fell under the detection limit.

### 6.6.1

#### PREPROCESSING AND STREAK DETECTION

This was solved by iteratively calculating the background. First a copy of the image was smoothed (i.e. convolved) with a fourth degree binomial mask  ${}^4\mathcal{B}$ , see equation (B.9), and subtracted, thereby removing most background structures. Based on this now “flat” image, its pixel value distribution was calculated. The idea is that all bright spots remaining must be caused spatially narrow structures, otherwise most of their signal would have been subtracted along with the preliminary background. The symmetry  ${}^4\mathcal{B}$  makes sure to not shift their positions. Using a rather low threshold, these remaining bright pixels were detected. From the *original* image a new background was then calculated, by replacing the remaining bright values by strongly negative values and median filtering. The bias in the median was then slightly shifted towards darker values. Finally the result was smoothed once more and subtracted. Even the less bright streaks were then found to deviate by more than 5 standard deviations from the background, making them easily detectable without the need for fine adjustments.

### 6.6.2

#### EVALUATION OF THE STREAKS

The part of the algorithm finding the surface and excluding the non-relevant fluid compartment, was excluded, since the surface detection was not possible based on the water-sided images. Beyond this stage, however, the algorithm for streak evaluation was left unchanged. Briefly explained, the final background was subtracted the raw image, refer to figure 6.9. Then, the resulting image was smoothed by a second degree binomial mask  ${}^2\mathcal{B}$ , see equation (B.9), and an orientation image was calculated by applying a structural tensor (refer to Bopp [2018] for details) to the smoothed image, thereby determining the direction of the flow. See figure 6.10 for a schematic. This enables the separation of streaks separated by less than the gap between the two streak parts. The black and white image resulting from the detected streaks is then dilated somewhat, to include surrounding pixels below the threshold values still belonging to the streaks. Using the orientation image, the streaks are then collected, and a line fitted along them, weighted by their grey values. Along this line, including an area of 1.5 pixels at each side of the line, the average gray values are determined for each position, with 0.5 pixel steps. This average is weighted by the overlap between the above mentioned area (mask) and the actual pixels. This leads to an one dimensional profile of the streak, whose length is used for evaluating the velocity.

As the laser pulses illuminating the streaks are created with one frequency, if the streak is long enough, a fast Fourier transform (FFT) can be used to determine its frequency in terms of pixels. Hence, this enables a straightforward first estimation of its

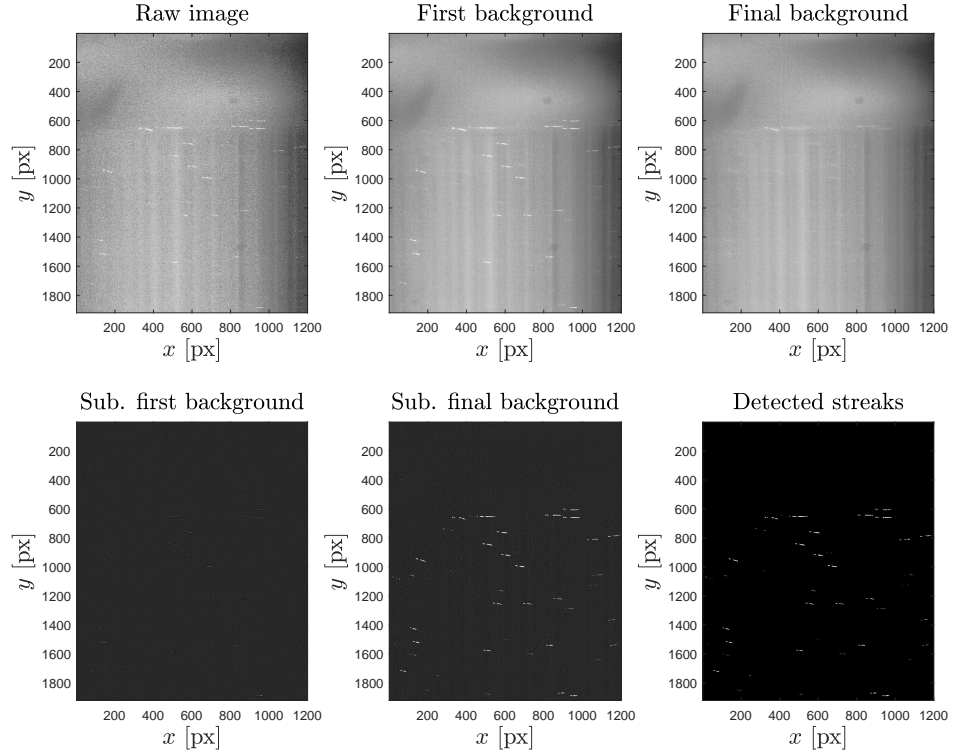


FIG 6.9.: Preprocessing of the PSV-images. The grey value ranges are identical in the three topmost plots. The lower left and middle also have equal gray scales, but differing from the upper. In the lower right image the pixels are either true (white) or false (black). The raw image, shown in the upper left plot, is smoothed (top middle), and then subtracted from the raw image, yielding the lower left image. The latter is used to determine the brightest small scale elements, which are then labelled. The new background is calculated by median filtering the raw image, with the labelled pixels set to strongly negative values, and then smoothed (upper right). This is then subtracted from the raw image (lower middle), with the streaks clearly distinct from the remaining background. These are then detected by a threshold based on the remaining background (right). The latter image has not been dilated yet. Note that the surface is not sharply visible due to total reflection, also a particle at  $x \approx 950$  is reflected. Also note that in the final background broader, bright structures remain and low magnitude “footprints” by streaks too weak to be detected in the first iteration.

length. For this a smoothed profile of the streak is first subtracted, removing lower order harmonics from the streak profile. For shorter streaks the pulses are no longer distinct, yielding two parts of continuous illumination. Here the Fourier transform estimate is no longer trusted.

The 1D profiles are in a final step fitted with model profiles, i.e. idealized, calculated streak patterns. The range of length of these profiles is limited to  $\pm 10\%$  of the estimated length by FFT for less computational effort, while for short streaks all profiles up to the lower limit where the FFT is trustworthy are also fitted. The short streaks are detected by the distance between start- and endpoint. The fitting is done by first performing a cross-correlation between the (normalized) profile and model, finding their relative

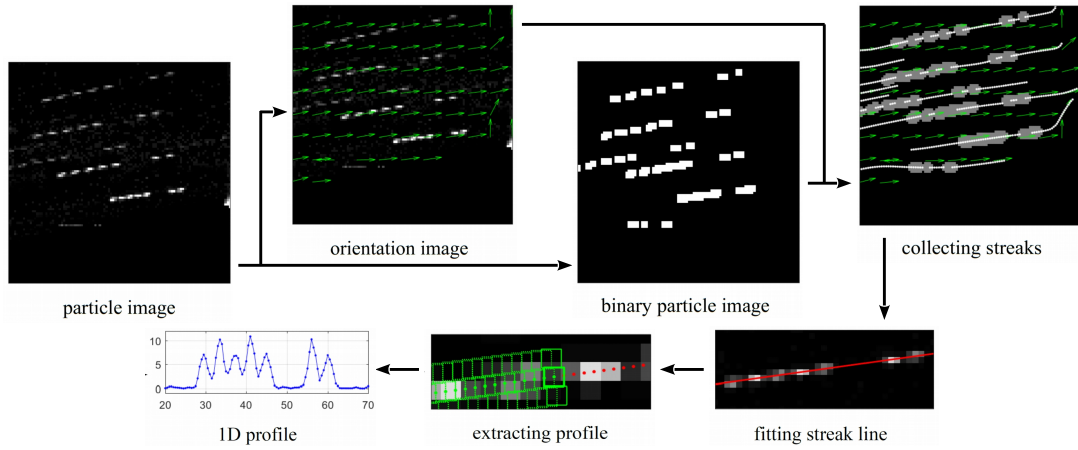


FIG 6.10.: The figure shows the first steps of the PSV algorithm after subtracting the final background (refer to figure 6.9). The particle image is used for calculating the streak orientations, enabling separation of streaks closer than the pulse gap, and for detecting the streaks (binary particle image). The streaks are then collected and fitted by a straight line, from which the profile is extracted using a mask of 3 pixels and weighting the pixel values according to the overlap by the mask. The figure is adapted and modified from Bopp [2018].

displacement, and subsequently minimizing the residuum  $\Theta$  normed by the model profile,

$$\Theta = \frac{\sum_i |g_{\text{model},i} - g_{\text{prof},i}|}{\sum_i g_{\text{model},i}}, \quad (6.12)$$

with  $g_{\text{model}}$  being the model profile and  $g_{\text{prof}}$  the extracted profile. The latter is used as a measure of goodness of fit. Note that the fit must be done with the model profile oriented in both directions.

Ideally, the best fit is the one in the correct direction, and the next best the same profile in the opposite direction. This means that both the velocity and direction is well determined, hence a small residuum and a distinct difference between the goodness of fit for the second best fit  $\Delta\Theta$  is desired. Bopp [2018] found selection criteria for the streaks based on numerically analysing the fit results of artificially created model images. These selection criteria, yielding good results also for the water-sided data, is adapted in this work:

$$\Theta < -0.21125 \exp(-0.74749\lambda_{\text{streak}}) + 0.38786 \quad (6.13)$$

$$\Delta\Theta > -0.36395 \exp(-3.104\lambda_{\text{streak}}) + 0.20327, \quad (6.14)$$

with  $\lambda_{\text{streak}}$  being the wavelength in pixel of one of the seven pulses comprising the streak. Particles passing the selection criteria are used for further analysis. The particle velocity is calculated based on the determined length, and the position based on the middle point of the streak.

### 6.6.3

#### EVALUATION OF THE PSV DATA

The streaks' position relative to the surface height is calculated from the LHC data, see above (section 6.5). This is done by using wave following coordinates  $(x^*, y^*, z^*)$ , where the horizontal coordinates remain unchanged and the vertical coordinate follows the surface, i.e. (Bopp [2018])

$$x^* = x \quad (6.15)$$

$$y^* = y \quad (6.16)$$

$$z^* = z - f(\vec{x}^*, t), \quad (6.17)$$

where  $f(\vec{x}^*, t)$  must be equal to the wave height  $\eta(\vec{x}, t)$  for  $z^* = 0$ . In this work a simple shift  $f(x^*, t) = \eta(x, t)$  is applied, with Jacobian  $J$  and its determinant

$$J_{ij} = \partial_{x_j} x_i^* \text{ and } \det(J) = 1, \quad (6.18)$$

respectively. The velocities  $v_i$  can be transformed to  $V_i$  by (Bopp [2018]):

$$V_k = \frac{1}{J} (v_k \partial_{x_k} x_i^* + \partial_t x_i^*). \quad (6.19)$$

The simple shift yields a physically questionable representation far away from the surface, where the waves have less influence than described by this shift. Bopp [2018] also used a declining shift on the air-side in addition to the simple shift, and found it to yield a better description - this is out of scope in this thesis, however.

The transformed viscous shear stress  $\tau_{\text{visc},xz^*}$  equals  $\tau_{\text{visc},\parallel} = \mu \partial_{z_\perp} u_\parallel$  (Bopp [2018]), with  $\partial_{z_\perp} u_\parallel$  being the gradient with respect to the perpendicular distance to surface of the tangential velocity. Note that the heated line will also follow the surface motion, and will be broadened according to  $\partial_{z_\perp} u_\parallel$ . Direct estimation of the gradient in each image is limited by the sparse streak density, hence only the mean quantity is computed. The perpendicular distance between a streak at  $(x_0, z_0)$  and the surface  $\eta(x, t)$ .  $z_\perp$  is found by solving

$$\partial_x \eta(x, t) \cdot (\eta(x, t) - y_0) - (x - x_0) = 0, \quad (6.20)$$

which represents a numerically slightly more stable implementation compared to the same equation divided by  $\partial_x \eta(x, t)$ . Moreover, the parallel and normal ( $w_\perp$ ) velocities of the streaks were found by decomposing the untransformed velocities by rotation analogues to equation (3.3). The surface inclination at the point corresponding to  $z_\perp$  was used. Note that since the water surface also moves vertically, a part of the  $z$ -velocity of the streak is caused by this motion, whereas the distance to the surface is wave following. Hence  $\partial_t \eta$  is subtracted before the decomposition. The resulting profiles of  $u_\parallel$  as function of  $z_\perp$  profiles are lastly fitted by cubic, penalized splines (B.15), in the lack of other parametrizations. The value of the derivative of this spline in the topmost half millimetre below the surface is then used for calculating the viscous shear stress. This is done both wave phase resolved and phase averaged, yielding  $\tilde{\tau}_{\text{visc}}$  and  $\bar{\tau}_{\text{visc}}$ , respectively. Since the spline is no model, the smoothing of the splines is arbitrary. This is reflected by varying the degree of smoothing, using the standard deviations of the values as an uncertainty estimate. Density variations in the particles with respect to phase are accounted for by normalization before averaging. As also done in Bopp [2018],

the velocity range of the middle 50% of particles for each depth and phase interval were considered, and those deviating by more than twice this range from the median, were considered to be outliers and discarded before averaging.



# 7 | RESULTS AND DISCUSSION

In this chapter the results and findings of the measurements are presented and discussed. The main focus is on the evaluation of the viscous shear stress  $\tau_{\text{visc}}$  by the active thermographic method, only occasionally other quantities will be considered. As before,  $\tau_{\text{visc}}$  denotes the mean, phase averaged shear stress, and only when phase resolved measurements are presented or discussed,  $\tilde{\tau}_{\text{visc}}$  (phase specific) and  $\bar{\tau}_{\text{visc}}$  (phase averaged) will be used. Moreover, in this chapter the wave period always refers to the period in the reference system moving with the mean surface velocity,  $T'$ , corresponding to the period experienced by the heated lines. A value is considered to be significantly deviating if the deviation is larger than three standard deviations. For the comparison of two results, Gaussian error propagation is applied.

First, the observations and outcomes of the evaluation of long time intervals of the measurements of January 2021 and the reanalysis of the stationary measurements by Emmel [2017] are considered. Then the results of the non-stationary evaluations are presented, before looking closer into the effects of surface dilation and compression on individual heated lines, followed by several additional findings. Finally, the outcomes of the reference measurements will be given.

## 7.1

### EVALUATION OF LONG TIME INTERVALS

Evaluating long time intervals poses the advantage of being able to collectively evaluate a large number of heated lines, reducing problems associated with poor statistics and highlighting persistent patterns in the data. In order to yield meaningful results, however, the conditions should not change considerably within the evaluation interval. The duration of the measurements of January 2021 (refer to section 4.2) are too short for the wind field to fully equilibrate with the water, hence the system may still change as the bulk velocities increase. As will be seen in section 7.2, changes in surface velocity and the viscous shear stress per time interval are found to be small after a initial transitional regime. Therefore, in the following the lines after 600 s after turning the wind on are evaluated collectively, for a time interval of 600 s. As explained in section 6.4, also an uncertainty by partitioning the collective evaluations into smaller intervals is evaluated, i.e. reflecting a possible temporal change in  $\tau_{\text{visc}}$ . These changes were found to be small, hence the collective evaluation of the whole interval is reasonable.

For the measurements of January 2021, considerable deviation between the simulated line widths and the measured characteristic line widths were found. This was not observed for the measurements by Emmel [2017]. Therefore, in section 7.1.1 an explanation for the observed deviations and the subsequent implications will be given, before the results for the viscous shear stress are discussed in section 7.1.2.

### 7.1.1

## INFLUENCE BY THE WAVES ON THE LONG TIME INTERVAL EVALUATIONS

### LOW WIND SPEEDS

Starting with the measurement of January 2021 at low wind speeds, it was found that the temporal evolution of the characteristic squared line widths  $\sigma^2(t)$  after heating coincided well with simulated line widths, indicating that using the peaks of the distributions - as argued in chapter 3 - represents the system well. Starting with the 5 Hz measurement, the influence by waves on the line widths are clearly seen when considering individual lines. This influence is exemplified in section 7.3. The distributions of  $\sigma^2(t)$  for given  $t$  for the collective evaluation also clearly show the influence, see figure 7.1. The distributions are skewed, with the long tail towards higher values of the squared line widths, as expected from the reasoning and analysis in section 3.5. More interestingly, mainly the first narrowing of the distributions that were found in the simplified numerical example after integer multiples of the wave period in the co-moving reference system  $T'$  experienced by the lines, refer<sup>1</sup> to figure 3.8, is indeed also observed in this measurement, see figure 7.1. The a broadening of the lines due to diffusion and subsequent Taylor dispersion is present, leading to an increase in  $\sigma^2(t)$ .

Briefly explained, the initial widening and subsequent narrowing of the distributions of the squared line widths is caused by wave associated motion, which compresses and stretches the widths of the fluid parcels encompassing the heated lines. Hence also the line widths are distorted. Upon heating, the lines have approximately the same width if the oscillation of the surface velocity due to orbital motion is small. The initial widening of the distributions then results from some line widths being stretched, whilst others are compressed. After one wave period, the fluid parcels are back in their initial state at the time of heating the line, hence the distributions of the squared line widths are narrowing. Since also  $T'$  is distributed, it varies from line to line, hence a second narrowing at  $t = 2T'$  is not clearly seen, caused by the stretching and compression of line widths being to a larger degree out of phase.

Considering the distributions of  $\sigma^2(t)$  themselves suggests the narrowing of the distributions to be seen in the 6.3 Hz measurement as well, though less pronounced. By closer scrutiny this may also be seen in figure A.4 in the appendix. For higher wind speeds, as the wave field becomes more irregular and steeper, the narrowing is no longer seen in the collective distributions of all lines. For the lowest wind setting in this work, the 2.5 Hz measurement (figure A.3 in the appendix), the influence of waves was found negligible with respect to the line width of the heated lines. The distributions of  $\sigma^2(t)$  were also close to symmetric, as expected for conditions without waves (Voigt [2019]).

### MIDDLE WIND SPEEDS

The curvature with respect to time of the temporal development of the simulated squared line widths,  $\partial_t^2 \sigma^2(t)$ , is larger (or equal in the absence of shear flow, see equation (2.63)) to zero for all times since heating the line. Hence the broadening per (infinitesimal) time interval of the lines is getting larger with time. It is expected that the curvature of the

---

<sup>1</sup>Note when comparing the figures in section 3.5 to the figures in this chapter, that the figures in section 3.5 show  $\sigma(t)$  and not  $\sigma^2(t)$ , since the former is the natural description of the stretching and compression of fluid parcels. Moreover, the diffusive broadening was neglected in section 3.5. In this chapter,  $\sigma^2(t)$  is used due to the good representation related to the diffusive broadening of the lines, refer to figure 6.4, which is of main interest due to the determination of the viscous shear stress  $\tau_{\text{visc}}$ .



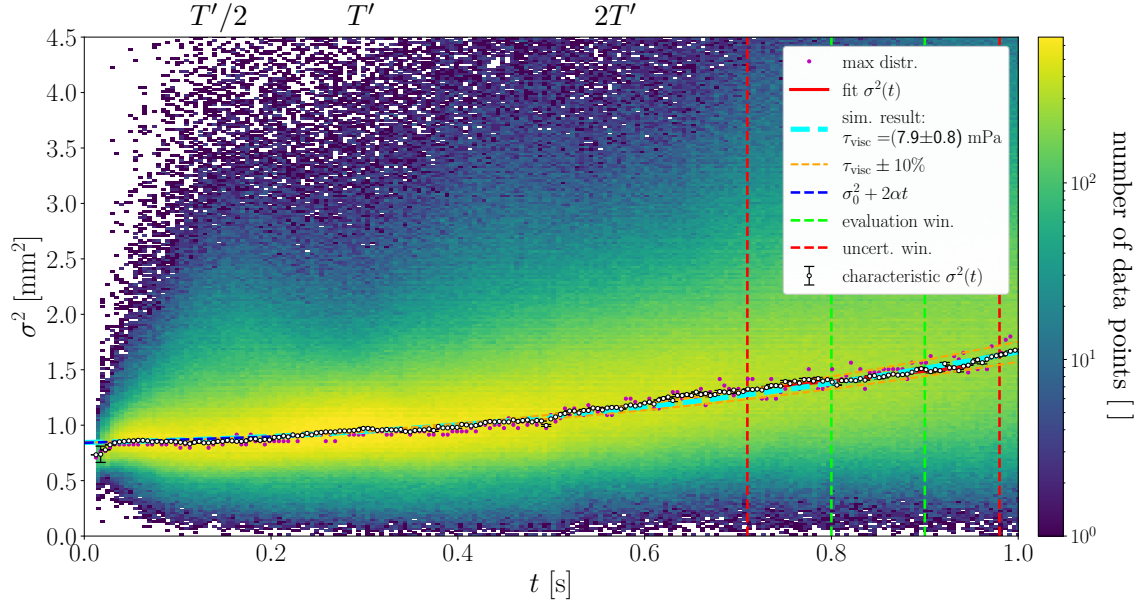


FIG 7.1.: Evaluation of the squared line widths  $\sigma^2(t)$  for the 5 Hz measurement. Refer to figure 6.5 and section 6.4 for further details. Note the broadening and successive narrowing of the distribution at  $t \approx T'/2$  and  $t = T'$  (indicated above the figure), respectively, with  $T' \approx 0.29$  s being the wave phase in the system co-moving with the mean surface velocity. A second narrowing at  $t = 2T'$  is not clearly seen, caused by the wave frequency being distributed and the stretching and compression of line widths being out of phase to a larger degree. The cyan dashed line shows the simulated curve for the result of the determined viscous shear stress  $\tau_{\text{visc}}$ , and the orange dashed lines indicate the simulated sensitivity towards a change of  $\tau_{\text{visc}}$  by  $\pm 10\%$ . The given uncertainty reflects the standard deviation of the estimated values of  $\tau_{\text{visc}}$  in the interval between the red vertical dashed lines. The best estimate for  $\tau_{\text{visc}}$  is evaluated between the lime dashed lines. Note the logarithmic colour scale, depicting number of data points per bin.

measured characteristic  $\sigma^2(t)$  changes sign at some point due to the fading of the broad lines for high times after heating. Hereby only narrow, brighter lines remain, causing a bias in the characteristic  $\sigma^2(t)$  towards low line widths. This causes the sign of the curvature to change. Especially from the 6.3 Hz measurement and onwards, however, the measured characteristic line widths show several changes of the sign of the curvature, which is consistent between the measurements. See figure 7.2 for the evaluation of the (unshifted line widths, refer to equation (6.10) and the discussion on phase dependent initial line widths below) 10 Hz measurement. For this measurement, at times similar to half a wave period  $T'/2 \approx 0.18$  s, the curvature is positive. When comparing to the simulated development of the squared line widths for  $\tau_{\text{visc}}$  evaluated at  $t \approx T'$  (cyan curve in figure 7.2), the line widths at  $t = T'/2$  are smaller than expected from the simulation. At about one period, the sign of the curvature is negative, and the squared line widths are close to those simulated. For  $t > T'$ , this pattern in the curvature is less prominent due to the fading of the lines and subsequent decreasing  $\sigma^2(t)$ , in combination with that the stretching and compression of the individual lines is to a larger degree out of phase.

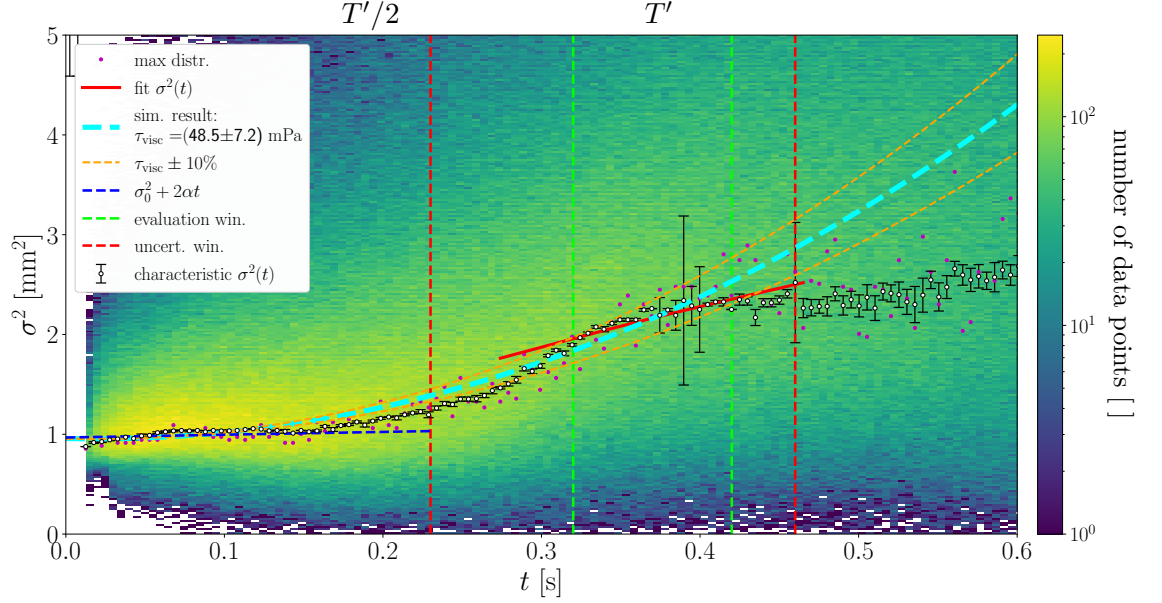


FIG 7.2.: Evaluation of the 10 Hz measurement, without shifting the individual line widths with respect to  $\sigma_0^2$  to a common  $\sigma_0$ . Note the change in curvature of the characteristic line widths, caused by the influence of surface compression on dilation. Briefly explained, at  $t = T' \approx 0.37$  s (indicated above of the figure) the influence is expected to be minimal, hence the measurement is evaluated at approximately that time (lime dashed lines), whereas at  $t = T'/2$  the more narrow distribution associated with compression of the lines slightly dominates, causing a bias towards low  $\sigma^2(t)$ . The observed pattern complicates the evaluation, as the evaluation time window becomes critical. This also gives rise to the large uncertainty, the time window of which is depicted by the red dashed line. This interval is asymmetrical in order to avoid a bias to small  $\sigma^2(t)$  caused by fading of the lines at high times.

These observed patterns for  $t \lesssim T'$  are clearly not random, as they are of similar shape for the different measurements and persistent even though a large number of lines are considered, and they are related to the wave period. Intriguingly, an analogous change of curvature was also seen in the numerical example in figure 3.8, though the transferability of the clearly simplified example must be treated with caution. However, as will be discussed in further detail below, the mechanism behind the pattern in the measured line widths is the same as that found for the numerical example.

Similarly to the widening of the distributions seen for the low wind speeds above, the patterns in the characteristic, squared line widths are caused by the stretching and compression of the fluid parcel widths. For the distributions of  $\sigma^2(t)$  around  $t = T'/2$ , one finds an lower “branch” corresponding to the lines heated in the wave trough ( $\varphi_0 = \pm\pi$ ), whose widths are only compressed after heating since the fluid parcels reach their maximum width in the trough. An analogous upper “branch” for the lines heated at the crest ( $\varphi_0 = 0$ ) is also found, caused by the fluid parcels having their minimum extent, hence the line widths are stretched for times  $0 < t < T'$ .

In section 3.5, the ratio of the line width  $\sigma(t)$  to the initial line width  $\sigma_0$  multiplied by a function accounting for diffusive broadening  $g(t)$ , as function of time and in dependence on the wave phase at the time of heating  $\varphi_0$ , was found to be described by a function,

see equation (3.16). This function  $f$  describes the width of the fluid parcel encompassing the heated line relative to the parcel's width at  $t = 0$ . The function  $f$  was found to be dependent on the inclination of the surface, the horizontal velocity component of the heated lines and the phase speed. In the real world application, one finds  $g(t > 0) > 1$ , in contrast to the examples given in section 3.5. For legibility,  $\sigma_{\text{theo}}(t) := \sigma_0 \cdot g(t)$  is introduced, hence describing the temporal broadening of the line widths without the alteration caused by compression and stretching of the surface layer. Then,  $f$  in relation to  $\sigma_{\text{theo}}$  is expressed as

$$f^2 = \frac{\sigma_{\text{meas}}^2(t)}{\sigma_{\text{theo}}^2(t)}, \quad (7.1)$$

where  $\sigma_{\text{meas}}$  is the observed (measured) line width. Intuitively speaking, this merely reflects that when the fluid parcels return to their state at  $t = 0$  after one wave period  $T'$ , hence  $f$  returns to  $f = 1$ , one would now expect to find  $\sigma_{\text{theo}}(T')$  instead of the initial line width  $\sigma_0$ , with  $\sigma_{\text{theo}}(T') > \sigma_0$ . A compression of the line widths corresponds to  $f < 1$  and a stretching to  $f > 1$ .

Note that only if assuming that (i) the viscous shear stress is constant and independent of the wave phase, and, as argued in section 3.5.3, that (ii) the diffusive broadening is independent of the change of the fluid parcel extents,  $\sigma_{\text{theo}}^2(t)$  is described by the simulated line widths based on the simulation in chapter 5. In particular condition (i) is, as will be seen in section 6.6 below, not fulfilled. However, since theoretical models as missing, the discussion and evaluation of the measurements will be continued with the simulated curves as an approximation.

The lines heated in the wave trough, which as explained above only are stretched, are hence described by  $f \leq 1$ . The lines heated at the crest, on the other hand, by  $f \geq 1$ . As found in section 3.5, there is an asymmetry of  $f(t)$  with respect to  $\varphi_0$  (see for example figure 3.6). Hence the range of values found for  $f < 1$  is smaller than for  $f > 1$ , leading to a more narrow and subsequently higher (counts per bin) distribution of the smaller compressed line widths corresponding to  $f < 1$ , when compared the stretched ( $f > 1$ ). A look at figure 7.3 for the 10 Hz measurement may clarify the matter, where the distributions of  $\sigma^2(t)$  for the lines heated in the trough (left) and the crest (right) is given. Since the peaks of the total distributions are used as characteristic line widths, the more narrow distributions for the compressed line widths with  $f < 1$  lead to a bias towards smaller  $\sigma^2(t \approx T'/2)$ . This causes the observed pattern described above, with the characteristic  $\sigma^2$  being smaller than expected from the simulated curves. Analogous figures to figure 7.3 for the 6.3 Hz of January 2021 and the 10 Hz measurement by Emmel [2017] are found in the appendix A.6 for comparison (figure A.15 and A.16, respectively). As can be seen, the 6.3 Hz measurement is less influenced, likely due to the wave field being less steep, and slightly lower values of the initial line widths  $\sigma_0$ . The lower initial line widths  $\sigma_0$  are likely also the reason why the 10 Hz measurement of Emmel [2017] is less influenced, as will be found below.

Ideally, for  $t \approx T'$ , all distributions should correspond to  $f \approx 1$ . Since the wave field is much more complex, this is at best fulfilled in a statistical sense. Therefore also the bias toward the smaller  $\sigma^2(t)$  is expected to be minimal at  $t = T'$ , before growing again when time is further increased. One can therefore argue that the most unbiased line widths occur for  $t \sim T'$  or integer multiples, and the measurement should be evaluated in a time window encompassing  $t = T'$ . For the lower wind speeds, up to 8.8 Hz measurements, the evaluation must be conducted after  $t > T'$  in order for the lines

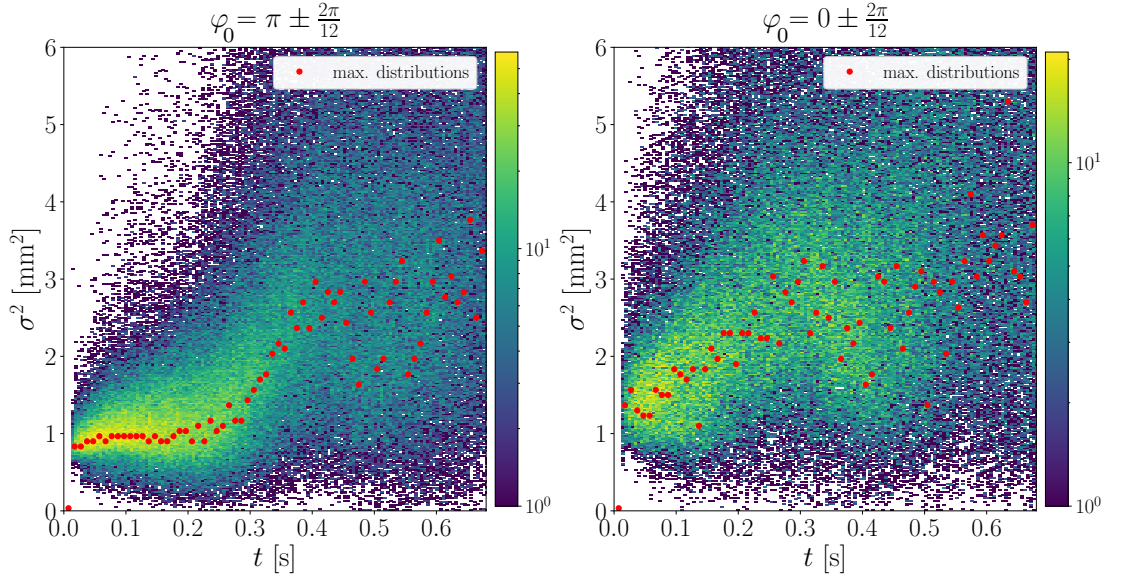


FIG 7.3.: The distributions of the squared line widths  $\sigma^2(t)$  of the heated lines heated at the wave trough (left) and at the crest (right) for the 10 Hz measurement. The red dots depict the maxima of the distributions, for a somewhat coarser binning than in the shown 2D histogram. The colours depict the number of data points per bin. A phase binning interval of  $\pm 2\pi/12$  was used in both cases. These two cases represent the outer bounds of the distributions of the line widths, as lines heated in the trough only can be compressed ( $f \leq 1$ , refer to equation (7.1)), whereas the lines heated at the crest may only be stretched ( $f \geq 1$ ). Note the different initial line widths, and that both distributions possess similar line widths starting at  $t \sim T' \approx 0.37$  s, corresponding to  $f \approx 1$ . Note the larger scattering for  $\varphi_0 \approx 0$  and subsequently the more narrow distributions and higher counts per bin for  $\varphi_0 \approx \pi$ , causing, along with similar initial phases, a bias towards lower  $\sigma^2(t)$  due to compression of the lines. The total number of data points is similar in both cases for  $t < 0.5$  s.

to broaden enough for a reliable evaluation. This is less of a problem since by then the bias is lower due to less coherency in the stretching and compression of the line widths, caused by frequency differences in the wave field. As will be seen below, the opposite is true for higher wind speeds, with evaluation for  $t < T'$ . Since the pattern causes an uncertainty with respect to the time interval where the line widths are evaluated, also larger uncertainties in the results for the viscous shear stress follow. As a side note,  $T'$  can for example be determined by either the orbital motion in the horizontal plane of the heated lines, or the mean drift in combination with the surface elevation measurements.

#### ROBUSTNESS TOWARDS HIGHER WIND SPEEDS

The bias towards lower line widths for  $t \sim T'/2$  described above gets more pronounced for higher wind speeds. This is caused by the wave steepness increasing along with a higher shear flow that enhances the broadening of the lines. Also the wave period gets higher as wavelengths increase. Several consequences arise; firstly, evaluation at  $T'$  may be prevented by the temperature amplitude of the lines being dispersed too fast, i.e. the lines fading before evaluation. Secondly, as the part of the distribution corresponding

to  $f > 1$  gets broader, this increases the bias towards the more narrow distribution for  $f < 1$ , and the bias is worsened as the stretching of the line width causes a weaker signal until the lines are too weak for evaluation. One therefore might deduce that the bias towards small characteristic line widths at some point becomes so prominent that the apparent shear stress resulting from the analysis starts to decrease.

This is indeed observed. For the 12.5 Hz measurement (figure A.6),  $T' \approx 0.5$  s, and the characteristic line widths should be evaluated before that time in order to avoid only the thinner, less faded parts of the lines remaining. The measurement is therefore evaluated in the range  $t = [0.24 \text{ s}, 0.34 \text{ s}]$ . This, however, represents an evaluation at  $t \sim T'/2$ , and an underlying bias towards too low values is hence expected to be present. The results must therefore be interpreted with caution. For even higher wind speeds, the effect of dominating compressed line widths is enhanced to the point that the characteristic line widths even decrease after heating, see figure A.7 in the appendix for the 20 Hz measurement.

A quantification of the bias requires phase specific considerations, which is complicated by the viscous shear stress being phase dependent, and hence  $\sigma_{\text{theo}}^2(t)$  in equation (7.1) is unknown. An approximation by the simulated curves of  $\sigma^2(t)$  would need a reliable value of  $\tau_{\text{visc}}$ . Moreover, also the values of  $f$  for the collectively evaluated lines are not known (refer to section 7.3). Hence, the bias could not be quantified in this work.

For field applications of the method, this effect is important to keep in mind, since at some high wind speed the determined  $\tau_{\text{visc}}$  will mistakenly be equal to that at lower wind speeds. Ideas towards how this can be handled will be given in section 7.4 below.

#### PHASE DEPENDENT INITIAL LINE WIDTH

Another issue that arises due to the initial wave phase when heating the line  $\varphi_0$  is seen in figure 7.3. As already noted in section 3.5, the phase dependent surface velocity causes different  $\sigma_0^2$  depending on  $\varphi_0$ . For the lines heated at the crest ( $\varphi_0 \approx 0$ ) the distribution is considerably broader and shifted towards higher values than for  $\varphi_0 \approx \pi$ , the latter being more narrow and higher, thus of stronger influence when determining  $\sigma_0^2$ . The distribution of  $\sigma_0^2$  should be independent of the wave phase in order to describe the whole system, this being especially important when considering that the determined  $\bar{\tau}_{\text{visc}}$  represents a phase averaged quantity, and the phase specific  $\tilde{\tau}_{\text{visc}}$  may vary considerably. Furthermore, as seen in the figure, at  $t \sim T'$ , with  $T' \approx 0.37$  s, the distinction between the distributions of  $\varphi_0 \approx \pi$  and  $\varphi_0 \sim 0$  is no longer clear, hence the initially broader lines corresponding to  $\varphi_0 \approx 0$  now contribute considerably to the characteristic  $\sigma^2(t)$ . Hence, recalling figure 6.4 in chapter 6, this then leads to a bias toward too high estimations of the viscous shear stress  $\tau_{\text{visc}}$ .

As explained in section 6.4, based on figure 6.4, for a given value of vertical velocity gradient in the flow ( $\partial_z u$ ), one may neglect the dependence of  $\sigma^2(t) - \sigma_0^2$  on  $\sigma_0$  since the discrepancies are small, and shift the distributions to a characteristic  $\sigma_0^2$  according to equation (6.10). This was done for the individual lines. Subsequently, the distributions of  $\sigma^2(t)$  became more narrowly peaked, see figure 7.4 for the shifted evaluation of the 10 Hz measurement. As can be seen, the wave influenced pattern is still visible, as well as the resulting lower values of  $\tau_{\text{visc}}$ , as expected (compare to figure 7.2 for the unshifted evaluation). The shifting made only minor difference for the outcome of the measurements with lower wind speeds, where  $\sigma_0^2$  was less influenced by  $\varphi_0$ . Notice that the approach of shifting the squared line widths is not valid with respect to the stretching

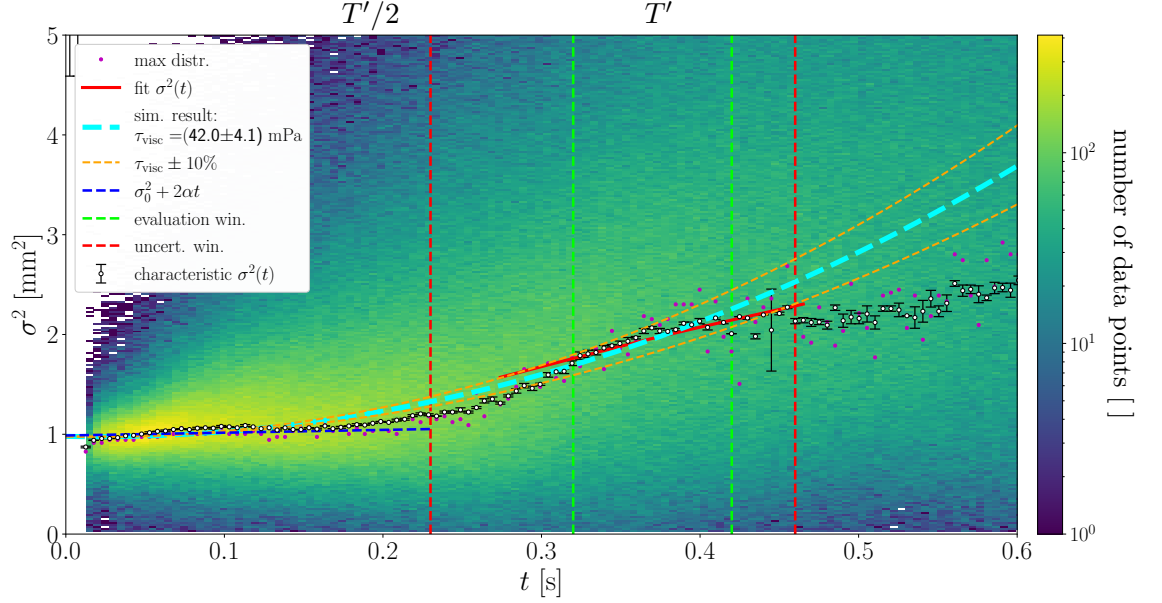


FIG 7.4.: The evaluation of the shifted result from the 10Hz measurement. The squared line widths  $\sigma^2(t)$  were shifted according to equation (6.10). Note the lower resulting value for  $\tau_{\text{visc}}$  compared to the unshifted evaluation seen in figure 7.2, and the more narrow distributions of  $\sigma^2(t)$ . Line widths being smaller than zero after the shift are disregarded in the evaluation.

and compression of the line widths, as it is altering  $f$ . However, for the characteristic line widths with  $f \sim 1$  and sufficiently small shifts, the error introduced is neglectable.

For completeness, both values for  $\tau_{\text{visc}}$  will be stated in the results, see figure 7.7 and table A.2, with the shifted values deemed as the best estimates.

#### SOME INSIGHTS REGARDING THE CHOICE OF INITIAL LINE WIDTH AND HEATING TIMES

Turning to the stationary measurements by Emmel [2017], the situation is different regarding the influence by the waves seen above. Interestingly, the observed influence by the waves in the temporal development in the squared line widths  $\sigma^2(t)$  seen above are not found in the distributions of the measurements from Emmel [2017]. The squared line widths  $\sigma^2(t)$  follows the development as expected from the simulations in a much more rigorous manner, see for example figure 7.5 for the evaluation of the 10 Hz measurement, considerably easing the evaluation as the evaluation time window is much less critical. Thereby also the uncertainties in the values of the viscous shear stress decrease. Further evaluations of the measurements of Emmel [2017] are found in the appendix A.2.3. The shorter heating time of the lines also yields a narrow distribution of  $\sigma_0^2$ , not requiring a shift in the line widths of the individual lines. The distributions are still skew, however, and upon considering the orbital motion of individual lines and the raw images, the presence of waves is confirmed. In the following, a possible explanation of the observed discrepancies with respect to the influence by waves for the different setups will be given.

The main difference between the setups for the measurements of January 2021 and that of Emmel [2017], is the width of the heated lines, being roughly 0.6 mm for Emmel [2017] and 0.9 mm for the laser of January 2021, refer to chapter 4. There is also a

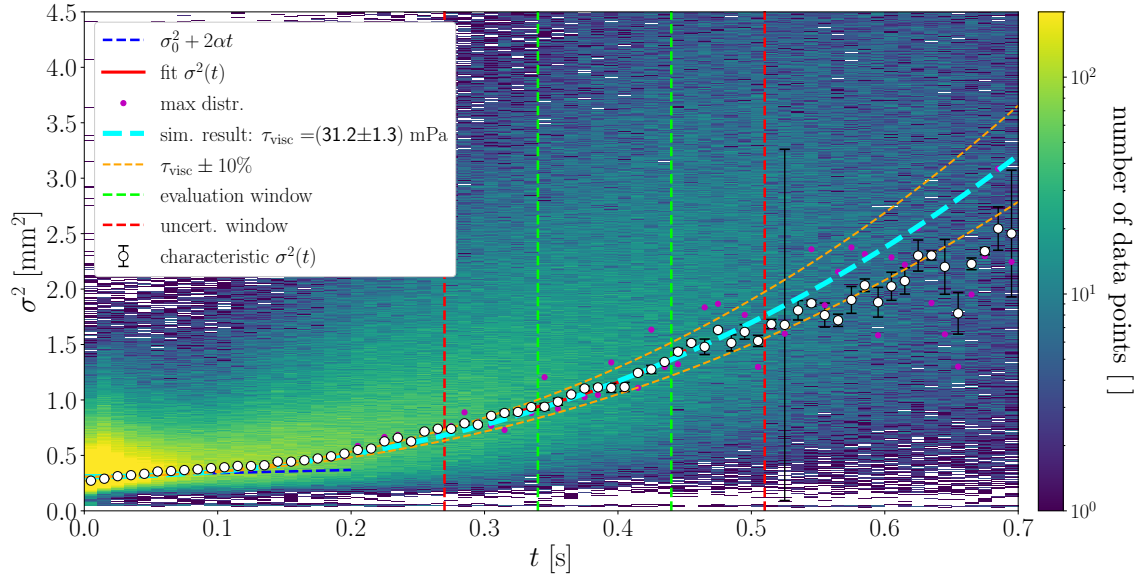


FIG 7.5.: The evaluation of the 10 Hz measurement of Emmel [2017]. The figure is analogous to figure 7.2. As can be seen, the clear pattern in the characteristic squared line widths  $\sigma^2(t)$  (white circles, black edge) seen in figure 7.2, is not seen here. This is most likely caused by the smaller initial line width. Note that the distributions are skewed towards high values of  $\sigma^2(t)$ . The colours depict the number of data points per bin. Surface elevation data are not available.

difference in the penetration depth of the lasers, but this is not expected to alter the behaviour with respect to the observed influence by the waves. Moreover, the line used in Emmel [2017] is longer, but the observed influence by the waves should not be a problem of poor statistics, since a large number of lines are evaluated in both cases.

It is illustrative to simplify the situation. As explained above,  $\sigma_{\text{sim}}^2(t) - \sigma_0^2 \approx h(t; \partial_z u)$  is fulfilled, with  $h$  thereby neglecting the modest dependence on  $\sigma_0$ , where  $\sigma_{\text{sim}}^2(t)$  was labelled in order to emphasize that it is the line width resulting from the model assumptions in chapter 5, ignoring any influence by the waves and phase dependent values of the viscous shear stress. In this simplified situation,  $\sigma_{\text{sim}}^2(t)$  replaces  $\sigma_{\text{theo}}^2(t)$  in equation (7.1). Therefore:

$$f^2 = \frac{\sigma_{\text{meas}}^2(t)}{h(t) + \sigma_0^2}. \quad (7.2)$$

Since  $f$  is a consequence of the flow acting on the fluid parcel, it cannot depend on the heated line. Hence  $f^2$  is unaltered irrespective of initial line width, which for a given value of  $\partial_z u$  also holds for  $h(t)$  under assumptions given above. As can be seen, increasing  $\sigma_0$  means that  $\sigma_{\text{meas}}^2(t)$  must compensate in order to leave  $f^2$  unaltered, hence distributions of the squared line widths are broader for wider lines. This is especially pronounced as long as  $h(t)$  is small, i.e. for short times after heating the line. In other words, observed discrepancies with regard to the patterns seen in the characteristic line widths for the different setups are apparently caused by the system being described by the squared line widths, with similar  $h(t)$  for different  $\sigma_0$ . Due to the line widths being squared, however, the influence is pronounced for wide lines.

In order to illustrate the effect, an example can be given. Refer to figure 3.6 for a

plot of  $f$  for different initial wave phases  $\varphi_0$  for a third order Stokes wave with steepness  $\epsilon = 0.25$ . Moreover, recall that the ratio between  $f_{\max}$  and  $f_{\min}$  must be equal for all  $\varphi_0$ , since this is a property of the fluid parcels. Lines heated in the wave trough, under the influence of *constant* (phase independent)  $\tau_{\text{visc}} = 30$  mPa, would in the first wave period reach a minimum width of  $\sigma^2(T'/2) \approx 0.16$  mm<sup>2</sup> in the case of the line of Emmel [2017], and  $\sigma^2(T'/2) \approx 0.31$  mm<sup>2</sup> for the laser used in January 2021. For the lines heated at the crest, the corresponding numbers are  $\sigma^2(T'/2) \approx 1.48$  mm<sup>2</sup> and  $\sigma^2(T'/2) \approx 2.85$  mm<sup>2</sup>, respectively, so the range of  $\sigma^2(T'/2)$  would be roughly twice as wide only by changing the width of the laser beams from 0.6 mm to 0.9 mm. The same argument holds for the value corresponding to the peak of the distributions of  $f$ , which is assumed to ideally correspond to  $f = 1$  for all  $t$  (refer to section 3.5 for clarity), but found to be slightly deviating, especially at  $t = T'/2$ . This deviation of  $f \neq 1$  propagates to  $\sigma^2$ , and is amplified by larger  $\sigma_0$ . This is likely explaining why the observed patterns in the characteristic squared line widths found above are pronounced in the measurement of January 2021, but not in those by Emmel [2017]. For future applications of the method, if the viscous shear stress is the interesting quantity, it is therefore recommended to keep the laser line as thin as feasible. If the wave induced dynamics and alteration of fluid parcel extents within the boundary layer is the main focus, a larger initial line width is preferable.

In order to achieve a distribution of the initial line widths as thin and phase independent as possible, the heating time  $t_{\text{laser on}}$  of the lines should be kept as low as possible. A measurement by Emmel [2017] with  $t_{\text{laser on}} = 5$  ms for the 10 Hz measurement was reanalysed. For the other measurements that were reanalysed, the heating time was  $t_{\text{laser on}} = 10$  ms. As seen in figure 7.6, showing the 5 ms measurement, the distributions of  $\sigma^2(t)$  end abruptly; below half a second after heating, most lines are no longer evaluable. This is caused by the heating time yielding weaker (i.e. lower temperature amplitude) lines. Therefore, while short heating times are advantageous, the laser must also possess enough power. The main issue arising is that this is prone to causing a bias towards smaller line widths, since the broader lines may fade before the lines are evaluated. The result is lower for the measurement with the short heating time compared to the equivalent measurement with  $t_{\text{laser on}} = 10$  ms;  $\tau_{\text{visc}} = (28.2 \pm 1.3)$  mPa and  $\tau_{\text{visc}} = (31.2 \pm 1.3)$  mPa, respectively. Though not significantly deviating, the issue is expected to be of higher importance with increasing wind speeds, as the viscous shear stress increases and varies considerably with the wave phase.

### 7.1.2

#### RESULTS FOR THE VISCOUS SHEAR STRESS

The results for the viscous shear stress  $\tau_{\text{visc}}$  for the long time interval evaluations collectively considering a large number of lines, are discussed in this section. The values are provided in table A.2 in the appendix, and shown in figure 7.7 in dependence on wind reference frequency. Note that results with a white marker colour in the middle indicate values subject to a bias, and cannot be trusted. An equivalent figure, but in dependence of the estimated values of reference wind speed in 10 m height,  $u_{10}$ , can be found in the appendix, figure A.2. In the following, the best estimate for  $\tau_{\text{visc}}$  will be discussed, corresponding to the evaluations with the individual line widths shifted according to equation (6.10) (also refer to section 7.1.1 above).

As mentioned earlier in chapter 4, the measurement conditions in the measurements of January 2021 and the reanalysed measurements of Emmel [2017] are different.



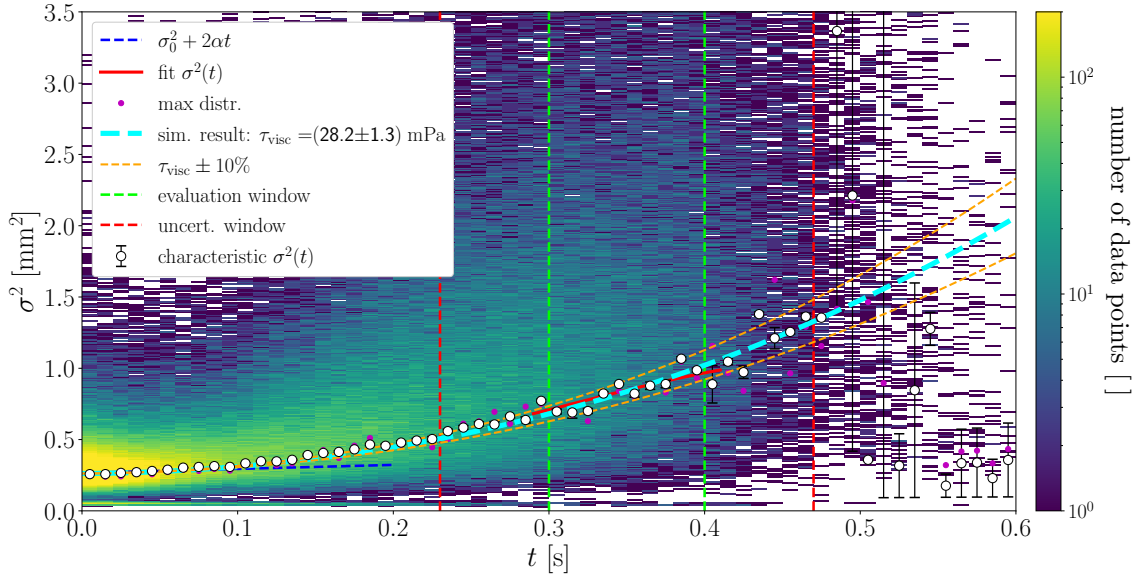


FIG 7.6.: The evaluation of the 10 Hz (wind reference) measurement of Emmel [2017] with heating time of the lines of 5 ms, in contrast to 10 ms in figure 7.5. The abrupt end of the distributions at  $t \sim 0.5$ s, is caused by the fading of the lines. There is likely a bias toward too low values of  $\tau_{\text{visc}}$  present due to the broader lines fading before evaluation, and this shows the possible issue associated with low heating times.

The results for January 2021 are evaluated in the time interval  $t_m \in [600\text{s}, 1200\text{s}]$  after turning the wind on, with the 10 Hz measurement being longer than the other measurements and also evaluated in the interval  $t_m \in [2160\text{s}, 2760\text{s}]$  after turning the wind on. In the case of Emmel [2017], at least 120 minutes had passed before conducting the measurement, corresponding to stationary conditions.

Interestingly, as seen in figure 7.7, the 5 Hz and 6.3 Hz measurements of January 2021 and Emmel [2017] do not deviate significantly, neither does the 7.9 Hz measurement of Emmel [2017] when compared to the 7.5 Hz measurement. This indicates the viscous shear stress had reached the proximity of its asymptotic values within 20 minutes after turning the wind on. It must be noted that the data basis consists of few measurements, hence robust conclusions are not possible. The reference measurement method, particle streak velocimetry (PSV), showed no significant deviations ( $< 1$  standard deviation) for the stationary 5 Hz and 7.5 Hz measurements.

The result of the 10 Hz measurement shows a large spread of the values for  $\tau_{\text{visc}}$ . It must be mentioned that when excluding the result for the  $t_{\text{laser on}} = 5$  ms measurement by Emmel [2017] due to the possible bias towards small line widths, as argued in section 7.1.1 above, however, none of the data points are significantly deviating (i.e.  $> 3$  standard deviations) from each other. This is mainly caused by the large uncertainty in the results of January 2021, caused by the observed patterns in the characteristic  $\sigma^2(t)$ , and reflecting the uncertainty in the value for  $\tau_{\text{visc}}$ . For the 10 Hz measurement of January 2021, the discrepancies in characteristic  $\sigma^2(t)$  between the  $[600\text{s}, 1200\text{s}]$ - and  $[2160\text{s}, 2760\text{s}]$ -intervals, however, are significant. Due to the different setup, such a comparison cannot be done for the measurement of Emmel [2017].

The results for the viscous shear stress for the  $[600\text{s}, 1200\text{s}]$  interval for the 10 Hz

measurement is  $\tau_{\text{visc}} = (42.0 \pm 4.1)$  mPa, whereas the evaluation for the [2160 s, 2760 s] interval yielded  $\tau_{\text{visc}} = (34.7 \pm 4.2)$  mPa. Moreover, the result of the stationary measurements are  $\tau_{\text{visc}} = (31.2 \pm 1.3)$  mPa for the measurement of Emmel [2017], and for the PSV-method (January 2019)  $\tau_{\text{visc}} = (35.0 \pm 1.6)$  mPa. The difference between the stationary results might be explained by the spatial coverage of the heated line of the measurement by Emmel [2017] being larger than the laser sheet used for the PSV measurement, as the wind velocities are expected to vary up to about 20% (Bopp [2014]) in the measurement section, which is likely to cause spatially differing values in the determined viscous shear stress. Further details will be given below.

Hence, this indicates decreasing values of the viscous shear stress with increasing time after turning the wind on, occurring after the initial large changes in the wave field associated with short times after turning the wind on, see section 7.2 below. This could be caused by further restructuring of the wave field. For the 10 Hz measurement of January 2021, the initial water velocity  $u_{s0} = (3.8 \pm 0.2)$  cm/s was close to the bulk velocity in stationary conditions  $u_b = (4.221 \pm 0.009)$  cm/s (Schwenk [2019]). Moreover, similar changes for times after the initial build-up of the wave field have been observed for the total momentum transfer in global momentum balance measurements (Schwenk [2019]). Interestingly, almost no difference in surface velocity was found:  $u_s = (12.3 \pm 0.8)$  cm/s for the first interval and  $u_s = (12.1 \pm 0.5)$  cm/s for the later interval of January 2021, compared to  $u_s = (12.3 \pm 0.4)$  cm/s (measurement of Emmel [2017]) and  $u_s = (11.7 \pm 0.1)$  cm/s (PSV). The corresponding bulk velocities are not known, but as mentioned above, the initial water velocities were close to the bulk velocities found in similar measurement conditions. This would correspond to a thinner boundary layer thickness for shorter times after turning the wind on. Note, however, that since this discussion is based on only one non-stationary measurement, the results must be interpreted with care.

The results for the 12.5 Hz and 15 Hz measurement are also given for completeness in figure 7.7, with a white marker centre. As mentioned, this is done for indicating that the values cannot be trusted. The reason for the bias is in both cases the evaluation for times considerably smaller than a wave period  $T'$ , refer to section 7.1.1.

In figure 7.7 also the results for  $\tau_{\text{visc}}$  measured in stationary conditions without waves are shown. Hereby the waves were suppressed with the surfactant Triton X-100, refer to Voigt [2019] for further details. As can be seen, the values are similar compared to  $\tau_{\text{visc}}$  measured in the presence of waves, with no clear differences to be found, except for the 7.5 Hz measurement, whose value for  $\tau_{\text{visc}}$  is lower. The latter deviation is non-significant when compared to the stationary PSV-evaluation, and significant with respect to the 7.9 Hz measurement of Emmel [2017]. Since the uncertainties are small, however, the latter significant deviation is likely caused by the differing wind speed. The implication of the values of  $\tau_{\text{visc}}$  being similar, will be further discussed in section 7.4.3.

Since the method is novel and few other methods for determining  $\tau_{\text{visc}}$  are developed, no further verification of values of  $\tau_{\text{visc}}$  the beyond the reference measurement evaluated in this work could be obtained. Measurements of the air-sided  $\tau_{\text{visc}}$  from PSV are available in Bopp [2018], a direct comparison is prevented, however, by the shorter fetch of 28 m used, yielding different measurement conditions, and the lack of comparable wind reference values. The values are of the same order, however. The results from momentum balance methods, e.g. Schwenk [2019], cannot separate the viscous shear stress from the total momentum transfer and are hence not comparable, besides yielding global measurements in contrast to the localized measurements of this work.

Lastly, as explained in section 6.4, a correction of the line widths for the measurements of January 2021 according to the surface inclination and camera mounting angle, see equation (6.4), was performed. The correction was not found to make a considerable difference in the determined values for the viscous shear stress for any of the measurements, with no systematic influence or changes above the order of a few percent. This can be attributed to the surface inclination mostly being small, the uncertainty of  $\tau_{\text{visc}}$  being dominated by the uncertainty relating to the stretching and compression of the line widths and the water elevation measurement being confined to a thin sheet, hence not representing the whole spatial extent covered by the heated lines.

#### RADIAL VARIATIONS IN THE VISCOUS SHEAR STRESS

The long line of Emmel [2017] also allows for a sequential evaluation, i.e. the spatial variation in  $\tau_{\text{visc}}$  with respect to radial position  $y$ , pointing towards the channel centre (refer to figure 4.3 for a sketch of the setup and coordinate system). The result of evaluating the viscous shear stress for pieces of 50 mm can be found in the appendix A.3. As can be seen, the variation is found to be mostly below 15 %. As the uncertainties are large compared to the variation, care must be taken by interpreting the patterns seen, but the results mostly seem to be in accordance with  $< 20\%$  for the considered part of the channel. The mean (radially averaged) values of  $\tau_{\text{visc}}$  do not deviate significantly from those obtained by evaluating the whole lines.

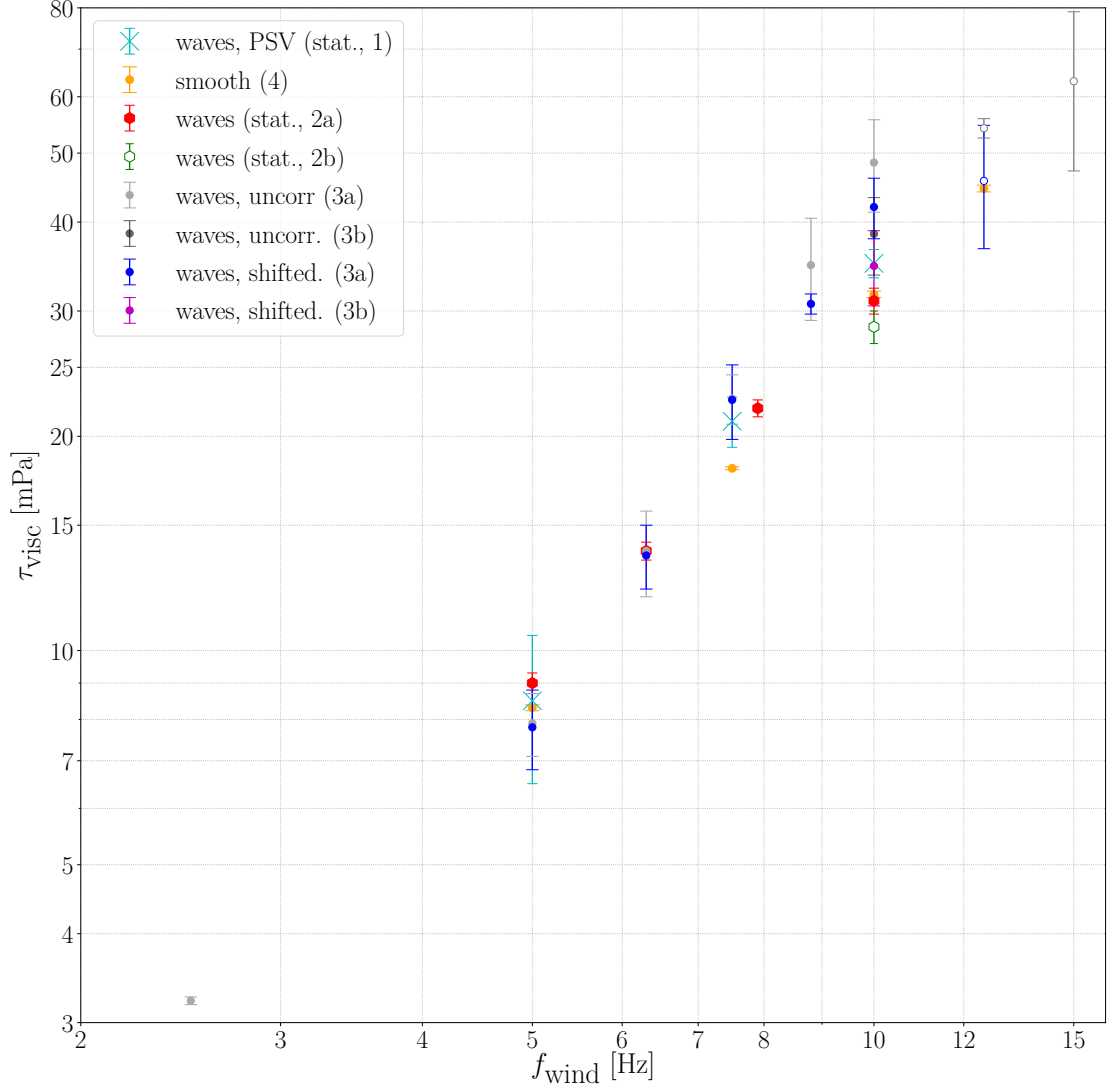


FIG 7.7.: All results for the long time interval evaluation of the viscous shear stress  $\tau_{\text{visc}}$ , in dependence of wind generator frequency  $f_{\text{wind}}$ . An equivalent plot in dependence of  $u_{10}$  can be found in the appendix A.2. Included are the PSV-results (cyan crosses) of the stationary measurement of January 2019 (label 1), and the results for stationary, wave-less (smooth, label 4) surface from Voigt [2019] (orange dots). The red hexagons mark the results of the stationary measurement of Emmel [2017] (label 2a) with a heating time of 10 ms, and the green hexagon the measurement with a heating time of 5 ms (2b). The remaining data points are from the measurement of January 2021. Shown are the evaluation in the time interval [600 s, 1200 s] (label 3a) and [2160 s, 2760 s] (label 3b) after turning the wind on. The best estimates of  $\tau_{\text{visc}}$  are based on the shifted evaluation of the line widths (magenta and blue markers refer to section 7.1.1 and equation (6.10)). Also shown is the evaluation of  $\tau_{\text{visc}}$  for the uncorrected line widths (gray, translucent black dots). Markers with a white centre are subject to a bias, and should not be trusted. Also note the (uncorrected) result for the 2.5 Hz measurement.

## 7.2

### SHORT TIME INTERVALS AND NON-STATIONARY CONDITIONS

One of the main advantages of the measurement method is the feasibility of high temporal resolution on the order of seconds. The temporal resolution is, if spatial sampling of the wave field is experimentally realised, only limited by the time needed for the lines to broaden. Hence, valuable insights into how the viscous shear stress develops and changes in non-stationary measurement settings may be achieved. Also in field conditions, where wind speeds may change within short times, this is a large advantage. An initial look into this can be provided by the measurements in January 2021, since these were conducted while turning the wind on, thereby capturing the first minutes after the change from a resting air compartment. The evaluation of five second intervals were chosen as a trade-off between sampling the wave phases and wave field as much as possible and loosing the possibility to capture rapid changes. For reference, initial heating frequencies were 2 Hz, with the exception of a heating frequency of 1 Hz for the  $f_{\text{wind}} = 5$  Hz measurement. Capturing the onset of the wind poses difficulties regarding overlap of the lines, as the surface velocity is initially low, before both velocity and shear stress rises rapidly and ideally the heating frequency should be increased accordingly for better statistics. A slight initial water velocity therefore eases this issue as it allows for a higher initial heating frequency, but should be kept in mind especially when considering the surface velocities and also the possible influence on the viscous shear.

The non-stationary evaluations were conducted for the measurements with wind generator frequency between 5 Hz and 10 Hz. If the figures are not presented in this chapter, they can be found in the appendix A.5. Beyond this wind speed, the number of data points in the 5 s intervals did not suffice for a stable evaluation, in addition to the changes taking place on shorter time scales. Furthermore, based on this set of measurements, without repeated measurements, robust conclusions are excluded, but some tendencies are found.

In all measurements a fast increase in surface velocity was found, with both a increased acceleration and shorter times before reaching the first maximum surface velocity for higher wind speeds, e.g.  $\sim 20$  s for the 10 Hz measurement and  $\sim 65$  s for the 5 Hz. After turning the wind on, the flow is first largely laminar, with mostly uniform flow velocities. The surface velocity increases, and reaches a maximum that represents an overshoot, as also found for a smooth surface in Voigt [2019]. The flow remains in this overshoot-regime for longer durations for lower wind velocities. This is also associated with an overshoot in  $\tau_{\text{visc}}$  for the 6.3 Hz and 5 Hz measurement, with  $\geq 50\%$  increased values. The overshoot is then relieved, possibly upon exceeding a critical Reynolds number, by a change of flow regime, associated with the break up of a mostly uniform flow pattern into more irregular patterns and velocity differences. Typically, also waves start to form. This regimes further develops by the patterns also including smaller structures, which then persists for higher times, and waves growing. At some point the waves stop growing and surface velocities level out to a temporally more steady value. This marks the end of the overshoot regime. The findings of the regimes are qualitatively similar to those in Klein [2019], who studies the fetch dependence on gas and heat exchange. Kunz and Jähne [2018] investigated short fetches and the effect on heat transfer velocities, and reached similar findings indicating an overshoot for small fetches. Note that the results of this work, given as a function of time after turning the wind on, are not directly transferable to conditions for different fetch lengths, since it is not clear which characteristic quantity should be used as reference.

Figures 7.8 and 7.9 exemplify the change of regimes for the 10 Hz measurement. The blue and red vertical lines in figure 7.9 mark the four times shown in figure 7.8. The patterns seen on the surface are caused by the air in the wind-wave facility still being dry, as it was the first measurement, causing evaporation and hence a cooling of the surface. When turning the wind on, the explained changes in the flow field, probably associated with the increased shear stress and subsequent thinning of the boundary layer, in combination with increased mixing by surface renewal events of warmer bulk water and possibly the onset of turbulence in lower fluid layers, causes this clearly colder surface to subside with time. Hence the surface appears more homogeneous in the image at  $t = 120.5$  s, and further changes in the flow field are not visible beyond this time.

Regarding the viscous shear stress, the measurements are not conclusive for the overshoot-regime. The lower wind speeds clearly show an overshoot, as mentioned, while those at higher wind speeds do not show this, especially the 7.5 Hz and 8.8 Hz measurement. The 10 Hz measurement is more unclear in this regard, refer to figure 7.9. The first steep increase in  $\tau_{\text{visc}}$  for the first  $\sim 30$  s after turning the wind on is seen in all cases, associated with regular (laminar) flow fields without much influence by waves, simplifying the evaluation with the thermographic approach. This then suddenly changes, often with a marked drop in the values of  $\tau_{\text{visc}}$  and large uncertainties, the latter indicative of scattering characteristic line widths. A look at the individual lines shows that this is mainly caused by insufficient statistics with broad distributions and the lines being strongly influenced by the flow, making evaluation more difficult. Most likely this is caused by a strong influence by the first short capillary-gravity waves, initiating the growth of the waves (Phillips [1957]). Large amplitude capillary waves are known to be capable of strongly modifying the boundary layers (Witting [1971]), which is consistent with the broad distributions of line widths observed. Moreover, for the 10 Hz measurement, the time  $t^*$  passing before the number of data points of the unsorted data set were halved (refer to section 6.4), was lower in the overshoot-regime than later on. This is indicative of a high shear stress as it leads to a faster fading of the lines, see section 7.4 for further discussion. For the measurements at lower wind speed  $t^*$  was longer, such that random events caused by the flow had a larger influence, yielding scattering values, and in combination with the fact that the heated lines are followed for a limited time only, a bias towards lower  $t^*$  was found. Hence  $t^*$  is deemed not meaningful in these cases.

Lastly, a non-stationary 10 Hz measurement was available from the measurements by Emmel [2017], see figure A.21, with the difference that the wind was first turned on at 15 Hz for 5 s for a faster build-up of the wind field. Also the initial water velocity was close to zero. The statistics due to the longer line is better, and an overshoot in  $\tau_{\text{visc}}$  is seen. Interestingly, the values for  $\tau_{\text{visc}}$  are considerably lower than seen in the corresponding measurement of January 2021, seemingly levelling out at  $\tau_{\text{visc}} = (26.3 \pm 3.4)$  mPa, which is lower than the result of the stationary measurement conducted with the same setup. Also in conditions without waves in Voigt [2019], the values for  $\tau_{\text{visc}}$  for the non-stationary measurement was higher, hence the discrepancies are most likely not caused by the presence of surfactants. The water velocities from the non-stationary measurement by Emmel [2017] are more consistent with the 7.5 Hz measurement of January 2021, which was also conducted with a initial water surface velocity close to zero. It is not known what causes these large differences for the seemingly same measurement conditions. Since no water elevation measurement is available for the measurements of Emmel [2017], a comparison of the wave fields is not possible. More measurements are required in order to verify if such large discrepancies are frequent, or have other causes.

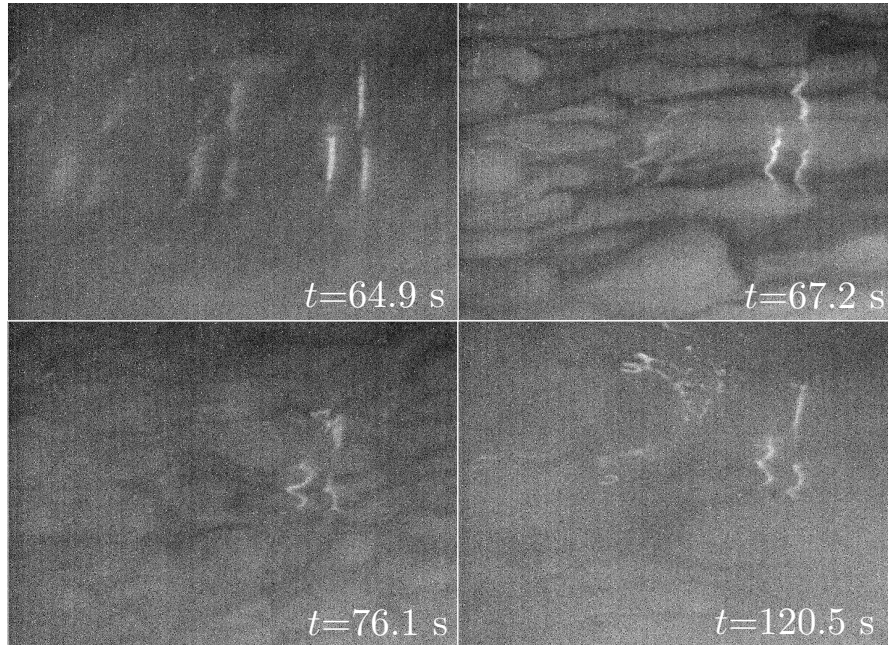


FIG 7.8.: The change of the flow field for short times after turning the wind on at  $t = 39$  s. The shown times are indicated in figure 7.9. The wind direction is from right to left. The air humidity was low, causing cooling of the surface by evaporation, hence structures arising with changes in the flow can be seen as warmer bulk water increasingly influences the upper layer. The colour scale is equal in all images, with bright colours indicating higher temperatures. Upper left: the flow field at the water surface is still largely laminar, with high velocities, before larger patches of higher temperatures arise (upper right) with the onset of horizontal flow velocity gradients. The mean velocities tend to decrease, and waves start to form. These structures further break up (bottom left), now also including smaller scales. For longer times (bottom right), these structures remain, which is not clearly seen since the temperature in the boundary layer is now fairly homogeneous, waves get larger and the mean velocity tends to level out. Note the bright structure in the upper middle part of the image, which is a reflex from the laser casing of the surface elevation measurement. The time since heating the lines is not equal in the images.

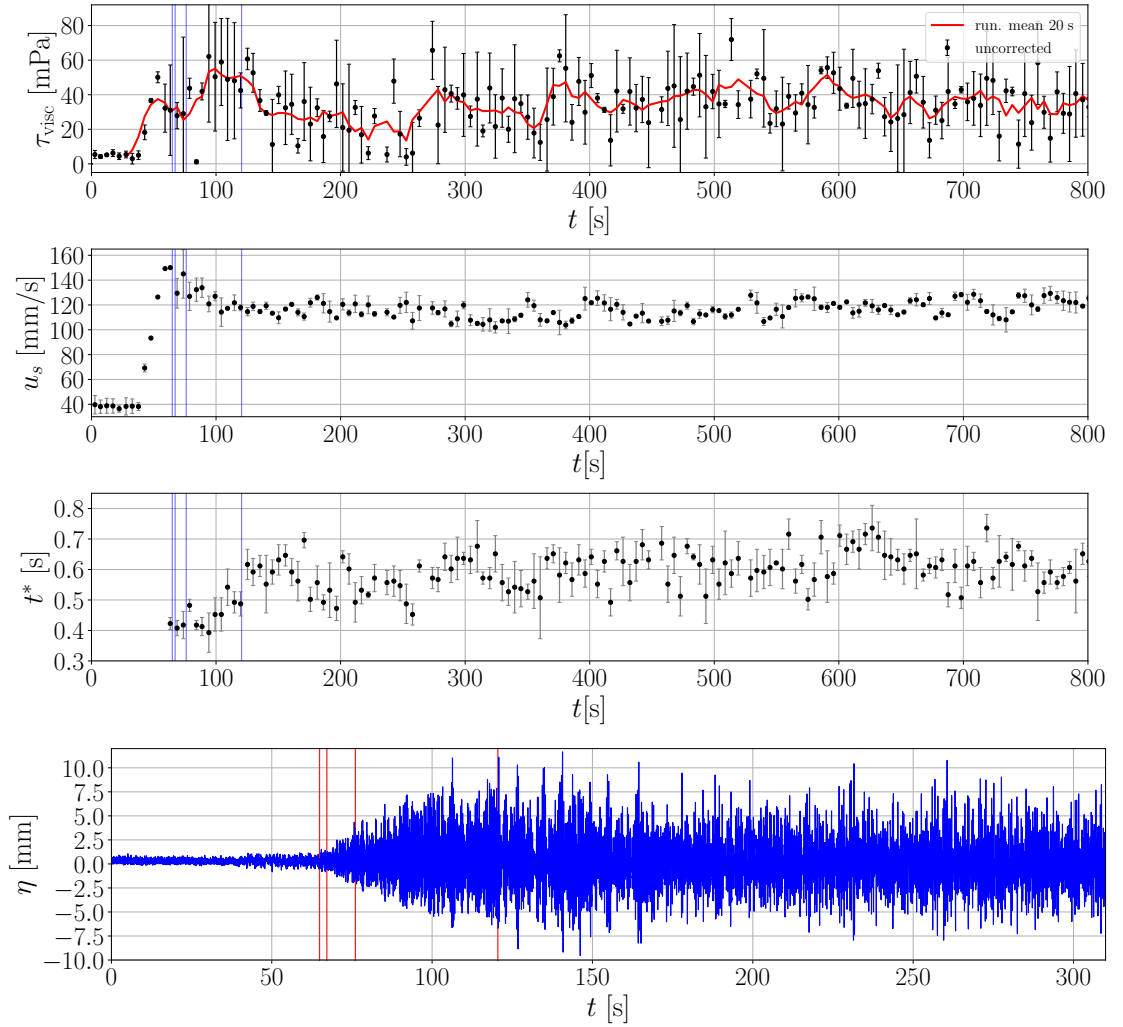


FIG 7.9.: The non-stationary result for 5 s intervals for the 10 Hz measurement of January 2021. The line widths were not corrected for surface compression and dilation, refer to section 7.3 for details. The abscissa shows time since starting the measurement in all plots, note a smaller temporal range in the lowest plot. The topmost plot shows the viscous shear stress  $\tau_{\text{visc}}$  along with a running mean of 20 s (red curve), the second plot from the top the mean surface velocity  $u_s$  and the second lowest plot the characteristic life time  $t^*$  of the lines. The lowest plot shows the surface elevation  $\eta$  in the middle of the laser sheet. The blue (upper 3 plots) and the red (lower plot) vertical lines indicate the times shown in figure 7.8. Note the overshoot in the surface velocity, and the lower values of  $t^*$  seen for short times after turning the wind on ( $t = 39$  s). The latter is associated with an increased  $\tau_{\text{visc}}$ , which is, however, not seen with certainty.



$f_{\text{wind}}$ [Hz]	$\tau_{\text{visc}}$ [mPa] (long time interval)	$\tau_{\text{visc}}$ [mPa] (5 s, mean $\pm$ std. dev.)
5.0	9.0 $\pm$ 0.3	8.7 $\pm$ 1.1
6.3	13.8 $\pm$ 0.4	12.9 $\pm$ 1.7
7.9	21.9 $\pm$ 0.3	21.1 $\pm$ 3.7
10.0	31.2 $\pm$ 1.3	33 $\pm$ 8

TABLE 7.1.: The table shows the values of the viscous shear stress  $\tau_{\text{visc}}$  evaluated for the stationary measurements of Emmel [2017] for four wind speeds with reference wind frequency  $f_{\text{wind}}$ , by collective evaluation of all lines ( $\sim 300$  s) (middle column) and evaluation of 5 s intervals (right column). The results for the 5 s intervals were averaged and the standard deviation computed, given as mean  $\pm$  standard deviation. As seen, the averaged values of the 5 s intervals deviate by less than 10%.

Based on the above indications, it is likely that the overshoot in  $\tau_{\text{visc}}$  is also present for higher wind speeds, and not seen in the evaluated values due to technical reasons regarding the setup. This must be verified in future studies, and cannot be stated with certainty.

A relatively large scattering of the results of  $\tau_{\text{visc}}$  for the evaluation of the 5 s intervals are found. This may have several causes. First and foremost, because the flow- and wave field is irregular, which besides causing fluctuations by itself, also is expected to lead to amplitude related differences in the phase dependent viscous shear stress (Bopp [2018]), with lower amplitudes being associated with less difference between the phases. Moreover, since relatively few lines are considered due to the short time intervals, only a smaller part of the wave field is sampled. Hence some scattering caused by the random timing of the heating of the lines is expected, which would be an artefact of the measurement technique and setup. This is especially true if the phase sampling is inadequate, which could happen if the heating frequency is similar to the wave frequency, leading to phase selective sampling. The mean values determined for the viscous shear stress by these shorter 5 s intervals for the part of the measurements corresponding to the long interval evaluations, are comparable to those found for the longer time intervals evaluation. This is found in the case of the stationary measurements of Emmel [2017] as well as for the measurements of January 2021, indicating that the approach is valid. Due to the small uncertainties of  $\tau_{\text{visc}}$  for the long time interval evaluation for the reanalysis of the stationary measurements of Emmel [2017], these results are given in comparison to the 5 s intervals in table 7.1.

It must be emphasized that several of the measurements were started with the initial water velocity  $u_{s0}$  being non-zero, including the 10 Hz measurement in figure 7.9 as stated in section 7.1.2, where it was about 90% of the bulk velocity's asymptotic value. This can be seen in the respective plots for the non-stationary evaluations, along with being stated in table A.1. The initial velocity could possibly influence the viscous shear. No conclusions regarding these changes can be made based on the available measurements, but these initial results show that the thermographic method could be used to study this dependence due to the temporal resolution in future measurements.

## 7.3

### SURFACE COMPRESSION AND DILATION

As already seen, the waves have an impact on the line widths. Several limitations follow, especially concerning phase resolved measurements of  $\tau_{\text{visc}}$ . Starting by considering individual lines, see figure 7.10 for examples from the 10 Hz measurement, one clearly sees the impact of the compression and stretching of the fluid parcels. This gives a possibility to verify the expression  $f$  (see equation 3.16). Also recall equation (7.1), where it was found that the observed line width  $\sigma_{\text{meas}}$  compared to the theoretical  $\sigma_{\text{theo}}$  is described by  $f$ . In the following analysis, since  $\sigma_{\text{theo}}$  is not known, it is approximated and fitted by a second order polynomial  $p_2(t)$ . A second order polynomial was found to approximately describe the simulated development of  $\sigma_{\text{sim}}^2(t)$  (Voigt [2019]). Note that this is not strictly applicable, as  $\tau_{\text{visc}}$  is not constant as a function of wave phase, refer to section 7.5 below, but used as a first approach. Hence  $f^2 \cdot p_2(t)$  was fitted to the squared mean line widths (red dots in figure 7.10), refer to section 6.4 for further details. As can be seen in the figure,  $f$  is in some cases describing the observed surface dynamics well, even to the point that the extrapolated curves fit well. While this indeed often holds, small scale events can have a large impact, causing the simple model to fail to describe the surface compression and dilation. Note that this implies that the fluid parcels are distorted in a way that a laminar flow field is induced in the interior, such that the temperature profile is “unmixed” upon returning to the same wave phase after a period. This is as expected for the viscous boundary layer and the small spatial scales of the fluid parcels encompassing the heated lines.

Equation (3.16) refers to fluid parcel velocity and phase speed, both in reality complicated due to superposition of the waves. As seen in figure 6.8, the estimated values for the phase speed vary, also on short time scales. Furthermore, non-linear phenomena associated with steeper waves, such as breaking waves, are not described by the equation, and it is also found experimentally to underestimate the compression and dilation for larger and steeper waves. This could partly be due to the horizontal velocities found by numerical derivation of the interpolated line position  $x(t)$  to be artificially dampened, or simply non-linear effects influencing the stretching and compression in a way not described by equation (3.16). Furthermore, capillary waves are known to distort the boundary layer considerably (Witting [1971]), but make almost no deflection in  $x(t)$ , hence being more or less unconsidered when applying equation (3.16). Since their frequency is higher than that of gravity waves, their contribution is prone to overlay the stretching and compression of the gravity waves, thus being of less importance when considering more lines at once.

Another issue is that the slope of the interpolation of  $x(t)$  is to some degree unreliable at the endpoints, notably at the time of heating the line, therefore the initial velocity is error prone. Lastly note that the surface elevation measurement was conducted at one  $y$ -position only (i.e. position radial to the channel, figure 4.3), whereas the lines are extended in this direction. This means that due to inhomogeneities in the wave field, the parameters at the line where the surface measurement was not available, are likely different (Rennebaum [2017]). Based on this, a correction (i.e. by  $\sigma_{\text{corr}}(t) = \sigma_{\text{meas}}^2(t)/f(t)^2$ , refer to equation (7.1)) of the line widths with respect to the compression and stretching, based on the short individual lines of January 2021, is deemed too uncertain to yield meaningful results due to the limited applicability of equation (3.16). It would, however, if managed in future work, improve the evaluation of the viscous shear stress, especially in the temporally resolved measurements, where individual events may

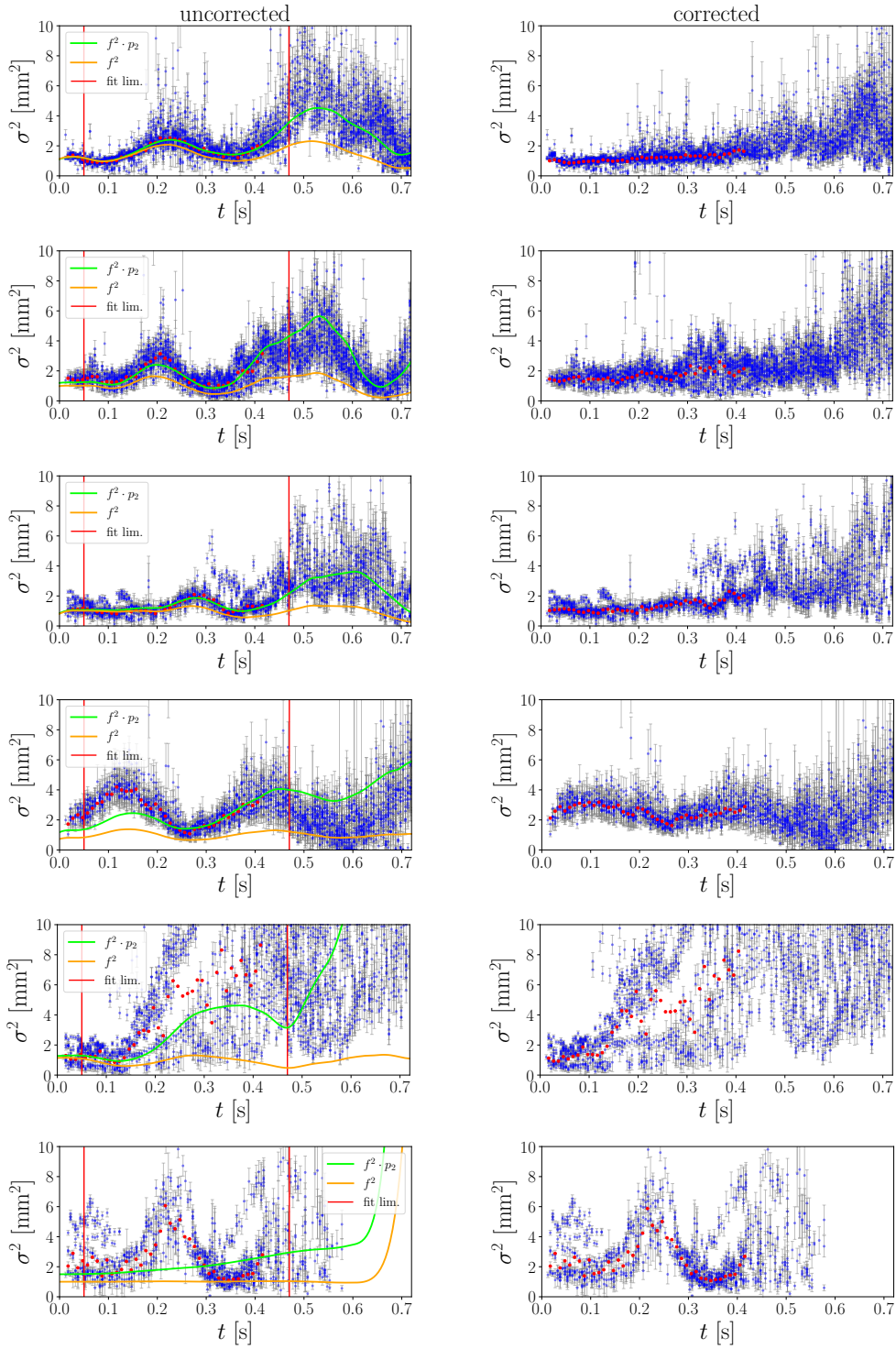


FIG 7.10.: Shown are uncorrected (left) and the corrected (right) squared line widths of individual lines. They are corrected for compression and stretching of the line widths, described by  $f^2$  (orange curve, see equation (3.16)). The upper three rows of plots show the correction of a set of three lines heated at the same time, for which a fit between the red lines of  $f^2 \cdot p_2(t)$  (lime curve) yields a good description, whereas the fit is poor for the three lower rows. The second order polynomial  $p_2(t)$  approximates the diffusive broadening of  $\sigma^2(t)$ . The lime curve is extrapolated beyond the fit range. The lowest row shows a stretching event where  $f \approx 1$ , hence the orbital motion was too modest for detection. The second lowest row shows a small scale event strongly influencing a part of the line.

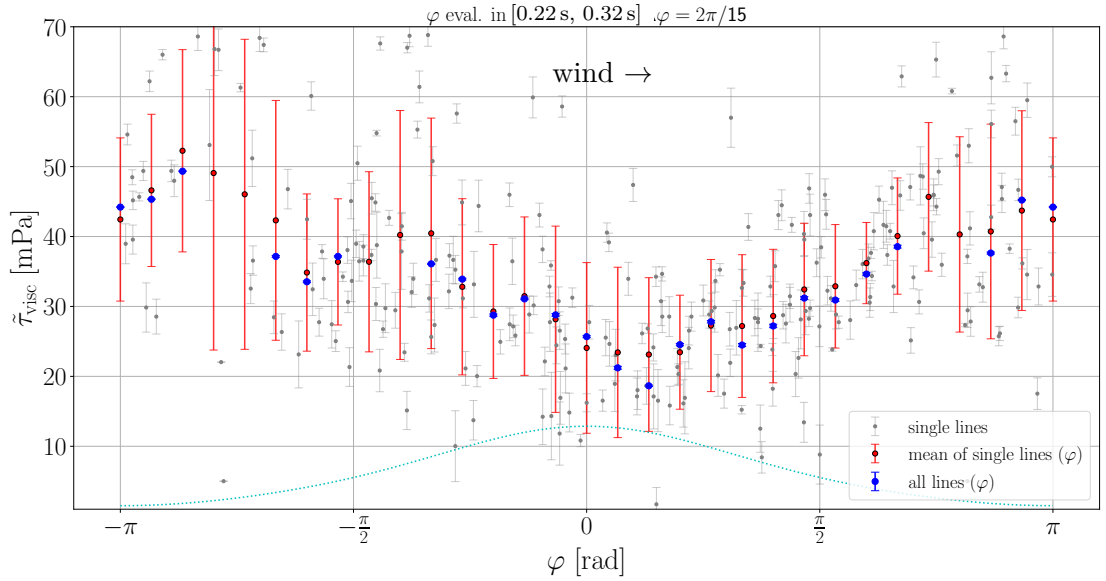


FIG 7.11.: The figure shows the evaluation of individual lines of the 10 Hz measurement (gray dots), their phase dependent mean (red dots, errorbar: standard deviation) and the collective phase dependent evaluation (blue points). The wave phase  $\varphi$  was estimated by a Hilbert transform of the horizontal orbital motion of the heated lines, and was evaluated in the same time interval ([0.22 s, 0.32 s] after heating the lines) as the (phase dependent) viscous shear stress  $\tilde{\tau}_{\text{visc}}$ . The cyan dotted line shows a third order Stokes wave with arbitrary wave height and steepness for illustration, and the wind direction is from left to right. Note the low values of  $\tau_{\text{visc}}$  at the crest and high values in the trough, opposite of what is expected, compare to the PSV measurements, figure 7.16.

have a larger impact due to few lines being collectively evaluated.

For illustration, a figure for the collectively evaluated, individually corrected lines for the 10 Hz measurement can be found in the appendix, see figure A.8. This figure is exemplary for most corrected results. As can be seen, the correction tends to over-correct the line widths for  $t \approx T'/2$ , effectively straightening out the temporal development of the heated lines to become nearly linear. This is most likely caused by equation (3.16) better describing the compression of the lines, again caused by the more narrow distribution of  $f < 1$  as explained in section 7.1, thereby introducing a bias towards poorly corrected large (stretched) line widths. This is also the case for  $t \sim T'$ , though corrections are smaller, as expected, therefore the determined values for  $\tau_{\text{visc}}$  do not change much.

Another option is to correct all lines with the same initial wave phase, by using a collectively evaluated velocity. This has a main disadvantage, however, as all lines are weighed equally for the mean velocity, yielding relatively small deviations from the mean velocity, whereas the line widths are considered squared, hence under- and over corrections do not cancel. This is especially problematic for  $\varphi_0 = 0$ , where the widths of the distributions of  $\sigma^2(t)$  are largest.

It is not clear whether the correction of longer lines - thus less influenced by small scale fluctuations - would perform better, as no surface elevation data is available in the measurements of Emmel [2017]. However, due to the long line and therefore a

large amount of data points, it might be tempting to evaluate also single lines in order to improve the temporal resolution. This is problematic, since the line widths are systematically compressed at the wave crest and stretched in the trough, thereby strongly influencing the determined viscous shear stress  $\tau_{\text{visc}}$ . This is especially an issue when the wave period is on the order of the time that passes before evaluating the heated lines. Hence, a systematic error occurs, see figure 7.11 for an example for the 10 Hz measurement. The wind direction is towards the right. The wave phase was estimated by a Hilbert transform (see equation (B.12)) of the observed horizontal velocity. Depicted is the wave phase at the time of evaluating the line. As can be seen, the determined (wave phase dependent)  $\tilde{\tau}_{\text{visc}}$ , both when collectively evaluating all lines with the same phase, and when considering single lines, is clearly lower at the crest than at the trough, which is contrary to the expected distribution (see section 7.5 below and Bopp [2018]). The slight phase shift is caused by the mounting angle of the camera, yielding a maximal observed velocity on the leeward side of the wave (see figure 4.3 for the setup), and that the heated line is influenced by the (phase dependent) shear stress also for the phases before the evaluation. Thereby it becomes clear that evaluating single lines underlies a strong influence by the wave phase at the time of evaluation. Hence, it is important to sample the wave phases as evenly as possible and to evaluate those lines collectively.

## 7.4

### ADDITIONAL OBSERVATIONS

#### 7.4.1

##### CHARACTERISTIC LIFE TIME OF THE HEATED LINES

A few other observations were made during the evaluation of the measurements. First, as already implicated, for the measurement of January 2021 the characteristic time scale or life time  $t^*$  of the heated lines was calculated by determining the time at which the number of all data points (line widths) reached half of the maximal number, refer to section 6.4 for further details. This time scale will be system, evaluation and setup dependent, since it reflects the detection and evaluation limits of the heated lines. The computation of  $t^*$  was found to be cost-efficient compared to the evaluation of  $\tau_{\text{visc}}$ . For the 2.5 Hz and 5 Hz measurements, this was not conducted as the life time turned out to be higher than the duration of their tracking, 1.8 s and 1.2 s, respectively. For the other wind speeds, however, they were found to be decreasing with increasing wind speed, with the exception for the 17.5 Hz and 20 Hz measurement, where they were approximately equal, see figure 7.12. This could either be due to lack of better accuracy, as indicated by the uncertainties, or due to the viscous shear stress saturating, thus  $t^*$  approaching a constant value. Several studies have found the air-sided viscous shear stress to saturate below 80 mPa (refer to Bopp [2018], page 98) in the presence of waves. The viscous shear stress could not be estimated for these wind speeds, such that a direct comparison could not be conducted.

For the 10 Hz measurement,  $t^*$  was found to be lower in the interval [600 s, 1200 s] after turning the wind on ( $t^* = (0.68 \pm 0.04)$  s), compared to the interval [2160 s, 2760 s] where it was determined to  $t^* = (0.72 \pm 0.06)$  s. This is in agreement with the decrease in the values of  $\tau_{\text{visc}}$  between the two intervals, refer to section 7.1.2.

As discussed above in section 7.1, at some point the line widths underlie a strong bias towards smaller line widths due to the compression of the widths of the fluid parcels, whereas the stretched lines become strongly scattered and partly non-evaluable.

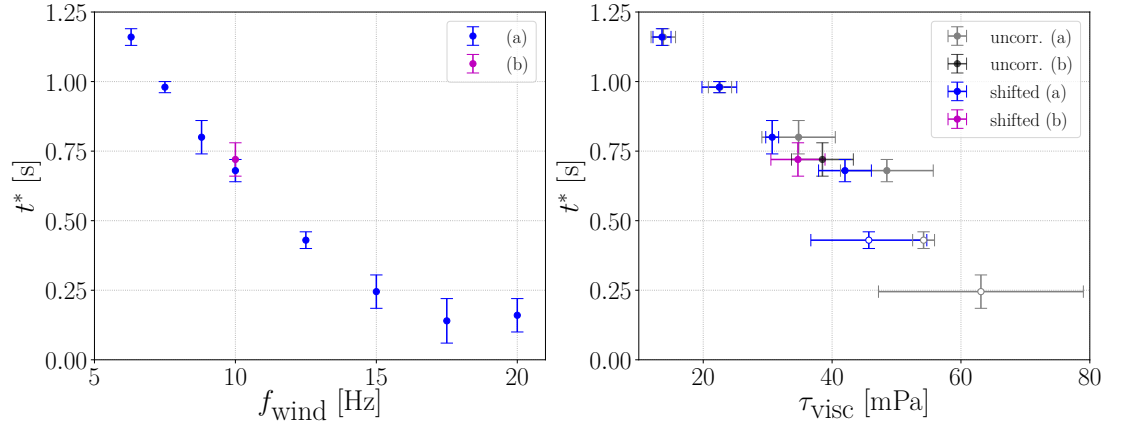


FIG 7.12.: The left plot shows the (setup dependent) characteristic life time of the heated lines  $t^*$  for the measurement of January 2021 in dependence of wind reference frequency  $f_{\text{wind}}$  (left) and estimated viscous shear stress  $\tau_{\text{visc}}$  (right).  $t^*$  was estimated as the time after heating the lines when the number of data points (line widths) had dropped to 50% of the maximum number, indicative of the broadening and hence fading of the lines. With increasing  $f_{\text{wind}}$  and hence wind speed,  $t^*$  decreases, and seems to level out at above 15 Hz. Moreover,  $t^*$  decreases with increasing viscous shear stress  $\tau_{\text{visc}}$ . Both the uncorrected values (gray and black points) and the shifted (best estimate, blue and magenta points) results (refer to section 7.1.1) are depicted for the 6.3 Hz to the 15 Hz measurement. Unfilled data points in the right plots indicate the values of  $\tau_{\text{visc}}$  underlying a bias. Blue and gray dots depict the evaluation in the interval [600 s,1200 s] (label (a)) after turning the wind on, whereas black and magenta dots the evaluation in the interval [2160 s,2760 s] (label (b)).

Therefore the determined viscous shear stress will sink falsely for higher wind speeds. Since  $t^*$  decreases with increasing  $\tau_{\text{visc}}$ , one could use  $t^*$  to sort out the erroneous values. This is especially relevant in a field setting with a high degree of varying wind. The characteristic time scales would require some sort of calibration.

#### 7.4.2

##### MEAN SURFACE VELOCITY

Moreover, the thermographic method is well suited to determine surface velocities  $u_s$ , as already implicated above. A plot of the mean surface velocities  $u_s$  determined by the long time interval evaluations can be found in figure 7.13. Note that the velocities for the measurement of January 2021 do not reflect the stationary limiting case, but are evaluated for the same time intervals ([600 s,1200 s] after turning the wind on) as described in section 7.1. The velocities for the stationary measurements of Emmel [2017] can be compared to the stationary results obtained by particle streak velocimetry (PSV) for the measurements with waves of January 2019, and agree within one standard deviation. Interestingly, for the measurements of January 2021 evaluated in section 7.2, the surface velocities show no clear dependence on the initial water velocity, with all measurements reaching velocities in the proximity of their values at the end of the measurements shortly after the overshoot regime. Most values also agree within one standard deviation to the stationary velocities, if the latter are available. The exception

is the non-stationary 10 Hz measurement by Emmel [2017], where the water surface velocity is also considerably lower than for the corresponding measurement of January 2021. As mentioned above (section 7.2), also the viscous shear stress is clearly lower in the former measurement. The number of measurements in this study is small, however, and repeated measurements of longer duration are lacking. If the independence of the velocity after the overshoot regime on the initial water velocity is confirmed in later studies, it would indicate that the surface velocity to be dependent on wind speed and state of the wave field, rather than the underlying drift. Clearly, this argument breaks down if the initial water speed is increased beyond the bulk velocity, which could be the case in field conditions. Further research is needed.

Additionally, the values for the stationary measurements conducted with smooth (without waves) surface conditions are given (Voigt [2019]). Compared to the stationary measurements of Emmel [2017] in the presence of waves, the surface velocities for the smooth case are higher than for the rough surface case for all considered wind speeds, though not significantly except for the 5 Hz measurement. For conditions with waves, however, Schwenk [2019] found the bulk velocities to be higher than in the case without waves. The latter is consistent with an increased total momentum transfer in the presence of waves, as also form drag contributes (Bopp [2018]). Similarly, a higher surface velocity might be explained by the momentum transfer entirely being caused by the viscous shear stress in the smooth case. This is not supported by the determined viscous shear, however, which in the smooth case is found to not be larger than in the rough case, refer to figure 7.7. Assuming the viscous shear stress to be equal in both cases, this would then imply an increased turbulent momentum transport closer to the interface in the presence of waves, hence slowing down the velocity at the surface, which corresponds to a smaller boundary layer thickness. The estimated values for the latter are in agreement with this reasoning, see below in section 7.4.3 and figure 7.14.

### 7.4.3

#### BOUNDARY LAYER THICKNESS

At the end of a measurement, after turning the wind off, the air compartment is slowed down much faster than the water body due to less inertia. Since the surface velocity is highly influenced by the shear stress, which in the water surface layer becomes negligible without the wind, the surface velocity is expected to drop quickly according to the wind speed, see the left plot in figure 7.14 for an example for the 10 Hz measurement. In the end, the water compartment will drive the air velocity, but since the density of air is low compared to water and the water velocities are much lower than the wind speeds, the resulting shear stress can be neglected as a first approximation. Hence the water velocity can be extrapolated to the point of turning the wind off and used as an estimation of the water velocity below the boundary layer  $u_b$ . Therefore, by measuring the surface velocity before and after turning off the wind, in combination with the velocity gradient determined by  $\partial_z u = \tau_{\text{visc}}/\mu$ , one can estimate the viscous boundary layer thickness  $\delta$  by a linear approximation,

$$\delta \approx \frac{u_s - u_b}{\partial_z u}. \quad (7.3)$$

This represents the most simple model, with the real velocity profiles possessing gradual transition to the bulk velocity, see for example the lower left plot in figure 7.16 for the mean tangential velocity ( $u_{\parallel}$ ) profile as function of perpendicular distance to the surface

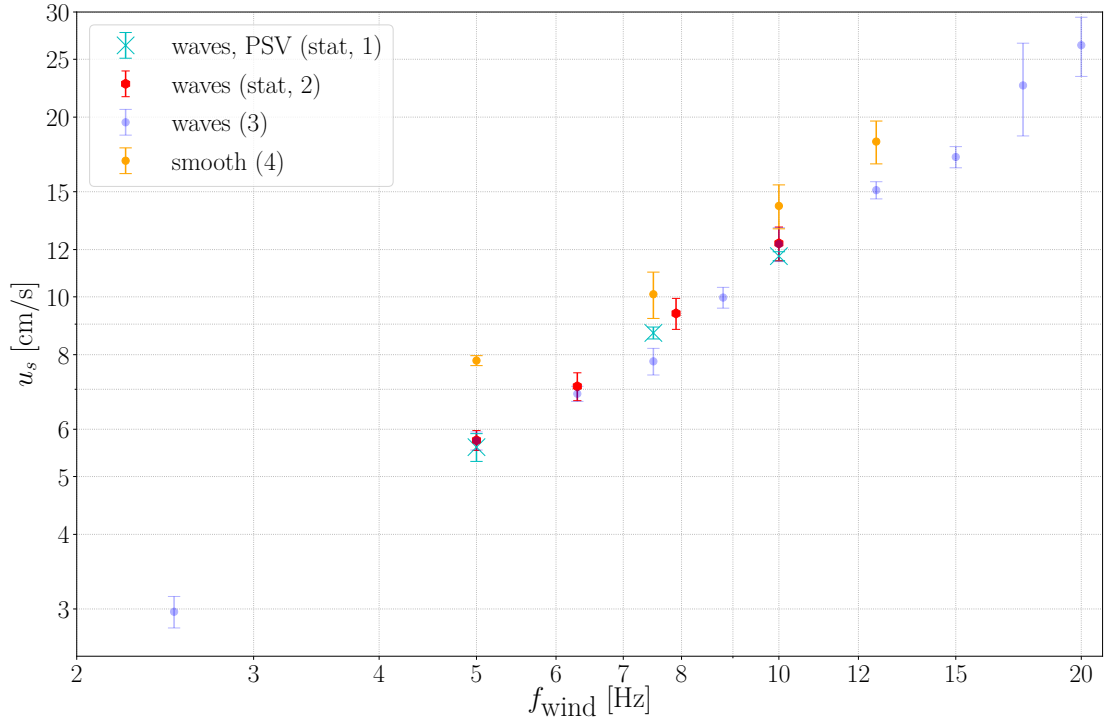


FIG 7.13.: The determined mean horizontal surface velocities  $u_s$  in dependence of wind generator frequency  $f_{\text{wind}}$ . Refer to figure A.1 for an analogous figure in dependence of  $u_{10}$ . The red markers show the results of the stationary measurement of Emmel [2017] (label 2), the cyan the speed determined by the PSV-method for the stationary measurement of January 2019 (label 1), and the orange points the velocities determined in Voigt [2019] for conditions without waves (smooth surface, label 4). Also shown are the velocities for the [600 s, 1200 s] time interval after turning the wind on for the measurements of January 2021 (blue, partly translucent points, label 3). Note the higher surface velocities in stationary conditions without waves, compared to the conditions with waves.

$z_{\perp}$ . Note that ideally  $u_{\parallel}$  should be used instead of  $u_s$  and  $u_b$ , but is here approximated by the mean horizontal velocity.

The results for  $\delta$  are given in the right plot of figure 7.14 and in table A.1 in the appendix, for the 5 Hz to the 10 Hz measurement. Note that the 10 Hz measurement is evaluated about 2800 s after turning the wind on, the other at  $t \sim 1400$  s. Recall that  $\tau_{\text{visc}}$  may decrease with increasing time after turning the wind on as found in 7.1.2, hence the values for  $\delta$  may not be directly comparable. In the case of the 2.5 Hz measurement the drop in surface velocity to bulk velocity was not clear and could not be evaluated. For the 12.5 Hz measurement and above, the value for  $\tau_{\text{visc}}$  is, as explained in section 7.1.1, uncertain due to a possible bias, and is hence left out.

The boundary layer thickness can be computed analogously with the results of the (stationary) PSV measurements, substituting the velocity at a depth of 15 mm as  $u_b$ , which is the maximal depth available. This might yield values for  $u_b$  that are not directly comparable to those evaluated for the thermographic approach as explained above. Moreover, a comparison to the values for  $\delta$  found for conditions without waves is



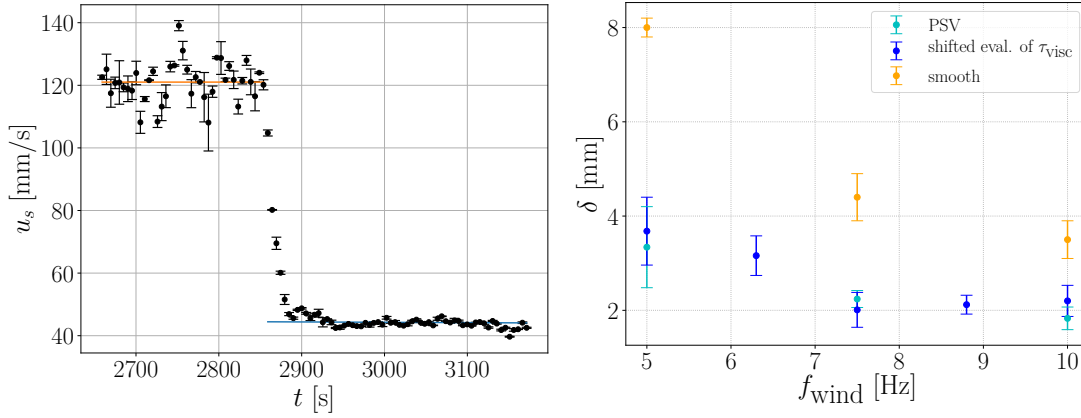


FIG 7.14.: The estimation of the mean surface velocities  $u_s$  for the 10 Hz measurement before and after turning the wind off (left), and the approximated viscous boundary layer thickness  $\delta$  in dependence of wind reference frequency  $f_{\text{wind}}$  (right). The velocities in the left figure are evaluated in 5 s intervals, and fitted for times before (orange) and after (blue) turning the wind off by a linear function. The latter is suitable as long as the considered time interval after turning off the wind is short. The surface velocities drop rapidly to the velocity of deeper water layers after turning off the wind ( $\sim 30$  s). The boundary layer thickness (right plot) is computed by equation (7.3) with estimated surface velocity, bulk velocity and viscous shear stress by the PSV method (cyan) and the thermographic best estimates (i.e. shifted line widths, refer to section 7.1.1, blue markers). There are no significant deviations between the methods of evaluation. Also  $\delta$  for conditions without waves are given (Voigt [2019]), these being larger than the values for the measurements with waves.  $\delta$  tends to decrease for higher  $f_{\text{wind}}$ , i.e. higher wind speed.

also given in figure 7.14 (orange data points, see Voigt [2019]). As can be seen, the viscous boundary layer thicknesses tends to decrease with higher wind speeds, as expected for higher Reynolds numbers and subsequent higher influence by turbulence, but based on these measurements to level out for higher wind speeds than 7.5 Hz. Moreover,  $\delta$  is smaller in the presence of waves, as also deduced in section 7.4.2 above, indicative of a higher turbulent momentum transport close to the surface for the rough surface. This is especially seen for the lowest wind speed, the 5 Hz measurement, where a small degree of velocity variation and correspondingly low turbulent momentum transport was found for the conditions without waves (Voigt [2019]). The tangential velocity component  $u_{\parallel}$  for the 5 Hz measurement with waves (figure A.22) shows a larger degree of variation, and the boundary layer thickness is significantly smaller, hence the turbulent transport can be expected to be higher.

This has implications for the thermographic method, since by model assumption the velocity gradient is constant in the topmost 2 mm. In the case of a thin boundary layer, with the gradient being constant for less than the topmost 2 mm and decreasing for deeper layers, this could lead to less broadening of the line widths relative to the simulated widths, and thus to an underestimation of the viscous shear stress. For the highest wind speeds given in figure 7.14,  $\delta$  is about 2 mm, hence it is not clear whether this is indeed of considerable influence as the wind speed increases further. Also the observed tendency of  $\delta$  to level out needs further verification, as the sample size is small.

## 7.5

### REFERENCE MEASUREMENT: PSV RESULTS

The reference method using particle streak velocimetry (PSV) provides valuable insights into the average flow field below the surface, in addition to the values for the mean shear stress. The orbital motion of the fluid parcels have been a central element, both as an indicator of the wave phase and also as the cause for the surface compression and dilation. In the following section,  $\tilde{q}$  refers to quantities averaged keeping the wave phase  $\varphi$  constant, whereas  $\bar{q}$  describes the average over all phases, refer to section 2.1.2 for further details.

The large influence by this motion on the flow field can be illustrated by the PSV measurements, see figure 7.15 for the stationary 10 Hz measurement of January 2019. Analogous plots are given for the 5 Hz and 7.5 Hz measurements in the appendix A.6. The uppermost plot shows the flow field as seen in the laboratory frame, relative to a mean surface profile, the lower shows a coordinate system moving with the mean velocity at a depth of 15 mm. Direction of propagation is from left to right. The colours indicate the absolute velocities, the arrows the velocity vectors. The central 50% of wave amplitude range were considered.

Especially clear in the lower plot is the orbital motion, manifested amongst others by the particle speed being approximately constant. Moreover the velocities farther away from the interface in the co-moving system are, as expected, directed in negative and positive  $x$ -direction (direction of wave propagation) for  $\varphi \approx \pi$  and  $\varphi \approx 0$ , respectively, whereas for  $\varphi \approx \pm\pi/2$  the velocities are vertical ( $\pm z$ -direction). Note the converging flow field clearly visible in the layers below the boundary layer, at  $\varphi \approx \pi/2$ , where the sign of the tangential velocity to the surface changes sign. This gives rise to a change of fluid parcel widths, refer to chapter 3, and when integrated over time, the compression of the fluid parcels at the crest. Likewise the flow field at  $\varphi \approx -\pi/2$  diverges, giving rise to the stretched fluid parcels in the trough. In the laboratory frame, the  $x$ -component of the velocity is close to zero, but positive, below the boundary layer in the wave trough, hence particle “orbits” do not intersect themselves in this system. The depicted depth is not large enough for dividing the underlying drift into contributions by bulk motion and Stokes drift.

More importantly, the layers close to the interface show clear deviations from the deeper layers, giving rise to velocity gradients. These are associated with the viscous part of the momentum transfer, more specifically the perpendicular (to the surface) gradient of tangential velocity, seen from a reference system moving vertically with the surface motion, refer to section 6.6. The mean of this velocity gradient is the quantity measured by the active thermographic approach in this work, proportional to the viscous shear stress. Note the clear phase dependence of the horizontal surface velocity is also seen, used in case of Emmel [2017] for estimating the wave phase.

Both the 5 Hz and 7.5 Hz (figures A.24 and A.25) show slightly increased orbital velocities for  $\varphi \approx \pm\pi/2$ , mainly caused by higher vertical velocity components. If correct, this would require a three dimensional flow structure in order for divergence of the flow field to vanish, i.e. a non-vanishing mean velocity component in  $y$ -direction. Caution must be taken when interpreting these results, however, as selection criteria regarding the streaks were applied (see section 6.6), which could therefore lead to artefacts of the evaluation if they were velocity selective.

In order to evaluate the mean viscous shear stress, the above tangential and per-

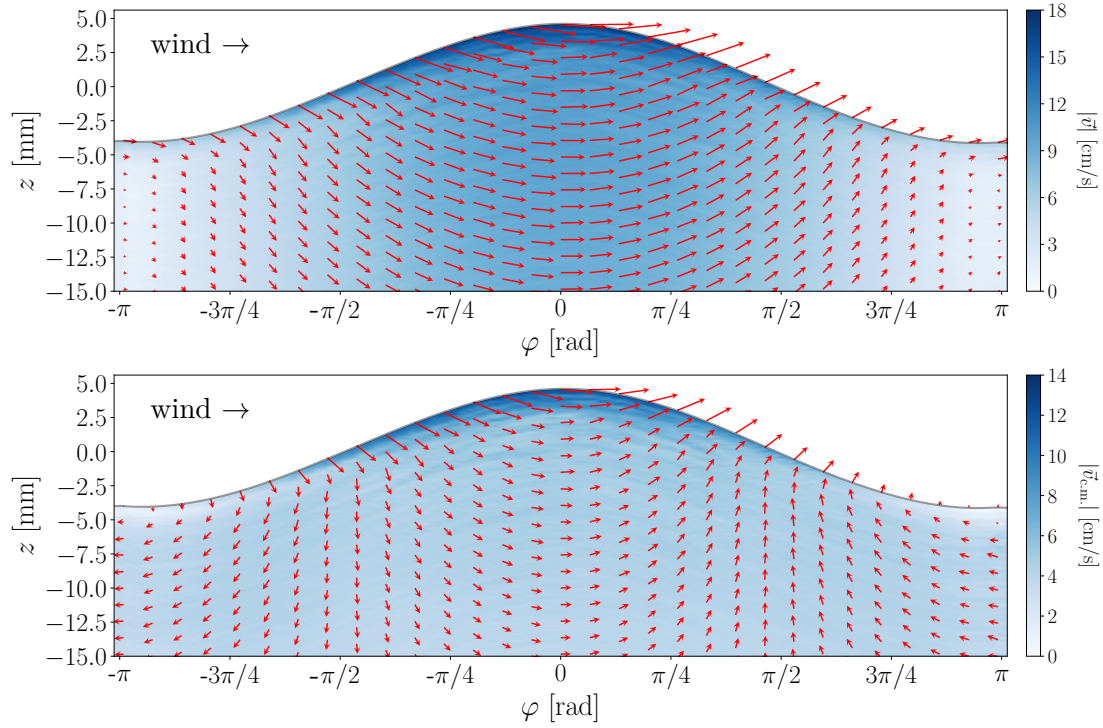


FIG 7.15.: The figure shows the mean water-sided flow field for the middle 50% of the amplitude range of the 10 Hz stationary measurement, with the wave propagating from left to right. The upper plot shows the field in the laboratory frame of view, the lower a reference system drifting with the mean velocity at  $z = -15$  mm. In the lower plot, the influence on the flow field by orbital motion is clearly seen, giving rise to the surface dilation and compression. In the laboratory frame, the  $x$ -components of the velocities are positive for all phases, hence particle trajectories do not intersect. Note the deviating velocities close to the air-water interface, whose perpendicular gradients (to the surface) of the tangential velocity in a reference system following the vertical motion of the surface, are proportional to the (phase dependent) viscous shear stress  $\tilde{\tau}_{\text{visc}}$ . The figure is created using bicubic interpolation for plotting, hence the smooth appearance of the colours. For reference, the wavelength is approximately 20 cm.

pendicular velocity components were computed in a coordinate system following wave motion, see figure 7.16 for an example for the 10 Hz measurement. The upper part of the figure shows examples of phase dependent evaluations of  $\tilde{\tau}_{\text{visc}}$  for the central 60% of the wave amplitudes with respect to wave amplitude. Shown is the tangential and perpendicular velocity  $\tilde{u}_{\parallel}$  (red dots) and  $\tilde{u}_{\perp}$  (lime crosses), respectively, as function of perpendicular distance  $z_{\perp}$  to the surface, refer to equation (6.20). The histogram below depicts  $u_{\parallel}$ . Close to the interface  $\tilde{u}_{\perp}$  should be zero in the system moving with the surface motion, which is approximately fulfilled. The average values for  $u_{\parallel}$  were, as explained in section 6.6, fitted by a penalized spline (red curve, see equation (B.15)), whose derivative is used for calculating the viscous shear stress. Again, note the influence by the orbital motion.

The lower left plot in figure 7.16 shows the evaluation of all particles at once for the

determination of the mean viscous shear stress  $\bar{\tau}_{\text{visc}}$ . Particle density variations with phase (more particles detected in the trough) and depth were accounted for. The result for  $\tilde{\tau}_{\text{visc}}$  is shown in the lower right plot, along with the mean viscous shear stress (lime line) and the average of  $\tilde{\tau}_{\text{visc}}$  (blue line). As can be seen, the latter quantities do not deviate significantly, but differ. This is caused by the phase dependent evaluation being sensitive to deviations caused by fluctuations in  $\tilde{u}_{\parallel}$  due to a low number of particles and the issues described below. Hence, as the best estimate for  $\bar{\tau}_{\text{visc}}$ , the values from the total velocity profile are used, the shape of which are comparable to those found by McLeish and Putland [1975]. Furthermore,  $\tilde{\tau}_{\text{visc}}$  varies considerably with wave phase, for the depicted amplitude range by a factor of about 2. The highest values are found on the upwind part of the crest. This is qualitatively in agreement with the results for the boundary layer in the air-compartment Bopp [2018], and water-sided measurements by Banner and Peirson [1998], Okuda et al. [1977] and Okuda [1982], though the distribution of the viscous shear stress in the latter study was more narrowly peaked at the crest.

The results of  $\tilde{\tau}_{\text{visc}}$  in this study show an additional peak at  $\varphi$  between  $\pi/4$  and  $\pi/2$ , which is most likely an artefact of the measurement and evaluation. This peak is not found in the above-mentioned studies. caused by timing deficiencies due to too low frame rates, as accelerations of the surface elevations are not captured and the distance covered by the surface between images is large. The duration of the (water-sided) streaks were 7.5 ms and the surface elevation was measured with an (air-sided) image every 5 ms. This is found to cause especially particles of larger amplitude waves, associated with higher orbital velocities, to be mapped too high (up to  $\sim 0.2$  mm above the surface), leading to enhanced gradients close to the surface since faster particles are found to be selectively mapped above slower ones, whilst they should have been averaged at the true value of the surface. Further down below the surface this is less of a problem, as the both faster and slower particles mapped slightly wrong are present at each depth, hence compensating and averaging out to a larger degree. This compensation changes at the (true) surface, where particles reach the maximal velocities irrespective of the amplitude, leading to somewhat distorted values at the mapped surface. Though the errors are small, the gradients are highly sensitive to such displacements. Likewise, the values of  $\tilde{\tau}_{\text{visc}}$  for  $\varphi \approx -\pi/2$  are likely too low for the analogous reason, i.e. causing streaks of larger amplitude waves to be mapped too far below the surface. The effect can be seen by close scrutiny in figure 7.16 when comparing the evaluation for  $\varphi \in [-99.3^\circ, -63.3^\circ]$  (upper right) and  $\varphi \in [63.3^\circ, 99.3^\circ]$  (lower left evaluation plot), and is enhanced when including higher amplitudes.

The mapping errors were found to be fairly symmetrical (i.e. mapping too far below and too far above the surface) for  $\pm\varphi$ , which was evaluated by exaggerating the issues by considering large amplitudes only. Therefore, the total (averaged over all phases) mean velocity profile is expected to be slightly rounded off at the surface, due to the smearing caused by the mapping issues. The total velocity gradient is found to be less influenced due to the mentioned symmetry, with possible deviations reflected in the uncertainty estimates. Still, the mapping problems must be taken into consideration when interpreting the results, especially for  $\tilde{\tau}_{\text{visc}}$ . For the 5 Hz measurement (figure A.22 in the appendix), the clear peak upwind to the crest is not found, instead  $\tilde{\tau}_{\text{visc}}$  has a peak for  $\varphi \approx \pm\pi/2$ . Also the mean velocity profile shows small deviation from the expected smooth profile with depth close to the surface, also slightly altering the profile of  $\bar{\tau}_{\text{visc}}(z_{\perp})$ .

As a side note, this illuminates some of the difficulties of particle imaging techniques. Moreover, the described issues, along with insufficient statistics, also prevented an

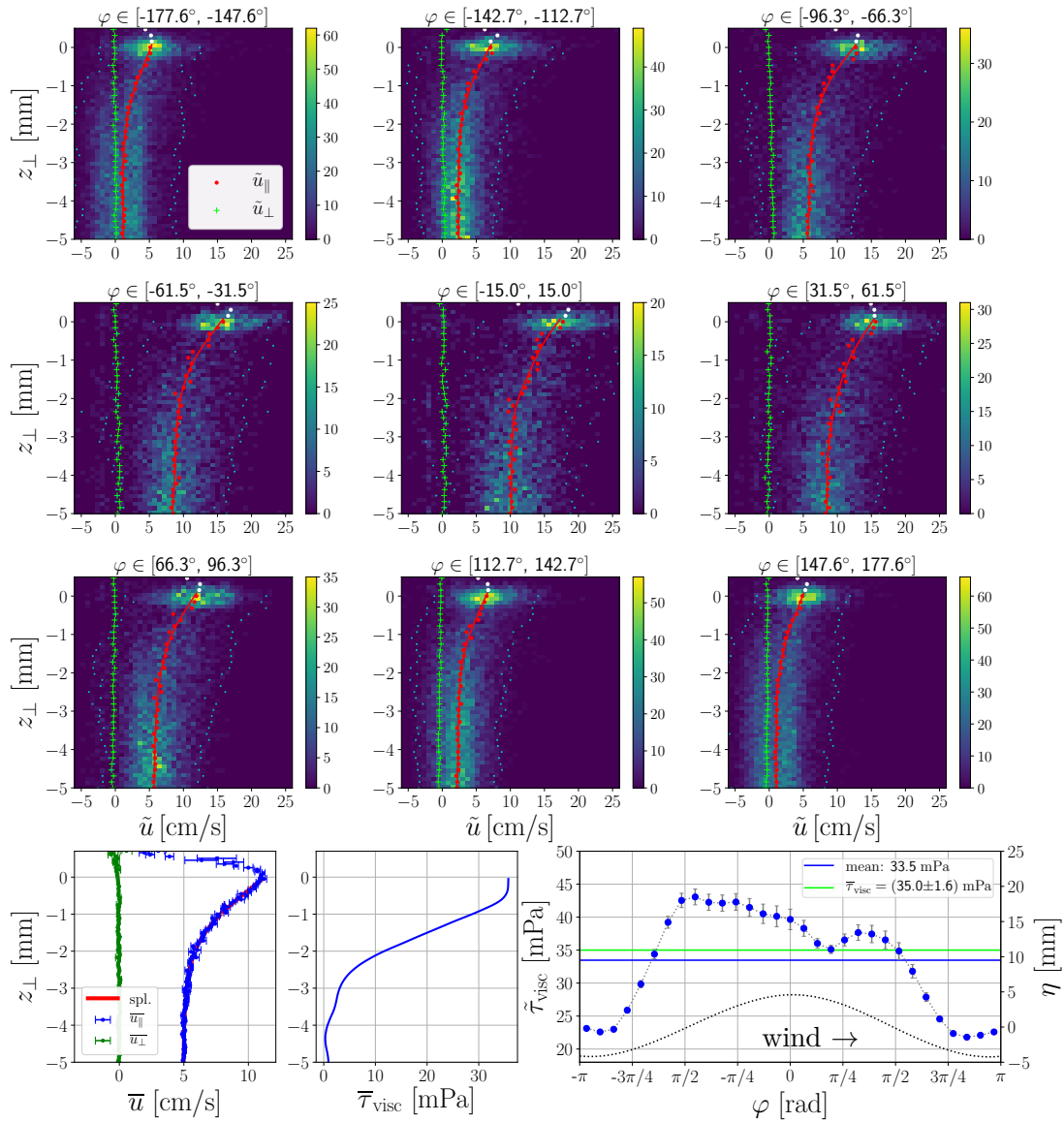


FIG 7.16.: Evaluation of the stationary 10 Hz measurement by particle streak velocimetry. The three upper rows show the velocity profiles for the middle 60% of particles with respect to the wave amplitude. Seen are the tangential velocity ( $\tilde{u}_\parallel$ , red dots), the spline used for evaluation the viscous shear stress  $\bar{\tau}_{\text{visc}}$  (red curve) and the perpendicular velocities ( $\tilde{u}_\perp$ , lime '+') as function of perpendicular distance to the surface  $z_\perp$ , for different wave phase  $\varphi$  intervals. Colours indicate the number of particles per bin, and the small cyan dots the cut-off criteria for outliers. White dots indicate values that have been excluded from the evaluation due to their location above the surface. The lower row of plots show (left) the mean (all particles) perpendicular ( $\bar{u}_\perp$ , green) and tangential velocities ( $\bar{u}_\parallel$ , blue) and the spline (red) for evaluating the phase averaged shear stress  $\bar{\tau}_{\text{visc}}$ . The latter is seen in the lower middle plot. The lower right plot shows  $\bar{\tau}_{\text{visc}}$  for the upper 0.5 mm (blue points), along with the average of these values (blue line), and the result for the upper 0.5 mm for  $\bar{\tau}_{\text{visc}}$  found in the middle plot (lime). The black dotted line indicates the mean wave profile  $\eta(\varphi)$  for the middle 60% of particles. The wind direction is towards the right.

estimation of the turbulent and wave coherent contributions to the momentum transfer, as the correlation terms close to the surface (see equation (2.9), and refer to Bopp [2018] for expressions in a wave following coordinate system) were strongly influenced by the timing- and mapping errors. The estimation of the turbulent contribution is furthermore found to be complicated by the dominance of orbital motion on the flow velocities. Based on this, for future applications the surface elevation should be measured at higher frame rates. Lowering the streak duration is difficult, as they come shorter.

Note that there apparently are detections (far) above the surface in figure 7.16. These are caused by the total reflection of the particles below the surface (hence appearing above), and as the number of these reflections decrease further away the surface, they are prone to scatter, partly being detected as particles having high velocities.

Quantitatively, the results for the phase averaged viscous shear stress do not deviate significantly from those found by the active thermographic method for the reanalysed measurements by Emmel [2017], which also were conducted in stationary conditions. In this case of the 7.5 Hz PSV-measurement, it was compared to the result of the 7.9 Hz measurement by Emmel [2017]. Refer to figure 7.7 for a plot of the determined  $\tau_{\text{visc}}$ , and to table A.2 for the values of  $\tau_{\text{visc}}$  and the mean horizontal surface velocity  $u_s$ . The observed phase dependence of  $\tau_{\text{visc}}$  has complications for the thermographic method, however, this will be discussed below.

### 7.5.1

#### IMPLICATIONS OF THE PHASE DEPENDENT SHEAR STRESS

First, the velocity profiles (refer to figure 7.16) in close proximity of the interface are approximately linear for all wave phases. This was seen by the derivatives of the splines fitted to the velocity profiles, and could thereby also to some degree be an artefact of the evaluation since the splines were penalized (see equation (B.15)). However, as long as the curvatures of the velocity profiles with depth close to the surface are approximately linear, the model assumptions used for simulating the line widths are approximately fulfilled. The phase dependent viscous shear stress, however, brings along an important point that has been neglected in the evaluation of  $\tau_{\text{visc}}$  for the thermographic method, namely that the assumption of a constant velocity gradient does not hold for broadening of the individual lines. Their broadening is therefore expected to deviate from the simulated curves. An evaluation of the impact of this on the collectively evaluated lines would require an analysis along the same line as for the surface dilation and compression in chapter 3, with the difference that theoretical models of  $\tilde{\tau}_{\text{visc}}$  are not available. The results above, beside the mentioned uncertainties due to the bias, are only given for the range of the middle 60% of the wave amplitudes, and the statistics did not allow for smaller amplitude binning. It is for example expected that the phase modulation of the viscous shear stress decreases for small amplitudes, vanishing in the limiting case of a smooth (i.e. without waves) surface. Likewise an increasing difference between the extremal values of  $\tilde{\tau}_{\text{visc}}$  for larger amplitudes was found on the air-side (Bopp [2018]), assuming a no-slip condition, this shear stress would need to transfer to the water-sided boundary layer. Since the models of  $\tilde{\tau}_{\text{visc}}$  are lacking, the influence on the line broadening and the subsequently determined values for  $\bar{\tau}_{\text{visc}}$  is not further studied in this work, instead relying on comparing the results for  $\bar{\tau}_{\text{visc}}$  by the thermographic and PSV methods. As already described, no significant deviations were found, but with solely three reference measurements, there is need for further verification.

## 8 | SUMMARY AND OUTLOOK

In this work, an active thermographic method was used to measure the viscous shear stress  $\tau_{\text{visc}}$  within the water-sided boundary layer of a wind-driven air-water interface in the presence of water waves. The measurement technique yields spatially localized measurements of the wave phase averaged shear stress, and was further developed from Voigt [2019] to be applicable to measurement conditions with waves. The measurements were conducted in an annular wind-wave facility, and a range of wind speeds up to  $u_{10} = (10.7 \pm 0.7)$  m/s were considered. Values for the best estimates of the viscous shear stress are limited to the lower range up to  $u_{10} = (4.8 \pm 0.3)$  m/s.

The measurement method uses a laser to heat a thin line perpendicular to the wind direction onto the water. A laser with an wavelength of  $\sim 1450$  nm is found well suited to enable absorption by the water without any dye and an adequate penetration depth. The lines are observed with an infrared sensitive camera. The infrared images are then analysed to yield the evolution of the line widths  $\sigma(t)$ . Due to the shear flow in the boundary layer, the broadening of the heated line is enhanced by Taylor dispersion, subsequently enabling the determination of the mean velocity gradient with depth  $\partial_z u$  within the boundary layer, and hence  $\tau_{\text{visc}} \propto \partial_z u$ . Hereby the velocity tangential to the surface is meant, and depth refers to the distance perpendicular to the surface. The velocity gradient is evaluated by comparing the broadening of the lines to numerically simulated line widths. Additionally, a camera and laser sheet for monitoring the surface elevation were applied in order to measure properties of the wave field and correct the observed line widths due to surface inclination. For the lower wind speeds where  $\tau_{\text{visc}}$  was determined, the correction was experimentally found to be negligible.

By model assumption the heated lines are influenced by a constant velocity gradient in the topmost 2 mm of the water compartment, and not subject to horizontal velocity gradients. Hence only the segments of the measured heated lines fulfilling this are used in the evaluation. Moreover, the enhanced broadening needs some time to develop, depending on the velocity gradient. At some point, the line widths are subject to a bias towards small line widths due to the broader lines fading too much for evaluation (Voigt [2019]). Hence the evaluation is restrained to an interval of intermediate times, which depends on the measurement conditions.

It was found in Voigt [2019] that the simulated broadening of the lines is dependent on the initial line width  $\sigma_0$ . Due to variations of the surface velocity in the presence of waves, this could, depending on the setup and the duration of the heating of the lines, represent an issue since a range of initial line widths could result. It is found by analysis of the simulation results that using squared line widths minimizes this issue, as  $\sigma^2(t) - \sigma_0^2$  only has a modest dependence on  $\sigma_0$  for given values of  $\partial_z u$ . Moreover, the viscous shear stress is wave phase dependent. In order to avoid wave phase selective evaluation of  $\tau_{\text{visc}}$  and to sample the wave field, the line widths of a large number of heated lines should

be evaluated collectively. In the case of a phase dependent  $\sigma_0$  due to surface velocity variations, problems arising with the (broad) phase dependent distributions of  $\sigma_0$  may be diminished by shifting  $\sigma^2(t)$  according to  $\sigma_0^2$  to a common, representative value of  $\sigma_0^2$ .

Water waves stretch and compress the spatial extents of the fluid parcels at the surface, in a way that their volume is unaltered, as expected for an incompressible fluid. This is in this work referred to as surface compression and dilation, and leads to the line widths being stretched in the wave troughs and compressed at the crests. The resulting distributions of  $\sigma^2(t)$  for a given time after heating the lines is expected and found to be skewed, with the long tail towards high values of the squared line widths. It is found that the peak of these distributions can be used as an approximation for the characteristic line widths that can be compared to the simulation, the latter being implemented without the flow dynamics induced by the waves. The peak of the distributions of  $\sigma^2(t)$  may be influenced by surface compression and dilation. This leads to deviations between the simulated temporal developments of  $\sigma^2(t)$  and the measured characteristic  $\sigma^2(t)$ , complicating the evaluation as the results may depend strongly on the used time interval. The influence is largest for times after heating corresponding to a half wave period, with the period in the reference system moving with the mean surface velocity and hence is experienced by the lines, where a bias towards lower values of the line widths is expected. This corresponds to compressions of the line widths. Evaluations for times similar to a half wave period are therefore expected to lead to a bias in the values of  $\tau_{\text{visc}}$  towards too low values. For times similar to one period, the influence is expected to be smallest, as the fluid parcels encompassing the lines return to their initial width. Therefore the line widths should be, if feasible, evaluated at times of approximately one wave period. For longer times since heating the lines, the influence is smaller due to wave frequency differences leading to the compression and stretching of the different lines being to a larger degree out of phase. Longer times before evaluation hence tends to be less of a problem. The influence by the waves on the characteristic  $\sigma^2(t)$  is found to depend on the initial line widths, with larger  $\sigma_0$  leading to a more pronounced effect and subsequent deviations from the simulated line widths. Hence, in a measurement of  $\tau_{\text{visc}}$ , the initial line width should be as small as feasible.

Correction of the distortion of the line widths was attempted, but found too unreliable, and needs further study to become applicable. If accomplished, it would ease the evaluation considerably. This is especially true if few lines are evaluated at once, such that individual events strongly affecting the line widths have a smaller impact on the outcome.

Furthermore, the temperature amplitude of the heated lines must be high enough for the stretched line widths not to fall below the detection limit, which leads to a bias towards too low values of  $\tau_{\text{visc}}$ . This was found to especially be a problem for higher wind speeds with increased wave steepness. Along with the bias towards compressed line widths caused by evaluation for times after heating the lines well below one wave period, it can lead to erroneously determined values for  $\tau_{\text{visc}}$  for high wind speeds. In a field application with varying wind speed, these false values may be detected by a low life time of the heated lines, seen by the number of evaluable line widths decreasing faster with time after heating the lines.

The evaluation of a large number of lines at once was compared to results of the phase averaged  $\tau_{\text{visc}}$  obtained by water-sided particle streak velocimetry (PSV), for the measurements with  $u_{10} = (2.4 \pm 0.2)$  m/s,  $u_{10} = (3.7 \pm 0.2)$  m/s and  $u_{10} = (4.8 \pm 0.3)$  m/s. These were found to not deviate significantly, with deviations below 15%. Moreover,  $\tau_{\text{visc}}$



was found to increase with wind speed. For the  $u_{10} = (4.8 \pm 0.3)$  m/s measurements, evaluations conducted in the intervals [10 min, 20 min] and [36 min, 46 min] after turning the wind on, along with a result for stationary conditions, indicated that  $\tau_{\text{visc}}$  decreases as the system approaches equilibrium between the air- and water compartment. While not seen for lower wind speeds, this observation is in agreement with (global) measurements by Schwenk [2019], and should be investigated further.

Moreover, this initial study showed promising results with regard to temporally resolved results for  $\tau_{\text{visc}}$ , on the order of seconds. Ideally, as far as the sampling of the wave phase and field is realized by the setup, the temporal resolution would be only limited by the time the heated lines must broaden before evaluation. In the case of a single line, the time intervals should be larger in order to ensure a sufficient sampling. The heating frequency should be as high as the current situation allows, as long as the lines are not overlapping. Overlapping can be caused by the wave associated orbital motion, as the downwind motion of the lines may be limited in the wave troughs. If caution is not taken, it could lead to phase selection as the overlapping lines are discarded. Lines at the same position with respect to the direction perpendicular to the wind, but only slightly shifted in wind direction, are prone to overlapping and tend to limit the heating frequency.

The non-stationary evaluation of 5 s intervals, showed several interesting features, especially shortly after turning the wind on, including an overshoot in the surface velocity, and, for low wind speeds, a pronounced overshoot in the viscous shear stress. It is likely that a similar, maybe of shorter duration, overshoot in the viscous shear stress is present for the higher wind speeds as well. Changes took place on time scales of some some tenths of seconds to seconds. The temporal resolution, in this case 5 s, of the method makes it well suited to study these phenomena, though the setup should be improved in order to handle the regime with the overshooting better. An improved setup, especially if the initial line widths are smaller and heating times are shorter, could also be used to study the method's upper limits regarding wind speed, being important knowledge for field applications. Likewise could a wider initial line width could be used to verify the calculations in this work, expecting a larger influence by the waves on the observed line widths.

Of special interest is also the influence of the build-up of the wave field and the bulk velocity on the viscous shear stress. The aforementioned decrease in  $\tau_{\text{visc}}$  for longer times after turning the wind on, could be caused by changes in the wave fields as well as bulk velocities approaching their asymptotic values, or both. The temporal resolution of the method makes it adequate to investigate this. For example, the problem could be approached by diminishing the influence by the bulk velocity, and study the influence of changes in the wave field alone. This could be achieved by letting the air- and water compartment equilibrate at a higher wind speed than that of interest, leading to an overshoot of the bulk velocity, then turning the wind off and waiting for the waves to subside. Thereafter the wind speed to be studied can be turned on. Done correctly, the bulk velocity will then have the asymptotic value for the wind speed of interest, hence the changes in  $\tau_{\text{visc}}$  will be caused by changes in the wave field. Monitoring the surface velocity simultaneously and its dependence on velocity before turning the wind on, would also be interesting.

The model was chosen due to its simplicity, and the largely unknown phase dependent water-sided velocity profiles. Hence, no condition dependent profiles are alleged, and the same method was used for a range of situations. The drawback naturally comes with

the model assumptions not being satisfied for the individual lines undergoing different wave phases. The validity of this approach was not verified beyond the three reference measurements by PSV and a comparison to the results obtained for a smooth (without waves) surface, with the value of  $\tau_{\text{visc}}$  in the presence of waves relative to the smooth case being unknown. Therefore, further studies for verification are required. The comparison with air-sided PSV measurements of the viscous shear stress would also be interesting. Lastly, the broadening of the heated lines was assumed independent of surface dilation and compression, irrespective of the wave period. Though the considerations of the individual lines did not oppose this assumption, this does not mean that the influence is indeed negligible. Careful considerations relating to how and if velocity gradients are altered when the small volume of the surface encompassing the line undergoes the distortion of its spatial extents, and of the flow field within the volume, would be needed. The influence on the broadening might then be estimated by numerical simulation.

# BIBLIOGRAPHY

- Andrews, T., Forster, P. M., and Gregory, J. M.: A Surface Energy Perspective on Climate Change, *Journal of Climate*, 22, 2557 – 2570, doi:10.1175/2008JCLI2759.1, 2009.
- Arnold, N.: Visualisierung des Gasaustauschs an der windbewegten Wasseroberfläche mittels vertikaler Konzentrationsfelder von gelöstem Sauerstoff quer zur Windrichtung, Bachelor's thesis, Institute of Environmental Physics, Department of Physics and Astronomy, University of Heidelberg, Germany, doi:10.11588/heidok.00018411, 2015.
- Banner, M. L. and Peirson, W. L.: An observational study of the aqueous surface layer structure beneath a wind-driven air-water interface, in: *Air-Water Gas Transfer, Selected Papers, 3rd Intern. Symp. on Air-Water Gas Transfer*, edited by Jähne, B. and Monahan, E., pp. 115–124, AEON, Hanau, doi:10.5281/zenodo.10571, 1995.
- Banner, M. L. and Peirson, W. L.: Tangential stress beneath wind-driven air-water interfaces, *J. Fluid Mech.*, 364, 115–145, doi:10.1017/S0022112098001128, 1998.
- Bopp, M.: Luft- und wasserseitige Strömungsverhältnisse im ringförmigen Heidelberger Wind-Wellen-Kanal (Aeolotron), Master's thesis, Institute of Environmental Physics, Department of Physics and Astronomy, University of Heidelberg, Germany, doi:10.11588/heidok.00017151, 2014.
- Bopp, M.: Air-Flow and Stress Partitioning over Wind Waves in a Linear Wind-Wave Facility, Dissertation, Institute of Environmental Physics, Department of Physics and Astronomy, University of Heidelberg, Germany, Heidelberg, doi:10.11588/heidok.00024741, 2018.
- Buckley, M. P. and Veron, F.: Structure of the airflow above surface waves, *J. Phys. Oceanogr.*, 46, 1377–1397, doi:10.1175/JPO-D-15-0135.1, 2016.
- Buckley, M. P. and Veron, F.: Airflow measurements at a wavy air-water interface using PIV and LIF, 58, 1–20, doi:10.1007/s00348-017-2439-2, 2017.
- Crank, J.: *The Mathematics of Diffusion*, Clarendon Press, Oxford, 2nd edn., 1975.
- Crooks, G.: *Field Guide to Continuous Probability Distributions*, Gavin E Crooks, 2019.
- de Boor, C.: *A Practical Guide to Splines*, Springer, 2001.
- Downing, H. D. and Williams, D.: Optical constants of water in the infrared, *Journal of Geophysical Research (1896-1977)*, 80, 1656–1661, doi:10.1029/JC080i012p01656, 1975.
- Emmel, A.: Bestimmung der Geschwindigkeit und des Geschwindigkeitsgradienten an der windgetriebenen Wasseroberfläche, Bachelor's thesis, Institute of Environmental Physics, Department of Physics and Astronomy, University of Heidelberg, Germany, doi:10.11588/heidok.00023754, 2017.

- Farid, H. and Simoncelli, E. P.: Optimally rotation-equivariant directional derivative kernels, in: *Computer Analysis of Images and Patterns*, edited by Sommer, G., Daniilidis, K., and Pauli, J., pp. 207–214, Springer Berlin Heidelberg, Berlin, Heidelberg, 1997.
- FLIR Systems, I.: Data sheet FLIR X8501sc Infrared camera, 2020.
- Francius, M. and Kharif, C.: Two-dimensional stability of finite-amplitude gravity waves on water of finite depth with constant vorticity, *Journal of Fluid Mechanics*, 830, 631 – 659, 2017.
- Friman, S. I.: Laboratory investigations of concentration and wind profiles close to the wind-driven wavy water surface, Dissertation, Institut für Umweltphysik, Fakultät für Physik und Astronomie, Univ. Heidelberg, Heidelberg, doi:10.11588/heidok.00028310, 2020.
- Garbe, C. S., Degreif, K., and Jähne, B.: Estimating the viscous shear stress at the water surface from active thermography, in: *Transport at the Air Sea Interface — Measurements, Models and Parameterizations*, edited by Garbe, C. S., Handler, R. A., and Jähne, B., pp. 223–239, Springer-Verlag, Berlin, Heidelberg, doi:10.1007/978-3-540-36906-6\_16, 2007.
- Gruber, N., Clement, D., Carter, B. R., Feely, R. A., van Heuven, S., Hoppema, M., Ishii, M., Key, R. M., Kozyr, A., Lauvset, S. K., Lo Monaco, C., Mathis, J. T., Murata, A., Olsen, A., Perez, F. F., Sabine, C. L., Tanhua, T., and Wanninkhof, R.: The oceanic sink for anthropogenic CO<sub>2</sub> from 1994 to 2007, *Science*, 363, 1193–1199, doi:10.1126/science.aau5153, 2019.
- Gutsche, M.: Surface Velocity Measurements at the Aeolotron by Means of Active Thermography, Masterarbeit, Institute of Environmental Physics, Department of Physics and Astronomy, University of Heidelberg, Germany, doi:10.11588/heidok.00017431, 2014.
- Haußecker, H.: Messung und Simulation von kleinskaligen Austauschvorgängen an der Ozeanoberfläche mittels Thermographie, Dissertation, IWR, Institute of Environmental Physics, Department of Physics and Astronomy, University of Heidelberg, Germany, doi:10.5281/zenodo.14789, 1996.
- Holtmann, L. G.: Aufbau eines aktiven Thermographiesystems zur Messung des Geschwindigkeitsgradienten in der windgetriebenen wasserseitigen viskosen Grenzschicht, Bachelor's thesis, Institute of Environmental Physics, Department of Physics and Astronomy, University of Heidelberg, Germany, doi:10.11588/heidok.00023754, 2017.
- Ilmberger, J.: Impulsübertrag und Strömungsverhältnisse in einem runden Wind-Wasser Kanal, Diplomarbeit, Institute of Environmental Physics, Department of Physics and Astronomy, University of Heidelberg, Germany, doi:10.5281/zenodo.13346, 1981.
- Jähne, B., Münnich, K., Böisinger, R., Dutzi, A., Huber, W., and Libner, P.: On the parameters influencing air–water gas exchange, *Journal of Geophysical Research*, 92, 1937–1949, 1987.
- Janssen, J. A. M.: Does wind stress depend on sea-state or not? - A statistical error analysis of HEXMAX data, *Boundary-Layer Meteorology*, 83, 479–503, doi:10.1023/A:1000336814021, 1997.
- Jähne, B.: *Digitale Bildverarbeitung*, Springer, Berlin, 7th edn., doi:10.1007/b138991, 2012.

- Jähne, B.: Air-Sea Gas Exchange, in: Encyclopedia of Ocean Sciences (Third Edition), edited by Cochran, J. K., Bokuniewicz, H. J., and Yager, P. L., pp. 1–13, Academic Press, Oxford, third edition edn., doi:10.1016/B978-0-12-409548-9.11613-6, 2019.
- Klein, A.: The Fetch Dependency of Small-Scale Air-Sea Interaction Processes at Low to Moderate Wind Speeds, Dissertation, Institute of Environmental Physics, Department of Physics and Astronomy, Heidelberg University, Germany, Heidelberg, doi:10.11588/heidok.00026559, 2019.
- Krall, K. E.: Laboratory Investigations of Air-Sea Gas Transfer under a Wide Range of Water Surface Conditions, Dissertation, Institute of Environmental Physics, Department of Physics and Astronomy, University of Heidelberg, Germany, doi:10.11588/heidok.00014392, 2013.
- Krall, K. E., Smith, A. W., Takagaki, N., and Jähne, B.: Air-sea gas exchange at wind speeds up to  $85 \text{ m s}^{-1}$ , *Ocean Science*, 15, 1783–1799, doi:10.5194/os-15-1783-2019, 2019.
- Kräuter, C.: Visualization of air-water gas exchange, Dissertation, Institute of Environmental Physics, Department of Physics, Heidelberg University, doi:10.11588/heidok.00018209, 2015.
- Kräuter, C., Trofimova, D., Kiefhaber, D., Krah, N., and Jähne, B.: High resolution 2-D fluorescence imaging of the mass boundary layer thickness at free water surfaces, *jeos*, 9, 14016, doi:10.2971/jeos.2014.14016, 2014.
- Kundu, P. K.: Fluid Mechanics, Academic Press, Elsevier, San Diego, CA, 4th edn., 2008.
- Kunz, J.: Active Thermography as a Tool for the Estimation of Air-Water Transfer Velocities, Ph.D. thesis, Institute of Environmental Physics, Department of Physics and Astronomy, Heidelberg University, Germany, doi:10.11588/heidok.00022903, 2017.
- Kunz, J. and Jähne, B.: Investigating small scale air-sea exchange processes via thermography, 4, 4, doi:10.3389/fmech.2018.00004, 2018.
- Liss, P. S. and Johnson, M. T., eds.: Ocean-Atmosphere Interactions of Gases and Particles, Springer, doi:10.1007/978-3-642-25643-1, 2014.
- Liu, Y.-W.: Fourier Transform Applications, chap. Hilbert Transform and Applications, InTech, 2012.
- Longuet-Higgins, M.: On the Statistical Distribution of the Heights of Sea Waves, vol. 11, *Journal of Marine Research*, 1952.
- Longuet-Higgins, M. S.: Integral Properties of Periodic Gravity Waves of Finite Amplitude, *Proceedings of the Royal Society of London. Series A, Mathematical and Physical Sciences*, 342, 157–174, full publication date: Feb. 25, 1975, 1975.
- Lu, G., Tsai, W., and Jähne, B.: Decomposing Infrared Images of Wind Waves for Quantitative Separation into Characteristic Flow Processes, *IEEE Transactions Geosciences and Remote Sensing*, doi:10.1109/TGRS.2019.2920280, 2019.
- Lu, G.-h., Tsai, W.-t., Garbe, C., and Jähne, B.: Characteristics of Streaky Thermal Footprints on Wind Waves, *Journal of Geophysical Research: Oceans*, 126, e2021JC017385, doi:10.1029/2021JC017385, e2021JC017385 2021JC017385, 2021.
- McLeish, W. and Putland, G. E.: Measurements of wind-driven flow profiles in the top millimeter of water, *J. Phys. Oceanogr.*, 5, 516–518, doi:10.1175/1520-0485(1975)005<0516:MOWDFP>2.0.CO;2, 1975.
- Michell, J. H.: XLIV. The highest waves in water, *The London, Edinburgh, and*

- Dublin Philosophical Magazine and Journal of Science, 36, 430–437, doi:10.1080/14786449308620499, 1893.
- Murashige, S. and Choi, W.: Stability analysis of deep-water waves on a linear shear current using unsteady conformal mapping, *Journal of Fluid Mechanics*, 885, A41, doi:10.1017/jfm.2019.1021, 2020.
- Okuda, K.: The internal structure of short wind waves. Part I: On the internal vorticity structure, *J. Oceanogr. Soc. Japan*, 38, 28–42, doi:10.1007/BF02113819, 1982.
- Okuda, K.: Internal flow structure of short wind waves. Part III The generation of flow in excess of the phase speed, *Journal of the Oceanographical Society of Japan*, 40, 46–56, doi:10.1007/BF02071208, 1984.
- Okuda, K., Kawai, S., and Toba, Y.: Measurement of skin friction distribution along the surface of wind waves, *J. Oceanogr. Soc. Japan*, 33, 190–198, doi:10.1007/BF02109691, 1977.
- Oppenheim, A. V. and Schaffer, R. W.: *Discrete-Time Signal Processing*, Pearson, Upper Saddle River, NJ, 3 edn., 2010.
- Osborne, M. F. M.: The effect of convergent and divergent flow patterns on infrared and optical radiation from the sea, *Deutsche Hydrografische Zeitschrift*, 18, 1–25, doi:10.1007/BF02233218, 1965.
- Palmer, K. F. and Williams, D.: Optical properties of water in the near infrared, *J. Opt. Soc. Am.*, 64, 1107–1110, doi:10.1364/JOSA.64.001107, 1974.
- Peregrine, D., Cokelet, E., and McIver, P.: The fluid mechanics of waves approaching breaking, *Coastal Engineering Proceedings*, 1, 31, doi:10.9753/icce.v17.31, 1980.
- Phillips, O. M.: On the generation of waves by turbulent wind, *J. Fluid Mech.*, 2, 417–445, doi:10.1017/S0022112057000233, 1957.
- Prandtl, L.: Abriß der Strömungslehre, vol. 010 of *Göttinger Klassiker der Strömungsmechanik*, Universitätsverlag Göttingen, Göttingen, doi:10.17875/gup2017-1003, 2017.
- Reichl, B. G., Hara, T., and Ginis, I.: Sea state dependence of the wind stress over the ocean under hurricane winds, *Journal of Geophysical Research: Oceans*, 119, 30–51, doi:10.1002/2013JC009289, 2014.
- Rembeck, L. S.: Geschwindigkeit- und Geschwindigkeitsgradientenmessung an der windgetriebenen Wasseroberfläche mittels aktiver Thermographie, Bachelor's thesis, Institute of Environmental Physics, Department of Physics and Astronomy, University of Heidelberg, Germany, 2018.
- Rennebaum, A.: Spatio-Temporal Properties of the initial Wave Formation Phase at the Aeolotron, Master's thesis, Institute of Environmental Physics, Department of Physics and Astronomy, Heidelberg University, Germany, doi:10.11588/heidok.00023754, 2017.
- Roy-Barman, M. and Jeandel, C.: *Marine Geochemistry: Ocean Circulation, Carbon Cycle and Climate Change*, 2016.
- Scheimpflug, T.: Der Photospektrograph und seine Anwendungen, *Photographische Korrespondenz*, p. 516, 1906.
- Schwartz, L. W.: Computer extension and analytic continuation of Stokes expansion for gravity waves, *Journal of Fluid Mechanics*, 62, 553578, doi:10.1017/S0022112074000802, 1974.
- Schwartz, L. W. and Fenton, J. D.: Strongly nonlinear waves., 14, 39, 1982.

- Schwarz, K.: Spatio-Temporal Measurements of Water-Wave Height and Slope using Laser-Induced Fluorescence and Splines, Bachelor's thesis, Institute of Environmental Physics, Department of Physics and Astronomy, Heidelberg University, Germany, doi:10.11588/heidok.00021977, 2016.
- Schwenk, C.: Messung der Schubspannungsgeschwindigkeit am Heidelberger Aeolotron unter instationären Bedingungen, Bachelor's thesis, Institute of Environmental Physics, Department of Physics and Astronomy, Heidelberg University, Germany, 2019.
- Siddiqui, K. and Loewen, M.: Phase-averaged flow properties beneath microscale breaking waves, 134, 499–523, doi:10.1007/s10546-009-9447-6, 2010.
- Song, Z.-y., Zhao, H., Li, L., and Lü, G.: On the universal third order Stokes wave solution, *Science China Earth Sciences*, 56, doi:10.1007/s11430-012-4523-z, 2012.
- Stephens, G. L., Li, J., Wild, M., Clayson, C. A., Loeb, N., Kato, S., L'Ecuyer, T., Stackhouse, P. W., Lebsock, M., and Andrews, T.: An update on Earth's energy balance in light of the latest global observations, *Nature Geoscience*, 5, 691–696, doi:10.1038/ngeo1580, 2012.
- Stokes, G. G.: On the theory of oscillatory waves, *Trans. Camb. Philos. Soc.*, 8, 441, 1847.
- Toffoli, A. and Bitner-Gregersen, E. M.: Types of Ocean Surface Waves, *Wave Classification*, pp. 1–8, American Cancer Society, doi:10.1002/9781118476406.emoe077, 2017.
- Tsuchiya, Y. and Yasuda, T.: A new approach to Stokes Wave Theory, *Bulletin of the Disaster Prevention Research Institute*, 31, 1981.
- Voigt, P.: Simulation and Measurement of the Water-sided Viscous Shear Stress without Waves, Bachelor's thesis, Institute of Environmental Physics, Department of Physics and Astronomy, Heidelberg University, Germany, doi:10.11588/heidok.00026653, 2019.
- Wanninkhof, R., Asher, W. E., Ho, D. T., Sweeney, C., and McGillis, W. R.: Advances in Quantifying Air-Sea Gas Exchange and Environmental Forcing, *Annual Review of Marine Science*, 1, 213–244, doi:10.1146/annurev.marine.010908.163742, PMID: 21141036, 2009.
- Welch, P. D.: The use of fast Fourier transform for the estimation of power spectra: A method based on time averaging over short, modified periodograms, *Audio and Electroacoustics, IEEE Transactions on*, 15, 70–73, doi:10.1109/TAU.1967.1161901, 1967.
- Wild, M., Folini, D., Schär, C., Loeb, N., Dutton, E. G., and König-Langlo, G.: The global energy balance from a surface perspective, *Climate Dynamics*, 40, 3107–3134, doi:10.1007/s00382-012-1569-8, 2013.
- Witting, J.: Effects of plane progressive irrotational waves on thermal boundary layers, *J. Fluid Mech.*, 50, 321–334, doi:10.1017/S0022112071002593, 1971.
- Wurl, O., Wurl, E., Miller, L., Johnson, L., and Vagle, S.: Formation and global distribution of sea-surface microlayers, 8, 121–135, 2011.
- Zhong, X. and Liao, S.: On the limiting Stokes wave of extreme height in arbitrary water depth, *Journal of Fluid Mechanics*, 843, 653679, doi:10.1017/jfm.2018.171, 2018.





# A | APPENDIX

## A.1

### MAIN RESULTS

Here figures analogous to figure 7.7 and 7.13 in chapter 7 are shown, but in dependency of estimated values for  $u_{10}$  instead of wind reference frequency  $f_{\text{wind}}$ .

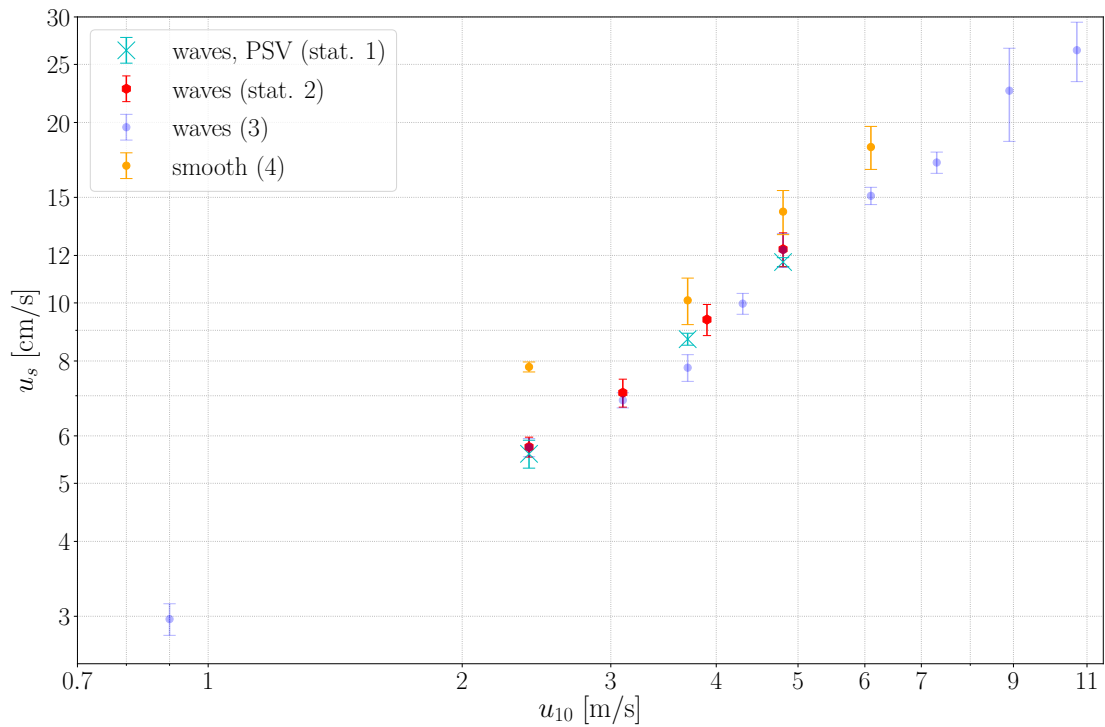


FIG A.1.: The determined mean horizontal surface velocities  $u_s$  in dependence of the estimated wind speed in 10 metres height  $u_{10}$ . For additional details see figure 7.13 in section 7.1, which is analogous except for the abscissa.

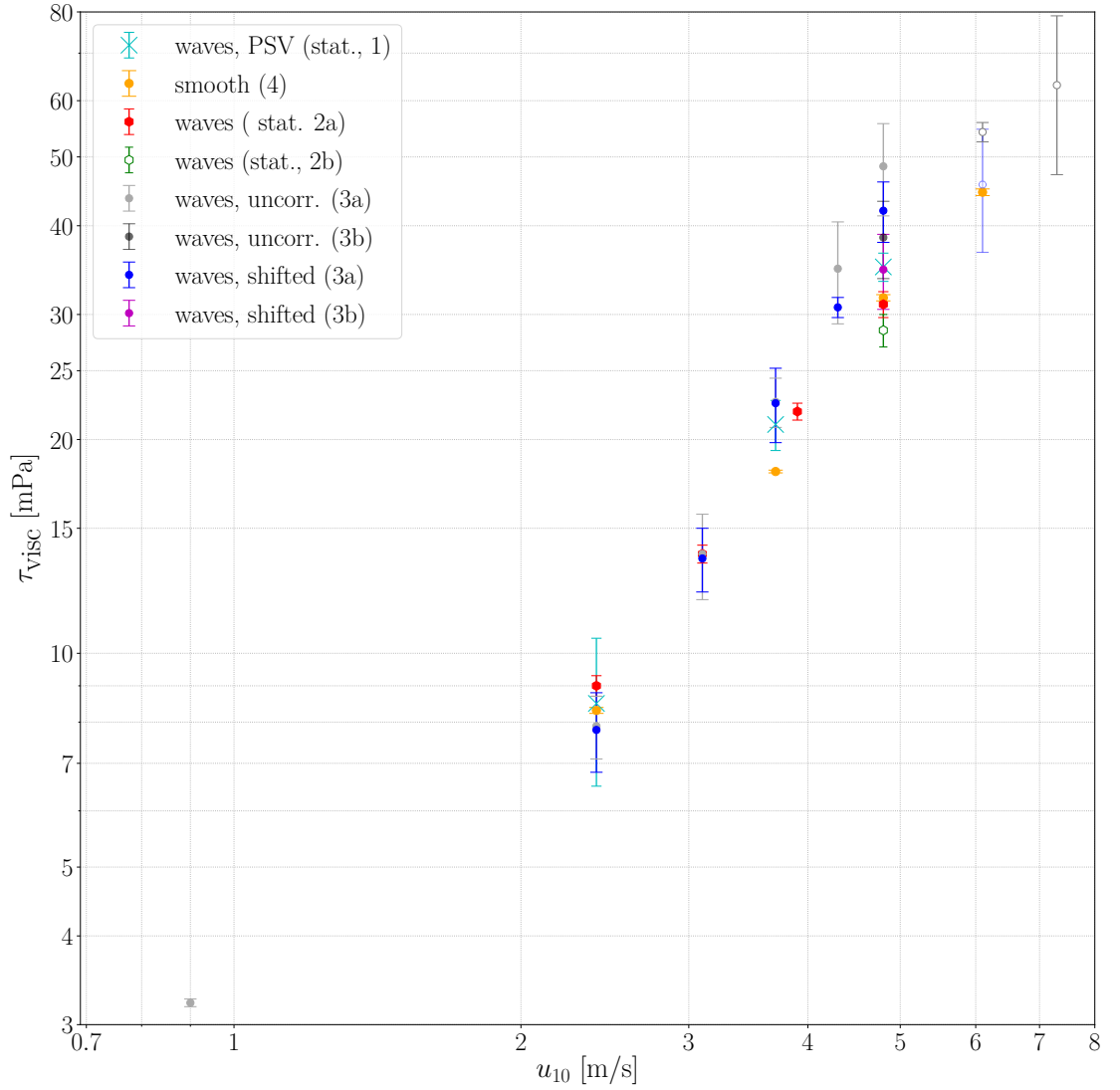


FIG A.2.: All results for the long time interval evaluation of the viscous shear stress  $\tau_{\text{visc}}$ , in dependence of the estimated wind speed in 10 metres height  $u_{10}$ . Refer to figure 7.7 in section 7.1, which is analogous except for the abscissa for details.

### A.1.1

#### MEASURED VALUES

In this section, the main results will be stated in tabular form. Values that are not available, are marked by “n.a.”.

Table A.1 states the parameters used for calculating the boundary layer thickness in section 7.4.3, along with the initial surface water velocity before starting the non-stationary measurements, refer to section 7.2.

The results of the long time interval evaluations and the reference measurements deploying particle streak velocimetry (PSV) are given in table A.2. Note that values marked with a star (\*) are subject to a bias and must not be trusted, refer to section 7.1. For the measurements of January 2021, two values for viscous shear stress  $\tau_{\text{visc}}$  are provided; the result of the evaluation of the uncorrected data set of line widths and the

$f_{\text{wind}}$ [Hz]	$u_{s0}$ [mm/s]	$u_s$ [mm/s]	$u_b$ [mm/s]	$\partial_z u$ [s <sup>-1</sup> ]	$\delta$ [mm]
5.0	20 ± 3	56 ± 3	28 ± 4	7.8 ± 0.8	3.7 ± 0.7
6.3	9 ± 2	74 ± 5	31 ± 3	13.8 ± 0.5	3.2 ± 0.4
7.5	-1 ± 1	83 ± 5	38 ± 3	20.5 ± 1.7	2.2 ± 0.4
8.8	6 ± 5	103 ± 5	41 ± 4	30.0 ± 1.0	2.1 ± 0.2
10.0	38 ± 2	121 ± 7	44 ± 3	34.7 ± 4.2	2.2 ± 0.3
5.0 (PSV)	n.a.	56.0 ± 3	28 ± 2	8.8 ± 2.0	3.2 ± 1.0
7.5 (PSV)	n.a.	87 ± 2	40 ± 2	21.0 ± 1.7	2.2 ± 0.2
10.0 (PSV)	n.a.	117 ± 2	53 ± 8	35.0 ± 1.6	1.8 ± 0.2

TABLE A.1.: Table with the initial water surface velocity before turning the wind on  $u_{s0}$  for the non-stationary measurements of January 2021 (section 7.2, and the parameters used for calculating the boundary layer thickness  $\delta$  (section 7.4.3). The measurements are labelled by the wind reference (generator) frequency  $f_{\text{wind}}$ . The symbols refer to: mean surface velocity before turning the wind off  $u_s$ , and the (extrapolated) bulk velocity  $u_b$  and the velocity gradient with depth in the boundary layer  $\partial_z u$ . The three lowest rows give the PSV results for the stationary measurement of January 2019.

best estimates based on shifting the individual lines according to their squared initial width, see equation (6.10) and refer to section 6.4 for further details. All results are given for the time interval [600 s, 1200 s] after turning the wind on, except the values for (a), which are given for the interval [2160 s, 2760 s].

Moreover, for the best estimate values of  $\tau_{\text{visc}}$  resulting from the thermographic method of this work, the three uncertainty estimates are provided, these are also discussed in the aforementioned section. The uncertainties  $(\cdot)_1$  reflect the uncertainty due to the choice of evaluation time (after heating the lines) and hence the agreement between the simulated line widths and the measured line widths, having a direct impact on the resulting values for  $\tau_{\text{visc}}$ . The values denoted with  $(\cdot)_2$  depict the uncertainty due to the determination of the initial line width and  $(\cdot)_3$  reflects the division of the long time intervals into 3 subintervals. The latter subintervals of enough heated lines in order for the evaluation to be stable, and therefore reflects the temporal change and/or fluctuation in the values for  $\tau_{\text{visc}}$  within the (total) interval. The values  $(\cdot)_1$  are provided in all plots.

The re-evaluated measurements of Emmel [2017] and January 2019 are stationary. The label (b) denotes a heating time of the lines of 5 ms, refer to section 7.1.1, chapter 7, in contrast to 10 ms for the other measurements of Emmel [2017].

The surface velocity denoted by  $u_s$  and the characteristic life time of the heated lines  $t^*$  are also given in table A.2.

$f_{\text{wind}}$ [Hz]	$\tau_{\text{visc}}$ [mPa] (best estimate)	$\tau_{\text{visc}}$ [mPa] (uncorr.)	$u_s$ [mm/s]	$t^*$ [s]
January 2021				
2.5	$3.22 \pm (0.04)_1 \pm (0.91)_2 \pm (0.08)_3$	n.a.	$29.7 \pm 0.1$	n.a.
5.0	$7.8 \pm (1.0)_1 \pm (0.2)_2 \pm (0.6)_3$	$7.9 \pm (0.8)_1$	$57 \pm 2$	n.a.
6.3	$13.6 \pm (1.4)_1 \pm (0.2)_2 \pm (0.4)_3$	$13.8 \pm (1.9)_1$	$69 \pm 2$	$1.16 \pm 0.03$
7.5	$22.5 \pm (2.7)_1 \pm (0.6)_2 \pm (0.4)_3$	$22.6 \pm (1.8)_1$	$78 \pm 4$	$0.98 \pm 0.02$
8.8	$30.7 \pm (1.0)_1 \pm (0.7)_2 \pm (2.1)_3$	$34.8 \pm (5.7)_1$	$100 \pm 4$	$0.80 \pm 0.06$
10.0	$42 \pm (4.1)_1 \pm (1.3)_2 \pm (0.8)_3$	$48.5 \pm (7.2)_1$	$123 \pm 8$	$0.68 \pm 0.04$
10.0 (a)	$34.7 \pm (4.2)_1 \pm (0.9)_2 \pm (1.4)_3$	$38.5 \pm (4.8)_1$	$121 \pm 5$	$0.72 \pm 0.06$
12.5	$45.7^* \pm (8.9)_1 \pm (1.8)_2 \pm (3.5)_3$	$54.2^* \pm (1.7)_1$	$151 \pm 5$	$0.43 \pm 0.03$
15.0	n.a.	$63.1^* \pm (15.9)_1$	$172 \pm 7$	$0.25 \pm 0.06$
17.5	n.a.	n.a.	$226 \pm 4$	$0.14 \pm 0.08$
20.0	n.a.	n.a.	$264 \pm 3$	$0.16 \pm 0.06$
Emmel [2017]				
5.0	$9.0 \pm (0.3)_1 \pm (0.06)_2 \pm (0.2)_3$	n.a.	$56.0 \pm 0.3$	n.a.
6.3	$13.8 \pm (0.4)_1 \pm (0.2)_2 \pm (0.1)_3$	n.a.	$87 \pm 1$	n.a.
7.9	$21.9 \pm (0.3)_1 \pm (0.4)_2 \pm (0.6)_3$	n.a.	$117 \pm 1$	n.a.
10.0	$31.2 \pm (1.3)_1 \pm (1.6)_2 \pm (1.1)_3$	n.a.	$123 \pm 4$	n.a.
10.0 (b)	$28.2^* \pm (1.3)_1 \pm (1.2)_2 \pm (1.6)_3$	n.a.	$123 \pm 3$	n.a.
January 2019				
5.0 (PSV)	$8.5 \pm 2.0$	n.a.	$56 \pm 3$	
7.5 (PSV)	$21.0 \pm 1.7$	n.a.	$87 \pm 2$	
10.0 (PSV)	$35.0 \pm 1.6$	n.a.	$117 \pm 2$	

TABLE A.2.: The results of the long time interval evaluation and the reference measurements using particle streak velocimetry (PSV). Wind reference frequencies are denoted  $f_{\text{wind}}$ , refer to table 4.1, for approximate  $u_{10}$ -values. Values marked with a star (\*) are subject to a bias and must not be trusted. All values for the measurement of January 2021 are given for the interval [600 s, 1200 s] after turning the wind on, except the values for (a) which are given for the interval [2160 s, 2760 s]. The uncertainties  $(\cdot)_i$  reflect different uncertainty estimations, refer to section A.1.1 above. The measurements of Emmel [2017] and January 2019 are stationary. The label (b) denotes a heating time of the lines of 5 ms, refer to section 7.1.1, in contrast to 10 ms for the other measurements of Emmel [2017]. The surface velocity is denoted by  $u_s$  and the characteristic life time of the heated lines by  $t^*$ .

## A.2

### LONG TIME INTERVAL EVALUATIONS

#### A.2.1

JANUARY 2021

Some of the evaluations of  $\tau_{\text{visc}}$  are given in this section, for illustration of how the evaluations change with wind speed. Refer to section 6.4 and figure 6.5 for details. The uncorrected evaluations will be given, since show the discussed issues in section 7.1.

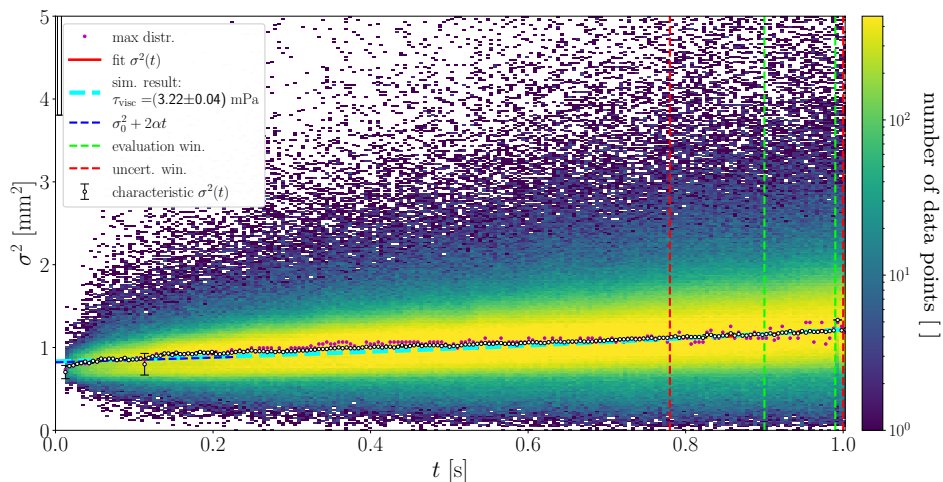


FIG A.3.: Analogous to figure 7.1, but shows the 2.5 Hz (wind reference) measurement. The influence by the waves is negligible, and the distributions of the squared line widths  $\sigma^2(t)$  are close to symmetric, as expected.

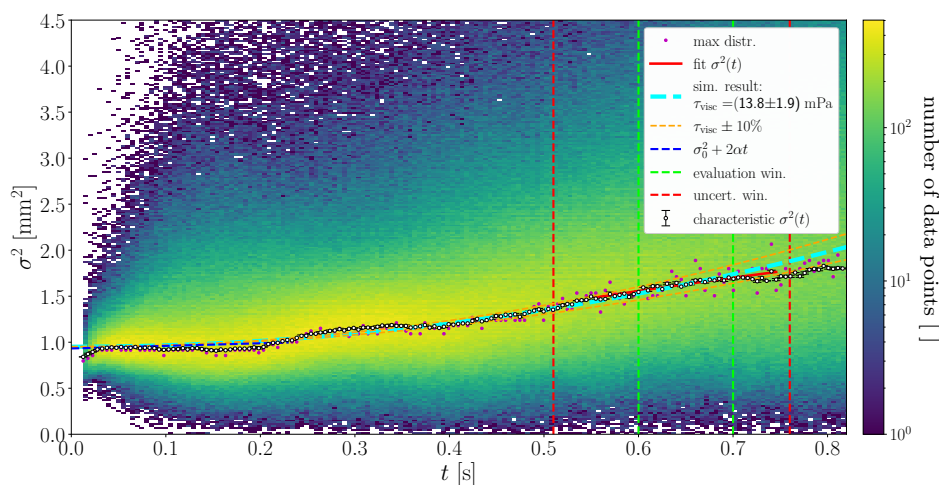


FIG A.4.: Analogous to figure 7.1, but shows the 6.3 Hz (wind reference) measurement, with wave period (co-moving ref. system)  $T' \approx 0.35$  s. A slight broadening at  $T'/2$  and narrowing for  $t \sim T'$  of the distributions of the squared line widths  $\sigma^2(t)$  can be seen, refer to section 7.1 for further details. Also see figure A.15.

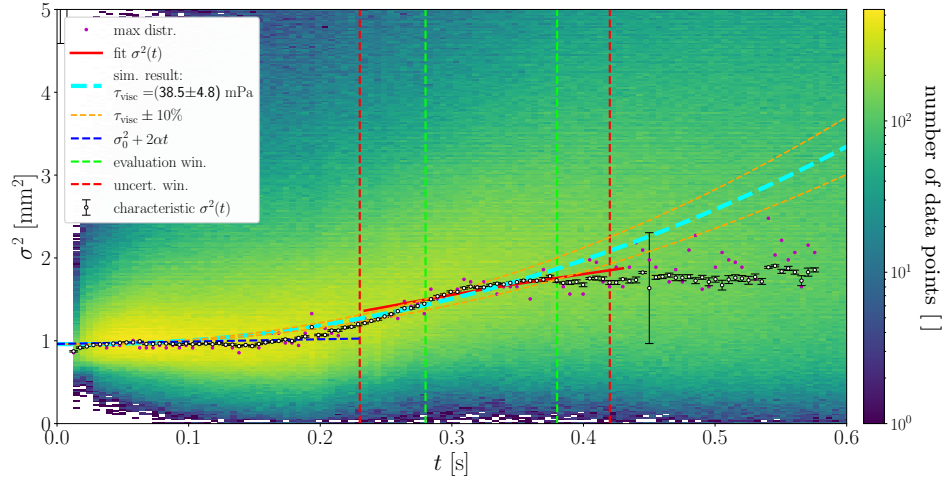


FIG A.5.: Analogous to figure 7.2, but shows the 10 Hz (wind reference) measurement in the time interval [2160s, 2760s] after turning the wind on. The characteristic squared line widths  $\sigma^2(t)$  are smaller than in figure 7.2, indicating that the viscous shear stress has decreased, which is confirmed upon evaluation. The pattern in the characteristic  $\sigma^2(t)$  caused by surface compression and dilation is present.

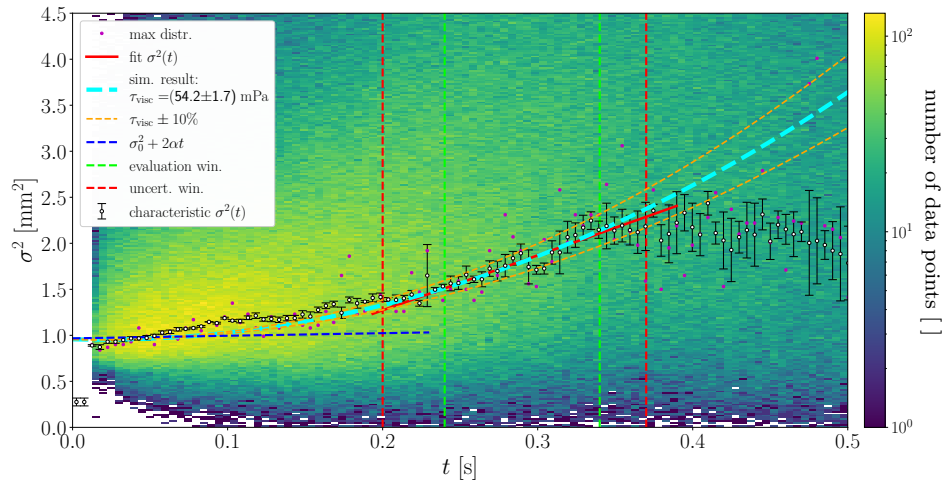


FIG A.6.: Analogous to figure 7.1, but shows the 12.5 Hz (wind reference) measurement. The result should not be trusted, due to a bias towards too low values of the viscous shear stress  $\tau_{\text{visc}}$  caused by the evaluation at approximately a half wave period  $T'$  in the co-moving reference system,  $T' \approx 0.5$  s. Note the decreasing characteristic squared line widths  $\sigma^2(t)$  after  $t \approx 0.35$  s. This is caused by the fading of broader lines, hence only the thin lines remain.

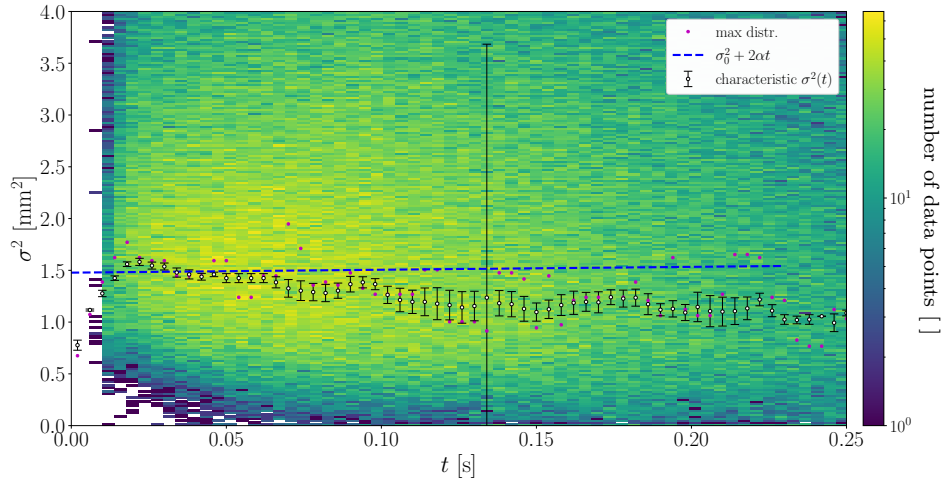


FIG A.7.: The evaluation of the squared characteristic line widths  $\sigma^2(t)$  for the 20 Hz (wind reference) measurement. The bias towards too low line widths (compressed lines) is high enough for  $\sigma^2(t)$  to decrease after heating. The characteristic life time of the lines is  $t^* = (0.16 \pm 0.06)$  s for reference.

## A.2.2

### CORRECTION OF SURFACE DILATION AND COMPRESSION

Here, the evaluation of the unshifted line widths (refer to section 6.4), corrected for surface compression and dilation according to equation (3.16), for the 10 Hz (wind reference) measurement of January 2021 in the interval [600 s, 1200 s] after turning the wind on, is shown. Refer to section 7.3 for further discussion.

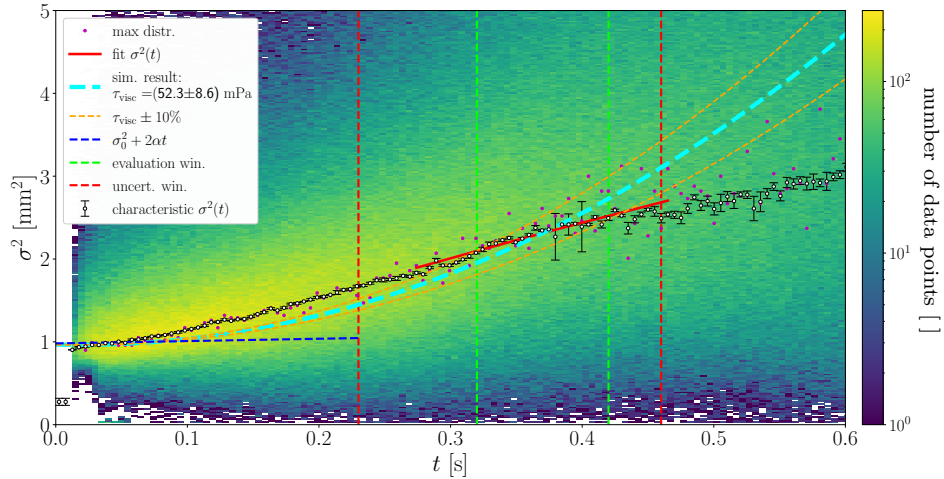


FIG A.8.: Evaluation of the unshifted (section 6.4), but corrected line widths according to equation (3.16) of the 10 Hz measurement of January 2021. Note the apparent overcorrection of the line widths  $\sigma(t)$  when comparing the characteristic  $\sigma^2(t)$  to the simulated curve (cyan dashed line) for times around half a wave period,  $t \sim T'/2 \approx 0.18$  s.

### A.2.3 MEASUREMENTS OF EMMEL [2017]

Figure A.9 and figure 7.6 show figures analogous to those in the section A.2.1 above, for the stationary measurements (5 Hz and 7.9 Hz) of Emmel [2017]. These evaluations are given for the sake of completeness. The main difference to the setup in January 2021 is a thinner heated line, refer to section 7.1.1. Refer to figure 7.1 for further explanation of the figures.

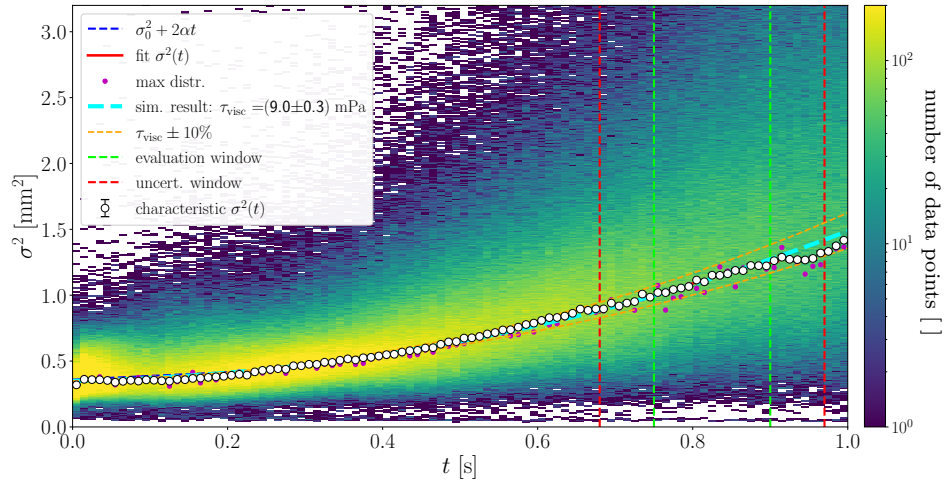


FIG A.9.: Evaluation of the 5 Hz (wind reference) measurement by Emmel [2017]. Note the widening and narrowing of the distributions of  $\sigma^2(t)$  seen in figure 7.1, which is analogous but with a wider heated line, is not seen here.

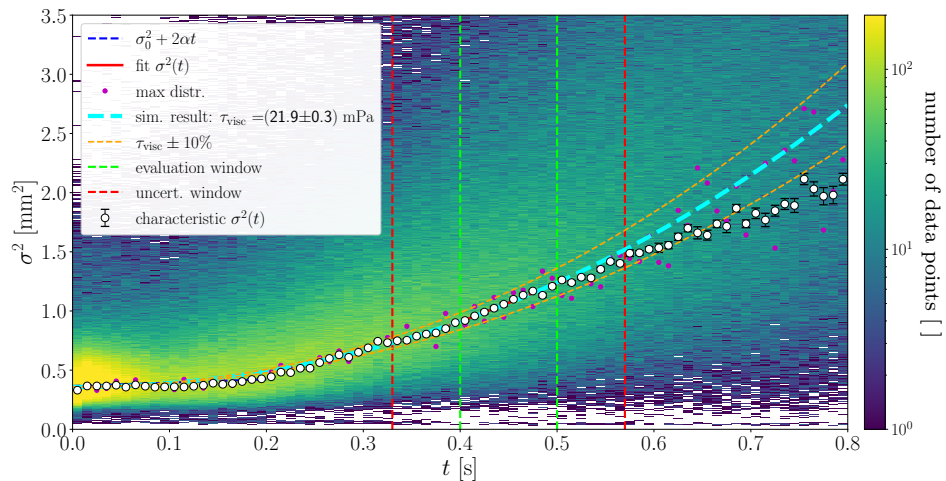


FIG A.10.: Evaluation of the 7.9 Hz (wind reference) measurement by Emmel [2017]. The figure is analogous to figure 7.5. Surface elevation data were not available.



### A.3

#### RADIAL VARIATIONS OF THE VISCOUS SHEAR STRESS

As explained in section 7.1.2 in chapter 7, the long heated line in the measurements of Emmel [2017] allows for determining the viscous shear stress  $\tau_{\text{visc}}$  for shorter partitions of 50 mm of the heated lines, hence the variation of  $\tau_{\text{visc}}$  along the heated line can be estimated. These pieces were considered at several positions along the line with overlap between the intervals considered for each data point. This corresponds to variations in radial direction of the wind-wave channel, with the  $y$ -direction directed towards the channel centre, see figure 4.3. The radially averaged value for  $\tau_{\text{visc}}$  is given in the legend of the figures, with the standard deviation as uncertainty.

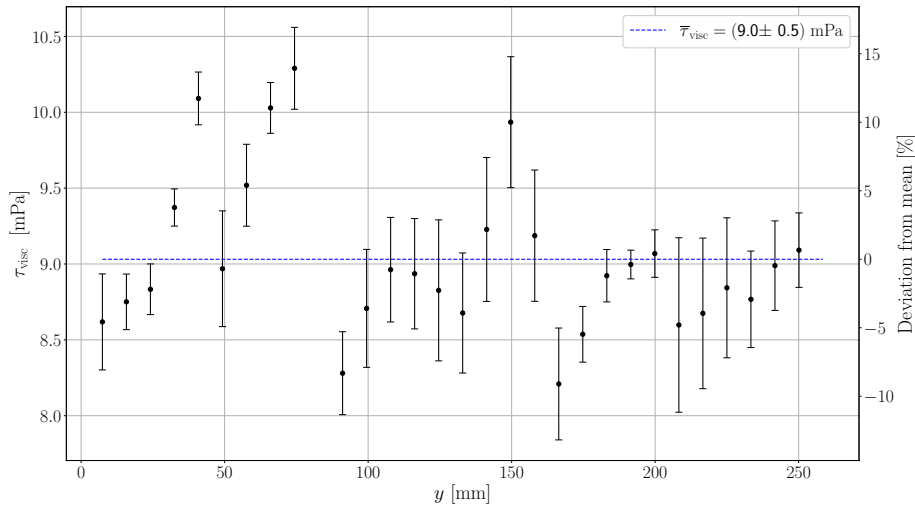


FIG A.11.: The viscous shear stress  $\tau_{\text{visc}}$  in dependence on position on the heated line, i.e. radially with respect to the channel, evaluated for 50 mm segments, for the 5 Hz (wind reference) measurement of Emmel [2017].

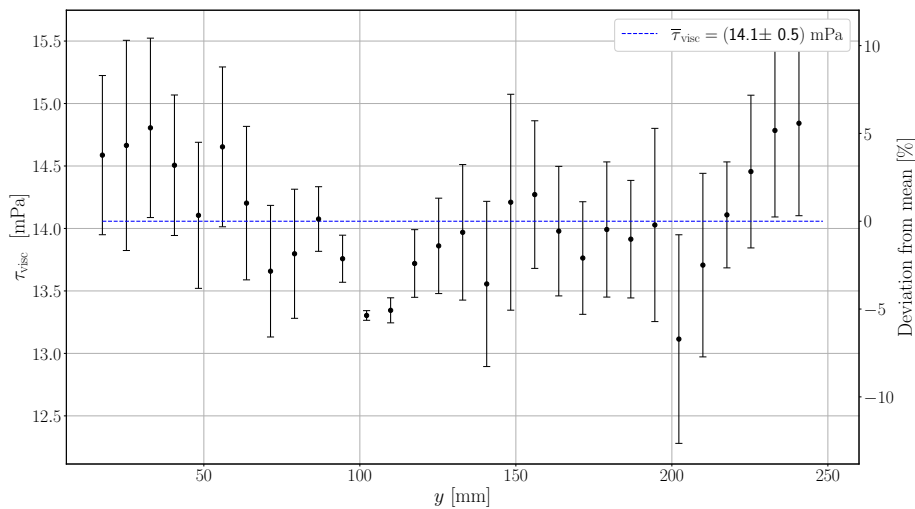


FIG A.12.: The viscous shear stress  $\tau_{\text{visc}}$  in dependence on position on the heated line, evaluated for 50 mm segments of the heated lines, for the 6.3 Hz (wind reference) measurement of Emmel [2017].

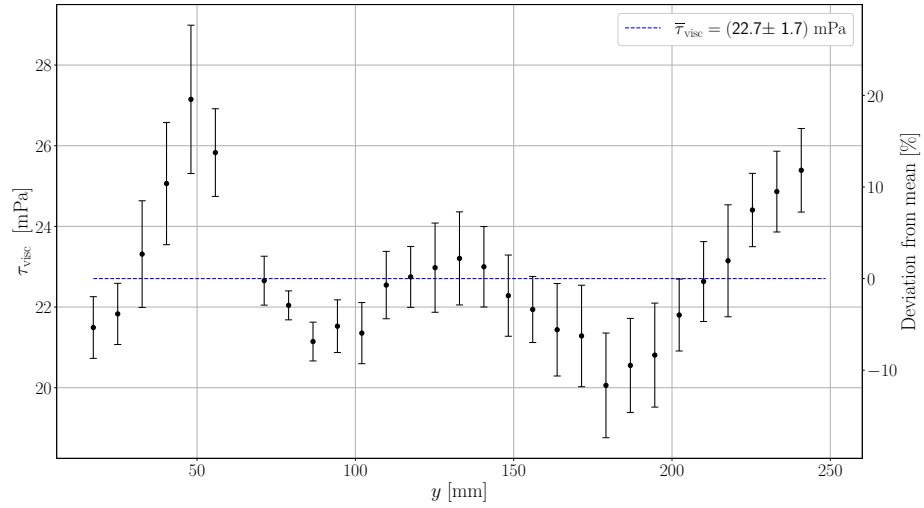


FIG A.13.: The viscous shear stress  $\tau_{\text{visc}}$  in dependence on position on the heated line evaluated for 50 mm segments of the heated lines, for the 7.9 Hz (wind reference) measurement of Emmel [2017].

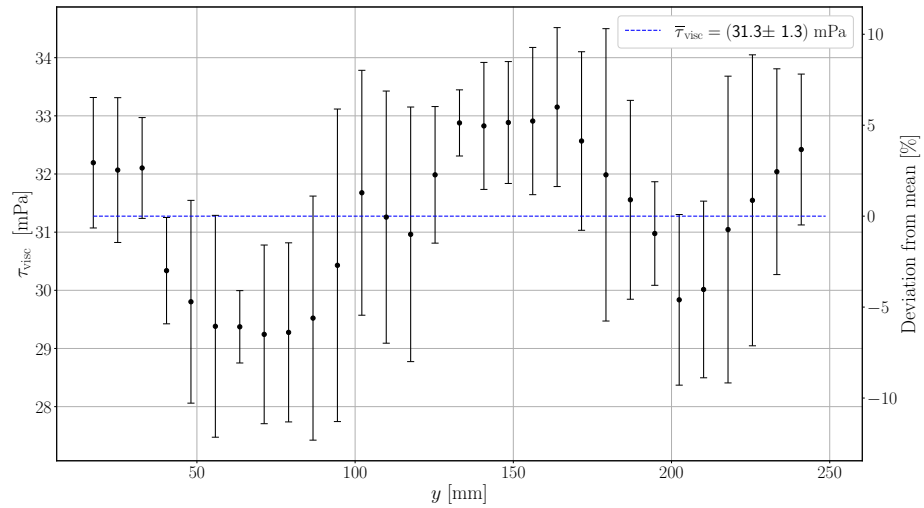


FIG A.14.: The viscous shear stress  $\tau_{\text{visc}}$  in dependence on position on the heated line evaluated for 50 mm segments of the heated lines, for the 10 Hz (wind reference) measurement of Emmel [2017].

## A.4

### LINE WIDTH DISTRIBUTIONS (CREST AND TROUGH)

Two examples for the line width distributions for lines heated in the wave trough (phase  $\varphi = \pi$ ) and at the wave crest (phase  $\varphi = 0$ ) are shown, figure A.15 (6.3 Hz measurement of January 2021) and figure A.16 (10 Hz measurement of Emmel [2017]). Refer to section 7.1.1 for the analogous figure 7.3 for the 10 Hz measurement of January 2021.

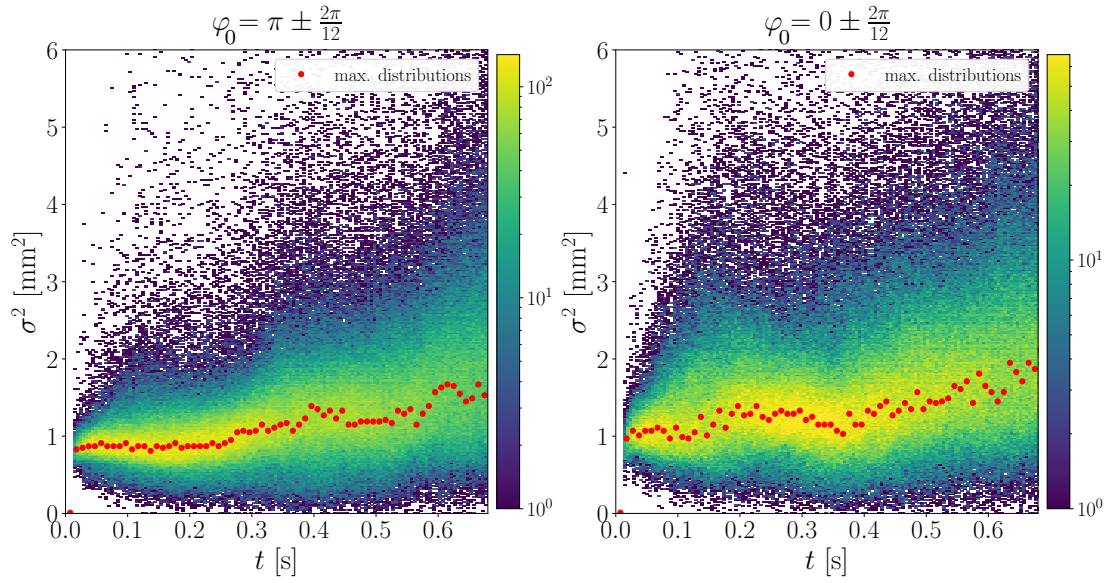


FIG A.15.: Shown are the line width distributions for lines heated in the wave trough (left) and at the crest (right), for the 6.3 Hz measurement of January 2021. Refer to figure 7.3 for further details, which is analogous. Note the more narrow distributions of  $\sigma^2(t)$  and smaller influence by the waves than for the 10 Hz measurement, and some lines being stretched in the left plot likely due to spatial inhomogeneities in the wave field. The wave period (co-moving system) is  $T' \approx 0.35$  s.

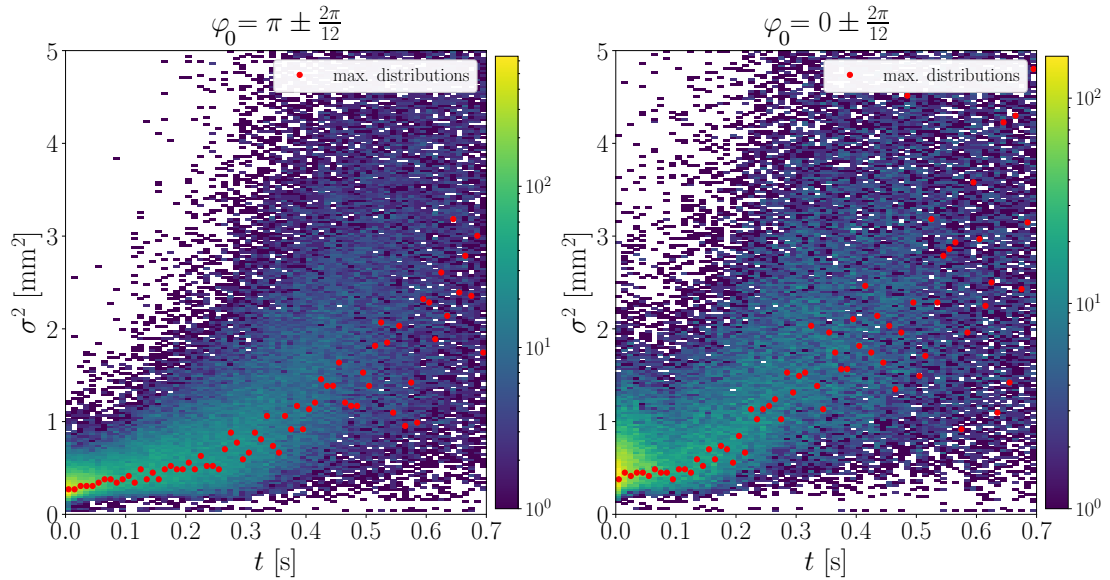


FIG A.16.: Shown are the line width distributions for lines heated in the wave trough (left) and at the crest (right), for the 10 Hz measurement of Emmel [2017]. Refer to figure 7.3 for further details, which is analogous. Note the smaller influence by the waves than for the 10 Hz measurement of January 2021, though the wind speed is the same.

## A.5

### NON-STATIONARY MEASUREMENTS

The temporal development of the viscous shear stress  $\tau_{\text{visc}}$  and surface velocity  $u_s$  for the non-stationary 5 Hz to the 8.8 Hz measurements of January 2021 are shown, and the non-stationary 10 Hz measurement by Emmel [2017]. Also the development of the water elevation  $\eta(t)$  is given for reference, for a fixed position on the laser sheet. Note the different temporal range in the plot of  $\eta$ , showing the first part of the measurements. More details regarding the seen developments are found in section 7.2.

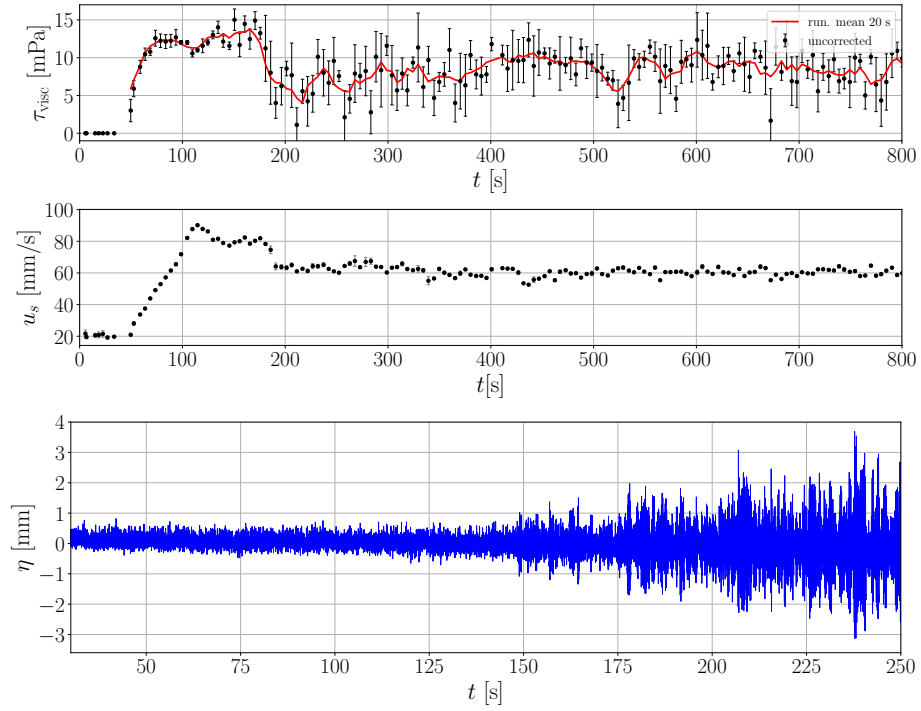


FIG A.17.: Viscous shear stress  $\tau_{\text{visc}}$  and mean surface velocity  $u_s$  for the non-stationary 5 Hz measurement and the evaluation of 5 s intervals. Refer to figure 7.9 for further details, which is analogous. There is a clear overshoot in  $u_s$  and  $\tau_{\text{visc}}$ . The temporal range in the plot of water elevation  $\eta$  differs from the two upper plots. The red curve in the upper plot shows the running mean of 20 s.

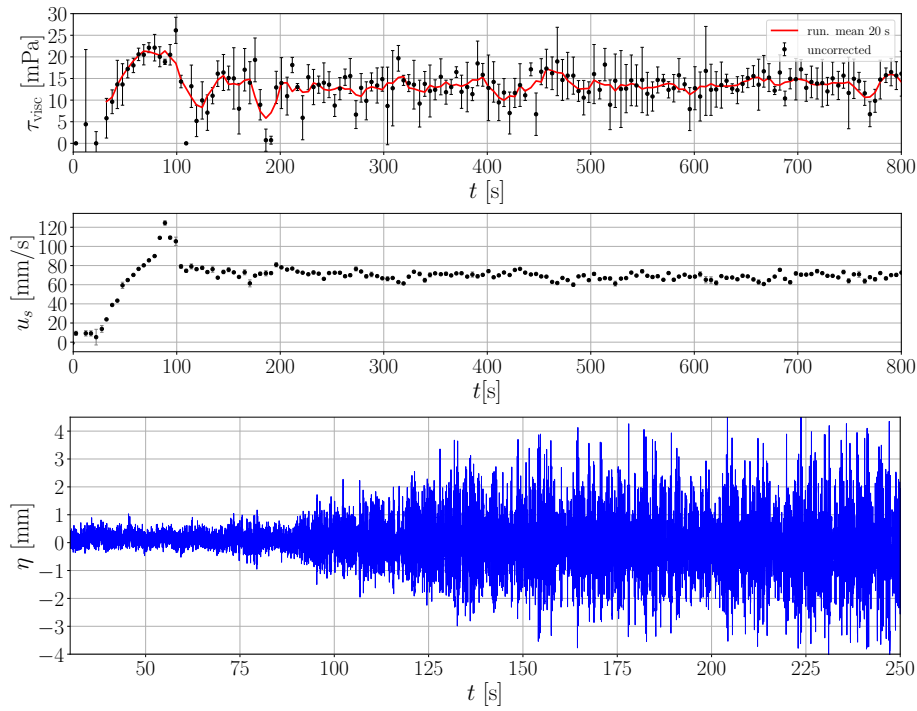


FIG A.18.: Viscous shear stress  $\tau_{\text{visc}}$  and mean surface velocity  $u_s$  for the non-stationary 6.3 Hz measurement and the evaluation of 5 s intervals. Refer to the analogous figure 7.9 for details. The temporal range in the plot of water elevation  $\eta$  differs from the two upper plots.

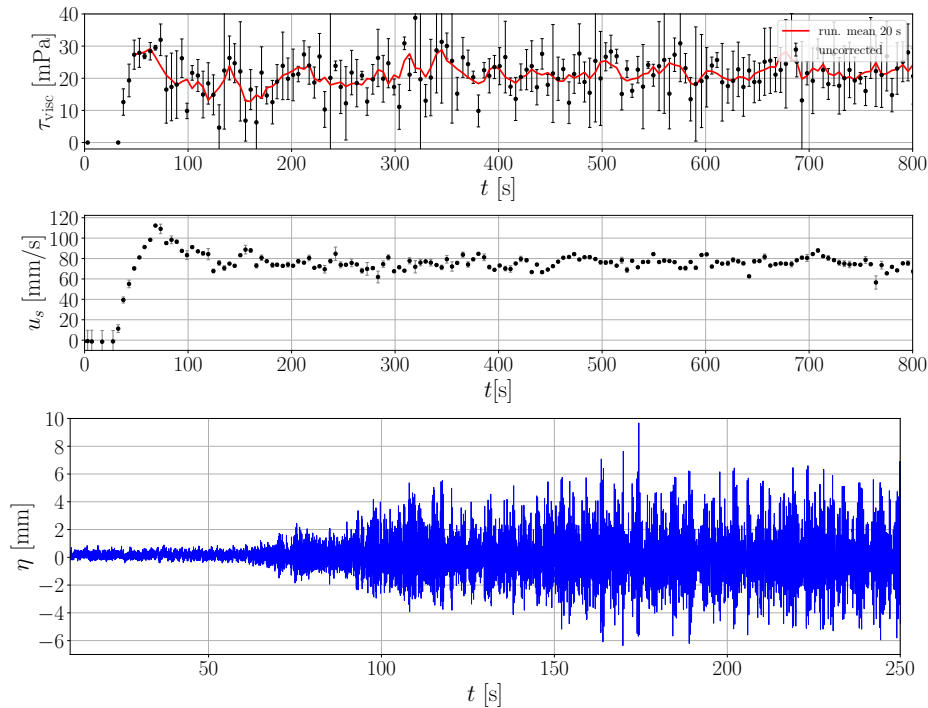


FIG A.19.: Viscous shear stress  $\tau_{\text{visc}}$  and mean surface velocity  $u_s$  for the non-stationary 7.5 Hz measurement and the evaluation of 5 s intervals. Refer to the analogous figure 7.9 for details. The temporal range in the plot of water elevation  $\eta$  differs from the two upper plots.

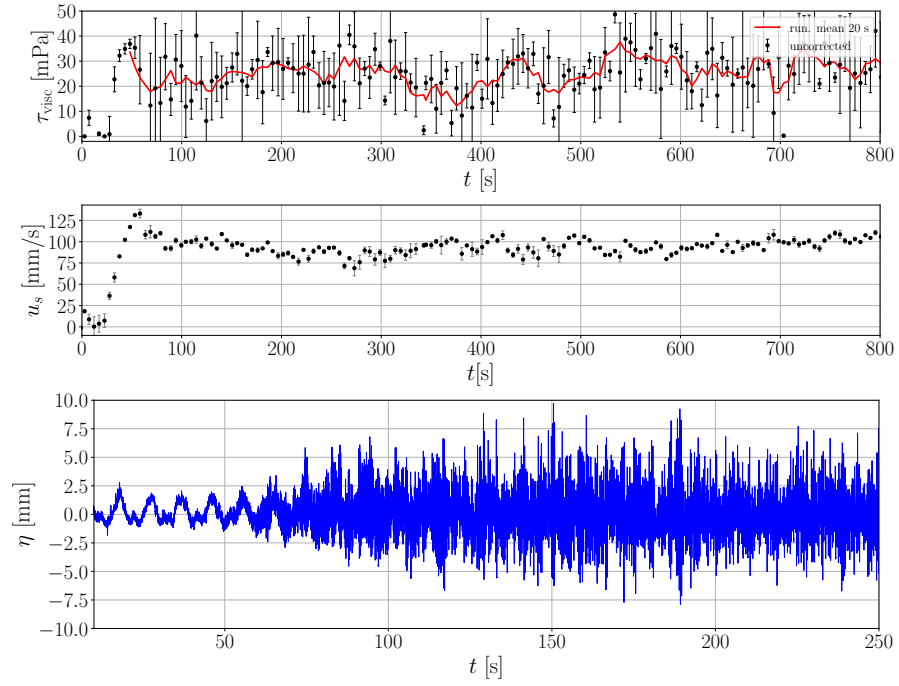


FIG A.20.: Viscous shear stress  $\tau_{\text{visc}}$  and mean surface velocity  $u_s$  for the non-stationary 8.8 Hz measurement and the evaluation of 5 s intervals. Refer to the analogous figure 7.9 for further details. The long-period waves of small amplitude in the water elevation  $\eta$ , also present before the wind was turned on, are caused by refilling water before the measurement. The temporal range in the plot of water elevation  $\eta$  differs from the two upper plots.

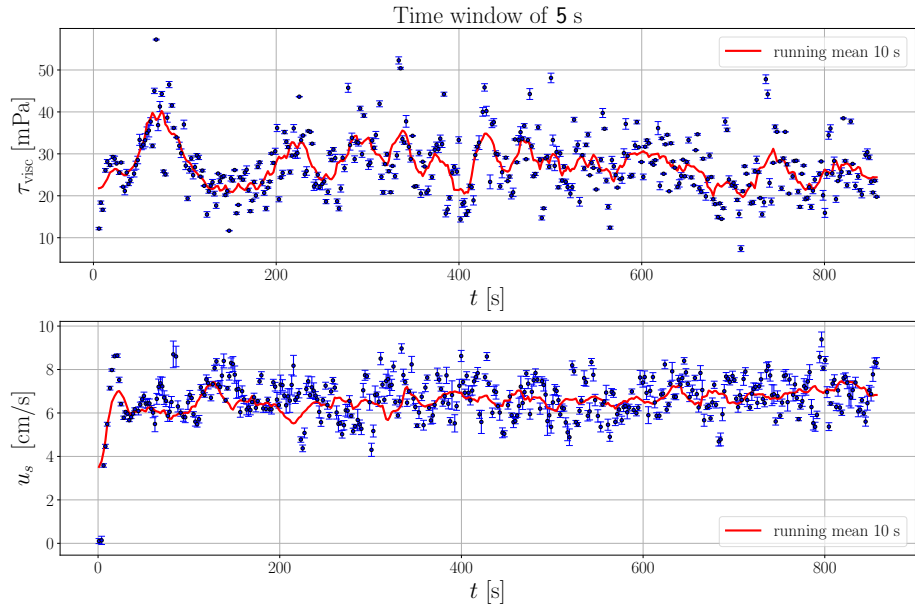


FIG A.21.: Viscous shear stress  $\tau_{\text{visc}}$  and mean surface velocity  $u_s$  for the non-stationary 10 Hz measurement of Emmel [2017] and the evaluation of 5 s intervals. Refer to figure 7.9 for further details, which is analogous. Both the surface velocity  $u_s$  and the viscous shear stress  $\tau_{\text{visc}}$  is considerably lower than for the 10 Hz measurement of January 2021, refer to section 7.2 for further discussion.

## A.6

### FURTHER PSV RESULTS

In the following the particle streak velocimetry results (PSV) for the stationary 5 Hz and the 7.5 Hz wind reference measurements of January 2019 are shown. Tilde (i.e.  $\tilde{a}$  for quantity  $a$ ) denote wave phase  $\varphi$  specific averaging and the overline ( $\bar{a}$ ) the average over all phases. The results must be interpreted with care, since artifacts of the measurement method are likely to be present. Refer to section 7.5 for further details.

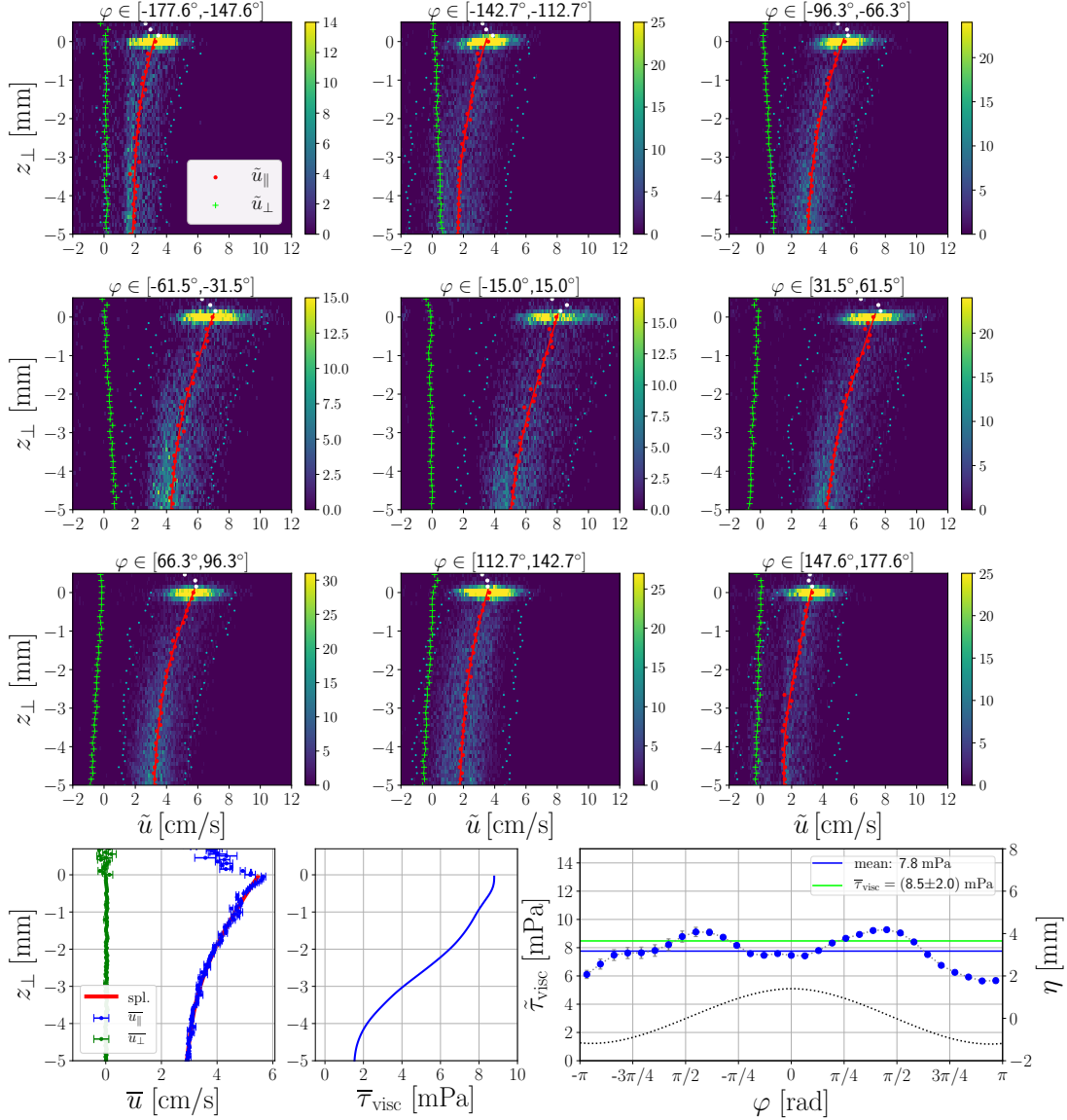


FIG A.22.: Profiles of the tangential  $u_{\parallel}$  and normal  $u_{\perp}$  velocity as function of depth normal to the surface  $z_{\perp}$  and the viscous shear stress  $\tau_{\text{visc}}$  for the 5 Hz measurement. Refer to the analogous figure 7.11 and section 7.5. The colour scales in the upper plots are oversaturated at the surface ( $z_{\perp} = 0$ ). The seen distribution of the shear stress in dependence of wave phase (lower left) may be considerably influenced by artifacts of the evaluation. The value used as reference is  $\bar{\tau}_{\text{visc}}$  from the mean velocity profile (lower left and middle plot).

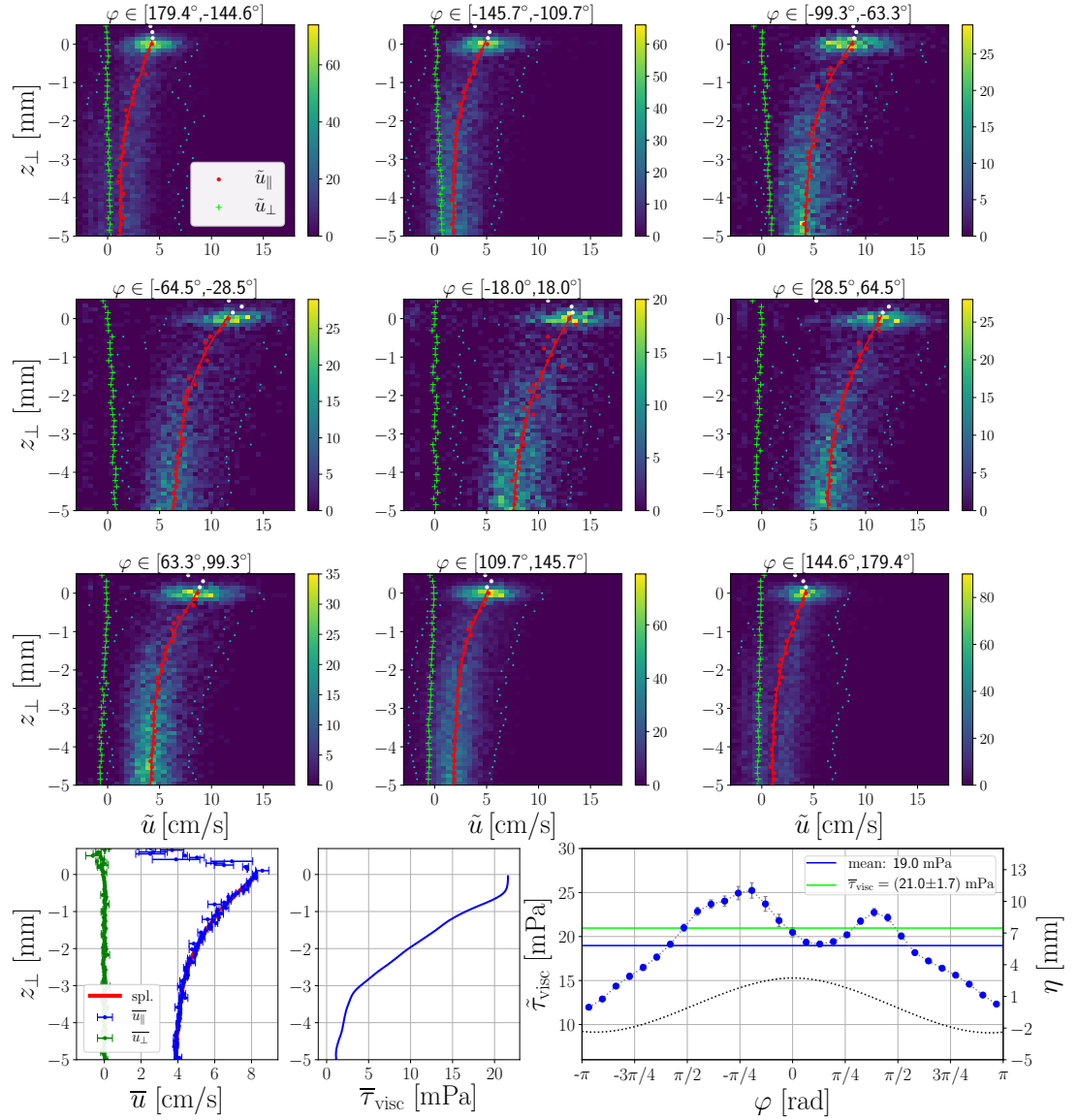


FIG A.23.: The evaluation of the viscous shear stress for the 7.5 Hz measurement. Refer to figure 7.11, which is analogous, and section 7.5 for further details. The seen distribution of the shear stress in dependence of wave phase (lower left) may be considerably influenced by artifacts of the evaluation. The value used as reference is  $\bar{\tau}_{\text{visc}}$  from the mean velocity profile, see the lower left and middle plot.



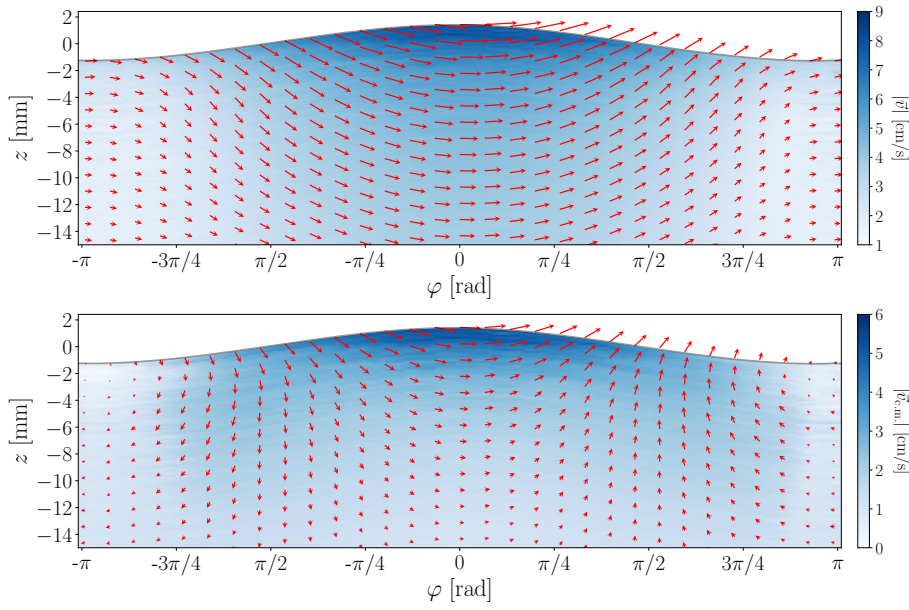


FIG A.24.: The mean velocity field for the 5 Hz measurement. Refer to the analogous figure 7.16 and section 7.5 for further details. Note the higher water speeds for  $\varphi \sim \pm\pi/2$ , best seen in the co-moving reference frame (lower plot), possibly an artifact of the evaluation. The increased velocities in the boundary layer give rise to the viscous shear stress. Note the large influence by orbital motion on the flow field.

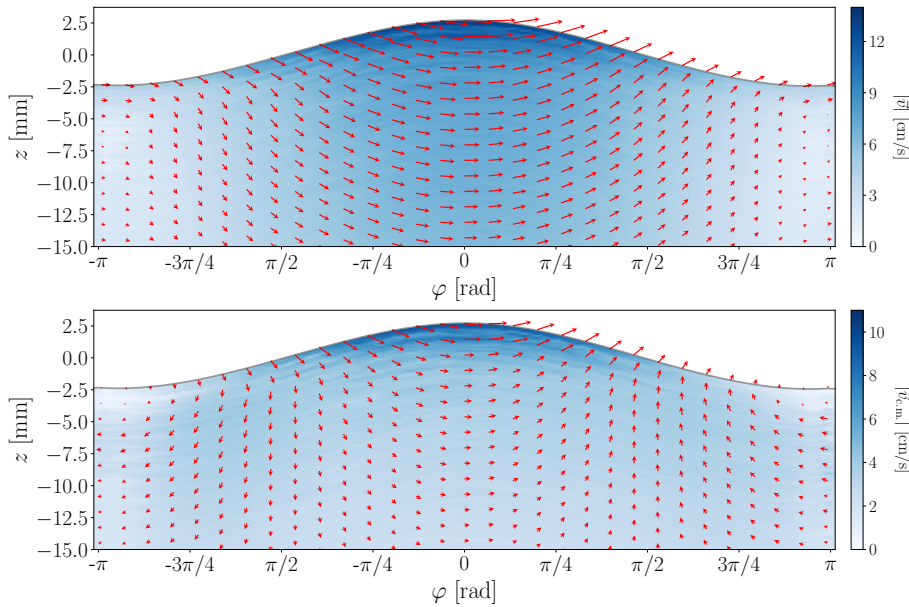


FIG A.25.: The mean velocity field for the 7.5 Hz measurement. Refer to the analogous figure 7.16 and section 7.5 for further details. Note the slightly higher water speeds for  $\varphi \sim \pm\pi/2$ , best seen in the co-moving reference frame (lower plot), possibly an artifact of the evaluation. The increased velocities in the boundary layer give rise to the viscous shear stress. Note the large influence by orbital motion on the flow field.

# B | MATHEMATICAL TOOLS

In this chapter some of the most important mathematical tools and formulas in this thesis are given. For further information, refer to Jähne [2012].

## THE FOURIER TRANSFORM

The continuous Fourier transform is given by

$$\hat{f}(\vec{k}) = \mathcal{F}\{f(\vec{x})\}_{\vec{k}} = \frac{1}{\sqrt{2\pi}^d} \int_{\mathbb{R}^d} f(\vec{x}') \exp(-i\vec{k} \cdot \vec{x}') d\vec{x}', \quad (\text{B.1})$$

with the inverse transform

$$\hat{f}(\vec{x}) = \mathcal{F}^{-1}\{f(\vec{k})\}_{\vec{x}} = \frac{1}{\sqrt{2\pi}^d} \int_{\mathbb{R}^d} f(\vec{k}') \exp(i\vec{k} \cdot \vec{x}') d\vec{k}', \quad (\text{B.2})$$

where  $\vec{x}$  and  $\vec{k}$  are  $d$ -dimensional conjugate variables, e.g. space and wave number vectors, and  $f$  and  $\hat{f}$  are referred to as Fourier transform pairs. The discrete Fourier transform of a (complex) sequence

$x_0, x_1, \dots, x_{N-1}$  to the transformed sequence  $X_0, X_1, \dots, X_{N-1}$ , and the inverse transform, is given by:

$$X_k = \sum_{n=0}^N x_n \exp(-i\frac{2\pi}{N}kn) \text{ and } x_n = \frac{1}{N} \sum_{k=0}^N X_k \exp(i\frac{2\pi}{N}kn), \quad (\text{B.3})$$

respectively. In analogy to equation (B.3) the transfer function  $\hat{\mathbf{A}}$  of a two dimensional mask (kernel), i.e. the discretized operator, can be calculated, with  $\kappa_i = 2\pi/N_i$

$$\hat{\mathbf{A}}(\kappa_x, \kappa_y) = \sum_m \left[ \sum_n A_{m,n} \exp(-i\kappa_x n) \right] \exp(-i\kappa_y m). \quad (\text{B.4})$$

## CONVOLUTION AND CROSS CORRELATION

Convolution of images by masks is a central part of the image processing of this thesis, and is in the continuous and real, one dimensional case given as

$$(f * g)(t) = \int_{-\infty}^{\infty} f(t')g(t - t') dt' \quad (\text{B.5})$$

where the asterisk denotes the convolution operator, or in the discrete case:

$$(f * g)_n = \sum_m f_m g_{n-m}. \quad (\text{B.6})$$

Both equations can be extended to higher dimensions. Moreover, the convolution theorem is given by:

$$\mathcal{F}\{(f * g)(\vec{x})\}_{\vec{k}} = \sqrt{2\pi}^d \hat{f}(\vec{k}) \cdot \hat{g}(\vec{k}), \quad (\text{B.7})$$

hence a convolution in real space corresponds to a multiplication in Fourier space. In the discrete case of multidimensional image processing, especially if the masks or images are large or the number of spatial dimensions high, it is computationally less expensive to transform into Fourier space by fast Fourier transforms, perform the multiplication, and transforming back, especially if the mask is separable into one dimensional masks (i.e.  $M = M_x * M_y$  for a two dimensional mask  $M$ ). The latter property enables the multiplication with the one dimensional masks, further reducing computational expense.

Related to the convolution is the cross-correlation,

$$(f \star g)(t) = \int_{-\infty}^{\infty} f(t')g(t+t') dt', \quad (\text{B.8})$$

used for finding the lag or displacements between signals, and can be discretized in analogy to equation B.6.

#### IMPORTANT MASKS IN THIS WORK

For the image processing used in this work, especially the binomial masks of degree two and degree four are important,

$${}^2\mathcal{B} = \frac{1}{4}[1 \ 2 \ 1] \text{ and } {}^4\mathcal{B} = \frac{1}{16}[1 \ 4 \ 6 \ 4 \ 1]. \quad (\text{B.9})$$

The two dimensional masks are then given by the convolution of the column- with the row vectors, hence they are separable by construction.

For the calculation of image gradients, the following 5 tap filters were used (refer to Farid and Simoncelli [1997] for further details):

$$\kappa = [0.030320 \ 0.249724 \ 0.439911 \ 0.249724 \ 0.030320] \quad (\text{B.10})$$

$$D = [0.104550 \ 0.292315 \ 0.000000 \ -0.292315 \ -0.104550], \quad (\text{B.11})$$

where  $\kappa$  is used for interpolation and  $D$  for differentiation. Note that  $D$  and  $\kappa$  are applied along different axes. In the case of computing a vertical gradient of an image,  $\kappa$  is horizontal (i.e. row vector) and  $d$  vertical (column vector).

#### THE HILBERT TRANSFORM

In order to calculate the phase and the envelope of a (real-valued) signal, a Hilbert transform can be computed,

$$\mathcal{H}\{f(x)\} = \frac{1}{\pi} \int_{-\infty}^{\infty} \frac{f(x')}{x' - x} dx', \quad (\text{B.12})$$

if the Cauchy principal value of the integral exists (Liu [2012]). The Hilbert transform can be used to calculate the complex analytic signal  $f_a$ , given by

$$f_a(x) = f(x) + i\mathcal{H}\{f(x)\}, \quad (\text{B.13})$$

from which the envelope  $a$  and phase  $\varphi$  is computed:

$$a(x) = |f_a(x)| \text{ and } \varphi(x) = \arg(f_a(x)). \quad (\text{B.14})$$

#### PENALIZED CUBIC SPLINES

For interpolation, or if a theoretical model is unavailable, splines are often used for describing the observations. These are piecewise polynomials, and e.g. cubic splines possess the advantage of being differentiable for all points except at their end points. The number of knots is adjusted until the requirement regarding the deviation from points to be interpolated is met. Mostly used in this work are penalized (smoothing) splines, with a few exceptions, where the curvature of the splines is penalized such that the resulting spline is smoother and less prone to overfitting. This is in this work done with de Boor's approach (refer to de Boor [2001]), for a cubic spline interpolant  $s_3$  achieved by minimizing the criteria

$$p \sum_i \left( \frac{y_i - s_3(x_i)}{\delta_i} \right)^2 + (1 - p) \int (s_3''(x))^2 dx, \quad (\text{B.15})$$

where  $\delta_i$  is the uncertainty of the data point  $(x_i, y_i)$ , yielding a weighting of the points, and  $p \in [0, 1]$  is the smoothing parameter for penalization of the curvature (second derivative) of the spline,  $s_3''(x)$ . The first term describes the squared differences, hence for  $p = 0$  a straight line results, and for  $p = 1$  the non-penalized spline interpolant.

# DANKSAGUNG

Ich möchte mich herzlich bei allen bedanken, die mich während dieser Arbeit unterstützt haben.

Bei Herrn Prof. Dr. Bernd Jähne möchte ich mich für die Ermöglichung dieser interdisziplinären Arbeit der Umweltphysik und Bildverarbeitung bedanken. Zusätzlich zur Bereitstellung der technischen Ausrüstung, war auch seine Wertschätzung eigenständiger Arbeit und die daraus resultierende Freiheit, interessanten Entdeckungen nachzugehen, höchst motivierend. Ich habe dadurch sehr viel gelernt. Dazu kommen seine hilfreichen Ideen, Vorschläge und seine Unterstützung.

Auch bei Herrn Prof. Dr. André Butz möchte ich mich für das Interesse an dieser Arbeit und die Übernahme des Zweitgutachtens bedanken.

Ein großer Dank geht an die Mitglieder der Windis-Arbeitsgruppe am IUP, die durch zahlreiche Ratschläge, Diskussionen und durch das Korrekturlesen zu dieser Arbeit beigetragen haben. Ein spezieller Dank geht an Kerstin Krall für die enge Zusammenarbeit, und an Günther Balschbach für viele interessante Einblicke und Gespräche. Ich möchte mich auch bei Arne Emmel bedanken für die Bereitstellung der Rohdaten seiner Bachelorarbeit.

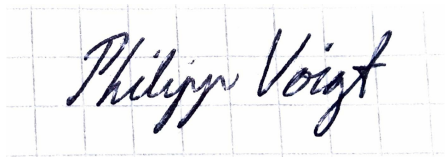
Für die Unterstützung während dieser Arbeit möchte ich mich auch bei meiner Familie und meinen Freunde bedanken. Ein besonderer Dank geht an meine Freundin Kathrin für das Beiseitestehen und auch für viele fachliche Diskussionen und das Korrekturlesen. Bei meinem Mitbewohner Jonas bedanke ich mich für die unzähligen Diskussionen zu allen Tageszeiten.

Jeg ønsker også å rette en takk til mine venner i Norge, som utover det sosiale har vært både tålmodige og støttende gjennom arbeidet. Tidligere Windis-medlem Sonja Friman ønsker jeg å takke for mange spennende diskusjoner også langt utover fagfeltet, i tillegg til et veldig stort engasjement i korrekturlesingen.



Erklärung:

Ich versichere, dass ich diese Arbeit selbstständig verfasst habe und keine anderen als die angegebenen Quellen und Hilfsmittel benutzt habe.

A handwritten signature in black ink, reading "Philipp Voigt", is written on a light gray grid background. The signature is in a cursive style.

Heidelberg, den 07.08.2021